University of Strathclyde

Department of Pure and Applied Chemistry

The Synthesis of stable nanotags for the detection of biomolecules using surface enhanced Raman Scattering

By Sian Sloan-Dennison

A thesis submitted to the Department of Pure and Applied Chemistry, University of Strathclyde, in fulfilment of the requirements for the degree of Doctor of Philosophy.

May 2017

The thesis is the result of the author's original research. It has been composed by the author and has not been previously submitted for examination which lead to the award if the degree. The copyright of this thesis belongs to the author under the terms of the United Kingdom copyrights act as qualified by University of Strathclyde Regulation 3.50. Due acknowledgment must always be made of the use of any material contained in, or derived from this thesis.

Signed: Date:

Acknowledgments

I would like to start by thanking my supervisors Professor Karen Faulds and Professor Duncan Graham for all their input, guidance and patience they have given me throughout my PhD. I have been given some fantastic opportunities and enjoyed my time at the centre for Nanometrology. I would also like to extend my thanks to Professor Neil Shand all his assistance and DSTL for funding

Huge thanks to all the members of the Centre for Nanometrology (old and new) for the countless nights out, all the group shenanigans and for finally awarding me with a Rammie. Special thanks to Laura Frame, Fay Nicolson, Craig Ward, Ryan Kane, Rachel Norman, Alex Girard and Pietro Gancitano for calming me down in the last 3 months, all the science chat and for the amazing SciX trip!

I would also like to thank all Dr Stacey O'Donnell for the SLISA help, Dr Sam Mabbott for his SEM expertise, Dr Kirsten Gracie for all her help in proof reading and Corrina Wetherill for providing me with cells.

Most importantly, thanks to my parents for always believing in me and my family and friends for their constant support.

And last but not least Kyle for putting up with me and keeping me sane. I am thankful for everything you have done.

Abstract

Artificial enzymes have become an increasingly interesting area of research due to their many advantages over natural protein enzymes which are expensive, difficult to isolate and unable to stand harsh environments. An important area of this research involves using metal nanoparticles as artificial enzymes, known as nanozymes, which exhibit peroxidase-like activity enabling them to catalyse the oxidation of substrates such as 3,3',5,5'-tetramethylbenzidine (TMB) and 2,2′-azino-bis(3-ethylbenzothiazoline-6-sulfonate) (ABTS) and in the presence of hydrogen peroxide (H_2O_2). This yields a colorimetric response which can be characterised using ultraviolet-visible (UV-vis) spectroscopy, Resonance Raman scattering (RRS) and surface enhanced resonance Raman scattering (SERRS). Nanozymes have been applied to various different applications, some of which are explored in this thesis.

The overall aim of this research was to investigate the synthesis of stable nanotags with a series of protective coatings to provide stability in harsh environments and catalytic activity. The catalytic activity of the nanotags were assessed using TMB and ABTS in the presence of H_2O_2 and the most promising were used for the detection of biomolecules with Raman spectroscopy which provided low limits of detection and were carried out on portable instruments making infield detection possible.

The catalytic activity of silver nanoparticles were also used in a surface based silver-linked immunosorbent assay to detect human C-reactive protein (CRP), an inflammatory marker and to detect oxidative stress in cancerous cells by monitoring the oxidation of TMB and analysing with SERRS.

Overall, nanozymes and Raman spectroscopy detection can be applied to a variety of applications leading to lower limits of detection of biomolecules in harsh environments and a cheaper alternative to enzymes.

Abbreviations

Ab	antibody
ABTS	2,2'-azino-bis(3-ethylbenzothiazoline-6-sulfonate)
Ag	silver
Au	gold
BSA	bovine serum Albumin
CRP	C-Reactive protein
CTC	charge transfer complex
CT(PEG)$_{12}$	carboxy-PEG-thiol
EDC	1-ethyl-3-(3-dimethylaminopropyl)carbodiimide
ELISA	Enzyme linked immunosorbent assay
Etd-1	ethidium homodimer
Fe$_2$O$_3$	ferromagnetic
FWHM	full width half maximum
H$_2$O$_2$	hydrogen peroxide
H$_2$PtCl$_6$	hexachloroplatinic acid
HCl	hydrochloric acid
HF	hydrofluoric acid
HRP	horse radish peroxidase
IgG	immunoglobulin
LSPR	localised surface plasmon resonance
MGITC	malachite green isothiocyanate
NaBH$_4$	sodium borohydride

NaCl	sodium borohydride
NP	nanoparticle
Pt	platinum
RPM	revolutions per minute
RRS	resonance Raman scattering
SEM	Scanning electron microscopy
SERRS	surface enhanced resonance Raman scattering
SERS	surface enhanced Raman scattering
SiO$_2$	silica
TMB	3,3'5,5'-tetramethybenzidine
UV-vis	Ultraviolet-Visible

Table of Contents

1. Introduction

In 1959, Richard P. Feynman gave a lecture describing the unknown field of nanotechnology and stated that 'There is plenty of room at the bottom', referring to bottom up design, instead of top down, which would allow key biological problems to be solved on the atomic scale.[1] Today his vision is practiced in the rapidly expanding field of nanotechnology and metal nanoparticles (NPs) are of great interest due to their unique optical properties and wide range of applications in areas such as imaging and treating cancer,[2] photothermal therapy,[3] biosensing[4] and DNA detection.[5]

1.1 Nanoparticles

NPs are defined as particles which have one or more dimension less than 100 nm.[6] A number of metallic elements can exist in this form such as gold (Au),[7] silver (Ag),[8] copper (Cu)[9] and platinum (Pt),[10] which exhibit different physical and chemical properties from their bulk metals. The first use of NP suspensions dates back to the 9th century, when Au and Ag NPs were unknowingly synthesised when being used to colour glass.[11] A popular example of this is the Lycurgus cup, which is dated back to the 1600's. The cup is made from glass containing gold and silver NPs, resulting in a colour change when the cup is viewed in reflected light, where the cup appears green, and when viewed in transmitted light the cup appears to be red as shown in Figure 1.1.[12]

Figure 1.1 The Lycurgus cup shown in reflected and transmitted light. [11]

1.1.1 Nanoparticle synthesis

The first scientific report of the synthesis of Au NPs was by Michael Faraday in 1857, who outlined a method of synthesis of Au NPs via the solution phase reduction of chloroauric acid using white phosphorus.[13] The optical properties of the Au NP solution differed greatly from the bulk material and this discovery formed the basis of metallic NP research.

Many synthesis methods have been developed since Faraday, and the most popular is the single phase reduction of a gold salt by citrate which was first devised by Turkevich in 1951[7] and later refined by Frens.[14] Typically, Au monodispersed NPs which are roughly 30 nm in size and red in colour with an extinction of 520 nm are synthesised.[15] However, different sizes can be obtained by controlling the ratio of gold to citrate as well as other shapes such as rods [16] or stars,[17] which have different optical properties and widen the applications of gold NPs.

Ag NPs are also widely used in nanotechnology and can be synthesised using the method reported by Lee and Meisel in 1982,[8] which uses silver nitrate combined with a sodium citrate solution which acts as both a reducing and stabilising agent. The negatively charged citrate ions coat the NPs with a negative charge which electrostatically repels them, also known as coulomb repulsion, from each other allowing them to remain stable in solution.[18] The Ag NPs produced are typically yellow in colour with a size of 70 nm and an extinction maximum of around 410 nm.[19] Other stabilising agents have also been used to stabilise Ag NPs and in 1986,

2

Schopfer *et al.* reported the reduction and capping of silver ions with ethylenediamineetetraacetic acid (EDTA).[20] The reduction of silver nitrate with hydroxylamine has also been reported and its simple and fast synthesis produces Ag NP which can be comparable and perhaps more advantageous than Lee-Meisel Ag NPs due to their rapid, more reproducible synthesis with no heating involved and the homogeneous and smaller sized NPs produced, between 40-50 nm.[21]

As well as Au and Ag, a variety of metals can be used to produce NPs. For example, ferromagnetic NPs have been prepared using an aqueous co-precipitation of $FeCl_3.6H_2O$ and $FeCl_2.4H_2O$, which when added to a base form magnetite (Fe_3O_4) NPs. The NP can then be oxidised upon the addition of ammonium hydroxide to maghemite (Fe_2O_3) NPs, which are black in appearance with a narrow size distribution and an average diameter of 12 nm.[22] The magnetic properties of Fe_3O_4 and Fe_2O_3 NPs allow them to compete with magnetic carriers for use in targeted-drug applications.[23]

Platinum (Pt) NPs are another well studied metal NP which can be easily synthesised by reducing a platinum salt, such as H_2PtCl_6, to Pt (O) creating a supersaturated mixture.[24] The Pt (O) then precipitates in the form of NPs which can then be capped and stabilised using sodium polyacrylic acid [25] or sodium citrate,[26] preventing aggregation and coalescence of the NPs.[10]

NPs display enhanced and useful radiative properties, such as Raman scattering and absorption due to their unique optical properties and the ability to control their size and shape, specifically tailoring their morphology towards diagnostic applications. A commonly exploited feature of NPs is their associated localised surface plasmon resonance which occurs when NP interact with light of a specific wavelength.

1.1.2 Localised Surface plasmon resonance

Spherical metal NPs have specific optical properties which are attributed to the collective oscillation of conduction electrons at their surface which is induced by interaction with the electromagnetic field of the incident light.[27] This oscillation of surface electrons (shown in Figure 1.2) is known as the localised surface plasmon resonance (LSPR).
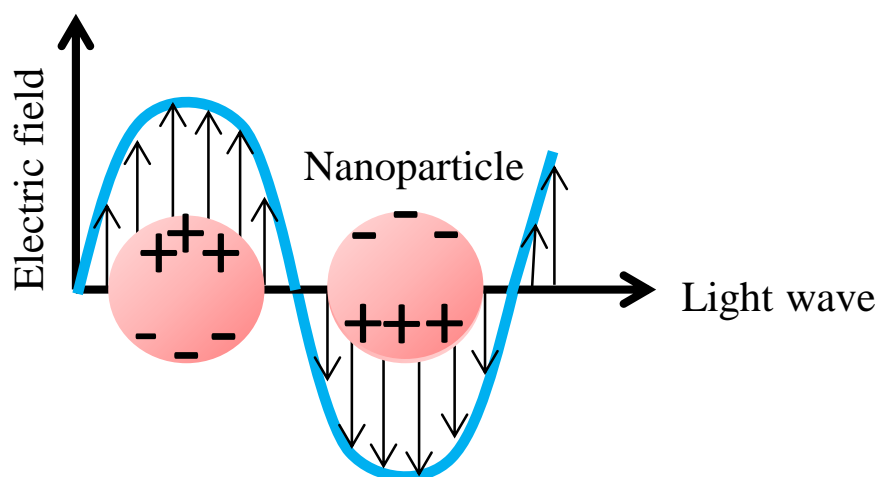
Figure 1.2 A schematic of localised surface plasmon resonance showing the oscillation of electrons in metal NPs in an electromagnetic field.

Gustav Mie first described the LSPR phenomenon in 1903 and deduced that the plasmon band was due to dipole oscillations of free electrons in the conductance band.[28] The excitation of the conductance band electrons results in strong absorption of the incident light and strongly scattered elastic light in the visible region resulting in the strong colours of noble metallic NPs.[29]

For small spheres of less than 100 nm in diameter, the LSPR is influenced by a number of factors. The size of the NPs will change the LSPR. When a NP increases in size, the surface area also increases and the LSPR exhibits a red shift.[30] The shape of NPs can also affect the LSPR, an example of this is the observed red shift associated with gold nanostars, with the degree of shift being determined by the length of the stars arms.[17] The change in dielectric constant of the NPs surrounding environments, which can occur due to surface modification, will also result in a LSPR shift and the same can also be said for the choice of metal used to form the NPs.[31] Changes due to different metals can be visualised by the dramatic change in LSPR of 30 nm Au NPs which is roughly 520 nm and 60 nm silver NPs which occurs at 410 nm.

The most commonly used feature of the LSPR of NPs, which makes them useful for bio-sensing, is the change in LSPR observed when the inter-particle distance of the NPs decreases. For example, 30 nm Au NPs typically will have an LSPR of 520 nm and be red in appearance, however when two gold NPs are in close proximity, their

LSPRs couple, which results in a red shift, and the greater the red shift, the shorter the inter-particle distance of the NPs. The solution will also visibly change colour to purple and this colour change can be used to detect aggregation of the NPs induced by specific biorecognition event for the detection of target biomolecules.[32]

1.2 Raman spectroscopy

Raman spectroscopy is a structural characterisation technique which relies on the inelastic scattering of monochromatic light. In 1923, Smekal theoretically predicted the inelastic scattering of light.[33] This was not demonstrated until Raman and Krishnan confirmed his hypothesis in 1928 by converged sunlight onto a material and detected the scattered light, which resulted in a change in energy. [34] The light detected, using complementary filters, was characterised by its 'feebleness in comparison with the ordinary scattering'[34] and became known as Raman scattering. With advances in instrumentation, as well as the development of advanced Raman techniques such as surface enhanced Raman spectroscopy (SERS) and surface enhance resonance Raman spectroscopy (SERRS), it has become an invaluable analytical technique for qualitative and quantitative analysis with a host of applications including bio-diagnostics,[4] explosive detection [35] and cancer imaging.[36]

1.2.1 Theory

When light interacts with a molecule it is either absorbed or scattered. If the energy of the incident photon coincides with the band gap energy of an electronic transition within the molecule, the molecule is promoted from the ground state to an excited electronic state. The loss of energy of the incident light, due to the absorption, can be measured. For scattering to occur, the incident photon does not have to match a band gap energy. When a photon interacts with a molecule, it can distort and polarise the cloud of electrons surrounding the nuclei, forming a short-lived, unstable 'virtual state'. [37] When the electron cloud relaxes, scattering occurs. Most of the scattering will occur at the same frequency as the incident photon and is known as Rayleigh scattering, which is shown in Figure 1.3.[37]

However, if energy from the incident photon is transferred to the molecule or from the molecule to the scattered photon, the resulting scattering is shifted by one vibrational unit, this is called Raman scattering. Raman scattering is therefore measured as the shift in energy from the laser frequency and there are two types of scattering that can occur; Stokes and anti-Stokes.[38]

Stokes scattering occurs when photons are scattered with a lower energy than that of the incident photon, due to the molecules relaxing to an excited vibrational state, which is higher in energy than the ground state. Anti-Stokes scattering occurs due to excitation by the incident photon of molecules which exist in a higher energy vibrational state; in this case energy is transferred from the molecule to the photon, resulting in the molecule returning to a lower energy vibrational state.[39] This can be better represented with the aid of a Jablonski diagram shown in Figure 1.3.
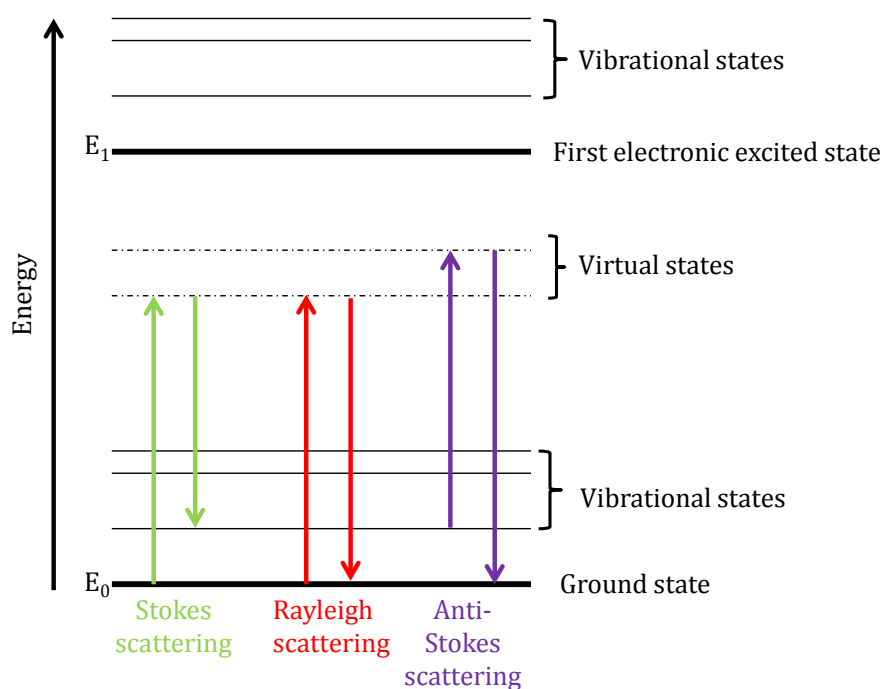
Figure 1.3 Jablonski diagram illustrating the process of Raman and Rayleigh scattering.

The energy difference between incident and scattered photons is represented by the length of the arrows. The energy difference between the initial and final vibrational levels (v) or Raman shift in wave-numbers (cm^{-1}) is calculated using Equation 2 in which λ represents the wavelength of the incident and scattered photons, respectively.[40]

$$v = \frac{1}{\lambda\ incident} - \frac{1}{\lambda\ scattered} \qquad\qquad \text{Equation 1}$$

The relative intensities of the two processes will depend on the population of the excited vibrational state. This is determined by the Boltzmann distribution (Equation 3).

$$\frac{N_n}{N_m} = \frac{g_n}{g_m} \exp\left[\frac{-(E_n - E_m)}{kT}\right] \qquad\qquad \text{Equation 2}$$

Where N_n is the number of molecules in the excited vibrational energy level, N_m is the molecules in the ground vibrational state, g is the degeneracy of levels m and n, E_n-E_m is the energy difference between vibrational energy levels, k is the Boltzmann constant and T is the temperature. The Boltzmann equation dictates that at room temperature most molecules are in the ground state prior to laser excitation; hence the majority of Raman scattering observed is Stokes scattering.[41] Anti-stokes, the weaker of the two processes at room temperature, occurs at higher temperatures as there is an increase in the number of molecules which are in a vibrationally excited state resulting in increased anti-Stokes scattering.

It should be noted that Raman scattering is an inherently weak process only 1 in every 10^{6-8} photons are Raman scattered, with the intensity of the Raman scattering being described by Equation 3.[42]

$$I = KI_L\alpha^2 v^4 \qquad\qquad \text{Equation 3}$$

Where I is the Raman intensity, K a constant, I_L is the power of the laser, α is the polarisability and v the frequency. The intensity of the Raman signal can therefore be improved by using a shorter excitation wavelength, which has a higher frequency/energy as the intensity is proportional to the frequency of the laser to the power of four.[43] However, by using shorter excitation wavelengths issues with

burning and sample degradation can occur, which can be avoided using resonance Raman scattering which can be used to increase the weak signals.

1.1.2 Resonance Raman scattering

Resonance Raman scattering (RRS) occurs when the frequency of the laser is close in energy to an electronic transition within the molecule being analysed. This results in Raman bands associated with the electronic transition being amplified in the order of 10^{3-4}.[44]

In Raman scattering, the molecule is promoted to a virtual energy state, however in RRS, the absorption of a photon from the 'resonant' incident laser causes the molecule to be promoted to an excited state within the first excited vibrational electronic state, which is depicted in the Jablonski diagram shown in Figure 1.4.[37]
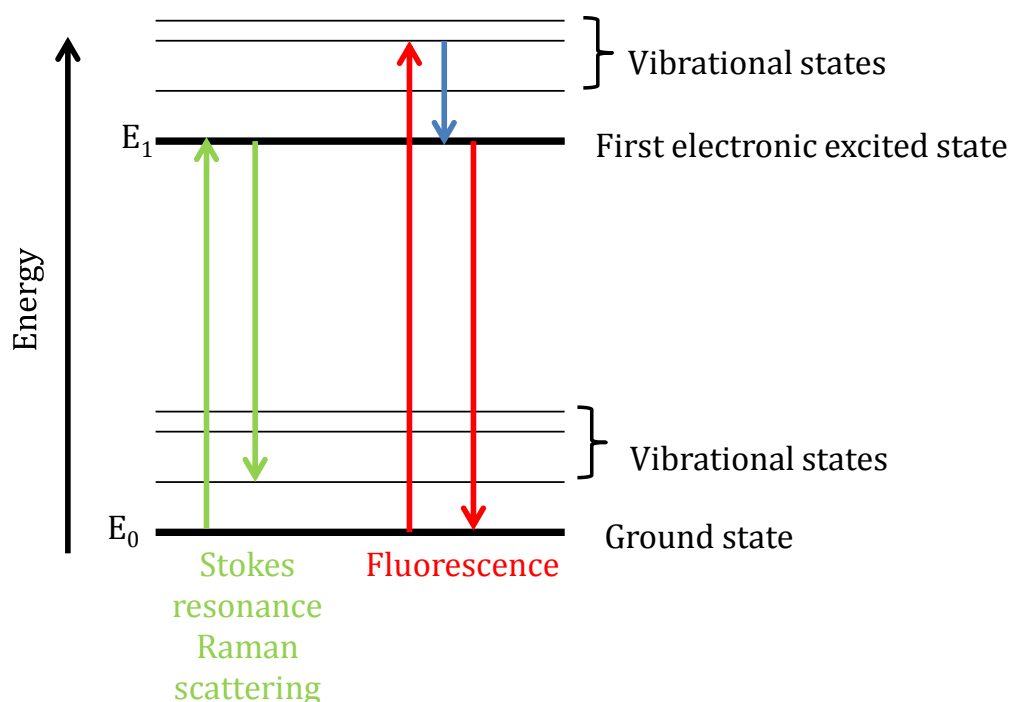
Figure 1.4 Jablonski diagram indicating the transitions between energy levels when the laser is in resonance with an electronic transition.

As a result of matching the laser energy to the electronic transition, fluorescence, a competing phenomenon shown in Figure 1.4, can also happen. Fluorescence occurs when the excitation photon is close to the transition energy between two states as

after the photon is absorbed is can relax from its vibrationally excited level back to the electronic state back to the lowest vibrational level of the electronic state. Fluorescence backgrounds can obscure Raman peaks, however due to the time scale, the fluorescence process typically requires more than nanoseconds while Raman is completed in picoseconds or less, pulsed lasers can be used to minimise the amount of fluorescence that can occur. The addition of NPs which can also reduce the background by quenching fluorescence and lead to surface enhanced Raman scattering.[38]

1.1.3 Surface enhanced Raman scattering

Raman scattering can be further enhanced when an analyte is adsorbed onto a roughened metal surface, this phenomenon is known as surface enhanced Raman spectroscopy (SERS). SERS was first observed by Fleischman *et al.* in 1974, [45] when a large Raman enhanced signal for pyridine was detected in the presence of a roughened silver electrode. Observation of this phenomenon led to different theories on the origin of the effect, with two groups offering opposing theories.

Jeanmaire and Van Duyne proposed that the enhancement was due to an electromagnetic effect,[46] whist Albrecht and Creighton suggested that it was because of a charge transfer effect.[47] However, both found that the overall enhancement was roughly 10^6 and agreed that it was due to light interacting with the roughened silver electrode as well as the molecule.[48]

The electromagnetic effect attributes the enhancement to an analyte being held close to, or adsorbed onto, the surface of a roughened metal surface, i.e. a NP, and an interaction occurring between the analyte and the LSPR. The incident light causes the surface electrons of the NP to oscillate creating the LSPR, which increases the local field experienced by analytes adsorbed onto the surface of the NP. The interaction of the analyte with the LSPR results in greater polarisation of the molecule and significantly increases the resulting scattering. The surface enhancement does not occur evenly around every isolated nanoparticle and is greatest at points where NPs touch or cluster. These are known as 'hot spots' and an enormous electric field is generated at the interstices between NPs and result in strong SERS.

Chemical, or charge transfer enhancement, is thought to give a smaller contribution to the overall enhancement. It occurs where a chemical bond is formed between the analyte and the metal surface, inducing a charge transfer between the molecule and the metal, creating new energy state which are in resonance with the laser excitation wavelength, therefore increasing the polarisability of the molecule hence enhancing the Raman scattering.[49]

Most researchers are in agreement that the SERS enhancement is due to a combination of both the electromagnetic and charge transfer mechanisms since it is impossible to completely describe all the observations by one mechanism alone.

To combine the enhancements and also take into account resonance from the analyte itself, Lombardi *et al.* published a 'unified expression' for the SERS intensity.[50] This incorporated all three effects in order to identify the parameters governing the amount of contribution and provided a systematic approach for the experimental determination of these contributions. This can be better understood by using the diagram in Figure 1.5 which indicates the observed resonances of Ag NPs functionalised with the Raman reporter crystal violet (CV).
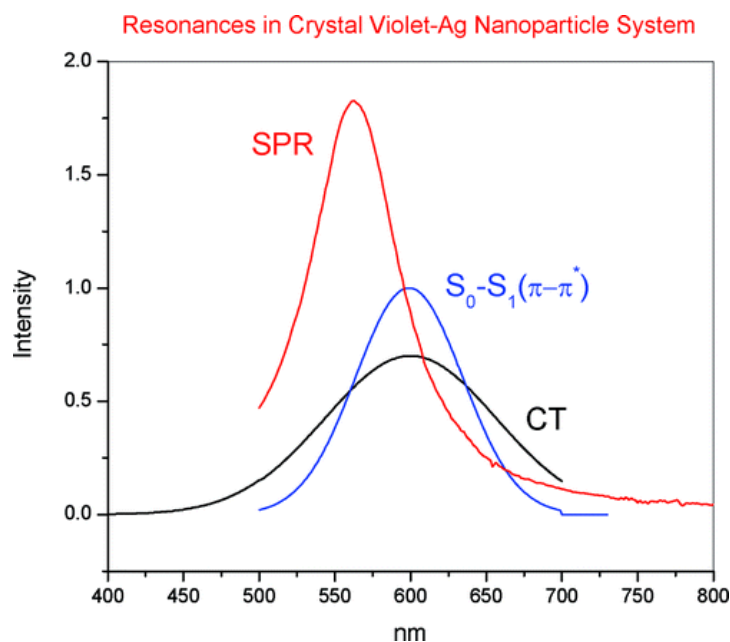
Figure 1.5 Observed resonances of Ag-NPs functionalised with CV. The SPR resonance indicated the resonance of the electromagnetic effect (red), S_0-S_1 (π- π)* is the absorbance maximum of CV which indicated the resonance contribution form the Raman reporter (blue) and CT is the resonance obtained from the formation of the charge transfer complex (black).[50] Reprinted with permission from Lombardi, J.R. and R.L. Birke, *A Unified View of Surface-Enhanced Raman Scattering.* Accounts of Chemical Research, 2009. **42**(6): p. 734-742. Copyright (2017) American Chemical Society.

Figure 1.5 illustrates the various resonances in a molecule-metal system for the popular Raman reporter CV and Ag NPs. All three resonances are in the visible region and overlap, with the highest intensity occurring around 575 nm, due to the SPR, and a very strong intense SERS signal would be obtained if interrogated with a laser excitation close to this due to the electromagnetic effect. At 600 nm, the SPR is no longer in resonance, however the molecule and the molecule-metal transitions are when the exciting light is around 600 nm, hence SERS can also be achieved using a laser excitation close to this, which would be due to the charge transfer mechanism and RRS.[50] This therefore emphasises that each contribution is important in understanding the relative intensities of a SERS spectrum.

As Lombardi reports, the resonance contribution from the analyte is important in the unified expression of SERS and the resonance enhancement combined with a roughened surface is commonly known as surface enhanced resonance Raman spectroscopy (SERRS).

1.1.4 Surface enhanced resonance Raman spectroscopy

Stacy and Van Duyne in 1983[51] first reported surface enhanced resonance Raman scattering (SERRS) which occurs when an analyte has a chromophore that is close in energy to the frequency of the excitation laser used to excite the plasmon of the roughened chemical surface. Therefore enhancement from plasmon resonance (SERS) and molecular resonance (RRS) both contribute to give enhanced Raman scattering of up to 10^{13}-10^{14} over normal Raman scattering.[52] One of the main advantages of SERRS is the ability of the metal surface to quench any fluorescence background obtained from a molecule, leading to improved spectra and a wider range of resonant molecules that can be used as SERRS analytes.

Using SERRS for the analysis of biomolecules has a distinct advantage over more conventional methods such as fluorescence or chemiluminescence based techniques, which provide limited characteristic structural information and broad emission spectra. Generally, detection techniques that use fluorophores give rise to broad emission bands, provide little characteristic structural information and large spectral overlap when multiple molecules are present. SERRS, however, gives sharp fingerprint spectra, that are molecularly specific, hence multiplexing is possible.[53]

SERS and SERRS are optical spectroscopy techniques which can be used to detect target biomolecules such as DNA and proteins in a fast, efficient and sensitive manner which has led to its progression in its use in the medical diagnostic field.[54] An example of the use of SERS for detecting DNA is by using a molecular beacon assay.[55] When a thiolated poly adenine DNA sequence is bound to the surface of Au nanoparticles, the adenine breathing mode will be enhanced depending on the orientation of the sequence on the nanoparticle. If the sequence is perpendicular to the surface, the adenine peak at 736 cm^{-1} will increase in intensity. However if it lies flat on the surface, the spectrum shows weak bands. Therefore, the open or closed conformation of the beacon due to hybridisation of a target sequence causes the orientation of the poly adenine DNA sequence to differ and this change can be detected using SERS.

Native proteins such as, lysozyme, avidin, bovine serum albumin, cytochrome c, and haemoglobin, have also been detected with SERS by monitoring the enhancement boost gained from using Ag nanoparticles which have been modified with iodine which prevented the direct interaction between the protein and metal surface.[56] This

therefore provided a label free, quantitative identification of proteins and further demonstrated the method could be extended for label-free multiplexing analysis of protein mixtures.

When nanoparticles have been functionalised with dyes they are capable of providing SERRS and when also conjugated to targeting moieties can be used in molecular imagining. For example when pegylated SERRS nanoparticles are administrated in preclinical cancer models, the highly sensitive detection of the tumour is achieved by Raman imaging the residual legions and the corresponding SERRS dye on the nanoparticle, indicating the infected area, is obtained.[57]

Overall, Raman spectroscopy provides characteristic structural information of a molecule which can be increased by using nanoparticles and resonant dyes. It can be used in many different applications, some of which are explored in this thesis.

2. Nanoparticles in harsh environments

2.1 Introduction

Metal NPs play an important role in biosensing due to their optical properties and the ability to functionalise their surface with molecules. Recently there has been a great interest in the investigation of Au and Ag NPs functionalised with protective coatings such as silica and other metals to create nanotags for use in different chemical and biological environments.[58]

2.1.1 Silica coated nanoparticles

Silica is being increasingly used for the shelling of metal NPs to provide robust surface protection with consistent surface chemistry.[59] The shell is considered to 'physically sequester' the NPs which allows the exploitation of the optical, electrical and catalytic properties of the core while protecting it from the environment.[60] Silica growth can be achieved using the Stober synthesis,[61] which involves the ammonium hydroxide-catalysed hydrolysis and condensation of alkoxy-silanes in low molecular-weight alcohols. Vitrophilising agents such as amino functionalised silane coupling molecules are used to facilitate the silica shell growth on the NP surface. They create a self-assembled monolayer around the NP which enhances the stability of the core in preparation for the harsh conditions required for silica growth and provide a vitreophilic surface for the growth of the silica shell via alkoxysilane condensation.[59]

In 2010, Tian and co-workers reported a 'shell isolated nanoparticle enhanced Raman spectroscopy' based system known as SHINERS.[62] SHINERS are nanotags that consist of Au NPs, encapsulated in a very thin silica or alumina shell. The silica or alumina shell protects the Au NP core from the surrounding environment and prevents any unwanted non-specific interactions of the Au NP with other species in the environment.[63]

By adding a Raman reporter to the surface of the Au NP, a SERS signal can be obtained from the tag as demonstrated by Schlucker *et al.*[64] In their approach, Au

NPs were functionalised with a monolayer of Raman reporter molecules, covered with a protective silica shell and then functionalised with a biorecognition molecule. By functionalising the tag with the biorecognition molecule it can then be used for biological analysis in vitro as the silica shell minimises cellular or tissue auto-fluorescence which can dramatically affect the signal to background ratio.[63] The Raman reporter molecule allows the location of the tag to be tracked using Raman, for example within a cell. Figure 2.1 shows the structure of the final nanotag.
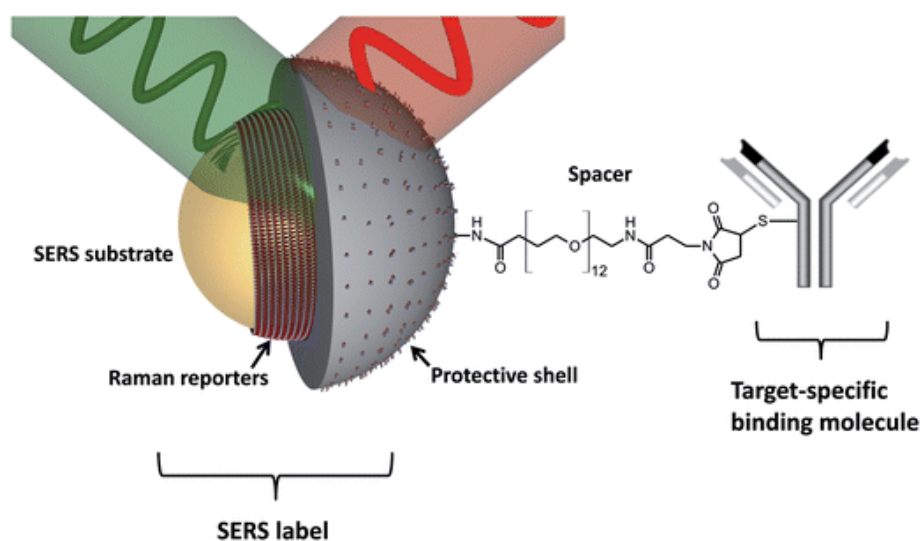
Figure 2.1 Au NPs with a self-assembled monolayer of Raman reporter molecule and a protective silica shell with amino groups, functionalised to a heterobifunctional polyethylene glycol spacer and a monoclonal antibody for antigen recognition.[64] Reprinted with permission from Küstner, B., et al., *SERS Labels for Red Laser Excitation: Silica-Encapsulated SAMs on tunable Gold/Silver nanoshells.* Angewandte Chemie International Edition, 2009, **48**(11): p. 1950-1953. American Chemical Society. Copyright (2017) John Wiley and Sons.

When creating a SERS active silica coated NPs, there is competition for space on the metal surface between the Raman reporter molecules and the vitreophilising agents which facilitates the silica coating on the NP surface. Successful silica encapsulation of Au NPs is easily achieved via covalent attachment of silica precursors and the Raman reporter to give a monolayer of both molecules. However, silica encapsulation of Ag NPs is more difficult and a SERS active molecule that can also provide a vitreophilic surface is required.

It 2010, Rock *et al.* investigated a reproducible method for the successful silica encapsulation of Ag NPs via a tri-functional reporter molecule.[59] Tri-functional benzotriazole dyes were designed to act as both a Raman reporter molecule for SERS and a precursor for the silica shelling of Ag NPs which allowed the controlled synthesis of silica shelled, dye coded, SERS active Ag nanotags. Ag–silica nanotags have a wide range of applications where gold has previously been used but offer the alternative optical properties of Ag and stronger SERS responses using visible Raman excitation wavelengths.

The applications of silica coated NPs show their versatility and applicability. However, these nanotags do have limitations as silica shells are not compatible with harsh environment. Acidic corrosion occurs by dissolving the alkali in the silica composition, leaving a porous surface consisting of the silica network with holes where the alkali has been removed which could expose the NP core allowing aggregation to occur. Whereas alkaline conditions attack the silica surface which simply dissolves it at a uniform rate and again this would expose the NP core causing aggregation.[32] The aggregation would have an adverse effect on the Raman reporter SERS signal, therefore to further protect NPs, metal shells can be applied to NPs.

2.1.2 Bimetallic NPs

2.1.2.1 Gold and silver nanoparticles

Recently, there has been a significant interest in bimetallic NPs as they exhibit optical, electronic, magnetic and catalytic properties which are distinct from the properties of the corresponding NPs.[65] Many different bimetallic NPs can be synthesised including Au-Ag core-shell nanotags.

Ag NPs can be easily oxidised, however by coating Au NPs with an Ag layer to form a core-shell structure, a unique electronic interaction occurs at the interface between the two metals occurs which increases the stability.[66]

The Au NPs are used as the template that controls the overall particle size. When a critical Ag shell thickness is applied to the Au NPs, the Ag cannot be oxidatively etched from the particles surface, unlike the complete oxidative etching that occurs

for Ag NPs.[66] Since the resulting Au-Ag nanotags display unique electronic properties and are stable against oxidation, they can be used in sensing applications that require the presence of high levels of salt. It has also been reported that Raman reporter can be entrapped in the shelling process and the nanotags can be used for quantitative SERS measurements were the reporter acts as an internal reference. [67]

2.1.2.2 Platinum coated silver nanoparticles

Another bimetallic nanotag consists of Ag NPs coated in a platinum shell (Ag-Pt) reported by Weaver *et al.*[68] which utilises both local and electrical field enhancement provided by the Ag NP core and allows for the probing of the vibrational properties of some absorbents on the Pt surface. These NPs are stable for a number of months and can be used for catalysis as Ag-Pt nanotags exhibit enhanced catalytic activity for methanol electro-oxidation,[69] catalytic oxidation of o-phenylenediamine (OPD) by hydrogen peroxide (H_2O_2) [69] and show higher activity towards the hydrogen evolution reaction.[70]   Ag-Pt nanotags are usually synthesised by the galvanic replacement reaction between Ag NP 'seeds' and potassium tetrachloroplatinate (K_2PtCl_4).[65] The reaction occurs between Ag and Pt as follows:

$$4Ag + PtCl_4^{2-} \longrightarrow Pt + 4AgCl$$
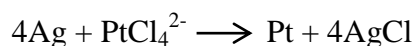
When $PtCl_4^{2-}$ is reduced, platinum is formed and deposited on the surface of the Ag NP and they resulting nanotags can be characterised using transmission electron microscopy and resonance light-scattering spectroscopy.[71]

2.1.2.3 Platinum coated gold nanoparticles

Au NPs have also been coated in Pt to create a Au-Pt nanotag which improved electrocatalyic activity towards the reduction of H_2O_2.[72]   There are a number of methods that Au NPs can be coated with Pt including the copper-underpotential deposition (Cu-UPD).[73] This involves coating the Au NP with a monolayer of Cu via a UPD, which was then replaced with Pt by undergoing a redox replacement. The Pt was reduced and simultaneously deposited on the Au NP creating an ultra-

thin layer. As well as the catalytic property of these NPs, Pt is known to be resistant to many acids (including hydrofluoric acid) [74], therefore a platinum coating on Au and Ag NPs could protect the NPs from being destroyed in harsh acidic environments.

2.2 Chapter Aims

The aim of this chapter was to synthesise a nanotag which would be stable in a variety of harsh environments, in particular hydrofluoric acid (HF), over time. HF is classified as a weak acid with a lower dissociation compared to stronger acids, due to the strength of the hydrogen-fluorine bond.[75] Hoverer, it is extremely hazardous and very corrosive due to its fluoride anion, therefore it is likely to dissolve almost all metal NPs and any Raman reporter molecules functionalised to the NP surface.[76] Therefore, if NPs are to remain stable in HF and retain a SERS signal, they have to be protected by a material resistant to HF. There are few materials that are resistant and these include polyethylene, polyaniline, fluorocarbon plastic, lead and bulk gold and platinum.[77]

By investigating coatings for the protection of Au NPs it was hoped that they would remain stable for up to a month. The nanotags stability was monitored by analysing the LSPR using extinction spectroscopy, the size using dynamic light scattering (DLS) and the SERS response using a Raman reporter on the surface of the protected NP.

2.3 Results and discussion

Au NPs were chosen as the core NP which would be protected by different coatings and exposed and characterised in harsh environments. It was selected due to its easy synthesis, stability during conjugation, ease of addition of additional coating and surface enhancement properties.

2.3.1 Synthesis of gold nanoparticles

Au NPs were prepared according to standard protocols developed by Turkevich and Frens.[14] Chloroauric acid ($HAuCl_4$) was reduced in the presence of citrate and the resulting NPs were subjected to characterisation techniques including extinction spectroscopy, dynamic light scattering (DLS), zeta measurements and scanning electron microscopy (SEM) to assess their stability. The results are shown in Figure 2.2.

a)

b)
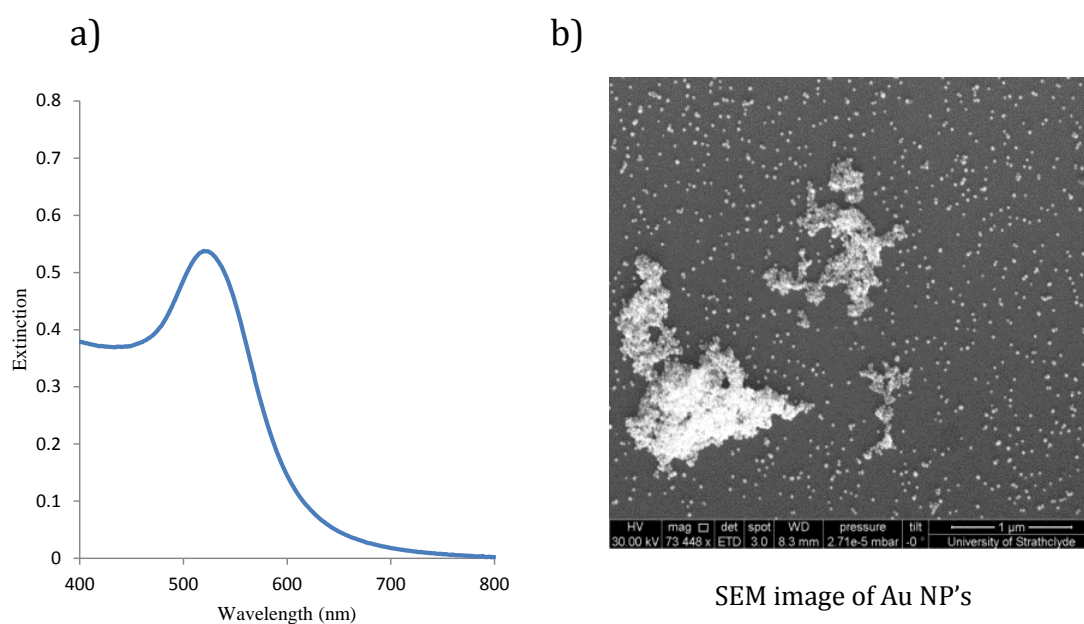
SEM image of Au NP's

Figure 2.2 (a) Extinction spectrum and (b) SEM image of Au NPs.

The extinction spectrum of the prepared Au NPs had an LSPR of 520 nm, a typical value expected for Au NPs (Figure 2.2 (a))[15]. The extinction spectrum also suggests that the NP were monodispersed, which was achieved by calculating the full width half maximum value (FWHM) of the LSPR peak. The smaller the LSPR FWHM

value is, the more monodispersed the NPs (under 100 is deemed acceptable).[78] The FWHM of the LSPR in this case was 75 nm, indicating monodispersity.

The NPs were then analysed using DLS to determine the particle size and the distribution of sizes within the NPs batch and zeta potential to give the charge. The Au NPs were 35.7±0.2 nm in diameter which was slightly smaller than expected. However, as there was only one size of NP in the batch, they could be used in subsequent experiments. The DLS was also used to measure the zeta potential of the surface of the NPs. Zeta potential values can be used to determine the stability of NPs, with any values under -20 mV deemed stable.[79] The zeta potential of the NPs was measured to be -38±2.5 mV, hence the NPs were stable. Using the Beer Lambert law and the extinction coefficient of 35 nm size Au NP, $8.25x10^9$ M^{-1} cm^{-1} as reported by Yguerabide [80], the concentration of the Au NPs were calculated to be 0.1 nM.

To further confirm the monodispersity and the size of the NPs, SEM was carried out. SEM is a technique which produces an image of a sample by scanning it with a focused beam of electrons. The electrons then interact with the atoms in the sample and produce secondary electrons that are detected. These signals contain information about the sample surface, topography and its composition. Once SEM images were obtained, software called Image J was then used to determine the size of each the NPs and the SEM image is shown in Figure 2.2 (b). Samples for SEM were prepared by spotting 10 µL of Au NPs onto a silica wafer and leaving it to dry overnight. The SEM image indicated that the NPs were all spherical, had an average size of 35±1.8 nm (calculated using image J) and were monodispersed, which was in good agreement with the DLS data. However, aggregation could be observed in the image and this was due to the drying of the NPs onto the silica wafer.

The lack of stability of bare Au NPs in different harsh environments was assessed by adding 400 µL of Au NPs to different reagents; 100 µL of 1 M saturated sodium chloride (NaCl), 1 M sodium hydroxide (NaOH), 2 M of hydrochloric acid (HCl) or 1 M hydrogen peroxide (H_2O_2). The samples were then characterised using extinction spectroscopy and the results are shown in Figure 2.3.
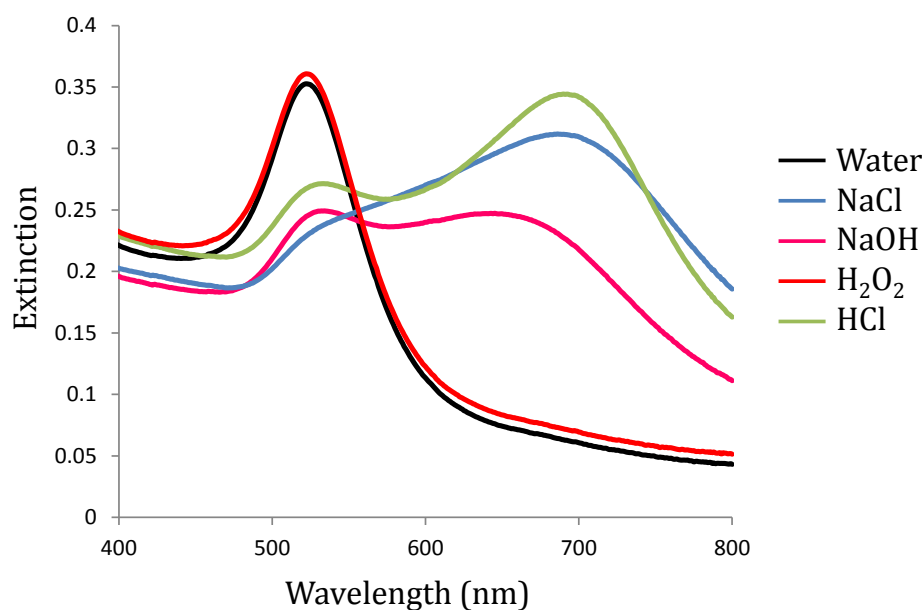
Figure 2.3 Extinction spectra of 400 μL of Au NP added to 100 μL of water (black), 1 M of saturated NaCl (blue), 1 M of NaOH (pink), 1 M of H_2O_2 (red) and 2 M of HCl (green).

When Au NPs were exposed to the harsh environments, aggregation was experienced immediately, and a colour change of the solution (pink to purple) was observed. The extinction spectra of the Au NPs exposed to HCl, NaOH and NaCl showed the aggregation occurred due to the appearance of a second red shifted LSPR which corresponded to large clusters of NPs (Figure 2.3). After 1 hour the NP clusters had become so large that they precipitated out of solution, confirming that, as expected, Au NPs had little stability in the harsh environments, and a protective coating was required.

2.3.2 Platinum coating

As a result of the instability of the Au NPs in harsh environments, different coatings were investigated to protect the Au NPs from aggregation. As already mentioned bulk Pt is resistant to HF acid, therefore Pt shelling directly onto the surface of the Au NPs was investigated.

The prepared nanotags had to also retain the ability to give a SERS response therefore, the Raman reporter molecule malachite green isothiocyanate (MGITC) was added to the surface of the Au NPs at a low concentration (0.1 μM) to prevent

aggregation. MGITC (structure shown in Figure 2.4 (a)) was chosen due to its thiol group which has an affinity for the Au metal surface, allowing for ease of functionalisation and surface enhancement. MGITC also has an absorbance maximum at 650 nm, therefore allowing resonance enhancement when a wavelength of 638 nm laser excitation was used, resulting in an intense SERRS signal.

To create a Pt shell on the surface of the Au NP, potassium hexachloroplatinate (H_2PtCl_6) was reduced on to the Au NP using sodium citrate to create a Au-MGITC-Pt nanotag. The SERRS properties of the Au-MGITC and Au-MCITC-Pt nanotags were then evaluated using 638 nm laser excitation and the results are shown in Figure 2.4 (b).
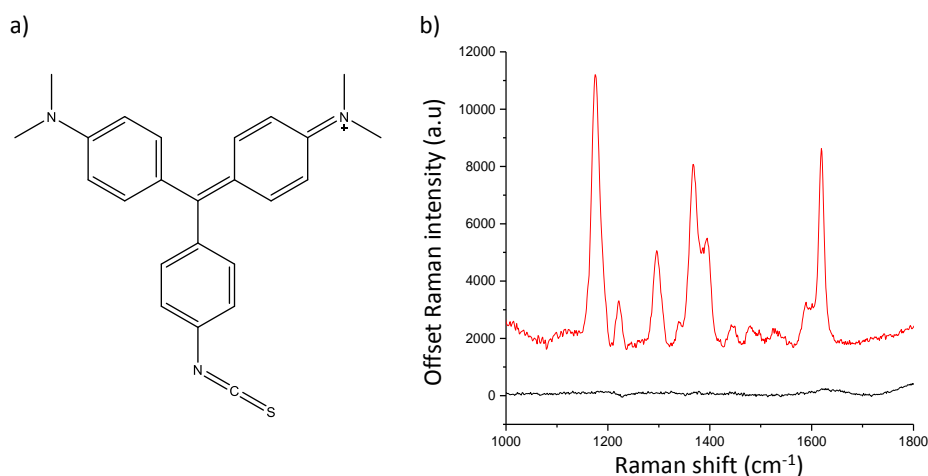
Figure 2.4 (a) Structure of MGITC and (b) SERRS response from MGITC on Au NPs (red) and signal obtained from Au-MGITC-Pt nanotag (black). Spectra were obtained using a 1 second accumulation time and 30 mW laser power. The spectra shown are the average of 5 measurements and have all been baseline corrected using Matlab.

The characteristic peaks of MGITC were present when 0.1 µM of MGITC was added to the surface of the Au NP (Figure 2.4 (a)). The main peaks of MGITC have been assigned as follows; 1615 cm^{-1} and 1365 cm^{-1} corresponded to stretching of phenyl–N and aromatic ring and 1177 cm^{-1} was assigned to the benzene mode.[81] However, when the Pt shell was added onto the Au NP, the resulting SERRS spectrum did not represent MGITC. It is proposed that the Pt shelling may have displaced and possibly changed the orientation of the MGITC on the surface resulting in the

22

change in spectrum. Therefore, Pt could not be added directly onto the surface of the Au NP and a spacer, which protected the MGITC from the Pt shell, was investigated.

2.3.3 Silica shell synthesis

As the coating of Pt straight onto the Au NP resulted in a poor SERRS spectrum, it was decided that a spacer layer was required to protect the MGITC on the surface of the Au NP from being displaced when the protective shell was added to the nanotag. Therefore, a silica (SiO_2) shell was investigated as a spacer to create stable Au-MGITC-SiO_2 nanotags which would protect the MGITC on the Au NP core from the subsequent addition of a Pt shell. It was also hoped that SiO_2 would offer additional stability by creating an additional barrier between the Au core and the harsh environment.

Using a method adapted from Tian *et al.*,[82] the SiO_2 shell was grown onto the surface of the Au NPs which had already been functionalised with 0.1 µM MGITC, thus creating Au-MGITC-SiO_2 nanotags. The formation of the SiO_2 shell on the Au NP was a two-step process. In order to create a vitreophilic surface on the metal, an amino functionalised silane coupling agent, 3-aminopropyl)-diethoxy-methylsilane (APTMS) was first added to facilitate the SiO_2 coating creating a mixed monolayer between the MGITC and APTMS. This was left stirring for three hours followed by sodium silicate (Na_2SiO_3) addition. By heating the solution to 90°C the speed of SiO_2 shell grown was increased, whereas if the reaction was carried out at room temperature, the growth took 2-3 days. The schematic in Figure 2.5 shows the mechanism of the Au-MGITC-SiO_2 nanotag synthesis.
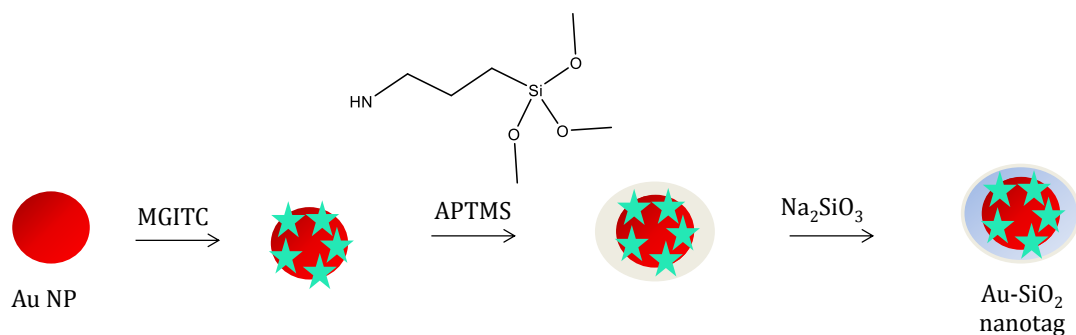
Figure 2.5 Schematic of Au-SiO$_2$ synthesis. Au NPs are functionalised MGITC and APTMS to create a mixed monolayer followed by the addition of Na$_2$SiO$_3$.

To investigate the effect of SiO$_2$ shell thickness on Au NP stability and on the MGITC SERRS response, three batches of Au-MGITC-SiO$_2$ nanotags with different shell thicknesses were synthesised by adding different concentrations of Na$_2$SiO$_3$ during the shelling process. Final concentrations of Na$_2$SiO$_3$ of 1.4 mM, 3.7 mM or 6.1 mM were added to Au NPs functionalised with 0.1 µM of MGITC and 0.3 mM of APTMS and left to stir at 90 ^{O}C for 30 minutes. After cooling, the Au-MGITC-SiO$_2$ nanotags were then characterised using DLS and extinction spectroscopy. The stability was also investigated with the addition of 100 µL of 1 M NaCl to 400 µL of the tag and again analysed using the same techniques. The results can be seen in Table 2.1 and Figure 2.6.

Table 2.1 Change in particle size after addition of SiO$_2$ shell, in presence and absence of 1 M NaCl.

Concentration of sodium silicate (mM)	Average particle size in water (nm)	Average particle size after addition of 1 M NaCl (nm)
0	38±0.7	409±1.3
1.4	39±0.3	323±2.4
3.7	41±0.7	53±0.6
6.1	48±0.9	48±0.5
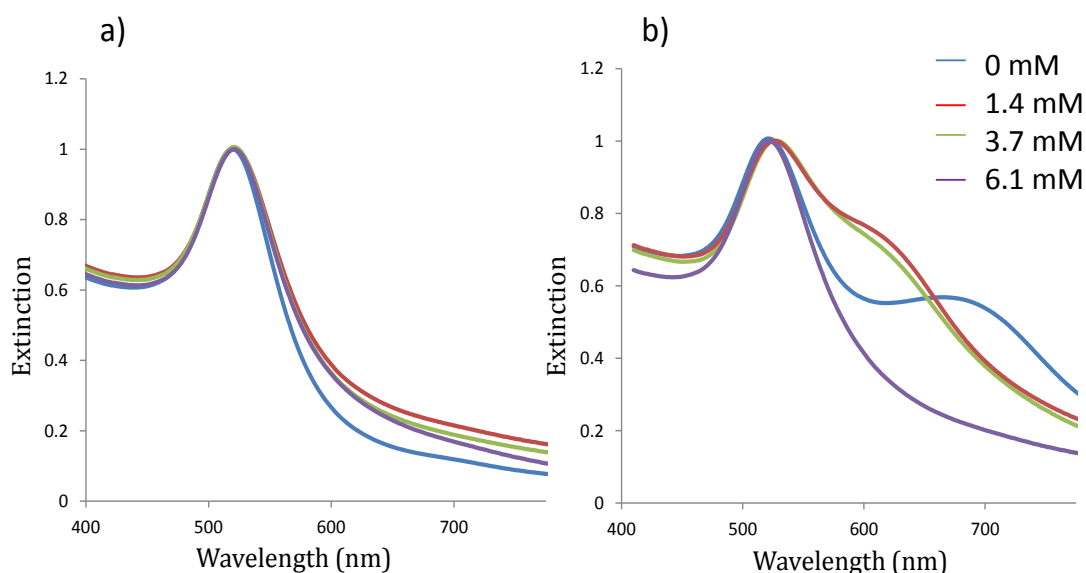
Figure 2.6 Extinction spectra of Au-SiO$_2$ nanotags synthesised with 0.3 mM APTMS and 0 mM (blue), 1.4 mM (red), 3.7 mM (green) and 6.1 mM (purple) of Na$_2$SiO$_3$ before (a) and after (b) the addition of 1 M NaCl. Spectra have been normalised to 1 for clarity.

As expected, addition of increasing concentrations of Na$_2$SiO$_3$ to the Au NP resulted in a different SiO$_2$ shell thickness being obtained. The lowest concentration of Na$_2$SiO$_3$ (1.4 mM) gave a very thin shell, around 0.5 nm thick. 3.7 mM of Na$_2$SiO$_3$, the concentration used in Tian *et al.*, gave a SiO$_2$ shell thickness of 1.5 mM and the highest concentration (6.1 mM) gave the greatest shell thickness, 5 nm.[82]   The

extinction spectra also suggests an increase in size due to a slight red shift in the LSPR and peak broadening as the thickness of the larger SiO_2 shells were present on the Au NPs. No aggregation of the Au NP core occurred during the SiO_2 shell synthesis.

To test the stability of the SiO_2 shell, 1 M NaCl was added to the Au NPs without SiO_2 protection and the three different batches of Au-MGITC-SiO_2 nanotags synthesised. Particle size and extinction spectra were also obtained before and immediately after the addition of 1 M NaCl. The results of the salt addition on the LSPR can be seen in Figure 2.6 (b) and the change in particle size in Table 2.1.

When 1 M NaCl was added to the Au NPs without SiO_2 coating aggregation occurred instantly, as expected, and a LSPR peak at 680 nm was observed (Figure 2.6 (b). The NPs also increased in size to 409 nm, again confirming the aggregation due to the unprotected surface. When 1 M NaCl was added to the nanotags with a SiO_2 shell, less aggregation was observed as the SiO_2 shell protected the Au NP core from coming into contact with the NaCl. However, a LSPR peak at 600 nm was obtained when a concentration of 1.5 and 3 mM of Na_2SiO_3 was used to create the nanotags. This could have been a result of an incomplete coating of SiO_2 on the Au surface resulting on partial aggregation of the nanotags and a shift in LSPR. The aggregation was also confirmed by the increase in size of the nanotags as shown in Table 2.1 (323, 53 nm). However, the nanotags with the thickest SiO_2 shell (5 nm) provided the nanotags with the most protection and little change was observed in the extinction spectra or size of the nanotags upon the addition of 1 M NaCl.

To investigate the effect that the SiO_2 shell had on the MGITC SERRS signal, the nanotags were analysed with 638 nm laser excitation, before and after the addition of 1 M NaCl. The results are shown in Figure 2.7.
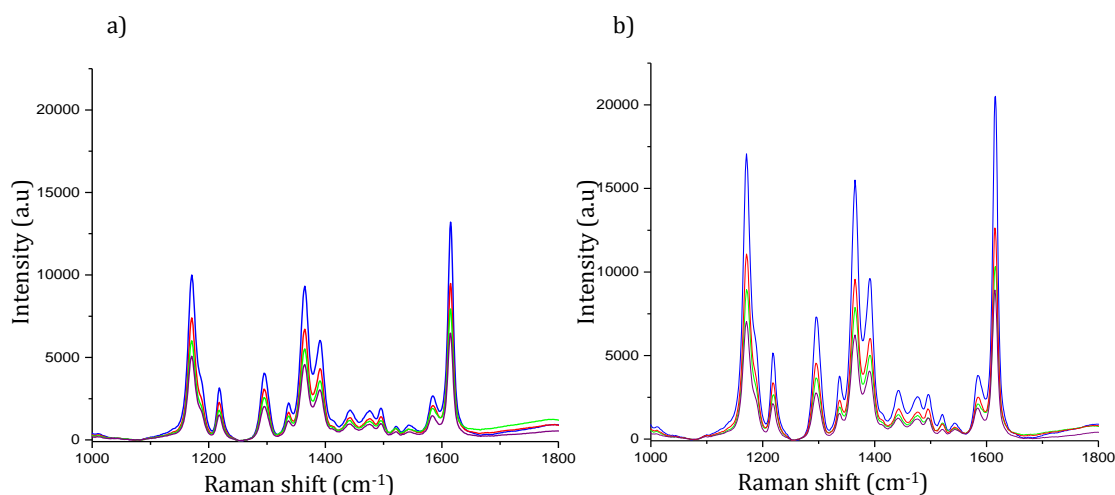
Figure 2.7 MGITC SERRS signal of nanotags with 0 (blue), 1.5 (red), 3 (green) and 6 (purple) sodium silicate (a) before and (b) after the addition of 1 M NaCl. Spectra were obtained using a 1 second accumulation time and 30 mW laser power. The spectra shown are the average of 5 measurements of 3 replicate samples and have all been baseline corrected using Matlab.

When only 0.3 mM of APTMS and 0.1 μM MGITC were added to the Au NP surface, an intense MGITC SERRS signal was obtained (Figure 2.7 (a) blue spectrum). However, the MGITC signal intensity decreased when the SiO_2 shell was added, suggesting that the SiO_2 had displaced some of the MGITC during the shelling process. However, enough MGITC remained present to give a strong SERRS signal using only a 1 second accumulation time even with the maximum SiO_2 shell thickness (Figure 2.7 (a) (purple spectrum)).

A noticeably enhanced SERRS signal was obtained when 1 M NaCl was added to Au NP functionalised with only APMTS and MGITC (Figure 2.7 (b) blue spectrum). This was due to the aggregation of the Au NPs resulting in an increased SERRS. This aggregation was also apparent in the extinction and DLS data (Figure 2.6 and Table 2.1). Less aggregation occurred when the Au NPs were covered with a SiO_2 shell of varying thickness, therefore smaller changes in MGITC SERRS signals were observed, suggesting less aggregation occurred. Little change in intensity was observed when 1 M NaCl was added to the nanotag with the thickest SiO_2 shell. Therefore suggesting this was the most stable nanotag in 1 M NaCl. There was also no change in size and extinction therefore this concentration of Na_2SiO_3 (6 mM) was used in future experiments due to its increased stability and the strong SERRS

response obtained from the nanotag. This nanotag was then used as the starting template for further Pt shelling.

2.3.4 Platinum coating of silica shell

Platinum (Pt) is one of the few metals that is resistant to HF attack,[77] therefore it was investigated as a resistant layer to coat Au-MGITC-SiO$_2$, nanotags, and could have the potential to protect the Au NPs at the core of the nanotag from being destroyed when exposed to HF.

Using a method adapted from that reported by Kamat *et al.* [83], H$_2$PtCl$_6$ was added to Au-MGITC-SiO$_2$ nanotags and left to coat the surface of the SiO$_2$. Sodium borohydride (NaBH$_4$) was then added to reduce the Pt (IV) on the surface to Pt (0), creating the Pt shell. A schematic for the addition of the Pt shell is shown in Figure 2.8.
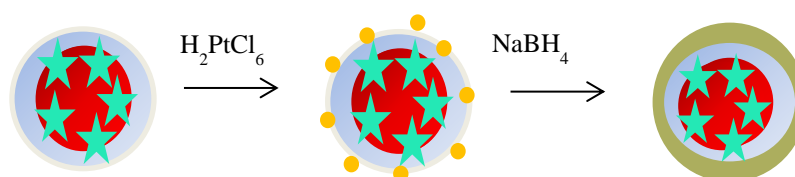
Figure 2.8 Schematic showing the addition of Pt shell to Au-MGITC-SiO$_2$ nanotag to form Au-MGITC-SiO$_2$-Pt nanotags with the addition of H$_2$PtCl$_6$ and NaBH$_4$.

The amount of H$_2$PtCl$_6$ and NaBH$_4$ used to create the Pt shell had to be optimised to ensure that enough Pt was applied to the SiO$_2$ surface. The aim was to ensure that enough Pt was added to protect the SiO$_2$, as if the SiO$_2$ was exposed to the harsh environments the tag could aggregate. Another consideration that had to be taken into account was if the Pt shell was too thick, the nanotags could become too dense and precipitate out of solution. In addition, a thick shell could obscure any scattering of MGITC from the surface of the Au NP core, rendering SERRS analysis ineffective.

To optimise the thickness of the Pt shell that would provide stability to the Au-MGITC-SiO$_2$ nanotag, final concentrations of 0.15, 0.3, 0.77, 1.5, 3.07 and 6.15 mM of H$_2$PtCl$_6$ were added to 400 µL of Au-MGITC-SiO$_2$ nanotags (synthesis outlined in

section 2.3.3, size 50.2±1.6) and left to shake for 30 minutes to allow the Pt salt to adsorb onto the negative SiO_2 surface. Then, to each tag 0.03, 0.15 or 0.8 mM of $NaBH_4$ was added to reduce the Pt (IV) and allow the Pt shell to grow around the SiO_2. The resulting Au-MGITC-SiO_2-Pt nanotags were characterised using extinction spectroscopy and DLS to estimate the Pt shell thickness and evaluate the stability of the nanotags. The results are shown in Figure 2.9 and 2.10.
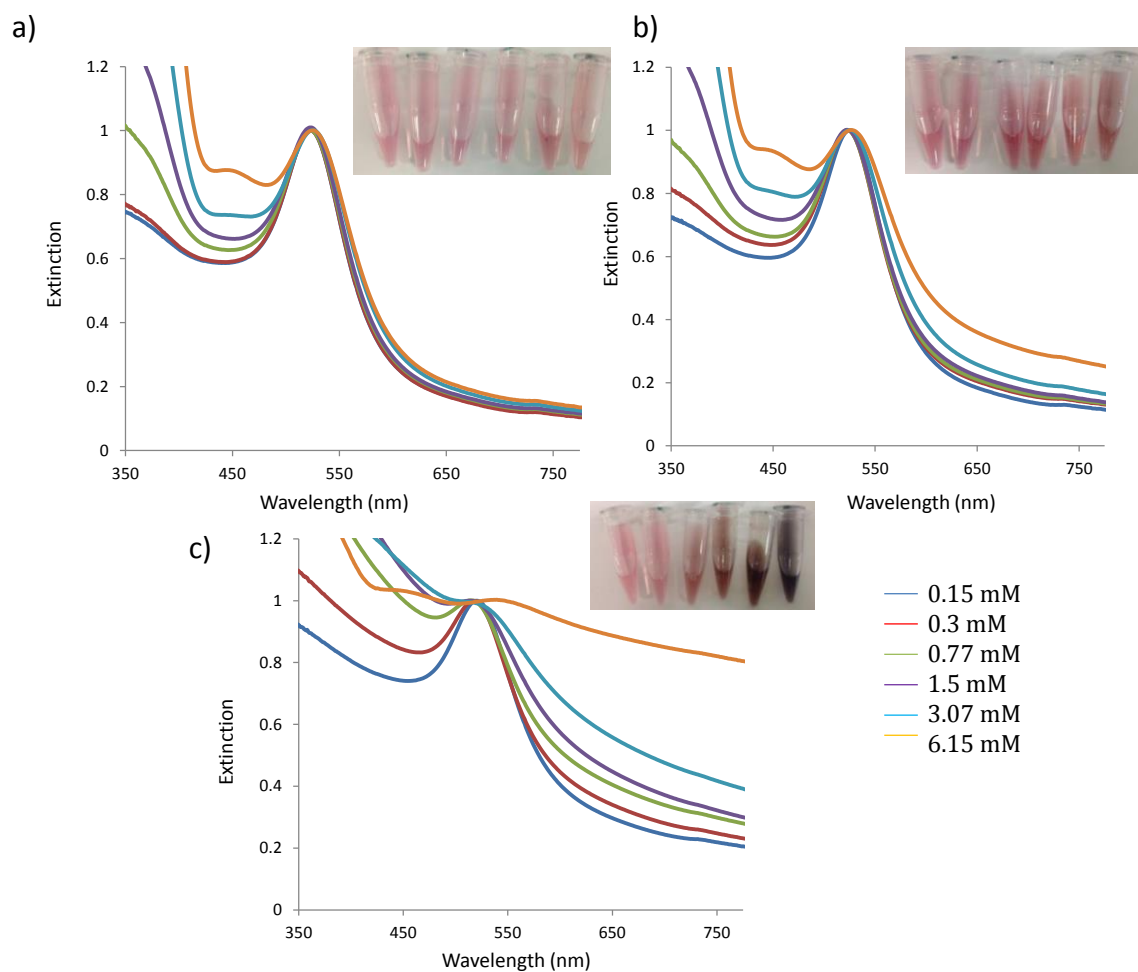
Figure 2.9 Extinction spectra of nanotags following the addition of 0.15 (dark blue), 0.3 (red), 0.77 (green), 1.5 (purple), 3.07 (light blue) and 6.15 (orange) mM of H_2PtCl_6 which was reduced by (a) 0.03 (b) 0.15 and (c) 0.8 mM of $NaBH_4$. Spectra have been normalised to 1 for clarity. The accompanying image shows the resulting colour of the Au-MGITC-SiO_2-Pt nanotags upon the addition of different concentrations of H_2PtCl_6 and $NaBH_4$.
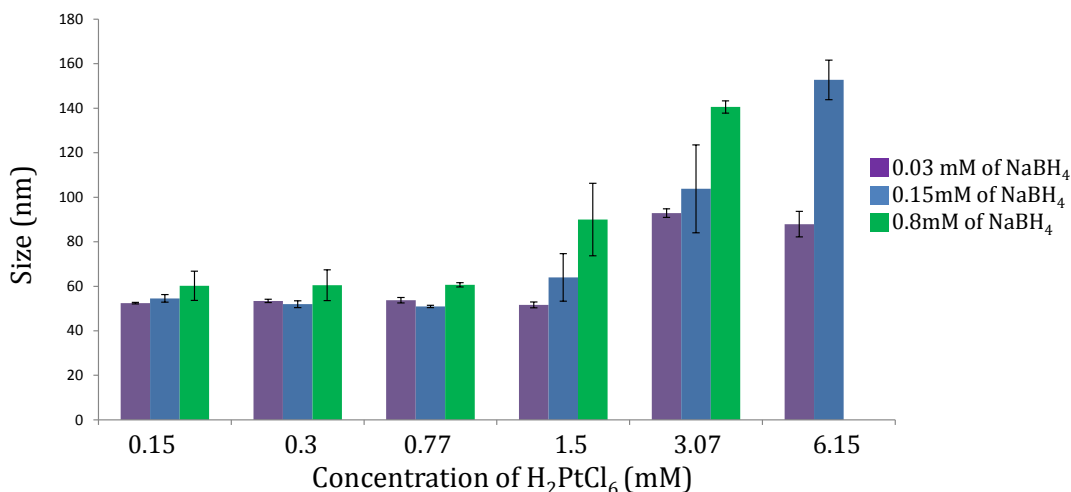
Figure 2.10 Bar graph indicating change in size of Au-MGITC-SiO$_2$-Pt nanotags as different concentrations of H$_2$PtCl$_6$ and NaBH$_4$ were added to the Au-SiO$_2$ nanotags measured using DLS. Error bars represent standard deviation of three measurements.

When H$_2$PtCl$_6$ was added to the SiO$_2$ surface and reduced using 0.03 mM of NaBH$_4$ (Figure 2.10 (a)), the LSPR experienced a red shift as increasing concentrations of H$_2$PtCl$_6$ (3.07 and 6.15 mM) were added and reduced onto the SiO$_2$ surface, indicating the formation of a Pt shell. DLS data confirmed that the nanotags had increased in size (93$\pm$1.9 and 84.6$\pm$6.4 nm) at these higher concentrations and Pt shells which were around 20 and 17 nm thick were present. There was no change in size or red shift when 0.15, 0.3, 0.77 and 1.5 mM of H$_2$PtCl$_6$ was added, which could be due to the low concentration of NaBH$_4$ not allowing enough reduction of the Pt salt.

At the highest concentrations of H$_2$PtCl$_6$ (6.15 mM) there was the appearance of a second peak in the extinction spectrum at 450 nm. This could be due to the formation of Pt NPs when the salt is reduced by 0.03 mM of NaBH$_4$, rather than Pt shelled nanotags.

The same trend was observed when higher concentrations of NaBH$_4$ (0.15 mM (Figure 2.9 (b)) and 0.8 mM (Figure 2.9 (c)) were used to reduce the Pt salt, however more peak broadening and further red shifting, from 525 nm to 530 nm occurred. This suggested that more Pt had been reduced onto the SiO$_2$ surface. Again, an increase in size was observed however, when higher concentrations of H$_2$PtCl$_6$ (1.5,

3.07 and 6.15 mM) were added, the resulting nanotags became unstable and aggregated which lead to an increase in size (over 100 nm, shown in Figure 2.10).

The nanotags changed colour from red to dark brown as higher concentrations of the Pt was added. It should be noted that the size for the Au-SiO$_2$-Pt nanotag resulting from the addition of 6 mM H$_2$PtCl$_6$ and 0.8 mM NaBH$_4$ was omitted from Figure 2.10 as this nanotag was over 1000 nm in size and the solution completely aggregated.

The SERRS spectra of the Au-MGITC-SiO$_2$-Pt nanotags were then obtained using 638 nm laser excitation to evaluate the effect that the addition of the Pt shell had on the MGITC SERRS response. The results are given in Figure 2.11.
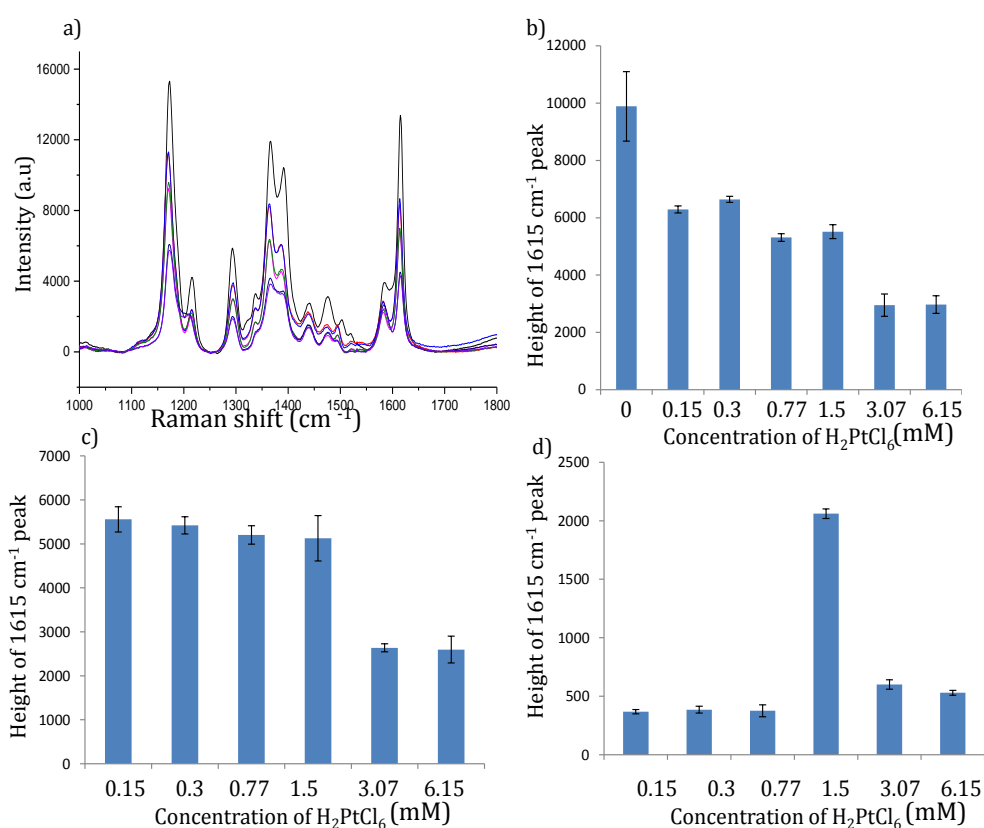
Figure 2.11 (a) Change in SERRS spectra obtained from Au-MGITC-SiO$_2$ nanotags (black) and Au-MGITC-SiO$_2$-Pt tag as H$_2$PtCl$_6$ were added (0.15, 0.3, 0.77, 1.5, 3.07 and 6.15 mM) and reduced by 0.03 mM of NaBH$_4$. Spectra were obtained using a 1 second accumulation time and 30 mW laser power. The spectra have all been baseline corrected using Matlab. The bar graphs show the intensity of 1615 cm^{-1} peak from Au-MGITC-SiO$_2$-Pt nanotags obtained when different concentrations of H$_2$PtCl$_6$ were reduced by (b) 0.03 mM (c) 0.15 mM and (d) 0.8 mM of NaBH$_4$ (blue). The spectra shown and error bars are the average and standard deviation of 5 measurements. The spectra have all been baseline corrected using Matlab.

Figure 2.11 (a) shows the SERRS spectra of the Au-MGITC-SiO$_2$ nanotags (black) and the expected decrease in MGITC SERRS signal due to the addition of a Pt shell. As higher concentrations of H$_2$PtCl$_6$ (3.07 and 6.15 m M) were added and reduced by 0.03 mM and 0.15 mM (Figure 2.11 (b) and (c)), the MGITC SERRS signal decreases was larger. This was due to the thicker Pt shells being functionalised suggesting that the laser excitation could penetrate through the Pt and SiO$_2$ shell to the MGITC functionalised Au NP core, however the SERRS signal was reduced, suggesting the Pt may be adsorbing some of the Raman scattered photons.

When the Pt salt was reduced using 0.8 mM NaBH$_4$, the MGITC SERRS signal obtained was very weak (Figure 2.11 (d)) suggesting that too much Pt was reduced onto the SiO$_2$ shell which lead to both aggregation of the nanotag and a thick Pt shell which diminished the SERRS signal. There was however an anomaly as when 1.5 mM of H$_2$PtCl$_6$ was functionalised to the SiO$_2$ surface and reduced by the high concentration of NaBH$_4$, the MGITC SERRS signal observed was larger than the other H$_2$PtCl$_6$ concentrations. This was due to aggregation of the tag creating hotspots and could be ignored. Due to the poor MGITC SERRS signal obtained, 0.8 mM of NaBH$_4$ was deemed too high a concentration and not used for further stability experiments.

The ideal stable Pt coated nanotags would be for the tag to experience little or no change in SERRS signal intensity upon the addition of harsh environments. The stability of the Pt shell was tested by the addition of 100 µL of 2 M HCl was added to 400 µL of nanotag and the change in SERRS measured and compared to Au-MGITC-SiO$_2$ nanotags. Figure 2.12 shows the decrease in SERRS spectra when HCl was added to Au-MGITC-SiO$_2$ and Au-MGITC-SiO$_2$-Pt nanotags. It should be noted that the volume of nanotags were kept constant by adding water to the tags that HCL was not added to.
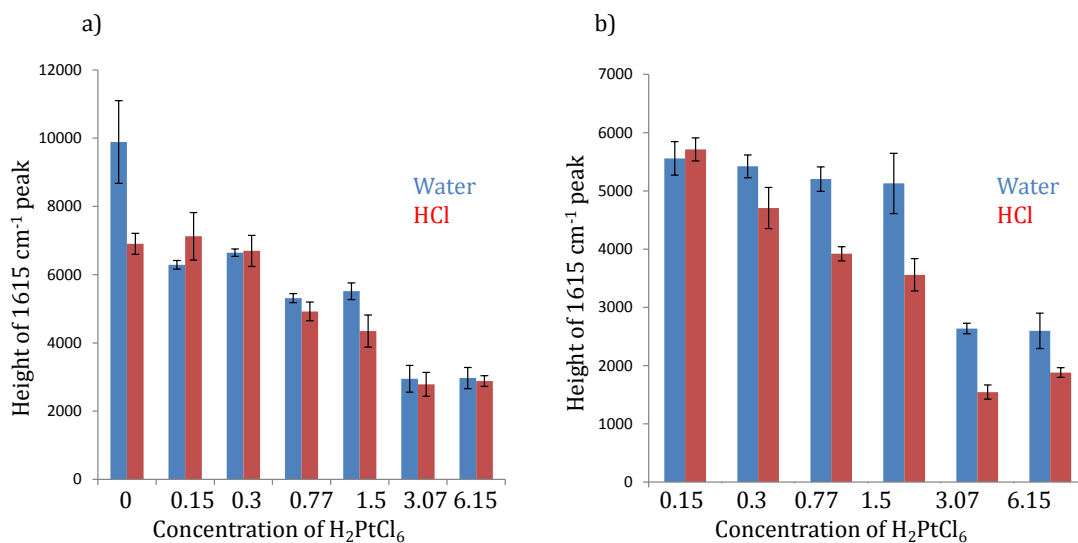
Figure 2.12 Bar graph showing decrease in intensity of 1615 cm^{-1} peak of MGITC SERRS signal obtained from Au-MGITC-SiO$_2$ and Au-MGITC-SiO$_2$-Pt nanotags synthesised with various concentrations of H$_2$PtCl$_6$ and reduced by (a) 0.03 and (b) 0.15 mM of NaBH$_4$ with water (blue) and with HCL(red).

As expected when 2 M of HCl was added to Au-MGITC-SiO$_2$ nanotags (Figure 2.12 (b)), the MGITC SERRS signal decreased due to a portion of the SiO$_2$ shell being destroyed by the HCl, therefore exposing the Au NP core and allowing for aggregation to occur and the SERRS signal to decrease. When the Pt was reduced by 0.03 mM of NaBH$_4$ (Figure 2.12 (a)), smaller changes in SERRS signals were experienced with and without HCl and it could be proposed that the Pt shell was protecting the Au-MGITC-SiO$_2$ nanotag.

The decreases in SERRS response was more noticeable with HCl, when Pt was reduced with the higher concentration of NaBH$_4$ (0.15 mM, Figure 2.13 (b)), therefore this concentration was not used for further experiments.

Little change in the SERRS signal intensity was observed for nanotags shelled using 3.07 mM H$_2$PtCl$_6$ reduced by 0.03 mM NaBH$_4$ and the extinction and DLS data indicated that there was a 20 nm thick Pt shell on the nanotag therefore this was the protocol that was used for all future experiments.

2.2.4.2 Platinum shell stability study

A suitable combination of H_2PtCl_6 and $NaBH_4$ which produced a Pt shell which did not cause aggregation to the Au-MGITC-SiO$_2$ tag, allowed a strong MGITC SERRS signal to be obtained and protection from HCl was achieved and analysed in harsh environments.

To evaluate the protection gained for the addition of a 20 nm Pt shell, Au-MGITC-SiO$_2$-Pt nanotags were exposed to a series of harsh environments and analysed over 1, 7 and 14 days using extinction spectroscopy (only day 1 and 7 shown), DLS and Raman spectroscopy and the results compared to Au-MGITC-SiO$_2$ nanotags without a Pt shell. Figure 2.13 indicates the change in LSPR of Au-MGITC-SiO$_2$ and Au-MGITC-SiO$_2$-Pt nanotags after day 1 and 7 when 250 µL of nanotag was added to 50 µL of 1 M NaCl, 1 M of NaOH, 1 M of H_2O_2 or 2 M HCl and the volume made up to 500 µL.
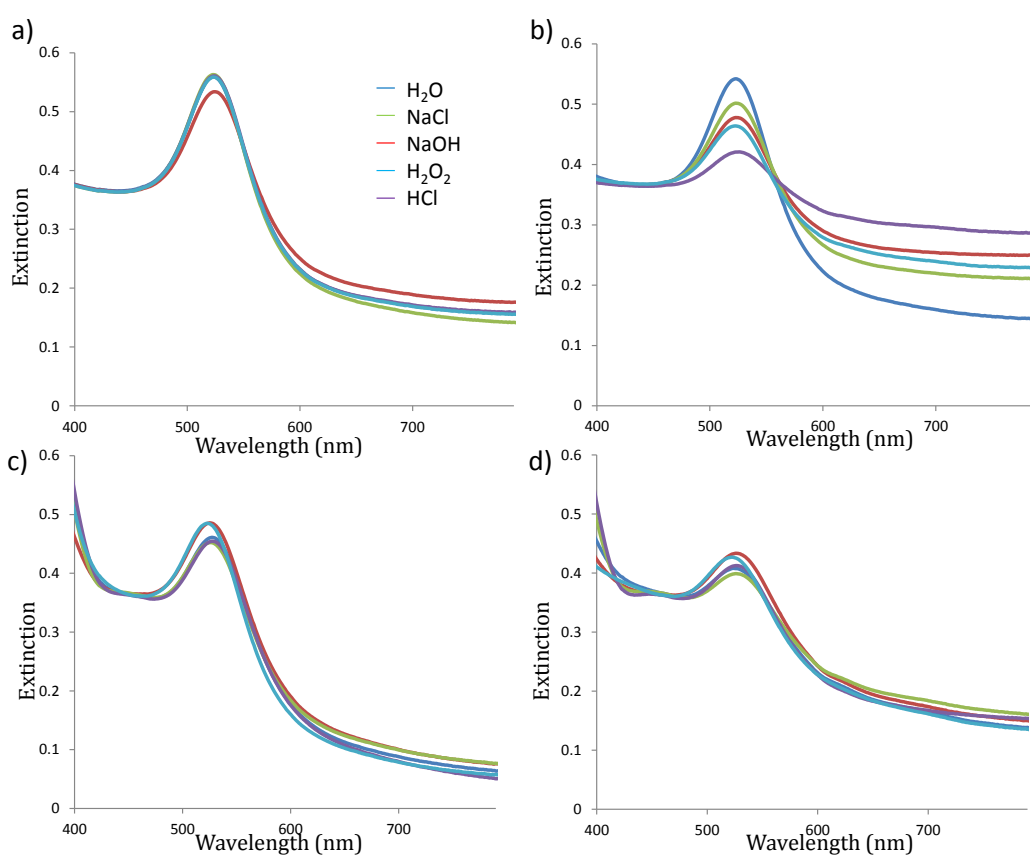
Figure 2.13 Extinction spectra of Au-MGITC-SiO$_2$ nanotags after day 1 (a) and day 7 (b) and extinction spectra of Au-MGITC-SiO$_2$-Pt nanotags after day 1 (c) and day 7 (d) when exposed to water (dark blue), 1 M of NaCl (green), 1 M of NaOH (red), 1 M of H_2O_2 (light blue) and 2 M of HCl (purple).

Figure 2.13 (a) and (c) shows that, as expected, there was little change in the LSPR on day 1 when Au-MGITC-SiO$_2$ and Au-MGITC-SiO$_2$-Pt nanotags were added to different harsh environments. This is in contrast to when Au NPs alone were added to harsh environments (Figure 2.3, section 2.3.1), where a large change in LSPR was observed. Therefore the SiO$_2$ and Pt shell offered protection to the Au NP core. However, on day 7, the extinction spectra of the Au-MGITC-SiO$_2$ nanotag in the harsh environments appeared differently from the control in water (Figure 2.13 (b)). The LSPR has decreased in all harsh environments due to the aggregation of the nanotags which was also visualised by the increase in extinction spectra at 700 nm. The largest change in LSPR was observed when the nanotags were exposed to HCl and peak broadening and red shifting was very apparent. By day 7, there was also a change in the extinction spectra of the Au-MGITC-SiO$_2$-Pt nanotags and the LSPR decreased; however the same change is also observed in the water control. This suggests that the nanotags were not stable over time in water, however as the change in extinction spectra was the same for water and the harsh environments and less than that observed in the absence of the Pt shell, the Pt shell offered some protection to the Au NP core.

The size of the nanotags was measured using DLS over 1, 7 and 14 days and the sizes obtained are shown in Table 2.2.

Table 2.2 Change in particle size of Au-MGITC-SiO$_2$ and Au-MGITC-SiO$_2$-Pt nanotags when exposed to harsh environments.

Harsh environment	Size of Au-MGITC-SiO$_2$ nanotags (nm)			Size of Au-MGITC-SiO$_2$-Pt nanotags (nm)		
	Day 1	Day 7	Day 14	Day 1	Day 7	Day 14
Water	48±2.3	50±4.6	55±1.8	101.5± 17.7	106.1± 35.8	473± 7.4
NaCl	57±6.2	121.5±9.0	982±98	118±21	247±45	393± 122
NaOH	53±0.9	388±307	382±93	77.6±5	68±11	115± 35
H$_2$0$_2$	58±7.2	35±7.2	54±7	110±10	114±24.3	444±76
HCl	109±21	638±239	2550± 1312	110±10.0	114±24.3	513±82.0

The data in Table 2.2 indicates that the Au-MGITC-SiO$_2$ nanotags experienced little change in size when exposed to the harsh environments after day 1, with the exception of 1 M of HCl, where the nanotags doubled in size. This suggests that the SiO$_2$ shell offered some protection to the Au NP core, however, by day 7 and 14 the size of the nanotags increased when compared to the control. Therefore the SiO$_2$ layer offered protection for only a limited period of time before the SiO$_2$ was destroyed and the Au NP core aggregated.

The sizes of the Au-MGITC-SiO$_2$-Pt nanotags measured over time in harsh environments are given in Table 2.2. It can be seen that there was little change in size after day 1, with the exception of 1 M of NaOH where the nanotags decreased in size, which could suggest that the NaOH was removing some of the Pt shell from the surface. After day 7 there was also little change in size, suggesting that the nanotags gained protection from the Pt shell, with the exception of NaCl and the nanotags did experience some aggregation and increased in size to 247±45 nm. However, after 14 days the nanotags with and without Pt protection had aggregated, suggesting that neither nanotag was stable. There was an anomaly in the NaOH size data and the nanotag after 14 days was 115 ± 35 nm.

However, over the 14 days that Pt shell did offer some stability compared to the Au-MGITC-SiO$_2$ nanotags, as the size did not increase to the same extent. To further investigate this, the SERRS spectra of the nanotags were measured over 1, 7 and 14 days using 638 nm laser excitation to evaluate the change in MGITC SERRS signal of the nanotags. Figure 2.14 shows the change in intensity of the 1615 cm^{-1} peak of the MGITC over 1, 7 and 14 days.
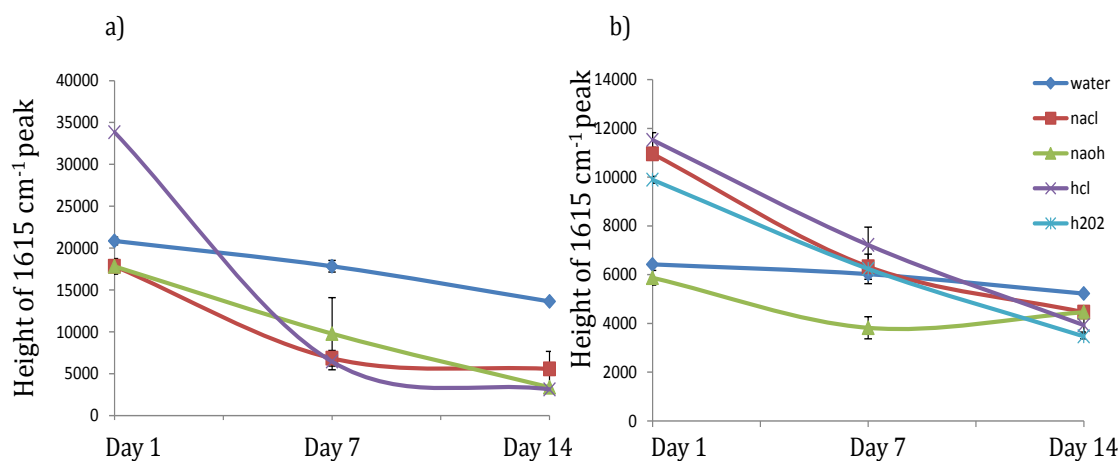
Figure 2.14 Change in the intensity of 1615 cm^{-1} peak the of MGITC for (a) Au-MGITC-SiO$_2$ and (b) Au-MGITC-SiO$_2$-Pt nanotags in harsh environments; 1 M of NaCl (red), 1 M of NaOH (green), 2 M of HCl (purple), 1 M of H$_2$O$_2$ (blue) and control (water) at day 1, 7 and 14. Spectra were obtained using 638 nm laser excitation, 5 second acquisition and a 30 mW laser power Spectra were baseline corrected using Matlab and error bars obtained from the measurements of 3 samples with 5 replicates.

The SERRS response from the Au-MGITC-SiO$_2$ nanotags in each harsh environment is given in Figure 2.14 (a) and it can be seen that the signal obtained from each tag was not consistent over time and the MGITC SERRS signal intensity decreased. On day 1, the MGITC signal from Au-SiO$_2$ nanotags did not differ much from the control (water), with the exception of HCl. The signal from the nanotags in HCl was higher due to the aggregation causing an increase in signal. By day 7, the SERRS response from the nanotag exposed to 2 M of HCl had decreased dramatically as the nanotags precipitated out of solution. This also occurred for the nanotags in the other harsh environments and the SERRS response was much lower than that of the control the SERRS signal on day 14.

The change in SERS over 14 days obtained from the Au-MGITC-SiO$_2$-Pt nanotags in harsh environment is shown in Figure 2.15 (b). On day 1, when the tags were

added to 1 M of NaCl, 1 M of H_2O_2 and 2 M of HCl, an increase in MGITC SERRS signal when compared to the control was observed. This was unexpected, but was probably due to the slight aggregation (which was also observed in the DLS data in Table 2.2). Another possibility could be due to the harsh environments removing some of the Pt shell and exposing the Au-MGITC-SiO$_2$ nanotag underneath, allowing for more of the MGITC SERRS signal to be scattered and detected. As the nanotags continued to aggregate over the 14 day period, the MGITC SERRS signal decreased due to the precipitation of the nanotags out of the solution. However, with the exceptions of NaOH, the decrease in SERS signal was consistent with the decrease in SERRS of the control. This differed from the unprotected Au-MGITC-SiO$_2$ nanotags which were roughly 9000 a.u. different from the control in water at after 14 days, compared to a drop of only 1000 a.u for the Au-MGITC-SiO$_2$-Pt nanotags. Therefore, suggesting that the Pt had added stability to the nanotags.

Overall the extinction, DLS and SERRS data suggested that the Pt shell did increase the stability of the nanotag, however, it was short lived and by day 14 the tags had aggregated and a low SERRS signal was obtained. The reduction in MGITC SERRS signal due to the Pt shell was also detrimental. To this and the instability past 7 days, commercially available Au-SiO$_2$ tags which had a thicker SiO$_2$ shell and more intense Raman reporter signal were investigated for Pt shelling.

2.3.5 Cabot nanotags

In an attempt to further increase the stability of the Au-SiO$_2$-Pt nanotags, commercially available Au-SiO$_2$ nanotags with a thicker SiO$_2$ shell were coated with Pt to create a tag which would hopefully have an increased stability in harsh environments.

Cabot nanotags are Au NPs coated in a very thick SiO$_2$ shell. The Cabot nanotag consists of small aggregates of Au NPs functionalised with a Raman reporter which in this case was 1,2-(Di(4-pyridyl)ethylene (BPE). The Au-BPE NPs are then coated in a thick SiO$_2$ shell, shown in Figure 2.15 (a), preventing further aggregation and increasing the stability of the nanotag.

The Cabot nanotags were first characterised using extinction spectroscopy and compared to the in-house synthesised Au-SiO$_2$ nanotags. The results are shown in

Figure 2.15 (b). It should be noted that the Cabot nanotags were very dark in appearance and had to be diluted 1 in 7 to obtain an optical density between 0.8 and 1.2.

a)

b)
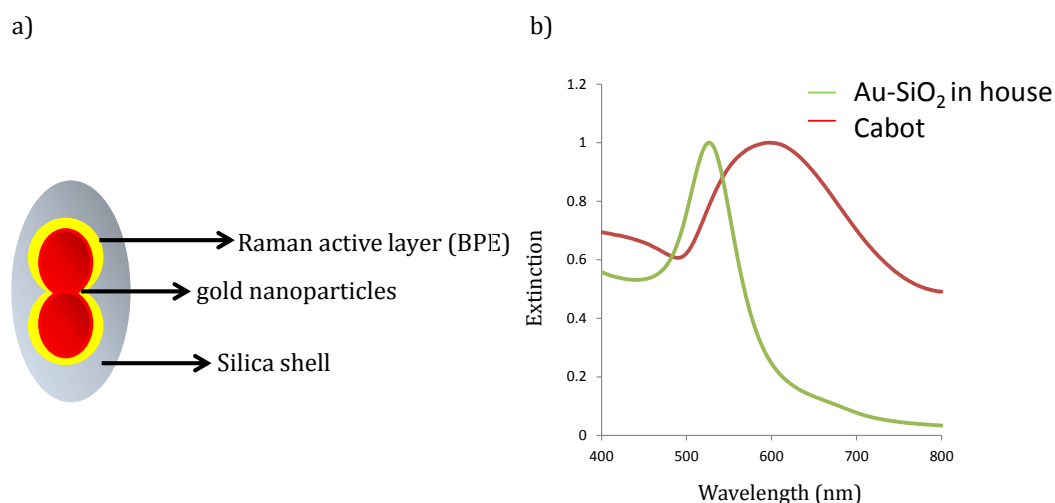
Figure 2.15 (a) Diagram of Cabot nanotags and (b) Extinction spectra of in-house Au-SiO$_2$ nanotags (green) and Cabot nanotags (red). Spectra have been normalised to 1 for clarity.

From the extinction spectra for the in-house Au-SiO$_2$ and Cabot nanotag, shown in Figure 2.15 (b), it can be seen that it is likely the Au NPs are aggregated during the SiO$_2$ shelling as the LSPR of the Cabot nanotag was red shifted to 614 nm indicating the presence of dimers and small aggregates. The peak is also very broad as the nanotags are much larger in diameter, which was confirmed using DLS data which gave a size of 197.0+2.4 nm.

The clustering of the NPs in the Cabot nanotags would hopefully lead to an increase in SERS and to investigate this, the SERS of the Cabot nanotag was obtained using 638 and 785 nm laser excitation. Both wavelengths were used as BPE does not having any resonance contribution and it was unknown what laser excitation would result in the most intense SERS signal. The SERS spectra of BPE at each wavelength and the structure of BPE are shown in Figure 2.16.
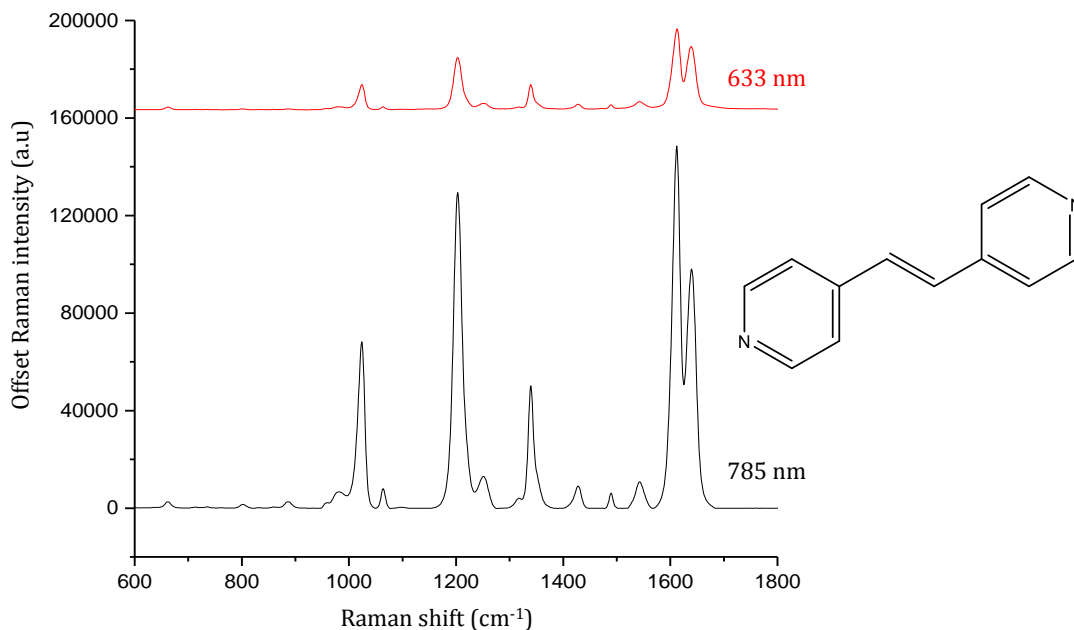
Figure 2.16 SERS spectra and structure of BPE from the Cabot nanotag when analysed with 638 nm laser wavelength (red) and 785 nm laser wavelength (black). Spectra were obtained using a 4.5 mW laser power and 5 second acquisition time. Spectra were normalised using an ethanol standard to take into account the performance of the different instruments and then baseline corrected using Matlab.

The characteristic vibrational modes of BPE are present in both the 638 and 785 nm spectra in Figure 2.16 and appear at 1200, 1612 and 1640 cm^{-1} which correspond to the C=C stretching, aromatic ring stretching and in-plane ring modes respectively.[84] The SERS spectrum obtained using 785 nm laser excitation is much more intense than that obtained at 638 nm after normalising. This was unexpected as this wavelength does not correspond to the spectral position of the LSPR which appears at 614 nm, therefore 638 nm laser excitation would be expected to give the most intense signal. This phenomenon has been discussed by Kleinman *et al.* and they suggest that the hotspots were capable of supporting other resonance and could amplify light in the near field at frequencies which are independent of the LSPR.[55] Therefore since the 785 nm gave the best SERS signal, this laser excitation was used for future experiments.

2.3.5.1 Platinum shelling of Cabot nanotags

A Pt shell was added to the Cabot nanotags using the method previously described in section 2.3.4. However, the concentrations of the H_2PtCl_6 and $NaBH_4$ had to be adapted to account for the difference in SiO_2 shell area and concentration of the nanotags.

The concentration of the Cabot tags was obtained using a NanoSight and the concentration was calculated to be 0.08 nM. As the solution was diluted by 7, the concentration of the resulting solution analysed was roughly 0.01 nM. This was 10 times less than the concentrations of $Au-SiO_2$ in house nanotags. Therefore, concentration of H_2PtCl_6 added should be 10 times lower. However, the Cabot nanotags have a much larger SiO_2 surface that could be coated with Pt, therefore high and low concentration of H_2PtCl_6 was added to the Cabot nanotags and reduced.

Final concentrations of 3 mM and 0.3 mM of H_2PtCl_6 were added to 100 μL of Cabot tags and the solution made up to 700 μL with water and left to shake for 30 minutes. 0.03 mM of $NaBH_4$ was then added to the solution to reduce the Pt (IV). When 3 mM of H_2PtCl_6 was added to the SiO_2 surface, the tags aggregated as too much Pt had been added to the surface, therefore the Cabot nanotags with the lower H_2PtCl_6 reduced onto the surface were characterised using extinction and Raman spectroscopy to investigate the effect that the Pt shell had on the LSPR and BPE SERS signal which is shown in Figure 2.17.
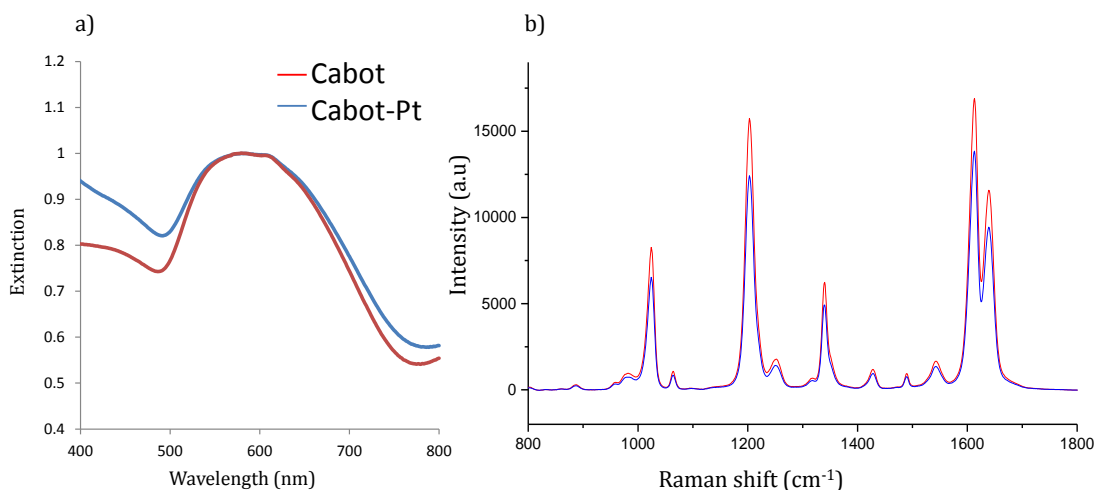
Figure 2.17 a) Extinction spectra of Cabot (red) and Cabot-Pt nanotags (blue) b) SERS spectra of BPE obtained from Cabot (red) and Cabot-Pt nanotag (blue). Extinction spectra have been normalised to 1 for clarity. The SERS spectra were obtained using 785 nm laser excitation, 1 second acquisition time at 4.5 mW laser power. Spectra were the average of 5 replaces and were baseline corrected using Matlab.

When a Pt shell was added to the SiO_2 shell of the Cabot nanotags, the resulting Cabot-Pt nanotags were black in appearance due to the Pt shell and were 508±61 nm in size, which was due to the Pt clustering the nanotags. However, despite the visible change in colour and increase in size, the LSPR of the Au dimers could still be observed using extinction spectroscopy (Figure 2.17 (a)) and could therefore be used to assess the stability of the Cabot-Pt nanotags in harsh environments.

Figure 2.17 (b) shows that the Pt shelling of Cabot-Pt nanotags had little effect on the SERS signal and a strong BPE SERS signal was still obtained when analysed with 785 nm laser excitation. This differed from the in-house Au-SiO_2-Pt nanotags, as the weak MGITC signal was adsorbed by the Pt shell. Hence, the Cabot-Pt nanotags had much better SERS properties and could be used in stability studies. This could be due to the lower concentration of Pt added to the surface or due to the fact that the SERS signal of BPE from the Cabot nanotag is so strong to begin with that the Pt shell had little effect on it.

To further confirm that the Pt had actually shelled the SiO_2 surface and that Pt NPs weren't synthesised, SEM was performed on the Cabot-Pt nanotags. The image in

Figure 2.18 indicates the size of the Cabot nanotags and the appearance of Pt on the surface of the SiO_2.
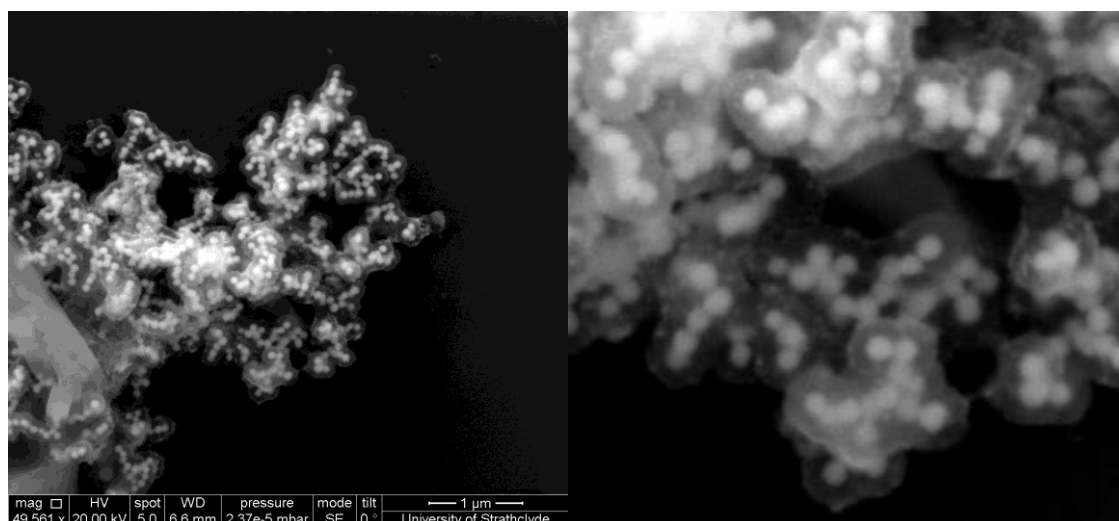
Figure 2.18 SEM image of Cabot-Pt nanotags and zoomed in image in which the Pt on the surface can be seen.

The Cabot-Pt nanotags are aggregated together with the SiO_2 surrounding multiple Au NPs, forming small clusters of NPs which account for the high SERS response and also the large size measured by DLS. In the image on the right, it is possible to see the Pt shell in the form of small Pt NPs that have attached onto the SiO_2 surface, however the Pt shell is not complete. This was to be expected as from previous studies when too much Pt was added, an adverse effect was experienced and the nanotags aggregated, hence achieving a full Pt shell is unrealistic and would be detrimental to the stability and SERS capability of the tag.

The stability of the Cabot-Pt nanotags, were investigated by exposing the nanotags to a series of harsh environments and characterised using extinction spectroscopy, DLS and SERS over a period of 4 weeks.

2.3.5.2 Stability of Cabot-Pt nanotags
The Cabot and Cabot-Pt nanotags were exposed to harsh environments and water, as control, to evaluate the stability of the nanotags. 100 µL of Cabot or Cabot-Pt nanotags were added to 100 µL of water (as a control), 100 µL of 1 M of saturated

NaCl, 100 µL of 1 M of NaOH, 100 µL of 1 M of H_2O_2 or 100 µL of 2 M of HCl and the volume made up to 600 µL with water and analysed over time.

Figure 2.19 shows the change in the LSPR from day 1 to day 28 for Cabot nanotags with no Pt protection, in each harsh environment and water. It should be noted that the solution had to be shaken prior to analysis as some of the nanotags had settled to the bottom of the solution.
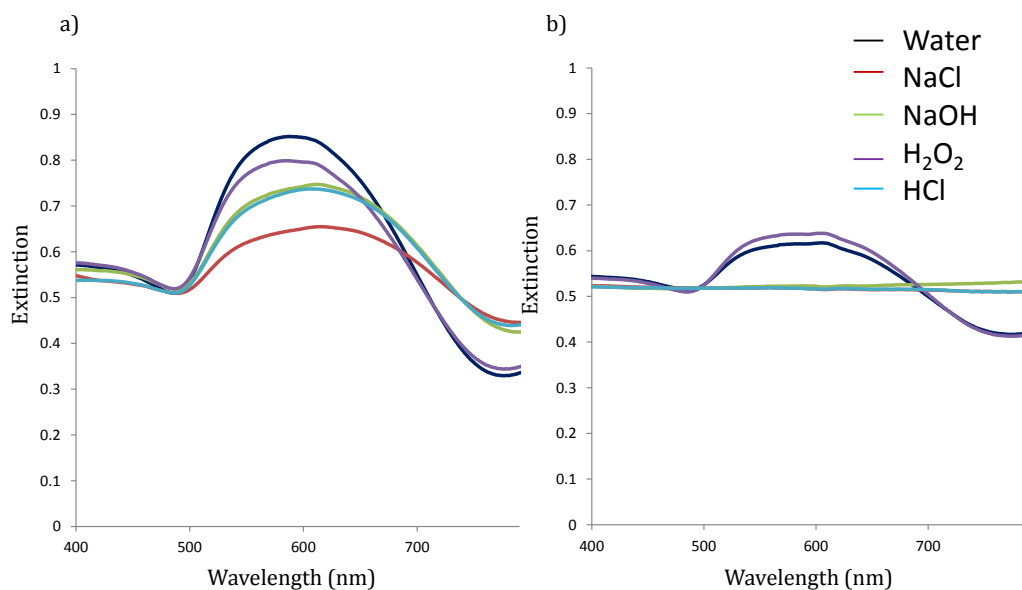
Figure 2.19 Extinction spectra of Cabot nanotags at (a) day 1 and (b) day 28 in water (black), 1 M of NaCl (red), 1 M of NaOH (green), 1 M of H_2O_2 (purple) and 2 M of HCl (blue).

Figure 2.19 shows there is a clear change in the extinction spectra when the Cabot nanotags were exposed to the harsh environments, even on day 1. When the nanotags were exposed to HCL, NaOH and HCL, a red shift in LSPR from 587 to as much as 611 nm was observed due to the aggregation of the nanotags, however the SiO_2 did provided some stability and the LSPR peak was still visible. After day 28 the nanotags completely aggregated since no LSPR peak was observed. The LSPR peak also decreased in water, which could have been due to loss of sample when transferring between sample vials for analysis or settling of the nanotags out of solution which did not join the rest of the solution when it was shaken. The nanotags in H_2O_2 experienced a similar decrease in LSPR as the nanotags in water, therefore, the nanotags were deemed to be stable or the concentration of H_2O_2 was not high enough to cause damage to the SiO_2 shell.

To ascertain whether the Pt shell added any extra stability, the Cabot-Pt nanotags were exposed to the same harsh environments and the extinction spectra was obtained after day 1, 7, 14, and 28. The change in extinction spectra of the Cabot-Pt nanotags in the harsh environments on day 1 and day 28 is show in Figure 2.20.
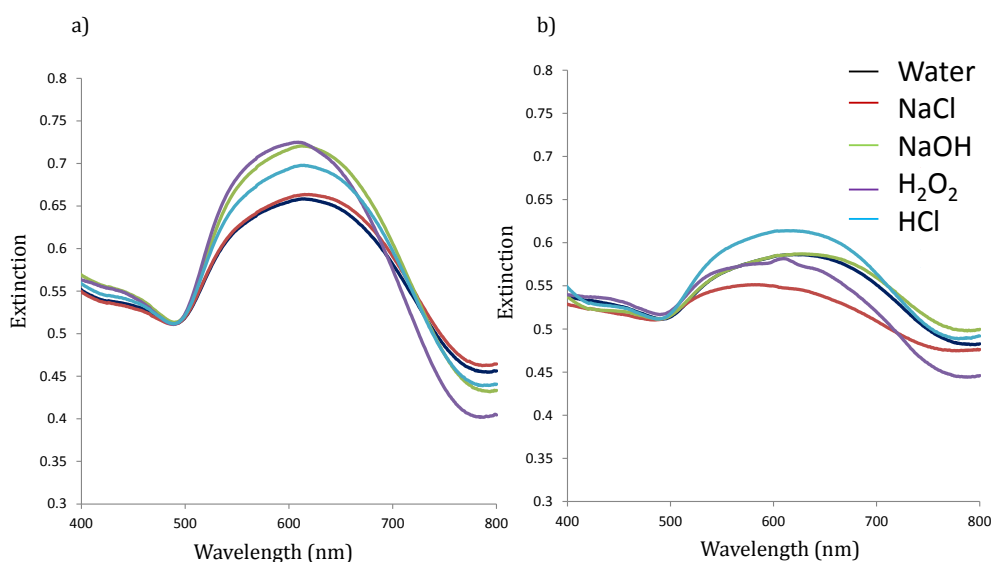
Figure 2.20 Extinction spectra of Cabot-Pt nanotags at (a) day 1 and (b) day 28 in water (black), 1 M of NaCl (red), 1 M of NaOH (green), 1 M of H_2O_2 (purple) and 2 M of HCl (blue).

When the Cabot-Pt nanotags were exposed to the harsh environment, an increase in the intensity of the LSPR from the nanotags in water was experienced. This was unexpected; however, the increase could be due to the harsh environments (NaOH, HCL and H_2O_2) interacting and possible removing some of the platinum shell, exposing the Cabot tag beneath, hence the increase in LSPR is from the Cabot nanotag itself. However, even though some of the Pt shell may have been removed, by Day 28, the LSPR was still visible in all 4 harsh environments; hence the Pt shell has provided the Cabot tag with extra stability.

Further confirmation of this stability was obtained using DLS and Figure 2.21 which shows the change in size over 1, 7, 14, 21 and 28 days of the unprotected and protected Cabot nanotags in the harsh environments and water.
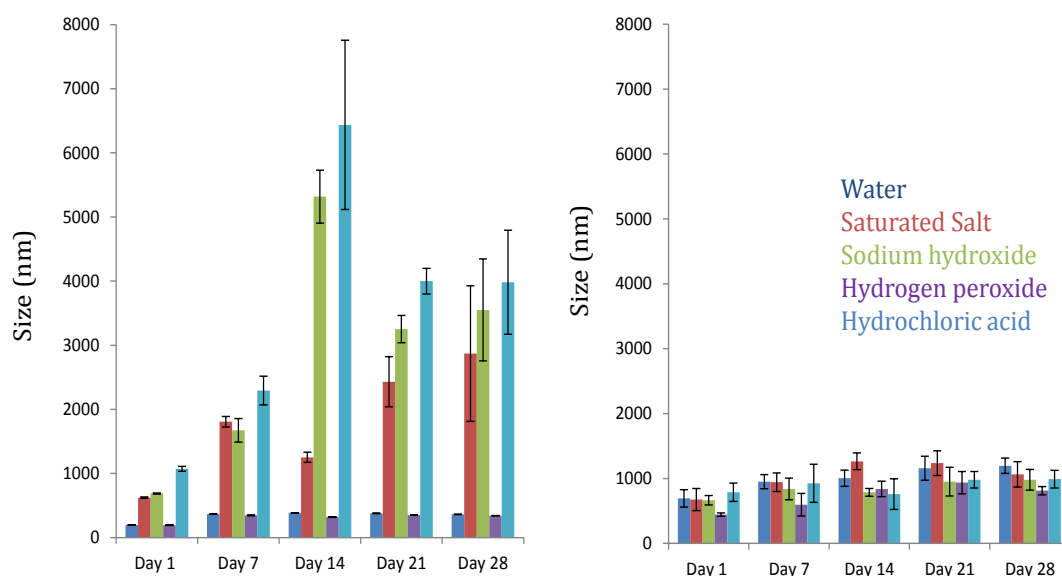
Figure 2.21 Bar graph indicating change in size from day 1, 7, 14, 21 and 28 of Cabot (a) and Cabot-Pt tags (b) in water (dark blue), 1 M of NaCl (red), 1 M of NaOH (green), 1 M of H_2O_2 (purple) and 2 M of HCl (blue). Error bars were obtained from the standard deviation of 3 samples with replicates of each taken.

The change in size of the uncoated nanotags when exposed to each harsh environment is shown in the bar graph in Figure 2.21 (a). When the tags are in water and H_2O_2, there was no change in size as expected, and the nanotags remained stable throughout the 4 week study with only slight aggregation observed.

However, when the Cabot nanotags were exposed to 1 M of NaCl, 1 M of NaOH or 2 M of HCl, an increase in size from the control was observed after day 1, indicating the instability of the nanotags in these environments. This was in agreement with the extinction spectroscopy data. Throughout the 4 week study, the nanotags increased in size and by day 14, the nanotags in HCl and NaOH had reached a critical size and the biggest nanotags started to drop out of solution resulting in smaller nanotags sizes at day 21 and 28 in these environments. This again, agreed with the disappearance of the LSPR obtained for each on day 28, as the nanotags had become so large that they dropped out of solution. Due to the dramatic increase in size the Cabot nanotags were not stable in NaCl, NaOH and HCl after day 1, further clarification of the need for a protective layer.

Unlike the uncoated Cabot nanotags, when Pt was added to the surface and the size taken in each harsh environment, a smaller increase in size was observed and closely resembled the increase in size of the control. The nanotags are, however 1000 nm in size, but this expected to be due to the clumping of the Cabot nanotags coated in Platinum which formed chains of NP (seen in SEM in Figure 2.18). Therefore, when the size was measured by the DLS it was not measuring the size of one particle but of NP chains hence the large size, which does not necessarily represent aggregation. This could also be true for the Cabot nanotags with no protection. Another indication to ignore the larger size was the fact the LSPR was still present after day 28, hence some of the nanotags were still in solution.

The nanotags were analysed using 785 nm laser excitation to ascertain if the nanotags retained the BPE SERS signal in the harsh environments. The decrease in SERS response of the Cabot and Cabot-Pt nanotags in each harsh environment was monitored over time and the change in height of the 1612 cm^{-1} peak of BPE from day 1 to day 28 is shown in Figure 2.22.
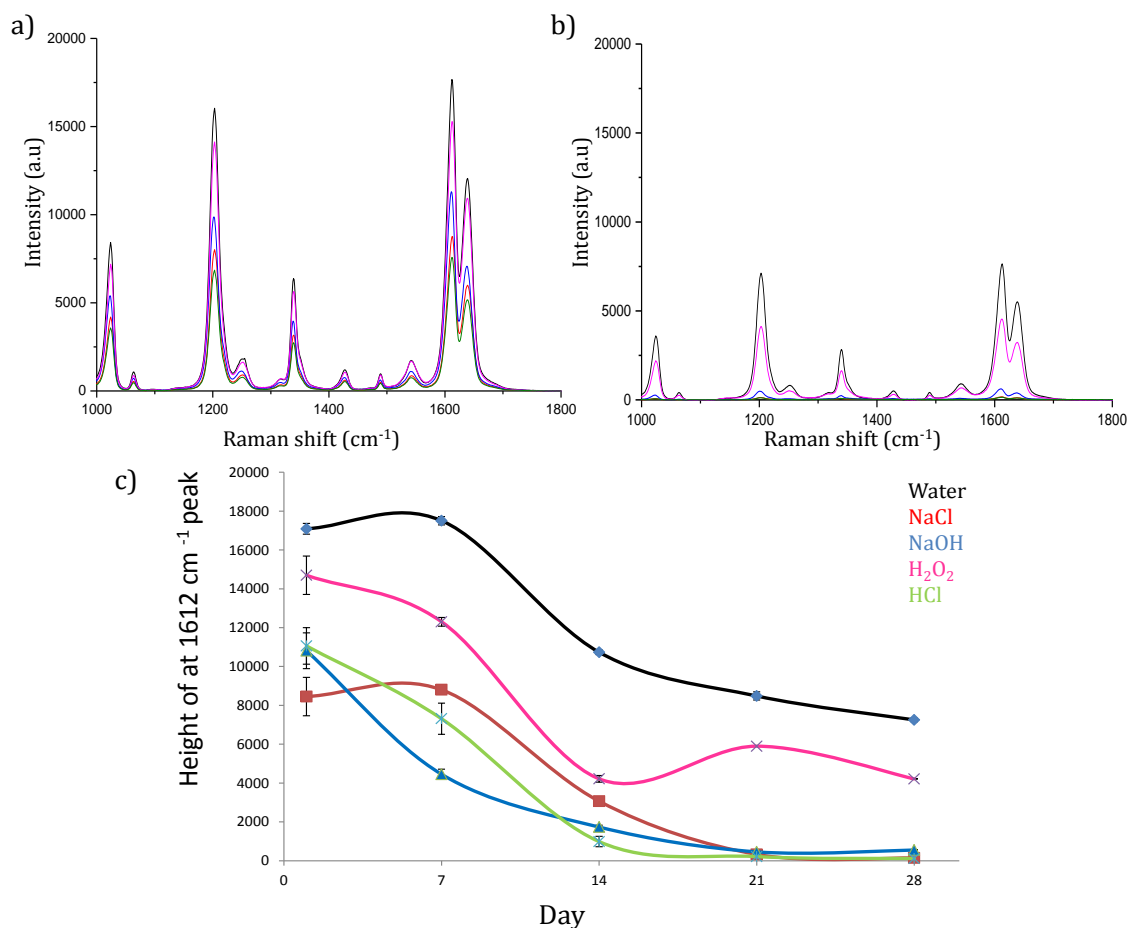
Figure 2.22 SERS response of Cabot nanotags in water (black), NaCl (red), NaOH (blue), H_2O_2 (pink)and HCl (green) on (a)day 1 and (b) day 28 and (c) Change in 1614 cm^{-1} peak of each tag in harsh environment at day 1, 7, 14, 21 and 28. Spectra taken using a 785 nm laser excitation, 5 second acquisition time and a 4.5 mW laser power. Spectra were baseline corrected using Matlab. Error bars were obtained from the standard deviation of 3 samples with replicates of each taken.

The data shown in Figure 2.22 (a), demonstrated that there was a clear drop in SERS intensity after only 1 day due to exposure of the Cabot nanotags to each harsh environment, as the Cabot nanotags already begin to aggregate and precipitate out of solution resulting in a low SERS signal. The nanotags, as expected, have the highest SERS response when only exposed to water and the signal decreases as much as 9000 a.u when the nanotags were exposed to 1 M of NaCl. Over the course of the time study, the SERS signal gradually decreases as the NPs precipitate out of the solution and by day 21 no SERS signal was obtained when the nanotags were exposed to NaCl, NaOH and HCl. H_2O_2 was the only harsh environment which still gives a SERS signal by day 28.

The SERS results from the exposure of the Cabot-Pt nanotags to the different environments are given in Figure 2.23.
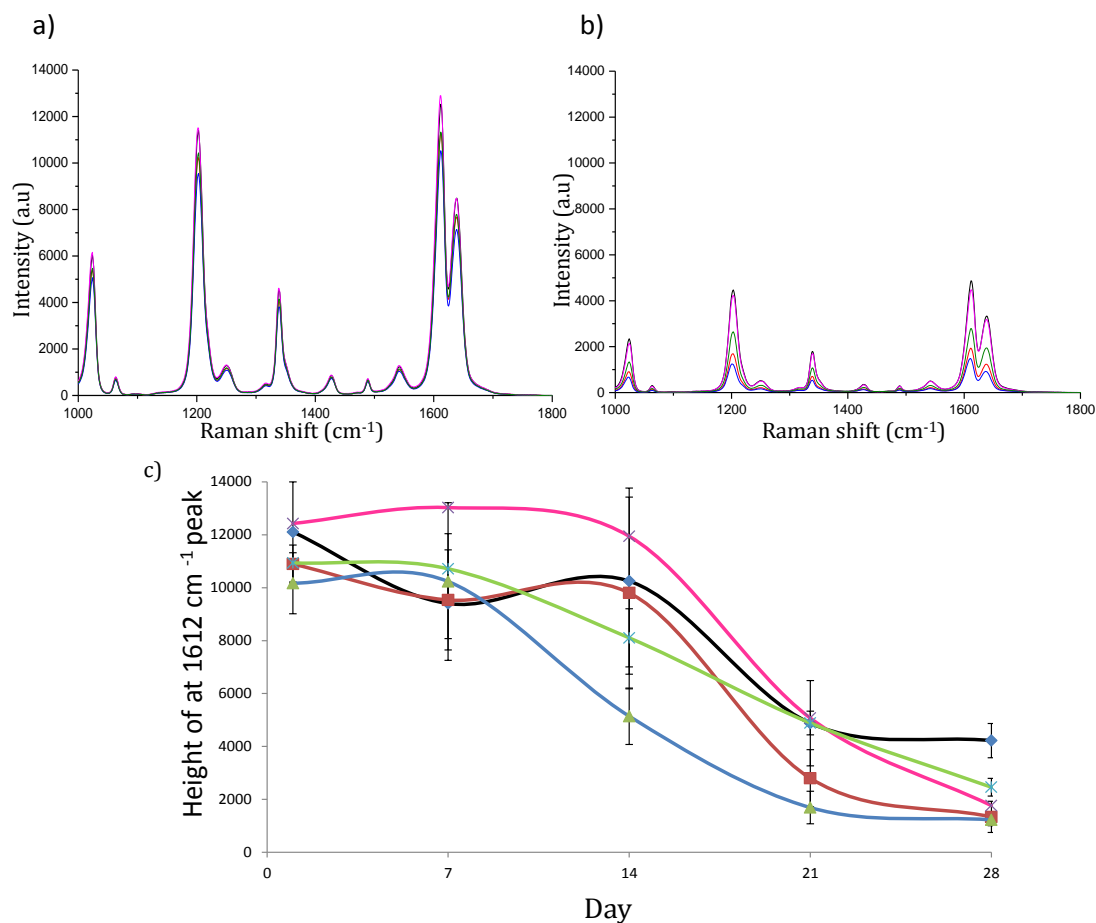
Figure 2.23 SERS response of Cabot-Pt nanotags in water (black), NaCl (red), NaOH (blue), H_2O_2 (pink)and HCl (green) on (a)day 1 and (b) day 28 and (c) Change in peak height of 1612 cm^{-1} peak of Cabot nanotags in each harsh environment at day 1, 7, 14, 21 and 28. Spectra taken using a 785 nm laser excitation, 5 second acquisition time and a 4.5 mW laser power. Spectra were baseline corrected using Matlab. Error bars were obtained from the standard deviation of 3 samples with replicates of each taken.

As shown in Figure 2.23 when the Cabot-Pt nanotags were exposed to the harsh environments, on day 1, only a small decrease in intensity of the 1612 cm^{-1} peak was observed from the control. This suggested that the nanotags were more stable as than unprotected nanotags, which exhibited a large decrease in intensity when the nanotags were exposed to NaCl, NaOH and HCl. The unprotected nanotags decreased by roughly 7000 a.u compared to the control, whereas as the protected

nanotags decreased by 1000 a.u compared to the control. This suggests that the partial Pt shell was protecting the Cabot nanotag from aggregating.

The decrease in intensity (Figure 2.23 (c)) was monitored by plotting the height of the 1612 cm^{-1} peak from BPE over time. Little change in the SERS intensity from the nanotags exposed to the harsh environments was observed after one week, however by day 7-14 the SERS intensity of the nanotags had decreased substantially and much weaker BPE signals were obtained due to the nanotags precipitating out of solution.

The change in LSPR and BPE SERS signal in each harsh environment over days 1, 7, 14, 21 and 28 of the Cabot and Cabot-Pt nanotags are shown in appendix 8.1-8.5 and again it is seen that the LSPR and BPE SERS signal is sustained for longer when the Pt shell is present.

Although the signal was weaker, a BPE signal was still visible after 21 and 28 days, which was not the case in the unprotected Cabot nanotags, therefore suggesting the Pt had a protective role.

2.4 Conclusion

It is important to develop nanotags that are stable in harsh environments as it can increase the use of NPs in a variety of different mediums, eliminating aggregation and diminished SERS signals obtained when unprotected Au NPs are used. For example, for applications that require a high concentration of salt or an acidic/alkali environments, uncoated Au NPs will experience aggregation and would not maintain a steady SERS signal,[85] however by using protected nanotags, NPs could be used.

Pt could be synthesised onto the surface of the in house synthesised Au-MGITC-SiO$_2$ and Cabot nanotags. The stability of each nanotags, along with their unprotected core nanotags, was assessed in harsh environments and monitored over a period of time using extinction spectroscopy, DLS and Raman scattering. It was seen that when in house Au-MGITC-SiO$_2$ nanotags were coated in Pt, A small increase in stability was obtained and the SERRS signal was visible for longer (7 -14 days). However Pt shelling of Cabot nanotags proved to be much more effective and there was a clear increase in stability due to only a small decrease in LSPR and

SERS from day 1 to day 7 when Pt was added to protect the nanotags. However, after day 14 the SERS and LSPR decreased and the stability was limited to two week, likely due to the degradation and loss of Pt shell after this point. Although the Pt shelling of the Cabot tags did have an increased stability over the in-house nanotags, due to the increase in size, the nanotags settled to the bottom of the solution and shaking prior to analysis had to take place. This could be detrimental to the analysis and future work would be to improve this issue.

The stable Pt coated nanotags could also be used in enhanced oil recovery (EOR) which requires harsh environments to recover trapped oil in reservoirs, as an alternative to the conventionally used polymer coated NPs have been used. [86]

More future work would be to investigate other protective coatings, such a polyaniline, to protect the nanotag from aggregating in harsh environments.

3. Catalytic activity of nanoparticles

3.1 Introduction

Artificial enzymes have become an increasingly interesting area of research due to their many advantages over natural protein enzymes which are expensive, difficult to isolate and unable to withstand harsh environments.[87] An important area of this research involves using metallic NPs as artificial enzymes, known as nanozymes. Nanozymes exhibit peroxidase-like activity enabling them to catalyse the oxidation of substrates such as 3,3',5,5'-tetramethylbenzidine (TMB) in the presence of hydrogen peroxide (H_2O_2), giving a colourimetric response.[88, 89] Conventionally, nanozymes have been used for the detection of H_2O_2[90] and glucose[89] but have recently been incorporated into immunoassays, replacing the conventional enzymes that are used in enzyme linked immunosorbent assays (ELISAs).[88]

3.1.1 Oxidation of TMB and ABTS

TMB and 2,2′-azino-bis(3-ethylbenzothiazoline-6-sulfonate) (ABTS) are peroxidase substrates which undergo a colour change when oxidised by H_2O_2 in the presence of an enzyme.[91] The vivid colour changes make them ideal chromogenic substrates for using in ELISAs for the detection of different antigens. ELISAs are discussed in more detail in section 4.1.

The oxidation of TMB occurs via a two-step, two-electron oxidation. The first one-electron oxidation produces a radical cation (TMB^+), with an absorbance maximum at 370 nm which exists in equilibrium with a blue charge transfer complex (CTC) that has an absorbance maximum at 650 nm. The addition of a strong inorganic acid initiates the second electron oxidation, terminating the reaction, and yielding the yellow diamine product (TMB^{2+}) which has an absorbance maximum at 450 nm.[92] The oxidation of TMB to its two states is shown in Figure 3.1.
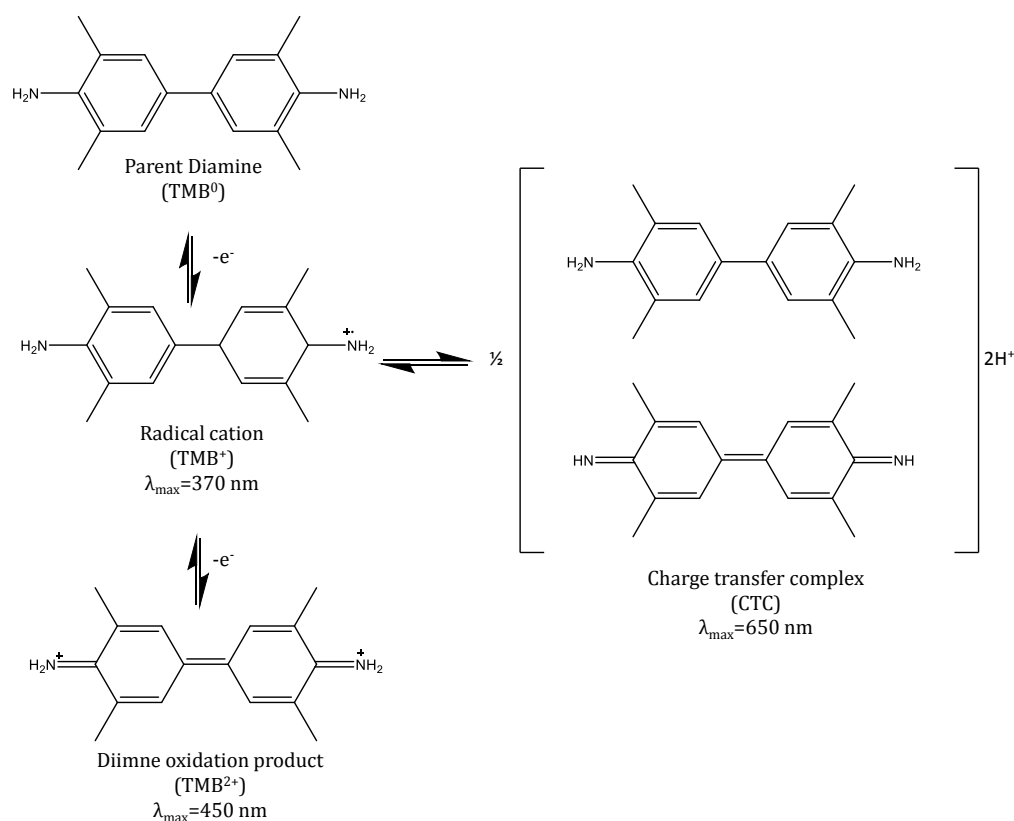
Figure 3.1 Oxidation of TMB by H_2O_2 in the presence of an enzyme to the 1st and 2nd electron oxidation products.

As well as having chromogenic properties, TMB is electroactive and is often been used as an electrochemical substrate for the direct detection of the enzyme horseradish peroxidase (HRP) with a limit of detection of 8.5 x 10^{-14} M.[93]

The oxidation of ABTS is shown in Figure 3.2 and like TMB, it yields a radical cation (ABTS$^{.+}$) which is green in colour and has a distinct UV-vis spectrum with absorbance bands at 650 nm, 735 nm and 815 nm.[94] There is also a second oxidation product, ABTS^{2+}, which gives the same absorbance spectrum.
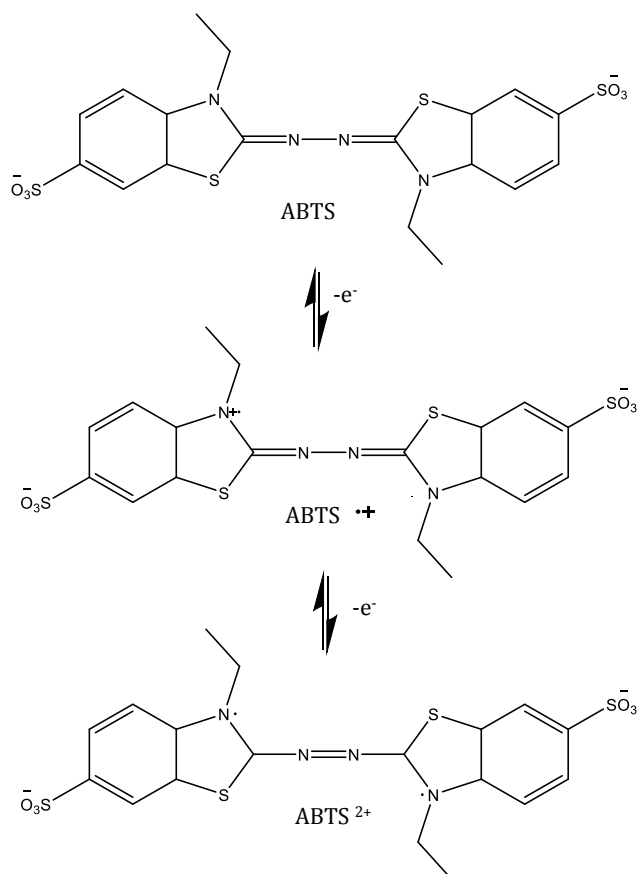
Figure 3.2 Oxidation of ABTS by H_2O_2 to ABTS·+ and ABTS^{2+} product.

As well as its role in ELISAs, ABTS is also used to detect antioxidant molecules using the ABTS decolourisation assay. This assay involves the reduction of antioxidants, such a glutathione, which causes the reduction of the oxidised ABTS that results in the decolourisation of the radical, which can be monitored using UV-vis spectroscopy.[95]

As already mentioned, the oxidation of TMB and ABTS requires an enzyme to facilitate the decomposition of H_2O_2. Commonly used enzymes include alkaline phosphatase (ALP) and HRP with the latter being the most ideal due to its stability, it is less expensive compared to other enzymes and its high turnover rate, producing strong signals in a short time frame.[96]

HRP is made up of metal centres, two calcium atoms and one heme group. The heme group has a planar structure, which holds an iron (Fe) atom in the middle of a porphyrin ring (made up of four pyrrole molecules).[97] Its structure is shown in Figure 3.3.
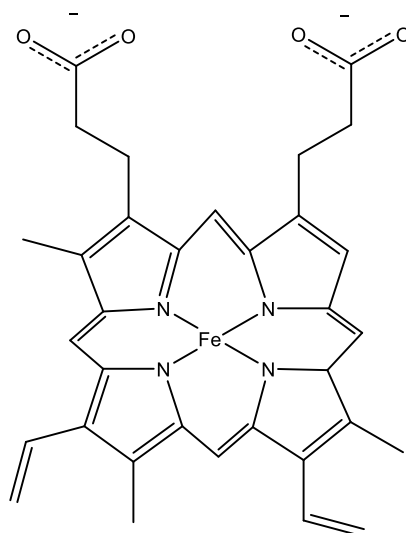
Figure 3.3 Structure of Fe heme group in HRP.

The heme group has a vacant position on the Fe atom which is free for hydrogen bonding to occur during reduction-oxidation reactions and is therefore considered the active site of the enzyme.[97] When HRP is in the presence of H_2O_2, an oxygen of the H_2O_2 binds to the vacant position on the Fe atom initiating the reduction of HRP via the formation of two intermediate compounds shown in Figure 3.4.
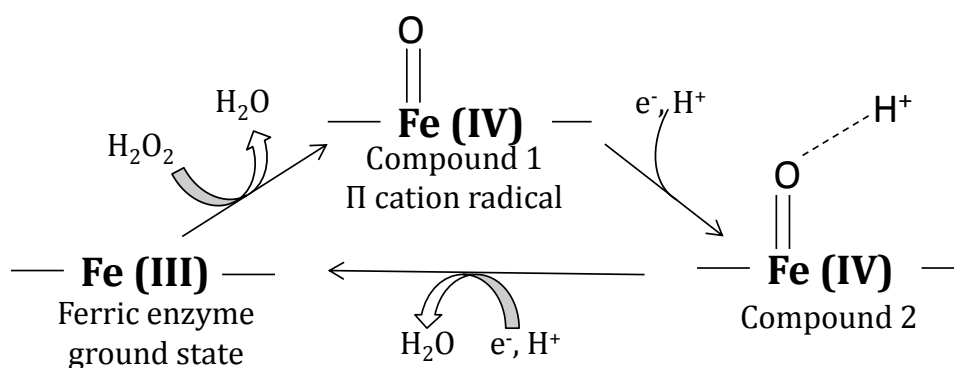
Figure 3.4 Reduction of HRP by H_2O_2.

The Fe exists first as Fe (III) which is oxidised to Fe (IV) as the H_2O_2 is converted to water, leaving the remaining oxygen to bind to the Fe, giving compound 1. An electron and H^+ ion from the peroxidase substrate then forms a bond with the oxygen to form compound 2. Finally, another electron and H^+ forms water with the oxygen bonded to the Fe to allow the iron to return to Fe (III). As the HRP is reduced,

substrates such as TMB and ABTS are oxidised resulting in the desired coloured product.[97] Although HRP is widely used in ELISAs, it can be expensive and difficult to isolate, therefore there is a growing interest in NPs as artificial enzymes.[98]

3.1.2 Catalytic activity of nanoparticles

Recently, it has been found that metal NPs possess an intrinsic enzyme mimetic activity. The first example of this activity was reported by Yan *et al.* in 2007, who discovered that ferromagnetic NPs possess peroxidase-like activity.[88] In this study they compared the catalytic activity of Fe_3O_4 NPs to that of HRP and demonstrated that Fe_3O_4 NPs could catalyse the oxidation of 3 different peroxidase substrates (TMB, 3,3'diaminobenzidine (DAB) and o-phenylenediamine (OPD)) with H_2O_2 to give the same colour changes as HRP over a broader range of pH and temperature.

It was suggested that these catalytic properties would make them ideal for a number of applications such as catalysing the oxidation of organic substrates to reduce their toxicity[99] or as a detection tool which can produce a colour change in wastewater treatment.[100] Although the discovery that Fe_3O_4 NPs had peroxidase like activity was surprising, it was not unexpected as Fe^{2+}/Fe^{3+} ions are also found in HRP which, as discussed in section 3.1.1, catalyses the breakdown of H_2O_2.

After this initial discovery, the catalytic activities of other metals NPs were investigated and the term 'nanozyme' was coined to describe their enzyme mimicking properties. However, the catalytic activity of other metal NPs proved to be harder to explain and different explanations have been proposed.

Jv *et al.* investigated the nanozyme properties of positively charged Au NPs and their ability to catalyse the oxidation of TMB by H_2O_2, providing a simple approach for the colorimetric detection of H_2O_2 with a detection limit of 500 nM.[101] They stated that this catalytic activity was only present with positively charged Au NPs and that citrate capped negatively charged Au NPs did not demonstrate catalytic properties. They suggested that this was due to the catalytic activity being attributed to the adsorption of H_2O_2 on the surface of the Au NPs, the oxygen bond being broken and two free radicals being formed stabilising the Au surface *via* the partial electron exchange interaction.[101] This implied that the positive and negative surface charges

would influence the adsorption of H_2O_2 and the particle-mediated electron transfer processes.

However, Wang *et al.* compared the peroxidase like activity of unmodified, amino modified and citrate capped Au NPs and disagreed with the previous conclusion.[102] Using TMB and colorimetric detection to investigate the catalytic activity, they reported that all three types of NPs had catalytic behaviour, which was in contrast to the work of Jv *et al.* They suggested that the amine moieties of the TMB had a stronger affinity for the negatively charged citrate capped Au NP surface which increased its catalytic activity over that of positively charged amino modified Au NPs. They supported this claim by using the NPs to catalyse the oxidation of ABTS, which has two sulfo groups per molecule and is negatively charged. They observed that the amino modified Au NPs catalysed the reaction of ABTS more efficiently than the negatively charged citrate capped Au NPs therefore suggesting that the charge of the NPs and substrate plays a very important role in the catalytic activity.

More recently, the enzyme mimicking activity of Ag NPs has been investigated. In 2012 Huang *et al.* demonstrated that Chitosan stabilised Ag NPs (Ch-Ag-NPs) possessed intrinsic peroxidase-like activity and could catalyse the oxidation of the peroxidase substrates TMB and OPD.[89] They came to the same conclusion as Jv *et al.*, proposing the Ch-Ag-NPs effectively catalysed the decomposition of H_2O_2 into OH radicals which would then go on to oxidise the TMB as shown in Figure 3.5. Ch-Ag NPs were used for the simple, sensitive and selective visual and colorimetric detection of glucose, with a detection limit as low as 100 nM.
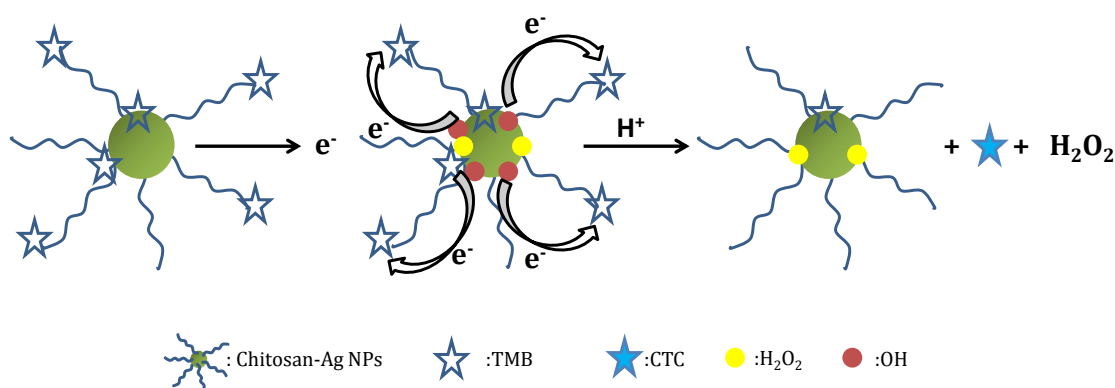
Figure 3.5 Proposed oxidation of TMB using the catalytic properties of Ch-Ag NPs. TMB and H_2O_2 were added to Ch-Ag NPs and the H_2O_2 was decomposed into OH radicals due to the Ag NP surface. The OH radicals then oxidised the TMB to the CTC which could be detected using UV-vis spectroscopy. Adapted from Jiang, H., et al., *Peroxidase-like activity of chitosan stabilized silver nanoparticles for visual and colorimetric detection of glucose.* Analyst, 2012. **137**(23): p. 5560-5564with permission of The Royal Society of Chemistry.

In the examples so far, UV-vis spectroscopy was used as the detection method however, the surface of the NPs have also been utilised to allow for SERRS detection of the oxidation of TMB.

In 2013, we investigated the inherent peroxidase-like activity of Ag NPs *via* the oxidation of TMB for the sensitive detection of H_2O_2.[90] As the absorbance maximum of the CTC is 650 nm, when Ag NPs catalyse the oxidation of TMB by H_2O_2, the resulting solution could be analysed with Raman spectroscopy using 633 nm laser excitation, which coincided with the CTC absorbance maximum, and detected *via* RRS. As well as RRS, surface enhancement of the CTC was also achieved as the Ag NPs do not just serve as the catalyst but as a roughened metal surface for the CTC to adsorb onto via the interaction with the negative Ag NP surface and positive CTC, resulting in both resonance and surface enhancement. The schematic in Figure 3.6 shows the oxidation of TMB to the CTC with Ag NPs and H_2O_2 and the corresponding SERRS spectrum achieved when the solution is interrogated with a laser with excitation wavelength of 633 nm.
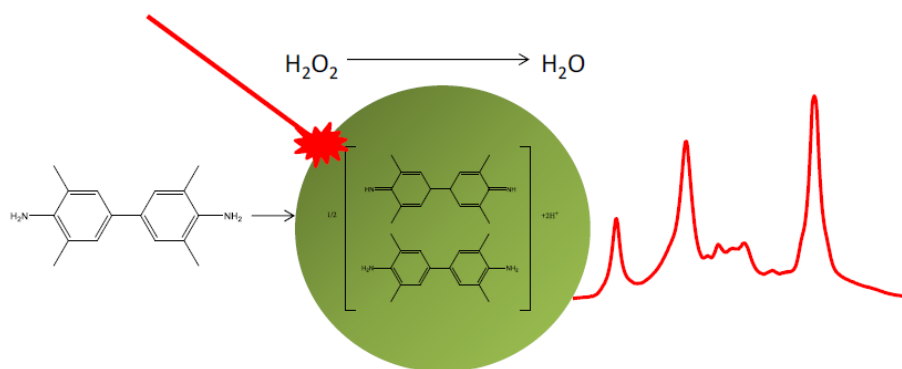
Figure 3.6 Oxidation of TMB in catalysed by Ag NP in the presence of H_2O_2 and the resulting SERRS spectrum of the CTC when interrogated with a 638 nm laser excitation. Adapted from McKeating, K.S., et al., *An investigation into the simultaneous enzymatic and SERRS properties of silver nanoparticles.* Analyst, 2013. **138**(21): p. 6347-6353 with permission of The Royal Society of Chemistry.

By applying SERRS for the detection of the oxidised TMB product, a sensitive and fast assay for the detection of H_2O_2 was achieved, with a detection limit of 100 nM.[90]

The catalytic activity of many NPs have been investigated and utilised for the detection of biomolecules. This chapter focuses on the catalytic activity of 4 different types of NPs and utilising them to catalyse the oxidation of TMB and ABTS in the presence of H_2O_2

3.2 Chapter Aims

The aim of this chapter was to investigate the catalytic activity of Ag, Au, Au-SiO$_2$-Pt and Fe_2O_3 NPs by the oxidation of the peroxidase substrate TMB and ABTS in the presence of H_2O_2. The oxidation of TMB and ABTS with each different metal NP was characterised using UV-vis spectroscopy, resonance Raman scattering and, where possible, SERRS. Figure 3.7 depicts the catalytic activity of the nanozyme, which causes the decomposition of H_2O_2 which in turn oxidises the TMB and ABTS to their blue and green oxidation products respectively.
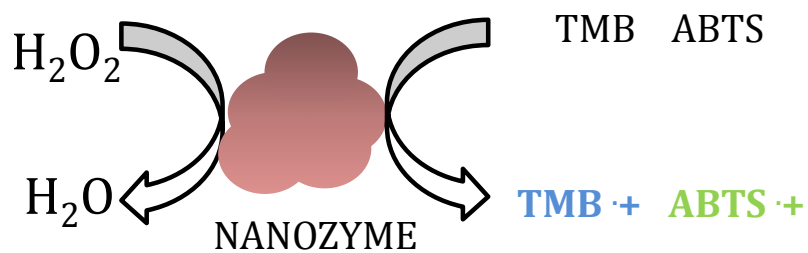
Figure 3.7 Catalytic activity of nanozyme. The nanozyme decomposes H_2O_2 producing OH radicals and H_2O, which then goes on to oxidises the TMB and ABTS producing the coloured oxidation products.

The catalytic activity of each type of NP was compared and the most promising metal NPs were chosen for use in assays for the detection of H_2O_2 and glutathione. By using NPs instead of conventional enzymes, the cost, synthesis and preparation of the detection assays could be lowered. Also, by applying Raman detection of the oxidised product, a more sensitive detection technique could be utilised providing more structural information than the conventionally used UV-vis spectroscopy.

3.3 Results and discussion

3.3.1 Nanoparticle synthesis and characterisation

Many different metal NPs have been reported to have peroxidase-like activity and can catalyse the oxidation of the peroxidase substrates TMB and ABTS in the presence of H_2O_2. In this work Ag, Au, Au-SiO$_2$-Pt and Fe$_2$O$_3$ NPs were synthesised, characterised and their catalytic activity evaluated using TMB and ABTS.

3.3.1.1 Synthesis of silver nanoparticles

Citrate capped Ag NPs were synthesised via a modified Lee and Meisel method which involved the reduction of silver ions to silver atoms in the presence of citrate and heat.[8] As well as the reducing agent, the citrate acted as a stabilising agent, providing the negative surface layer which prevented aggregation of the NPs due to electrostatic repulsion. The Ag NPs were characterised using extinction spectroscopy, DLS and SEM to evaluate their quality. The results from the extinction and SEM are shown in Figure 3.8.
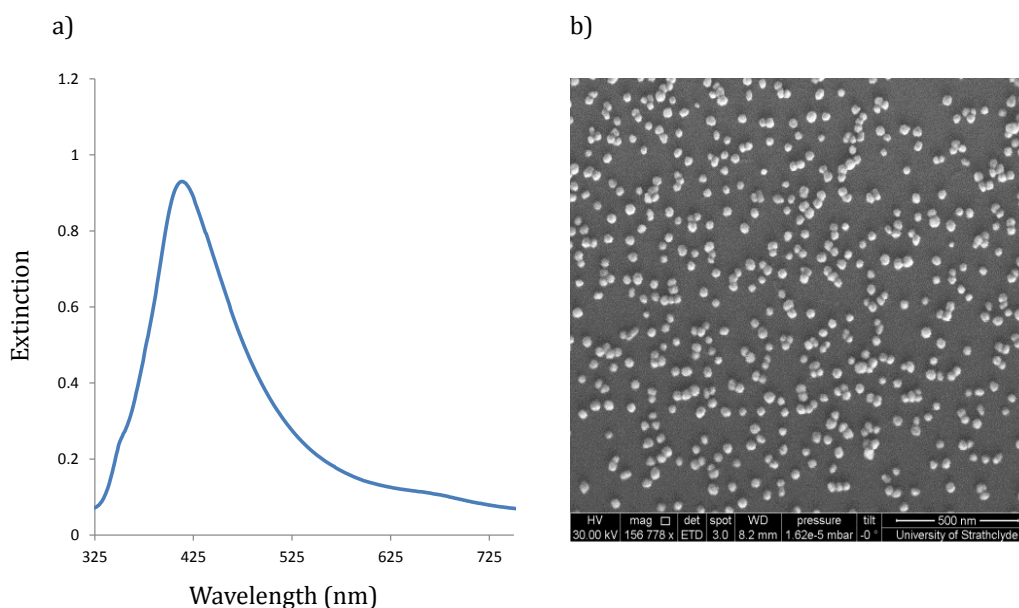
Figure 3.8 (a) Extinction spectrum of Ag NPs. (50 μL of Ag NPs diluted in 450 μL of distilled water) (b) SEM image of Ag NPs.

As observed in Figure 3.8 (a), the Ag NPs had an LSPR at 410 nm, a typical value expected for Ag NPs of this size.[103]   The DLS measured the NPs to be 70±2.1 nm, with a zeta potential of -37±0.6 mV. This demonstrated that the NPs were stable as it has been determined that NPs which have a zeta potential lower than -20 mV are stable in solution.[79] The concentration of the Ag NPs was obtained using the Beer-Lambert law and a molar extinction coefficient of $2x10^{10}$ M^{-1} cm^{-1},[104] and was calculated to be 0.3 nM

To confirm the monodispersity and the size of the NPs, SEM was also carried out. The SEM image in Figure 3.8 (b) indicated that the NPs were spherical, had a size of 74±3 nm and were monodisperse.

3.3.1.2 Synthesis of Fe_2O_3 nanoparticles

Maghemite (γFe_2O_3) NPs were synthesised using a co-precipitation method described by Donnelly et al.[105] In this method Fe salts were added to a base to form magnetite (Fe_3O_4) NPs which were then oxidised to form Fe_2O_3 NPs.   The resultant NP solution was brown/black in appearance and was characterised using extinction spectroscopy, DLS and SEM.   The extinction spectrum and SEM are shown in Figure 3.9.

a)   b)
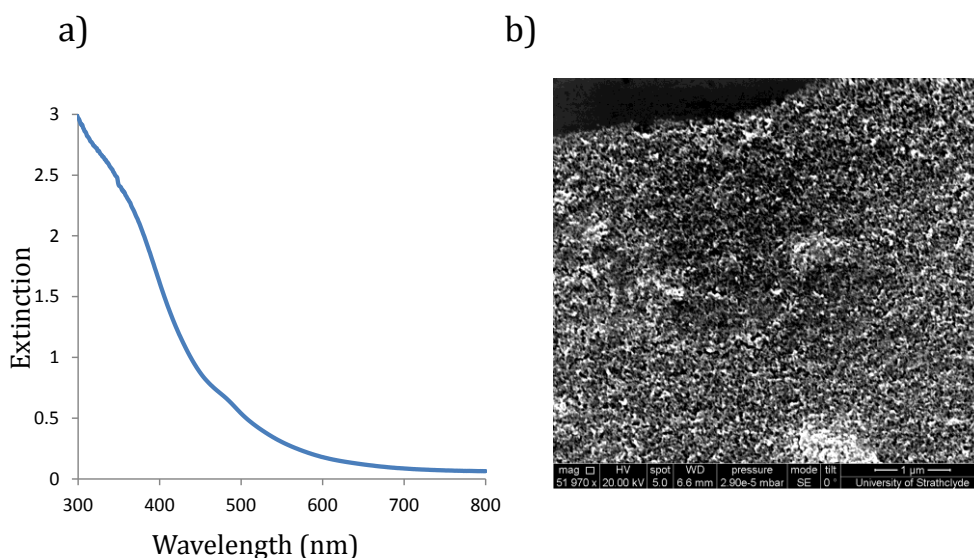
Figure 3.9 a) Extinction spectrum of Fe_2O_3 NPs (NPs diluted 1 in 20 to produce spectrum) and b) SEM image of Fe_2O_3 NPs.

Kumar *et al.* have reported that Fe_2O_3 NPs have a very weak absorbance band at 350 nm, due to the electronic excitation of oxygen lone pairs, which is present in the extinction spectrum of the synthesised NPs.[106] To obtain the extinction spectrum, the NPs had to be diluted 20 fold due to the high concentration of the solution which is evident in the SEM image which shows large clusters of Fe_2O_3 NPs. The DLS measured the size of the Fe_2O_3 NPs to be 154 ± 2.1 nm, suggesting that clusters of NPs held closely together instead of individual NPs were being measured as Kumar *et al.* report that the Fe_2O_3 NP are very small in size (10 nm).[106]

Stable Au NPs and Au-SiO$_2$-Pt nanotags were also synthesised as described in section 2.2.3. Due to the successful synthesis of each of the different metal NPs, the catalytic activity could then be assessed.

3.3.2 Oxidation of TMB

3.3.2.1 Oxidation of TMB using the catalytic activity of silver nanoparticles

It has previously been reported that Ag NPs demonstrate a catalytic activity and can oxidise TMB to its oxidised form (the CTC) in the presence of H_2O_2.[90] However the explanation as to why the Ag NP has this catalytic activity is not fully known therefore the catalytic activity was investigated and characterised in this work using the oxidation of TMB.

100 µL of 3 mM TMB (dissolved in DMSO) and 100 µL of 6 mM H_2O_2 was added to 100 µL of 0.3 nM citrate capped Ag NPs and made up to 500 µL with distilled water. Previous studies indicated that these concentrations of TMB and H_2O_2 were similar to that found in TMB true blue solution, a pre-made solution of TMB and H_2O_2 routinely used in ELISAs, and could provide satisfactory TMB oxidation when using HRP as the catalyst, yielding the characteristic blue CTC. Therefore, if the NPs exhibit catalytic activity they should be able to catalyse the reaction between these concentrations of TMB and H_2O_2 and the CTC signal should be obtained.

The solution was then characterised using extinction spectroscopy and DLS. Control experiments were also carried out to investigate the effect of TMB and H_2O_2 alone on Ag NPs. The results are shown in Figure 3.10.
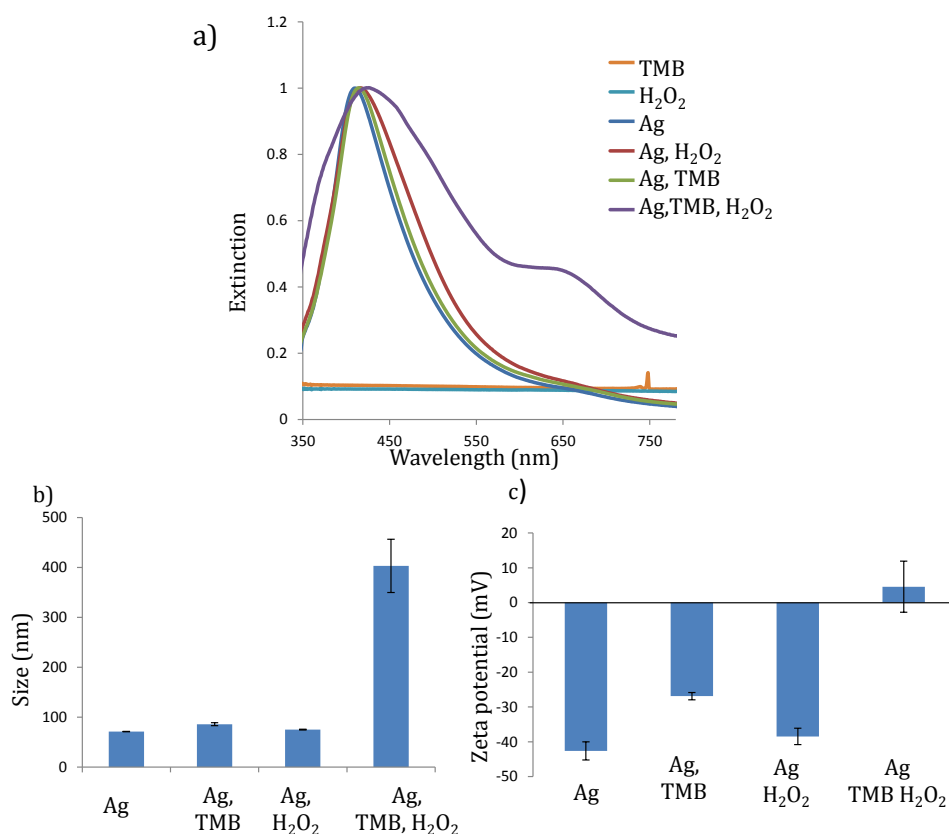
Figure 3.10 (a) Extinction spectra of TMB (orange), H_2O_2 (light blue), Ag NPs (dark blue), Ag NPs and H_2O_2 (red), Ag NPs and TMB (green) and Ag NPs, TMB and H_2O_2 (purple). Spectra have been normalised to 1 for clarity. Bar graph showing change in Ag NPs size (b) and zeta potential (c) as different components were added. Error bars obtained from the standard deviation of 3 samples with 5 replicates of each taken.

The extinction spectrum in Figure 3.10 (a) demonstrates that when TMB and H_2O_2 were added separately to the Ag NPs, a red shift in the LSPR and peak broadening was observed as the Ag NPs increased in size. Slight aggregation of the Ag NPs with the addition of TMB and H_2O_2 was also observed in the DLS data which indicated a size increase of 14 nm when TMB was added and 4 nm with H_2O_2 addition. Less negative zeta potentials were also observed upon the addition of TMB and H_2O_2. The aggregation due to the addition of TMB is most likely due to the amine groups of the TMB which will have an affinity for the Ag NP surface. The aggregation upon addition of H_2O_2 was also expected and was a result of H_2O_2 oxidising the Ag^0 ions to Ag^+ ions leading to an instability and increase in size.

When TMB and H_2O_2 were both added to the Ag NPs a large red shift in the LSPR peak was observed and noticeable peak broadening occurred, suggesting that a large degree of aggregation took place. This was also confirmed by DLS which showed the Ag NPs increased to roughly 400 nm and became positively charged. The aggregation and positively charged surface was due to the formation of the positive CTC which was electrostatically attracted to the negative Ag NP surface which pulled multiple Ag NPs closer together causing aggregation and NP instability. Another indication of the formation of the CTC was the appearance of the characteristic CTC peak at 650 nm in the extinction spectrum which was only present when all three components were added together, reinforcing that the Ag NPs had catalysed the oxidation of TMB in the presence of H_2O_2.

The same samples were then analysed by Raman using a 638 nm laser excitation which coincided with the absorbance maximum of the CTC and the resulting SERRS spectra are shown in Figure 3.11.
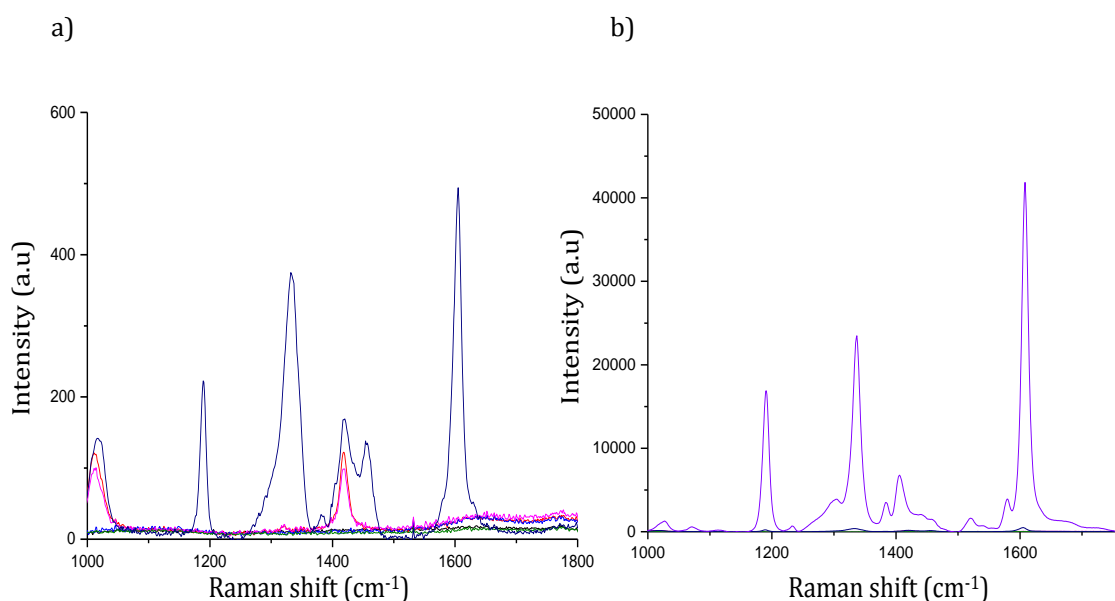
Figure 3.11 a) SERRS spectra obtained for control experiments (Ag NPs alone (light blue), TMB (red), H_2O_2 (green), TMB and H_2O_2 (pink), Ag NPs and H_2O_2 (black) and Ag NPs and TMB (dark blue) (b) SERRS spectrum of CTC formed due to the catalytic Ag NPs in the presence of H_2O_2 and TMB. Spectra were obtained using 638 nm laser excitation, 1 second accumulation time and 4.5 mW. The spectra shown are the average of 5 measurements of 3 replicate samples. The spectra were all baseline corrected using Matlab.

The SERRS spectra of the CTC (Figure 3.11 (b)) obtained when Ag NPs, TMB and H_2O_2 were all present indicated the three main characteristic peaks of the CTC at 1195 cm^{-1}, 1340 cm^{-1} and 1610 cm^{-1} which represent CH_3 bending modes, inter-ring stretching modes and a combination of ring-stretching and CH bending modes respectively.[107] As already shown in Figure 3.10, the formation of the positive CTC causes the Ag NPs to aggregate by electrostatically adsorbing onto the Ag NPs and destabilising them. This created areas of high electromagnetic enhancement resulting in the very intense SERRS spectrum of the CTC.

The catalytic activity of the Ag NPs was proposed to be attributed to the adsorption of H_2O_2 onto the surface of the Ag NPs, causing it to break into OH radicals as the Ag NP surface is oxidised from Ag^0 to Ag^+. The free radicals then proceed to cause the oxidation of the TMB to the CTC, forming H_2O in the process.

The control experiments (Figure3.11 (b)) performed indicated that a small amount of oxidation of TMB to the CTC occurred when Ag NPs and TMB were added together. This was probably due to H^+ ions being present as the Ag NP was already in the oxidised Ag^+ form. However, it was deemed negligible as when compared to the intensity of the CTC spectrum obtained when Ag, TMB and H_2O_2 were mixed together the spectrum obtained was almost 100 times more intense.

Due to the successful characterisation of the catalytic activity of Ag NPs with TMB and H_2O_2, the catalytic activity of Au NPs, synthesis and characterisation shown in Section 2.2, was assessed.

3.3.2.2 Oxidation of TMB using the catalytic activity of gold nanoparticles

Au NPs have also been reported to have catalytic activity, however there has been some debate on the NPs surface charge and how it affects the catalytic activity. Jv *et al*. proposed that only positively charged Au NPs could catalyse the oxidation and did not see any catalytic activity with negatively charged citrate when analysing with UV-vis spectroscopy. [101] Whereas Wang *et al*. reported that negatively charged citrate capped Au NPs had an increased catalytic activity when compared to positively charged amino modified amino Au NPs.[102] Since negatively charged citrate capped Ag NPs performed well in the oxidation of TMB, the catalytic activity

of negatively charged, citrate reduced Au NPs were assessed with UV-vis and Raman spectroscopy.

Using the same protocol, the catalytic activity of Au NPs where investigated. 100 µL of 3 mM TMB and 100 µL of 6 mM H_2O_2 were added to 100 µL of citrate capped Au NPs (0.1 nM) with 200 µL of d.H_2O and the resulting solution (along with controls) was characterised using extinction spectroscopy and SERRS using 638 nm laser excitation. The results are shown in Figure 3.12.
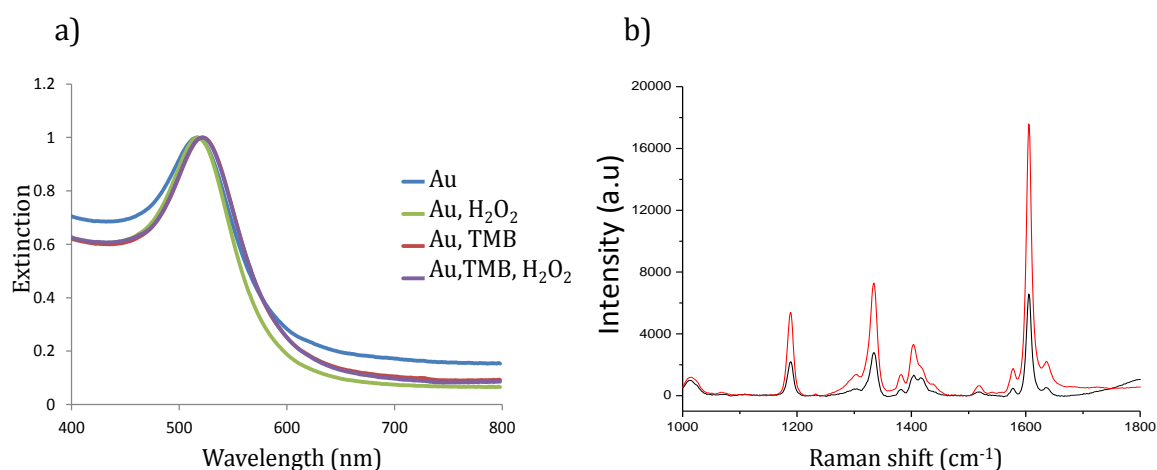
Figure 3.12 (a) Extinction spectra of Au NPs (blue), Au NPs and H_2O_2 (green), Au NPs and TMB (red) and Au NPs, H_2O_2 and TMB (purple). Spectra are normalised to 1 for clarity. (b) CTC SERRS spectrum due to the catalytic Au NPs on TMB with H_2O_2 (red) and without H_2O_2. Spectra were obtained using 638 nm laser excitation, 1 second accumulation time and 30 mW laser power. The spectra shown are the average of 5 measurements of 3 replicate samples and have all been baselined using Matlab.

Unlike Ag NPs, when TMB and H_2O_2 were added, both individually and together, to Au NPs, no aggregation was observed (Figure 3.12 (a)). There was also no appearance of the characteristic CTC peak at 650 nm, suggesting that the Au NPs did not catalyse the oxidation of TMB and no aggregation, due to the positive CTC, had occurred.

However, when the SERRS was obtained using a 638 nm laser excitation, there was a change in the CTC SERRS spectrum intensity with and without H_2O_2 (Figure 3.12 (b)). A more intense CTC SERRS signal was obtained when H_2O_2 was present

suggesting that some of the H_2O_2 was being decomposed to free radicals by the Au NP surface. However, the SERRS intensity was much lower than the CTC SERRS spectrum obtained when using Ag NPs (50% laser power used in Ag NP experiment compared to 100% laser power used to achieve same signal for Au NP) therefore the catalytic activity was deemed to be lower for the negatively charged Au NPs compared to the negatively charged citrate Ag NPs. This could be due to a number of reasons such as Au NPs not decomposing the H_2O_2 as efficiently as the Ag NPs, the CTC having more of an affinity towards the Ag NPs resulting in higher SERS or the lack of aggregation of the Au NPs resulting in a weaker CTC signal and Ag NPs exhibiting stronger SERS properties than Au NPs. Another reason could be due to the strong electrochemical properties of Ag NPs which have been consistently used as H_2O_2 sensors in electrochemical experiments, with a limit of detection of 1.7 μM.[108]

Despite some papers reporting that negatively charged citrate capped Au NPs do not have any catalytic activity, the results suggest otherwise. However, the lack of 650 nm absorbance band in the extinction spectra suggest that the catalytic activity is very weak and may have been one of the reasons as to why the catalytic activity was thought not to exist.

3.3.2.3 Oxidation of TMB using the catalytic activity of ferromagnetic nanoparticles

Fe_2O_3 NPs, whose catalytic activity has routinely been used for the detection of various biomolecules,[88] were next used to catalyse the oxidation of TMB with H_2O_2. 100 μL of 3 mM TMB and 100 μL of 6 mM H_2O_2 were added to 100 μL of Fe_2O_3 NPs and left to shake for 5 minutes. Due to their magnetic properties, the Fe_2O_3 NPs could then be removed from the solution using a strong magnet, effectively cleaning the solution; hence NPs could not interfere with the extinction or resonance Raman spectrum. The extinction spectrum of the TMB oxidised by Fe_2O_3 NPs and controls are shown along with a photograph of the resulting solutions in Figure 3.13.
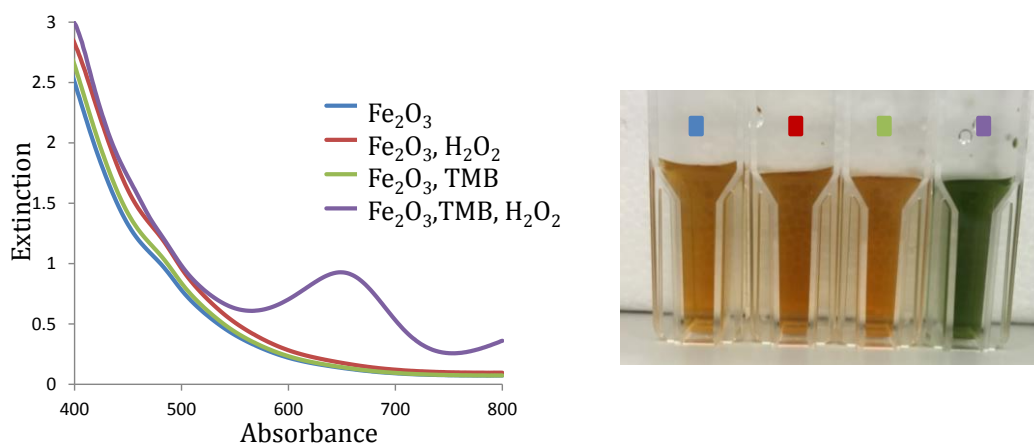
Figure 3.13 (a) Extinction spectra of Fe_2O_3 NPs (blue), Fe_2O_3 NPs and H_2O_2 (red), Fe_2O_3 NPs and TMB (green) and Fe_2O_3 NP, TMB and H_2O_2 (purple). (b) Corresponding image indicating colour change associated with the TMB oxidation.

When the Fe_2O_3 NPs were removed, using magnetic separation, from each sample, a weak orange solution of Fe_2O_3 NPs was obtained due to Fe_2O_3 NPs with weak magnetism not being completely removed from the solution. This resulted in an extinction spectrum with a peak below 400 nm. A visible colour change and change in extinction spectra was only observed when TMB and H_2O_2 were added to the Fe_2O_3 NPs and the solution turned green, which was the result of the orange Fe_2O_3 NPs solution mixing with the blue CTC product. As well as the visual colour change, the characteristic CTC absorbance peak at 370 and 650 nm were present, hence it was clear that oxidation of the TMB due to the Fe_2O_3 NPs and H_2O_2 had taken place.

As the Fe_2O_3 NPs have no surface enhancement properties, when the solutions were analysed using 638 nm laser excitation, only resonance Raman enhancement could be achieved. For this reason, the NPs were again removed, using magnetic separation, from the solution to allow a RRS spectrum of the CTC to be obtained in the absence of excess Fe_2O_3 NPs. The results are shown in Figure 3.14.

69
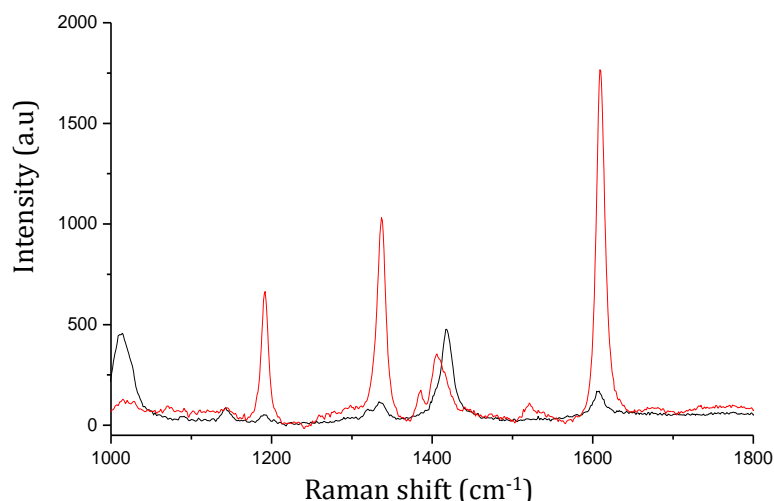
Figure 3.14 RRS spectra of Fe_2O_3 NPs and TMB (black) and Fe_2O_3 NPs, TMB and H_2O_2 (red). Spectra were obtained using 638 nm laser excitation, a 1 second accumulation time and 30 mW laser power. The spectra shown are the average of 5 measurements of 3 replicate samples and have all been baselined using Matlab.

As expected the RRS spectrum of the CTC was obtained when all of the components were added. There is a very weak CTC signal when there is no H_2O_2 present and also a peak at 1414 cm^{-1} which can be attributed to the unoxidised TMB.[90] However, this can be discarded and may be due to oxidised Fe^{2+} ions in the solution.

3.3.2.4 Oxidation of TMB using the catalytic activity of Au-SiO$_2$-Pt nanotags

The stable Au-MGITC-SiO$_2$-Pt nanotags synthesised in section 2.3.4 were also investigated to see if they had catalytic properties as Pt NPs are commonly used catalysts.[109] The peroxidase activity of Au-MGITC-SiO$_2$-Pt nanotags was again tested by adding 100 µL of 3 mM TMB, 100 µL of 6 mM H_2O_2 and 100 µL of Au-MGITC-SiO$_2$-Pt nanotags together and measuring the extinction spectroscopy to monitor the oxidation of TMB shown in Figure 3.15 along with a photograph showing the colour change of the tags when the TMB is oxidised.
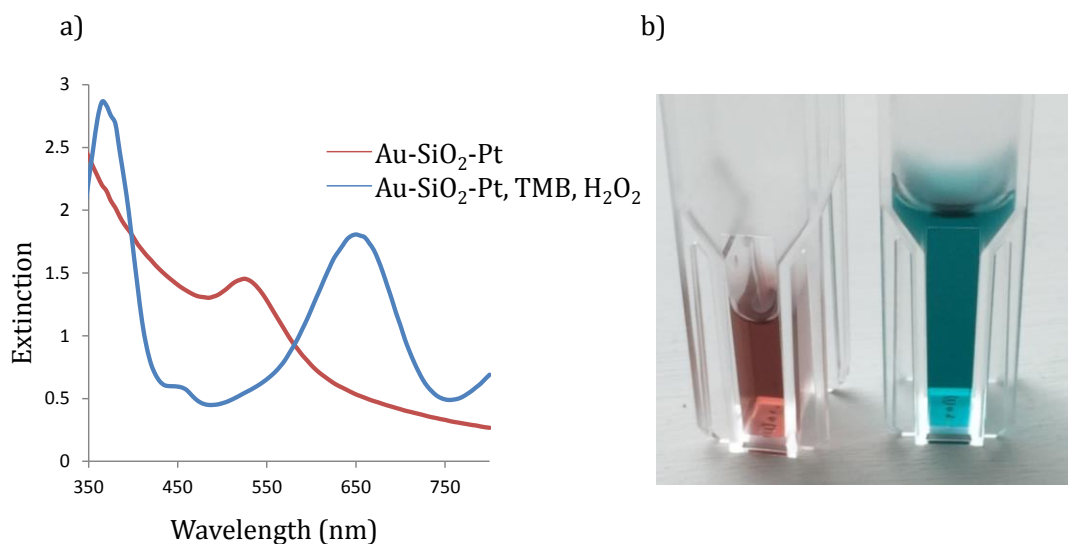
Figure 3.15 (a) Extinction spectra of Au-MGITC-SiO$_2$-Pt nanotags (red) and Au-MGITC-SiO$_2$-Pt nanotags with TMB and H$_2$O$_2$ (blue). (b) Corresponding images show the colour change associated with the oxidation of TMB.

As expected, the TMB was oxidised to the CTC and the characteristic absorbance peaks at 650 nm for the CTC and 370 nm for the radical TMB$^+$ were observed (Figure 3.15 (a)), completely obscuring the Au-MGITC-SiO$_2$-Pt nanotags LSPR which occurred at 520 nm. A small absorbance maximum for TMB^{2+} can also be observed in the oxidised TMB spectrum, suggesting that Pt has extremely good catalytic properties and provided enough decomposition of the H$_2$O$_2$ to facilitate the second oxidation step without the addition of acid.

The catalytic activity was due to the Pt shell as Au-MGITC-SiO$_2$ nanotags did not give any oxidation, due to the SiO$_2$ layer being chemically inactive. This was unsurprising as Pt is commonly used as a catalyst in many organic reaction schemes.[110] The resulting solutions were then analysed by Raman with 638 nm laser excitation and the resulting spectrum in Figure 3.16 were obtained.
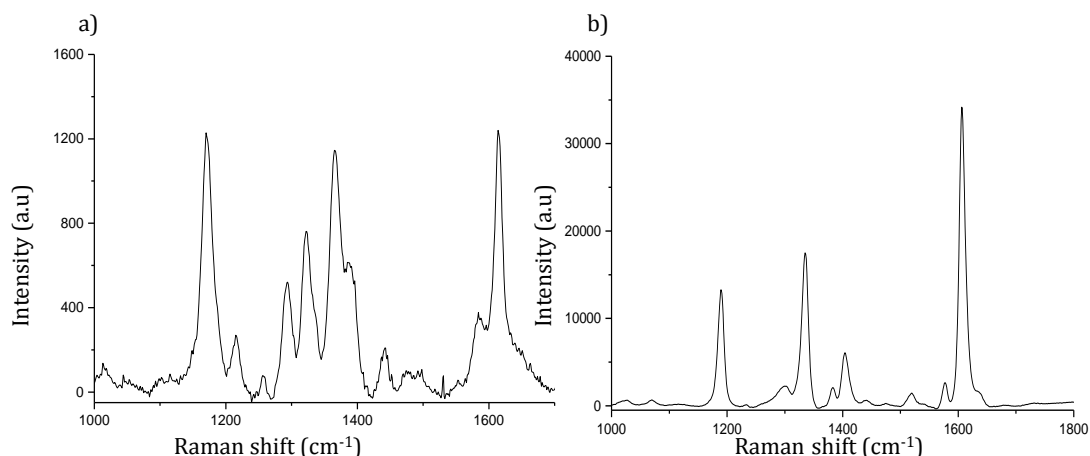
Figure 3.16 a) SERRS spectrum of MGITC obtained from Au-MGITC-SiO$_2$-Pt nanotags and b) CTC RRS spectrum due to the catalytic effect of Au-MGITC-SiO$_2$-Pt nanotags on TMB with H$_2$O$_2$. Spectra were obtained using 638 nm laser excitation, a 5 second accumulation time and 30 mW laser power. The spectra shown are the average of 5 measurements of 3 replicate samples and have all been baselined using Matlab.

The Au NP at the core of the Au-MGITC-SiO$_2$-Pt nanotags had already been functionalised with MGITC, see section 2.3, and the nanotags gave the unique property of being able to give two different Raman signals. Before the addition of TMB and H$_2$O$_2$ the nanotags (when analysed using 638 nm laser) gave the MGITC SERRS spectrum shown in Figure 3.16 (a). The signal then diminished when TMB and H$_2$O$_2$ were added and a very strong RRS spectrum of TMB was obtained (Figure 3.16 (b)). The signal is only due to RRS as Pt does not offer any surface enhancement of the CTC, and the TMB will be held too far from the Au NP core for enhancement to occur.

As the absorbance band of the CTC is much more prominent when using Au-MGITC-SiO$_2$-Pt nanotags compared to both Ag and Au NP, it can be deduced that the catalytic activity of the Au- MGITC-SiO$_2$-Pt nanotags is very large and this corresponded to the strong RRS signal obtained.

When comparing the catalytic activity of Ag, Au, Au-MGITC-SiO$_2$-Pt and Fe$_2$O$_3$ NPs by observing the extinction spectra, the intensity of the CTC absorbance band is very large when using Fe$_2$O$_3$ NPs and Au-SiO$_2$-Pt NPs (650 nm peak height of roughly 0.5 and 1). This is probably due to them having a greater catalytic activity,

although the signal is also aided by the removal of the Fe$_2$O$_3$ NPs and the absorbance band not being obscured by the extinction of the NPs. Au-SiO$_2$-Pt NPs were not removed from the solution but a very intense CTC absorbance band and colour change was still observed, due to the excellent catalytic properties of Pt.

As the Ag and Au NPs have a much stronger extinction band close to the absorbance of the CTC and were not removed from the solution, the extinction of the aggregated Ag NPs overlapped with the CTC absorbance. However, even though Au-SiO$_2$-Pt NPs were deemed to be more catalytic, the CTC RRS signal obtained using a 5 second acquisition 30 mW laser power was the same intensity as the SERRS signal obtained for the CTC when using Ag NPs with a 1 second acquisition and 5.4 mW laser power. Therefore, the SERRS capability of the Ag NPs outweighed the small CTC absorbance peak obtained. As Au NPs did not give a very intense CTC SERRS signal and gave no appearance of the 650 nm absorbance band in the extinction spectra, their catalytic activity was not as promising as the other metal NPs.

However, it should be noted that each of the NP types had different concentrations and sizes which would also have had an effect on their catalytic activity. For example, although the concentration of the Au and Ag NPs were roughly the same (0.1 and 0.3 nM), the increase in surface area of the Ag NP due to them being larger in size, would increase the concentration of H$_2$O$_2$ that would be broken down into free radicals and then go on to oxidise TMB. The larger surface area would also allow more CTC molecules to be electrostatically attracted to the surface and be surface enhanced, hence the larger SERRS signal obtained with Ag NPs. Therefore this comparison in catalytic activity is only qualitative.

Ag NPs were selected as the nanozyme which would be used for the detection of H$_2$O$_2$ due to their catalytic properties and their ability to give the best SERS response. By monitoring the decrease in the CTC SERRS signal as lower a lower concentration of H$_2$O$_2$ were added to Ag NPs with TMB, a limit of detection of H$_2$O$_2$ could be obtained.

3.3.3 Detection of hydrogen peroxide

To utilise the surface enhancement, Ag NPs were used for the detection of H$_2$O$_2$ via SERRS. As already discussed, many different nanozyme systems have been used

for the detection of H_2O_2. For example Fe_2O_3 NPs have been used to detect H_2O_2 colourmetrically with a limit of detection of 3 μM,[88] as have positively charged Au NPs, with an even lower limit of 0.5 μM using colourimetric detection.[111] We have also recently reported on the SERRS detection of H_2O_2 using the catalytic activity of Ag NPs with SERRS detection on an InVia Renishaw Raman instrument with a limit of detection of 100 nM.[90] All of these approaches used bench top instruments to detect the oxidation and, as there is a growing interest in portable assays, the H_2O_2 detection system was carried out on a small portable instrument (Snowy Range) to investigate if low concentrations of H_2O_2 could still be achieved. The portability aspect could prove very useful in wastewater management [112] and also in forensic applications as H_2O_2 is a commonly used molecule in the synthesis of explosives.[113]

To find the limit of detection, 100 μL of Ag NPs (0.3 nM) were added to 100 μL of 3 mM TMB and 200 μL of water. Final concentrations of H_2O_2 (450, 270, 90, 45, 9 and 0 μM) were then added and the solutions analysed using a 638 nm laser excitation on a Snowy Range Raman instrument. Figure 3.17 shows the change in the SERRS spectrum of the CTC as different concentrations of H_2O_2 were added, along with the change in intensity of the 1610 cm^{-1} peak at each concentration.
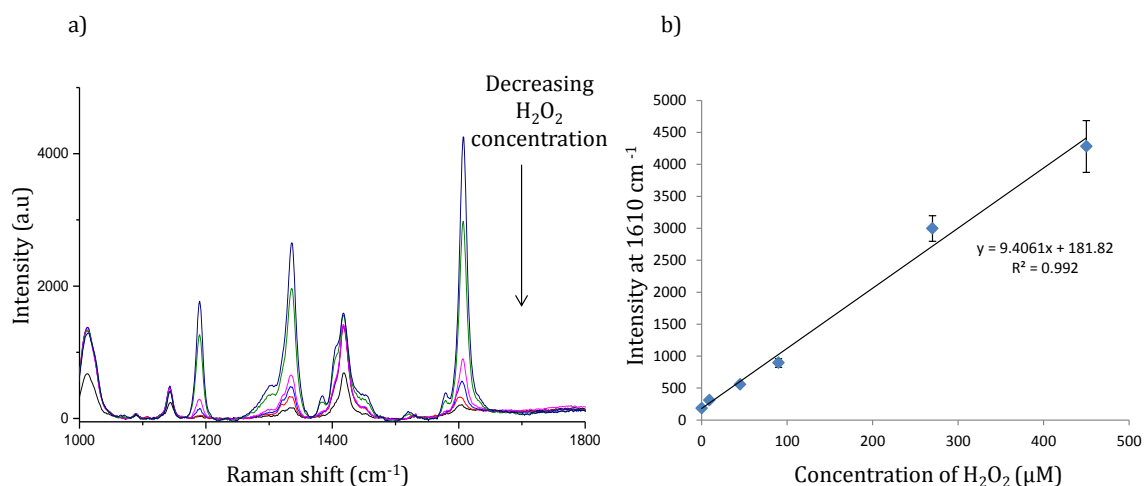
Figure 3.17 (a) Resulting SERRS spectra of CTC when different concentrations of H_2O_2 were added to Ag NPs and TMB, (450 μM (dark blue), 270 (green), 90 (pink), 45 (blue), 9 (red), 0 (black)) and (b) Intensity of 1610 cm^{-1} peak vs concentration of H_2O_2. Spectra were obtained using 638 nm laser excitation, a 1 second accumulation time and 30 mW laser power. The spectra and error shown are the average and standard deviation of 5 measurements of 3 replicate samples. The spectra have all been baseline corrected using Matlab.

Figure 3.17(a) indicates that when lower concentrations of H_2O_2 were added to Ag NP with TMB, the CTC SERRS signal decreases as expected. This is due to less H_2O_2 molecules being present to be decomposed by the Ag NP surface and take part in the oxidation of TMB. This also means that a lower degree of aggregation would occur, leading to a lower SERRS signal for the CTC. A linear response (Figure 3.17 (b)) was obtained when plotting the intensity of the 1610 cm^{-1} peak against the H_2O_2 concentration and a calculated limit of detection of 3 µM was obtained. This was calculated using an international standard approach involving 3 times the standard deviation of the blank divided by the gradient of the line. The previous Ag NP catalytic activity study reported a limit of detection of H_2O_2 of 100 nM,[90] but as expected, by transferring the system onto a portable instrument a small degree of sensitivity was lost. However, H_2O_2 was still detected at a low concentration with a portable instrument making it a promising assay for in-field detection.

3.3.4 Oxidation of ABTS

3.3.4.1 Oxidation of ABTS with ferromagnetic nanoparticles

To investigate and characterise the oxidation of ABTS, Fe_2O_3 NPs were first used to catalyse the oxidation of ABTS due to their excellent catalytic properties observed when used to catalyse the oxidation of TMB. 100 µL of 3 mM ABTS and 100 µL of 6 mM of H_2O_2 were added to 100 µL of Fe_2O_3 NPs and left to shake for 5 minutes. The Fe_2O_3 NPs were then removed from the solution using a strong magnet leaving the green ABTS oxidised solution behind. Figure 3.18 shows the resulting UV-vis spectrum of the oxidised ABTS product.
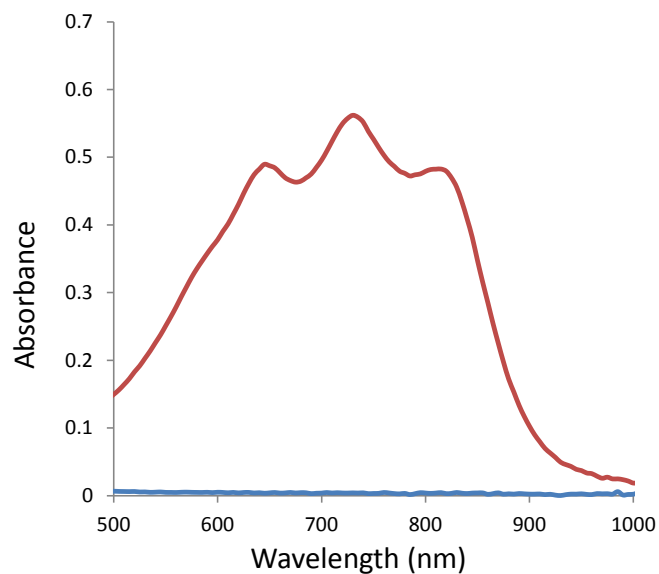
Figure 3.18 UV-vis spectrum of Fe_2O_3 NPs and ABTS (blue) and Fe_2O_3 NPs, ABTS and H_2O_2 (red).

The oxidised ABTS spectrum has 3 absorbance peaks at 650, 735 and 815 nm, which were only present when all three components were added (Figure 3.18). Unlike when TMB was used as the peroxidase substrate, when ABTS was added to the Fe_2O_3 NPs and the NPs removed with a magnet, the resulting solution appeared colourless. This was due to the aggregating effect the ABTS had on the Fe_2O_3 NPs, as the positive NP surface interacts with the negative SO_3 moieties on the ABTS, therefore electrostatically aggregating the NPs hence making removal with the magnet easier. When H_2O_2 was added, the NPs also aggregated and upon their removal, the green oxidised ABTS solution was left behind with no interference from the NPs.

The Raman properties of the oxidised ABTS were then investigated next by analysing the unoxidised and oxidised solution using a laser excitation close to the absorbance peaks at 650 nm and 730 nm, shown in the UV-vis spectrum in Figure 3.18. Figure 3.19 depicts the Raman spectra of the unoxidised and oxidised ABTS obtained using 638 nm and 785 nm laser excitation.
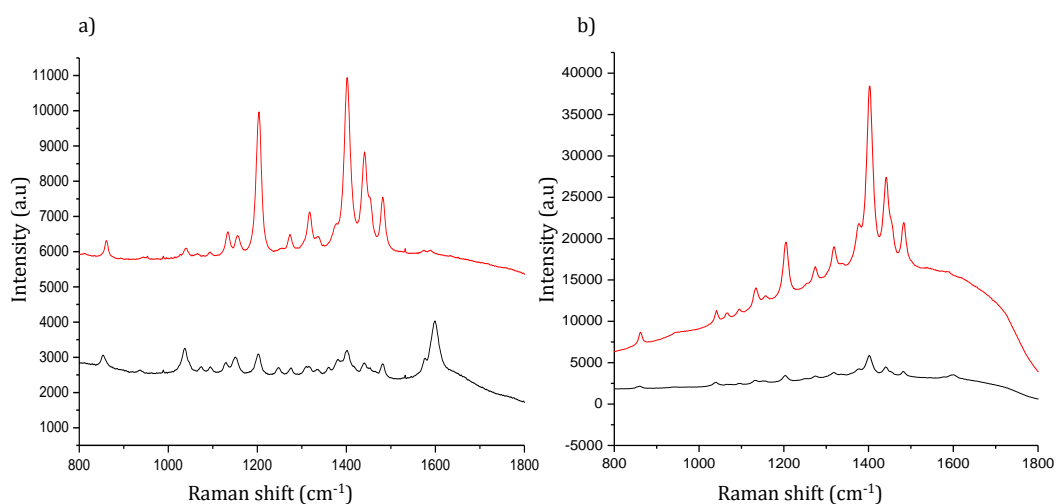
Figure 3.19 (a) Unoxidised ABTS spectrum obtained when Fe_2O_3 NPs and ABTS were mixed together, taken using a 638 nm (black) and 785 nm (red) laser excitation and (b) Oxidised ABTS spectra obtained when H_2O_2 was added to Fe_2O_3 NP and ABTS, taken using 638 nm (black) and 785 nm (red) laser excitation. Spectra were obtained using a 5 second accumulation time and 30 mW (638 nm) and 45 mW (785 nm) laser power. The spectra shown are the average of 5 measurements of 3 replicate samples. The spectra have all been baseline corrected using Matlab. Spectra have been normalised against an ethanol standard to account for the difference in laser excitation and power.

Figure 3.19 (a) shows the change in unoxidised ABTS signal when interrogated with a 638 and 785 nm laser excitation. Although similar peak positions are present, the ratio between the intensities are very different and there is a much more prominent 1600 cm^{-1} peak present in the 638 nm spectrum, which is not visible in the 785 nm spectrum. As this peak is not present in the oxidised ABTS spectra (Figure 3.20 (b)), it can be deduced that this is from the unoxidised ABTS hence analysing with a 638 nm laser excitation gave more information about the oxidation state of the ABTS.

The other peaks present in both spectra of the unoxidised spectra (Figure 3.19 (a)) are also present in the oxidised spectra (Figure 3.20 (b)), therefore they are due to the low concentration of ABTS which is already oxidised. The same result was also present when Fe_2O_3 NPs and TMB were added together and a low concentration of TMB was oxidised without the presence of H_2O_2. This was due to some OH radical being present in the Fe_2O_3 NPs solution and being able to oxidise the ABTS.

The resulting Raman spectra of the oxidised ABTS at each laser wavelength (Figure 3.19 (b)) gave the same peaks with similar relative intensities but a much greater intensity was obtained using 785 nm laser excitation. No computational calculations were found for the assignment of the peaks of the oxidised ABTS Raman spectrum, however Garcia *et al*. have used vibrational analysis of structurally related molecules to assign the peaks.[114] Table 3.1 lists the main characteristic peaks in the spectrum and the assignments for the peaks.

Table 3.1 Most probable band assignment of the radical cation of ABTS

Peak (cm^{-1})	Assignment
1202	νas(SO3-H)
1318	δ(CH); ν(CC); δ(CH3)
1403	ν(N=N)
1439	γ(CH3); ν (CH3); ν (CC)BM
1485	δ(CH3); ν(CC)BM

δ:In plane bending; ν:stretching; γ: out of plane; as: anti-symmetrical; BM: Benzene moiety

There are three absorbance bands present in the oxidised ABTS UV-vis spectrum with the maximum occurring at 735 nm. It is proposed that the stronger Raman signal obtained when exciting the radical cation with 785 nm laser excitation is due to resonance Raman scattering. As the 785 nm laser excitation is less than 50 nm from the maximum, whilst the 638 nm is over 100 nm away, it is evident why the 785 nm spectrum is more intense when compared to 638 nm laser excitation spectrum. The similarity between the two spectra and the relative intensities of the peaks in the spectra, suggest the same chromophore is being enhanced at both wavelengths but to differing degrees.

Despite the 638 nm laser excitation giving a greater change in the overall spectrum for unoxidised to oxidised ABTS, the greater intensity obtained for the oxidised ABTS at 785 nm outweighed this advantage and 785 nm was used as the laser wavelength to evaluate the catalytic activity of Au and Ag NPs with ABTS to try to

achieve the best possible signal by coinciding with the absorbance maximum of the oxidised ABTS.

3.3.4.2 Oxidation of ABTS using silver and gold nanoparticles

Since Ag and Au NPs have been shown to successfully catalyse the oxidation of TMB (section 3.2.2.2 and 3.2.2.3) and when Ag NPs were used, resulted in an intense SERRS spectrum, their catalytic activity was used to catalyse the oxidation of ABTS and the resultant oxidation product characterised. It should be noted that the Ag and Au NPs were negatively charged and this may have an adverse effect on the ability of the negatively charged ABTS to interact with the NPs surface to give SERRS.

100 µL of 3 mM ABTS and 100 µL of 6 mM H_2O_2 were added to 100 µL of Ag NPs (0.3 nM) or 100 µL of Au NPs (0.3 nM) and characterised using extinction and Raman spectroscopy using 785 nm laser excitation. The results are shown in Figure 3.20.
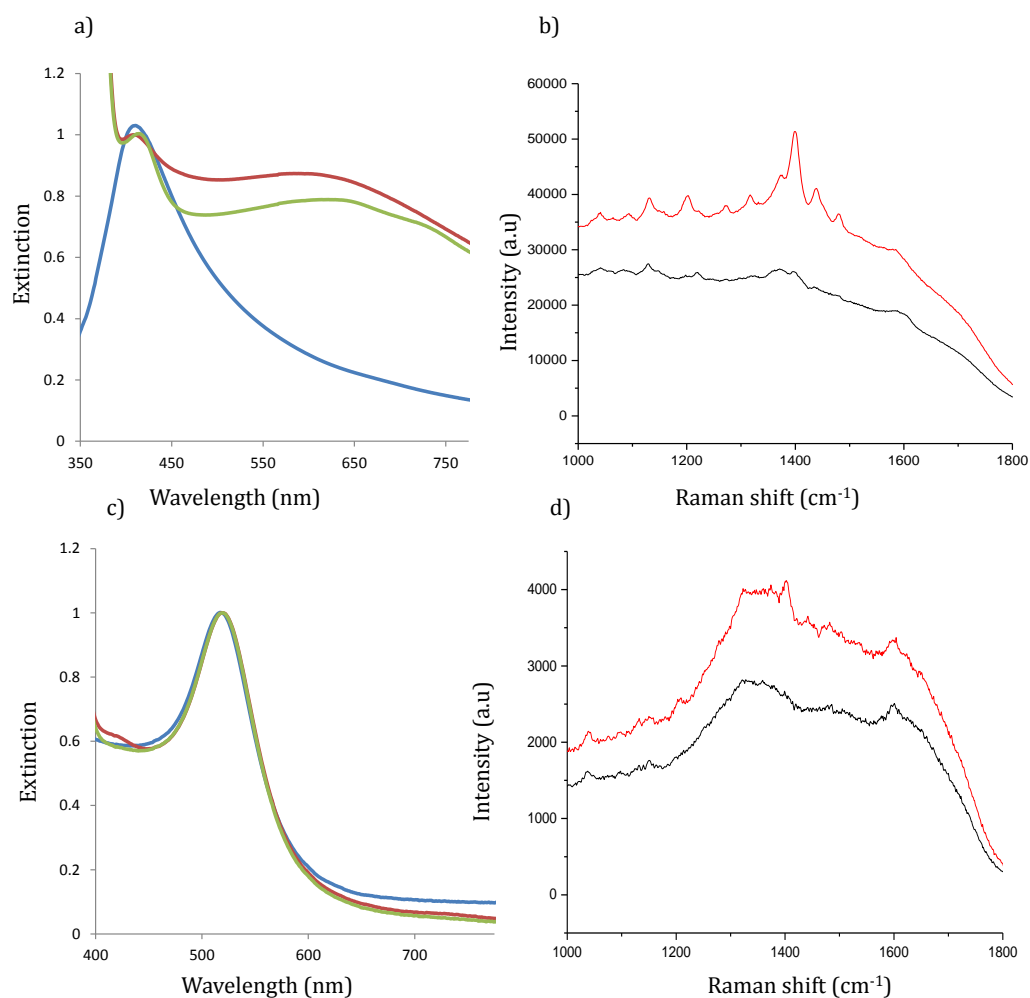
Figure 3.20 (a) Extinction spectrum of Ag NPs (blue), Ag NPs and ABTS (red) and Ag NPs, ABTS and H_2O_2. Spectra have been normalised to 1 for clarity. (b) SERRS spectra obtained from Ag NPs and ABTS (black) and Ag NPs, ABTS and H_2O_2 (red) (c) Extinction spectrum of Au NPs (blue), Au NPs and ABTS (red) and Au NPs, ABTS and H_2O (green). Spectra have been normalised to 1 for clarity. (d) SERRS spectra obtained from Au NPs and ABTS (black) and Au NPs, ABTS and H_2O_2 (red). Spectra obtained using 785 nm laser excitation, a 10 second accumulation time and 45 mW laser power. The spectra shown are the average of 5 measurements of 3 replicate samples.

When Ag NPs were added to the ABTS, the extinction spectrum indicated peak broadening and an appearance of a broad band at 640 nm suggested that the NPs aggregated (Figure 3.20 (a)). This was probably due to the instability of the Ag NPs and the high concentration of ABTS added to them. A change in extinction spectrum was observed when H_2O_2 is added to the Ag NPs and ABTS; the oxidised ABTS absorbance bands at 630 and 730 nm started to appear. They are, however, very weak as the signal is swamped by the Ag NP aggregation peak.

There is also a noticeable change in the SERRS spectrum due to the presence of oxidised ABTS. Oxidised ABTS peaks at 1202, 1318, 1403, 1439 and 1485 cm^{-1} are present in the Ag NPs, ABTS and H_2O_2 solution and missing from the Ag and ABTS solution. However, the intensity of the oxidised peak is very weak (a 10 second acquisition time was needed to achieve signal) and it can deduced that SERRS of the ABTS is not achieved and this may in fact be a resonance Raman spectrum due to the negatively charged ABTS not going down onto the Ag NP surface. The RRS signal is not as intense as the RRS spectrum obtained in the oxidation of ABTS when Fe_2O_3 NPs are present as the Ag NPs are not as efficient at causing the H_2O_2 decomposition.

The lack of SERRS obtained from the oxidised ABTS is due to the charge. As Ag NPs and ABTS are both negatively charged, the ABTS is not electrostatically attracted to the Ag NPs surface and is unlikely to experience surface enhancement. This complements the results achieved when Ag NP are used to catalyse the TMB oxidation which have opposite charges and the positively charged TMB can be electrostatically attracted to the Ag NP surface resulting in a very intense CTC SERRS spectra.

The extinction and SERS results obtained when using Au NPs were used to catalyse the oxidation of ABTS confirmed that the surface charge plays a significant role in catalytic activity. No change in extinction spectrum was obtained when ABTS and H_2O_2 were added to Au NPs, suggesting that the ABTS has not been oxidised as there are no visible oxidation peaks of ABTS or aggregation of the Au NPs was observed. Furthermore, there is very little change in the Raman spectra with and without H_2O_2. A small 1403 cm^{-1} peak does suggest a small amount of H_2O_2 was decomposed by the metal surface however the signal intensity was very low, suggesting Au NPs are very poor at catalysing the oxidation of ABTS. Again, this is due to the charge on the Au NPs which is the same as the ABTS and was expected following the result with the Ag NPs.

Due to the excellent catalytic activity of the positively charged Fe_2O_3 NPs with the negatively charged ABTS and the resonance enhanced Raman radical ABTS spectrum obtained using a 785 nm laser excitation, the system was chosen to produce oxidised ABTS, which would then be used in an ABTS decolourisation assay for the detection of antioxidant activity.

3.3.5 ABTS decolourisation assay for detection of glutathione

Antioxidant activity measures a molecule's intrinsic reactivity towards free radicals and reactive oxidative species. There are many assays that have been reported for the detection and quantification of this activity including the oxygen radical absorption capacity (ORAC) assay,[115] the ferric reducing ability of plasma (FRAP) assay [116] and an ABTS decolourisation assay.[117] In the two step ABTS decolourisation assay for the detection of antioxidants, the colourless ABTS is first oxidised to its green radical cation, which can be achieved using a number of different substrates such as Ag^+ ion,[118] potassium persulfate,[95] metmyoglobin [95] or HRP.[94] The second step then detects the presence of the antioxidant, by utilising the decolourisation of the oxidised ABTS which is reduced to the colourless ABTS by the antioxidant, which is hydrogen donating. The reduction of the oxidised ABTS is usually detected via UV-vis spectroscopy, by monitoring the decrease in absorbance at 735 nm, as the concentrations of antioxidants increases.[95] This assay is generally favoured over other antioxidant detection assays as it is relatively inexpensive, easy to use, has a good stability over a range of pH and gives fast reaction times. [115]

A number of antioxidants can be detected using this method including glutathione which is an important antioxidant involved in protecting cells from oxidative stress.[119] Depletion of glutathione has also been correlated with a poor immune system leaving the body more susceptible to infection.[120]

As already shown in section 3.3.5.1, Fe_2O_3 NPs can catalyse the oxidation of ABTS in the presence of H_2O_2 generating the oxidised ABTS. The oxidised ABTS can then be reduced by glutathione and the reduction monitored using RRS, replacing the conventional UV-vis detection method with a molecularly specific vibrational technique that could potentially lower the limits of detection. Furthermore, the assay can be analysed using a handheld portable Raman spectrometer which can replace less portable UV-vis spectrometers and allows for the system to potentially be used in clinical environments, while still maintaining a low limit of detection. Figure 3.21 shows a schematic for the assay and the change in colour experienced by the ABTS due to the addition of glutathione.
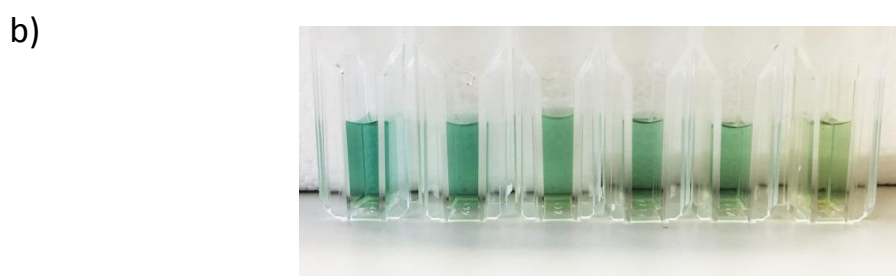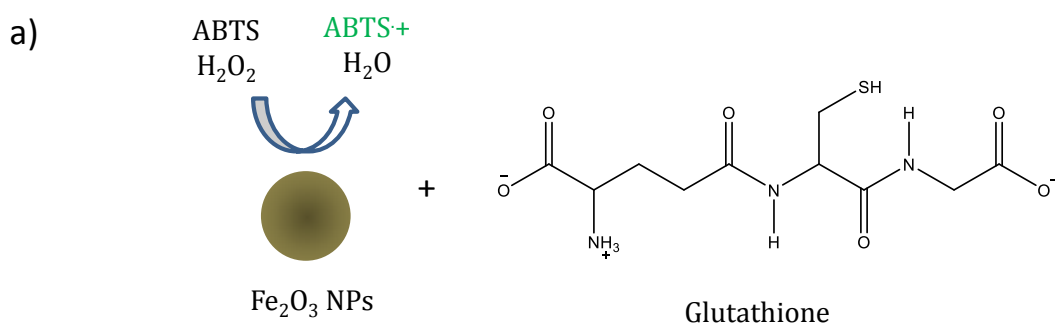
Figure 3.21 (a) Schematic of the oxidation of ABTS decolourisation assay. Fe_2O_3 nanoparticles are used to decompose H_2O_2, initiating the oxidation of ABTS to oxidised ABTS. The addition of glutathione then reduces the ABTS + and the decolourisation is observed shown in (b) when different concentrations of glutathione are added.

100 µL of Fe_2O_3 NPs, 100 µL of 3 mM ABTS and 10 µL of 9 M H_2O_2 were mixed together to form the oxidised ABTS. A high concentration of H_2O_2 was added to ensure maximum oxidation of the ABTS occurred. The solution was left to shake for 5 minutes and the aggregated NPs removed using a strong magnet. Final concentrations of 0, 200, 400, 800, 1200, 1600, and 2000 nM of glutathione were then added to the oxidised ABTS solution. The mixture was analysed using a Snowy Range CBex portable 785 nm laser excitation Raman instrument 5 minutes after the addition of glutathione. As higher concentrations of glutathione were added, the reduction of the oxidised ABTS increased, which is evident due to the decreasing intensity of the RRS spectrum as shown in Figure 3.22 (a).
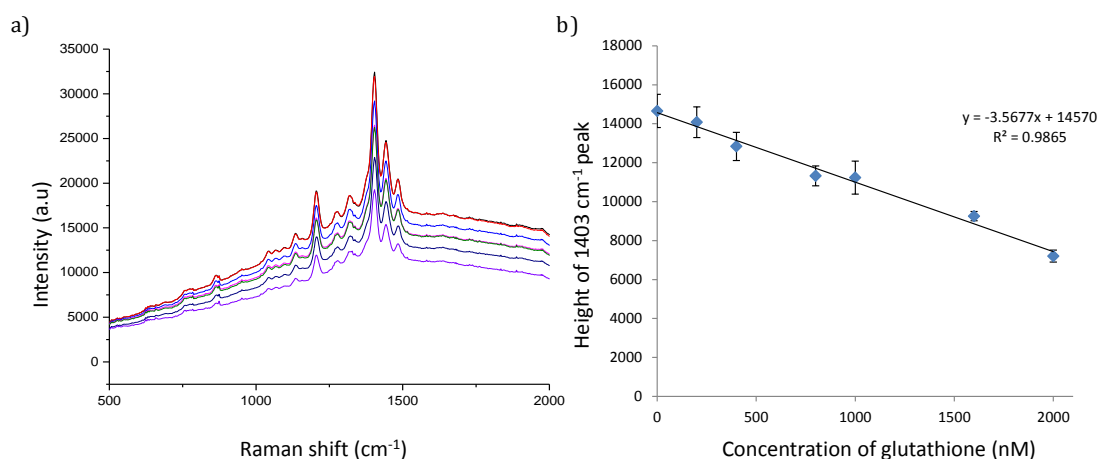
Figure 3.22 (a) RRS spectra of oxidised ABTS obtained when different concentrations of glutathione were added (0 (black), 200 (red), 400 (light blue), 800 (pink), 1200 (green), 1600 (dark blue) and 2000 nM (purple)). (b) Intensity of 1403 cm^{-1} peak vs concentration of glutathione. The spectra were obtained using 785 nm laser excitation with a 1 second accumulation time and 45 mW laser power. Average spectra and error bars obtained from 5 measurements of 3 replicate samples.

It can be observed in Figure 3.22 (b) that when the height of the 1403 cm^{-1} peak was plotted against the glutathione concentration, a linear relationship was observed over the range of 0-2000 nM with a correlation coefficient of 0.99. The observable limit of detection was 200 nM, which was 10 times lower than UV-vis detection of the reduction of ABTS.[121] The portability and low limit of detection in this assay gave encouraging results and could be applied for the detection of a variety of different antioxidants in a clinical environment.

3.4 Conclusion

There has been a recent surge in research on artificial enzymes, specifically nanoparticles, as an alternative to natural enzymes. When nanoparticles are able to mimic the structure and function of natural enzymes they are known as nanozymes and have specific properties, such as size and composition, which can be exploited to carry out specific activities, for example catalysing the oxidation of peroxidase substrates in the presence of H_2O_2. Nanozymes are seen as a cheaper alternative to natural enzymes and can be mass produced, have an increased stability in harsh environments and long term storage capabilities. Therefore there is a growing need

to understand the oxidation of substrates using the catalytic activity of nanozymes and develop more strategies of which the oxidised product can be characterised.

Au, Ag, Fe_2O_3 and Au-SiO_2-Pt NPs were employed to catalyse the oxidation of TMB and ABTS and the oxidation was characterised using UV-vis and Raman spectroscopy. It was found that the surface of the metal NP played an important part in the catalytic activity and negatively charged NPs (Au and Ag) catalysed the oxidation of the neutral TMB to the positive CTC producing an intense SERRS spectrum of the CTC but performed poorly with negativity charged ABTS substrate. The opposite was observed for the positively charged Fe_2O_3 NPs which successfully catalysed the oxidation of ABTS producing the vivid green radical cation, the only nanozyme investigated to do so.

Due to the enhanced CTC SERRS signal obtained using Ag NPs, these NPs were used for the detection of H_2O_2 on a portable Raman spectrometer. By monitoring the decrease in CTC intensity at lower concentrations of H_2O_2, a limit of detection of 3 µM was achieved. The novel assay has the potential to be applied for in-field detection of H_2O_2 which could be beneficial for wastewater analysis and forensic applications.

The catalytic oxidation of ABTS using Fe_2O_3 NPs was applied for the detection of the antioxidant glutathione. The hydrogen donating glutathione reduced the oxidised ABTS and the change in the 1403 cm^{-1} peak at different concentration was used to obtain an observable detection limit of 200 nM.

Overall, different metal NPs can catalyse the oxidation of peroxide substrates which can be followed using UV-vis spectroscopy, RRS and SERRS. By evaluating the catalytic activity, the nanozymes which show the most promise can be applied for the detection of H_2O_2 and glutathione. By replacing conventional enzymes with nanozymes and utilising RRS and SERS detection, lower limit of detection of commonly utilised detection assays, for example detection of glucose which utilises the enzymes glucose oxidase and HRP with UV-vis detection,[122] could be achieved.

4. Silver nanoparticle linked immunosorbent assay

4.1 Introduction

There has been a recent increase in publications where NPs have been used in enzyme linked immunosorbent assays (ELISAs), to not only increase the output signal and sensitivity, but to also replace the enzyme used to turn over a coloured substrate producing a detectable change in oxidation state. This chapter focuses on incorporating Ag NPs into an immunoassay, in place of the conventional enzyme, to allow for the SERRS detection of specific antigens.

4.1.1 Introduction to Biomolecules

4.1.1.1 Antibodies

Antibodies, also known as immunoglobulins (Ig), are large Y shaped glycoproteins made up of amino acids that naturally occur in living cells, specifically B cells.[123] They are used as part of the body's immune reaction to intruding foreign objects and to identify and/or neutralise pathogens, such as bacteria and viruses, by recognising a unique protein on the pathogen called an antigen.[124] Antibodies are roughly 150 kDa in size and are made up of 4 polypeptide chains; two identical heavy chains and two identical light chains, which are held together by disulphide bridges.[125] The structure of an IgG antibody is shown in Figure 4.1.
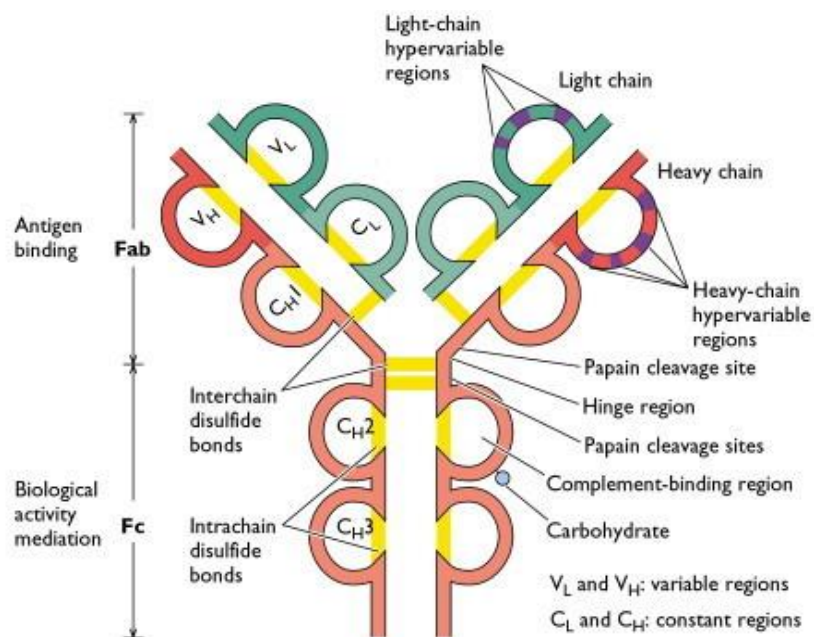
Figure 4.1 Structure of an antibody.[126]

An antibody is comprised of 2 sections, the fragment antigen binding (Fab) and the fragment crystallisable region (Fc). The Fab region consists of one constant and one variable domain of the heavy and light chain. It is the light chain which varies from antigen to antigen due to its variable amine terminated paratope, which binds to the epitope of its target antigen. In contrast, the Fc is the tail region of the Ab and is made up of the heavy chains which do not differ significantly between different antibodies. [123]

The binding between the paratope and epitope has a special complementary (lock and key) mechanism.[127] Molecular forces involved in the binding are weak and non-specific (electrostatic, hydrogen bonding, hydrophilic interactions and van der Waals), therefore the binding is reversible and antibody affinity towards the antigen is relative rather than absolute. [128]

One such antigen of interest which can be detected using antibodies is C-reactive protein, an inflammation biomarker.

4.1.1.2 C-reactive protein

C-reactive protein (CRP) is an acute phase protein which is synthesised primarily in the liver by the hepatocytes in response to proinflammatory cytokines (IL6), making it an important inflammation biomarker.[129] It consists of 5 identical non-glycosylated polypeptide subunits, each consisting of 206 amino acid residues.[130] The subunits are non-covalently bound in a cyclic pentameric structure which is shown in Figure 4.2.
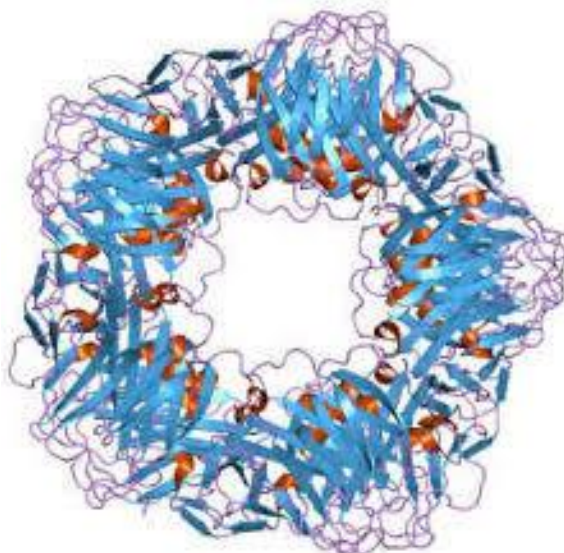
Figure 4.2 Structure of C-reactive protein. [131]

Although it is considered a non-specific biomarker, research has shown that an elevated base level of CRP is associated with diabetes,[132] sepsis [133] and cardiovascular disease.[134] Thus, monitoring CRP levels is considered a useful method for disease screening and management. CRP is conventionally detected using an ELISA, which is a commonly employed method for the detection and quantification of biomarkers.

4.1.2 Enzyme linked immunosorbent assay

An ELISA is a biochemical technique used to detect the presence of a specific antibody or antigen. There are many different ELISA formats of which the most commonly used is the sandwich ELISA.[135]

There are three main steps in a sandwich ELISA: coating, blocking and detection. First, a high affinity binding surface such as an epoxy or nitrocellulose coated glass slides are treated with capture antibody, immobilising the antibody and coating the surface. An unrelated protein solution is then added to the surface, blocking all sites where the antibody has not been immobilised. A commonly used protein blocking solution used is bovine serum albumin (BSA) which is a large protein capable of binding to the free surface without capture antibody, therefore preventing other components of the ELISA binding to the surface non-specifically. The antigen of interest is then added and binds specifically to the capture antibody. Finally, a detection antibody, functionalised with an enzyme, binds to the antigen and completes the sandwich ELISA. To obtain a detectable signal, the enzyme then catalyses the oxidation of a substrate to produce a coloured substrate which and can be analysed using UV-vis spectroscopy. The intensity of the colour is directly related to the concentration of the antigen present; therefore the strength of the oxidised signal can be used to quantify the amount of analyte present. A general sandwich ELISA schematic which utilises HRP as the enzyme, TMB as the substrate and CRP as the antigen to detect is shown in Figure 4.3.
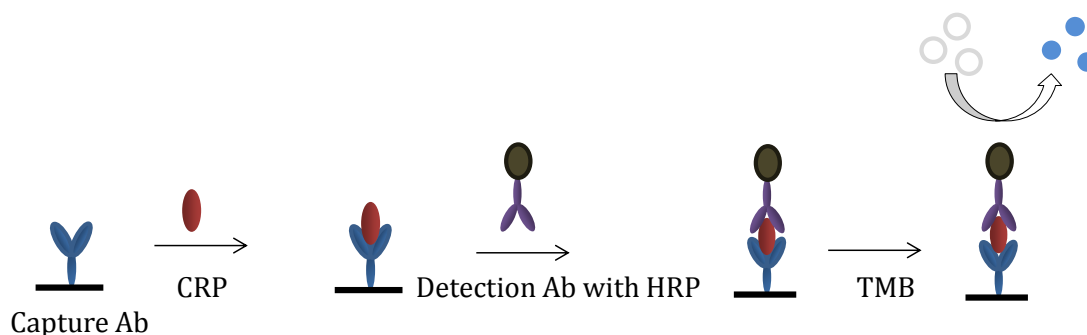
Figure 4.3 Schematic of sandwich ELISA for CRP detection. Capture antibody (Ab) is first immobilised onto a high affinity binding surface followed by the addition of CRP which binds to the antibody. A detection Ab functionalised with HRP then binds to the CRP completing the sandwich ELISA. Upon the addition of TMB, the HRP catalyses the oxidation to the CTC which can then be detected and the signal related to how much antigen is present.

Other ELISA formats include: direct ELISAs, where the antigen is immobilised onto a solid phase followed by an enzyme labelled Ab; indirect ELISAs, which also have an antigen immobilised onto a solid surface, however this time two antibodies (a

primary and enzyme labelled secondary) are incorporated; competitive ELISAs, where antibodies or proteins compete for binding leading to a decrease in signal.[135]

The ELISA is a robust format but the sensitivity of the colourimetric analysis can limit detection limits. Therefore, various techniques have been used to increase the sensitivity. For example, RRS has been utilised for the detection of TNF-α using standard ELISA in combination with TMB oxidation.[107] In this method, the CTC product was detected using Raman with 633 nm laser excitation, which is in resonance with the absorbance maximum of the CTC. It was demonstrated that by using RRS in place of the traditional colorimetric detection method, that a 50 times lower detection limit of TNF-α could be achieved.

4.1.2.1 Enhancement of ELISA signal using nanoparticles

To further increase the sensitivity, NPs have also been incorporated into ELISAs. Mekoci *et al.* first demonstrated the use of Au NPs which had been conjugated to Ab, labelled with HRP, in order to achieve amplification of the signal (Figure 4.4).[136]
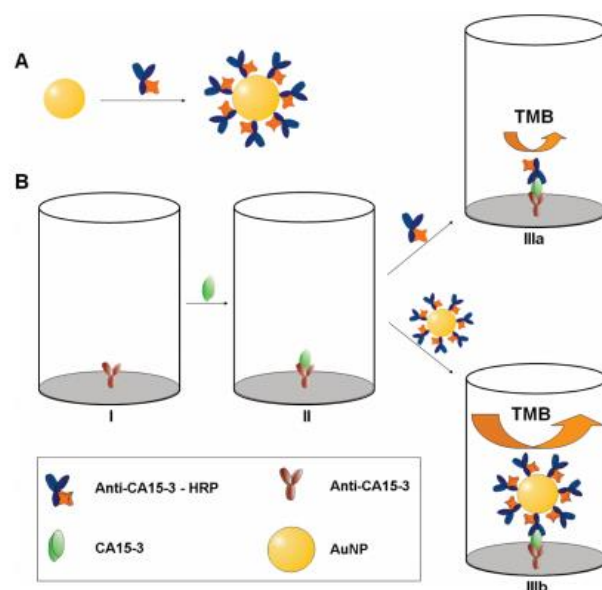
Figure 4.4 (a) Conjugation of Au NPs to anti-CA15-3-HRP (b) ELISA protocol; anti-CA15-3-HRP immobilised onto bottom of well followed by the antigen CA115-3. Au NP conjugated to anti-CA15-3-HRP or anti-CA15-3 HRP was then added to the well which bound to the CA15-3 antigen. When TMB was added an increased oxidised signal was observed in the well when Au-anti-CA15-3-HRP was added.[136] Reprinted with permission from Ambrosi. A., F. Airo and A. Merkoci, *Enhanced gold nanoparticle ELISA for a breast cancer biomarker*. Anal Chem, 2010. **82**(3);p1151-6. Copyright (2017) American Chemical Society.

The Au NPs allowed more HRP to be present per antigen-antibody interaction, therefore an increase in HRP-mediated TMB oxidation took place and a more intense UV-vis spectrum of oxidised CTC was obtained for the detection of CA15-3, a tumour marker for breast cancer.

NPs have also been incorporated into a dual colour response ELISA to improve the accuracy of visual detection. Gou *et al*. reported that the second oxidation product of TMB (TMB^{2+}) can quantitatively etch Au NPs, hence by including Au NPs in commercially available TMB ELISA kits, different colours could be observed as the concentrations of antigen changed.[137] After the standard ELISA had been performed and the TMB was oxidised to TMB^{2+} (with the addition of a strong acid), Au NPs were added to the solution. The solution was red due to the presence of the NPs; however, at higher antigen concentrations, when more TMB^{2+} was present, etching of the Au NPs occurred, reducing the optical density and turning the solution yellow. The dual-colour response of the ELISA allowed the detection of prostate

specific antigen (PSA) in human serum, with a visual limit of detection of 9.3 pg/mL. [137]

Another benefit of using NPs in an ELISA is the ability to adsorb coloured probes to their roughened surface, allowing analysis by SERRS. Graham *et al.*[138] first reported the use of SERRS as a readout technique in an ELISA by using ABTS as the enzyme-transformable chromogen. After the completion of the ELISA, using ABTS as a substrate, Au NPs were added to the oxidised ABTS which was then adsorbed onto their surface and SERRS analysis was carried out using a 514 nm laser excitation. Using this method, pg/mL detection levels of human prostate-specific antigen in clinical samples was achieved.

Graham *et al.* also reported that CRP can be detected by SERRS analysis of ELISA products.[139] In this method, the peroxidase substrate bromochloroindolylphosphate (BCIP) was oxidised by alkaline phosphatase (ALP), conjugated to a detection antibody, generating a blue dimeric species with an absorbance maximum at 615 nm. On the addition of Au NPs, the solution was analysed using a 633 nm laser excitation and the SERRS spectra obtained was correlated to the amount of CRP present in the sample with a detection limit of 0.3 ng/mL.

The methods described so far used NPs in addition to an enzyme; however, recently nanoparticles have been shown to have enzymatic properties and used to replace enzymes in an effort to reduce the cost and complexity of ELISAs.

4.1.3 Nanozyme linked immunosorbent assay

By conjugating an antibody to a NP, or nanozyme, rather than an enzyme, nanozyme technology can be utilised in immunoassays. Efforts have been made to develop immunoassays with nanozymes and different formats have been reported where the nanozymes are used as signalling generating moieties. [87]

Gao *et al.* who, as previously discussed in section 3.1, first reported on Fe_3O_4 NPs with peroxidase activity, also developed a novel immunoassay for the detection of myocardial infraction.[88] By conjugating the antibody for cardiac troponin-I (cTnI), to Fe_3O_4 NPs, the myocardial infraction antigen could be captured by binding to the anti-cTnI functionalised NPs which was then separated using a magnet. The solution

could then be transferred into a 96 well ELISA plate which was coated with anti-cTnI antibody, thus creating a sandwich ELISA. Following wash steps, the bound Fe_3O_4 NPs catalysed the oxidation of TMB with H_2O_2 and the solution was analysed using UV-Vis spectroscopy to obtain a colorimetric response which correlated to the concentration of cTnI in the sample, allowing detection of myocardial infraction.[88]

The catalytic properties of Fe_3O_4 NPs have also been developed to detect the glycoprotein of the Ebola virus (EBOV) using an immunochromatographic strip, also known as a lateral flow strip. [140] By labelling the Fe_3O_4 NPs with an anti-EBOV antibody and applying it to the strip, a line of NPs was left where the EBOV had been immobilised. The peroxidase substrate, 3,3'-Diaminobenzidine (DAB), was then applied to the strip, where it was oxidised to its coloured product due to the presence of the NPs, and the signal on the strip was significantly enhanced due to addition of this coloured product as well as the colour of the Fe_3O_4 NPs. Concentrations of EBOV were detected as low as 1 ng/mL with visual detection, which was 100-fold more sensitive than using Au NPs with no DAB. A schematic diagram of the immunochromatographic strip is shown in Figure 4.5.
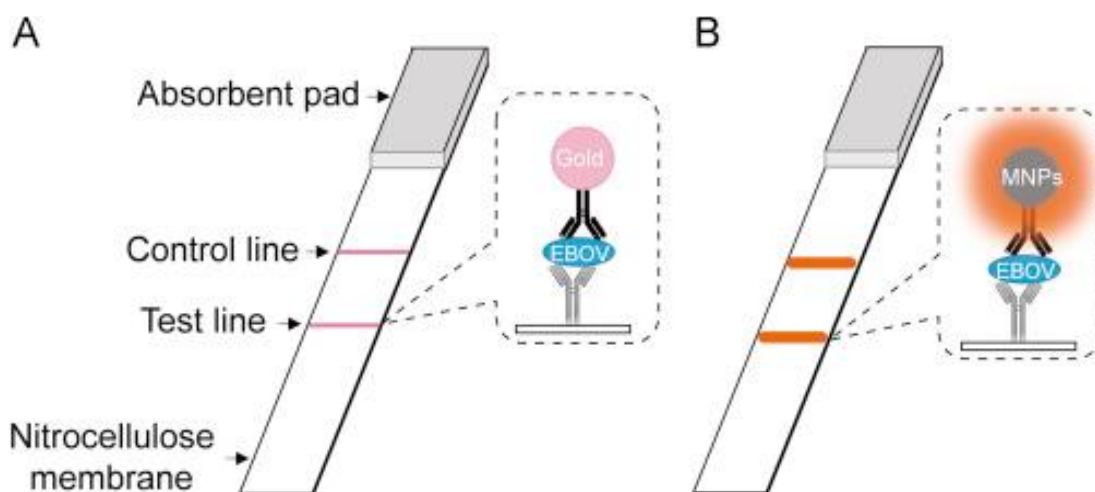
Figure 4.5 (a) Au NPs on lateral flow strip (b) Fe_3O_4 NPs on strip generating coloured reaction with DAB, significantly enhancing the signal which can be visualised with the naked eye.[140] Reprinted from Duan, D., et al., *Nanozyme-strip for rapid local diagnosis of Ebola.* Biosensors and Bioelectronics, 2015. **74**: p. 134-141. Permission from Elsevier.

Using this approach not only increased the sensitivity, but was a much faster and simpler method than solution based ELISAs, providing a simple and valuable screening method for the diagnosis of Ebola infection.

Furthermore, multiple research groups have investigated and adopted the classic sandwich immunoassay format for detection using different peroxidase mimicking nanozymes.[87] For example, Kim *et al.* demonstrated the incorporation of Fe_3O_4 NPs with Pt NPs in ordered mesoporous carbon, which led to a significant enhancement of the catalytic activity of free Fe_3O_4 NPs (50 times higher catalytic efficiency). [141] The nanocomposite was then employed as the signalling element in an immunoassay, when functionalised with antibodies, and could detect human epidermal growth factor receptor (EGFR) with a limit of detection of 1.5 ng/mL.[141]

As well as colorimetric detection, the amount of oxygen gas produced when nanozymes catalyses the decomposition of H_2O_2 can be measured and related to the concentration of an antigen. For example, Pt NPs were functionalised with antibodies and deployed in an immunoassay so that when H_2O_2 was added, the Pt NPs decomposed the H_2O_2 to hydrogen gas and the volume of gas produced could be measured using a volumetric bar chart chip. [142] The setup is shown in Figure 4.6.
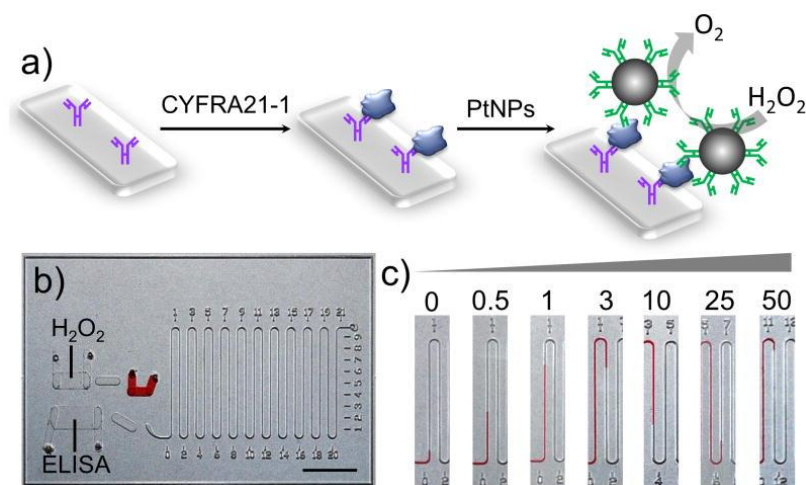
Figure 4.6 (a) ELISA schematic for the detection of CYFRA21-1 using Ab-Pt NPs. CYFRA21-1 was added to assay wells and bound to immobilised capture antibodies. Ab-Pt NPs were them added the assay and formed sandwich structures. Ab-Pt NPs could then react with H_2O_2 to produce oxygen gas (b) Image of volumetric-chip c) Image of results for different concentrations of CYFRA21-1.[142] Reprinted from Song, Y., et al., *Integration of Platinum Nanoparticles with a Volumetric Bar Chart Chip for Biomarker Assays.* Angewandte Chemie (International ed. in English), 2014. **53**(46): p. 12451-12455. Permission from John Wiley and Sons.

This method could be used to sensitively detect cancer biomarkers, such as CYFRA21-1, in both serum and on the cell surface.

In conclusion, the addition of NPs to an ELISA can be used to increase the Raman signals obtained from a chromogenic substrate. As well as producing SERS signals which can lower the limit of detection of many analytes, NPs can replace enzymes that are used in ELISAs, as they too can catalyse the oxidation of peroxidase substrate in the presence of H_2O_2. Due to their cheaper and easier synthesis, NPs and their inclusion into ELISA has become an increasingly interest area of research. This chapter focuses on replacing enzymes used in ELISAs with Ag NPs, creating a sliver-linked immunosorbent assay for the detection of CRP with SERRS.

4.2 Chapter aim

The aim of this chapter was to first investigate the catalytic activity of Ag NPs functionalised with antibodies (Ab-Ag NPs) and to subsequently use them to replace conventional enzymes used in ELISAs to create a silver-linked immunosorbent assay (SLISA), for the detection of CRP with SERRS. By functionalising Ag NPs with antibodies, the Ab-Ag NP could potentially be used in an immunoassay. The presence of the Ag NPs should also allow the oxidation of the peroxidase substrate TMB, to the Raman active CTC, which when analysed using 633 nm laser excitation, produces a characteristic SERRS signal. Figure 4.7 depicts a schematic diagram of the proposed SLISA design.
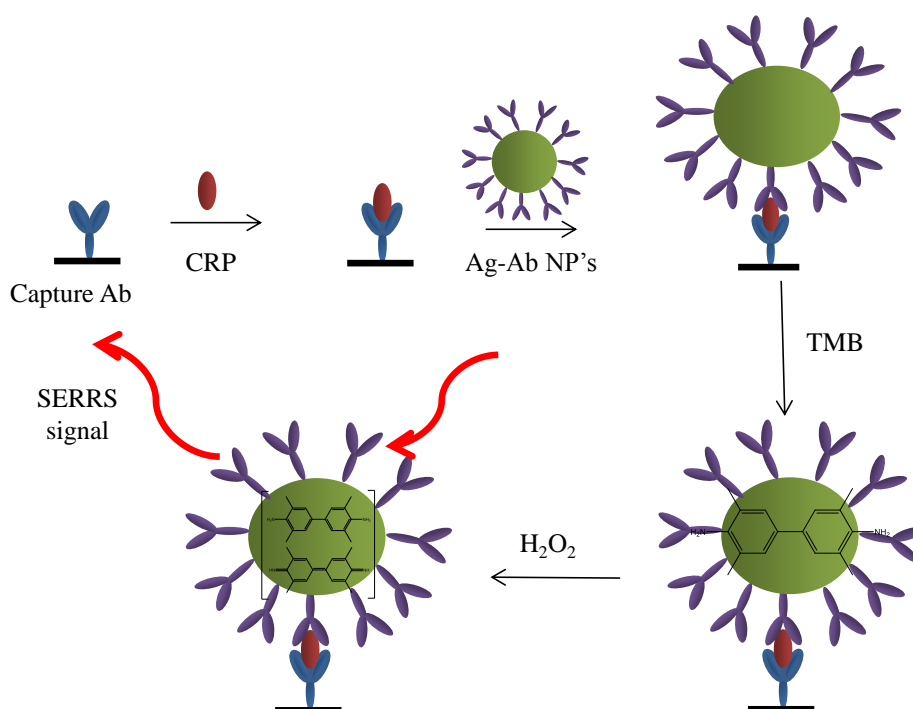
Figure 4.7 Schematic diagram showing SLISA format. Capture antibody is allowed to attach onto a surface which is then used to capture CRP. Ab-Ag NPs were then added which created the SLISA by binding to the CRP. Next, TMB and H_2O_2 were added and the TMB oxidised to the CTC, due to the presence of Ag NPs, which could then be detected by SERRS using 633 nm laser excitation.

It was proposed that at higher concentrations of CRP, more Ab-Ag NPs would be present in the SLISA and therefore more oxidation of TMB would occur, leading to a more intense SERRS signal from the CTC. The novel SLISA, combined with SERRS detection, could therefore lower the limit of detection of CRP and reduce the time taken to analyse when compared to conventional ELISAs.

4.3 Results and discussion

Ag NPs have been shown to have catalytic activity and are very effective at catalysing the oxidation of TMB, yielding an intense SERRS spectrum of the oxidised CTC when analysed using 638 nm laser excitation.[90] The catalytic activity of Ag NP is due to the breakdown of H_2O_2 at the metal surface, therefore a large amount of TMB oxidation occurs when the Ag NPs are bare. However, for Ag NPs to be included in the SLISA, they had to be coated in antibodies which could have a detrimental effect on the catalytic activity. To investigate the effect of TMB oxidation when NPs were functionalised with antibodies, carboxyl-polyethylene glycol-thiol (CT(PEG)$_{12}$) was first conjugated to Ag NPs as a model molecule. It was chosen due to its low cost and easy conjugation protocol when compared to more expensive antibodies that require more challenging conjugation procedures. It was proposed that by functionalising the Ag NPs surface with higher concentrations of CT(PEG)$_{12}$, that the available surface area of the Ag metal would be reduced and a lower amount of H_2O_2 and TMB molecules would reach the metal surface, therefore decreasing the amount of oxidised TMB, and subsequently, the CTC SERRS signal obtained.

4.3.1 PEG-Ag nanoparticles

4.3.1.1 Functionalisation and characterisation of PEG-Ag nanoparticles

CT(PEG)$_{12}$ (Figure 4.8) contains a thiol and carboxylic acid terminus joined via a short PEG chain. The terminal thiol groups have a strong binding affinity for the silver and readily functionalise the surface of the Ag NPs. The carboxylic acid groups, which are exposed, can be used later to conjugate antibodies to the Ag NPs by acting as a linker and stabiliser.

The concentration of CT(PEG)$_{12}$ that would be needed to create full monolayer coverage of CT(PEG)$_{12}$ on the surface of 70 nm citrate capped Ag NPs, with a concentration of 0.3 nM, was calculated to be 1 µM; therefore, concentrations above and below this were conjugated to the Ag NP surface to investigate the effect of functionalisation on catalytic activity.
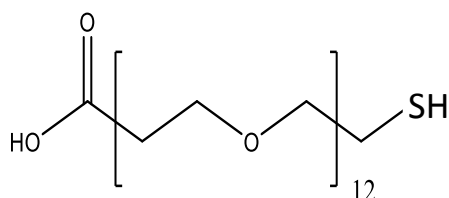
Figure 4.8 Structure of CT(PEG)$_{12}$.

Final concentrations of 100, 10, 1, 0.1 and 0.01 µM of CT(PEG)$_{12}$ were added to 1 mL of citrate capped Ag NPs (0.3 nM) and left to shake for 3 hours to allow full conjugation to occur. The PEG-Ag NPs were then centrifuged, the supernatum removed, and the pellet resuspended in 1 mL of distilled water to remove any unbound CT(PEG)$_{12}$. The resulting PEG-Ag NPs were then characterised using extinction spectroscopy and DLS to confirm the successful conjugation. The results are shown in Figure 4.9 and Table 4.1.
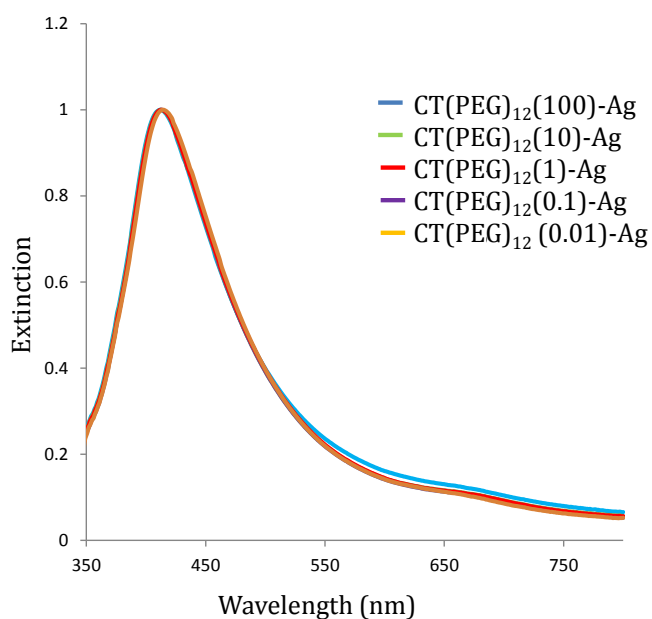
Figure 4.9 Extinction spectra of PEG-Ag NPs with different concentrations of CT(PEG)$_{12}$ (100 (blue), 10 (green) 1 (red)), 0.1 (purple) and 0.01 µM (orange) were added to the Ag NPs. Spectra have been normalised to 1 for clarity.

Table 4.1 Change in LSPR, size and zeta potential of Ag NPs upon the addition of CT(PEG)$_{12}$.

Concentration of CT(PEG)$_{12}$ (μM)	LSPR(nm)	Size (nm)	Zeta potential (mV)
0	410	75.3±0.3	-40±1.9
0.01	412	84.54±3.2	-38.2±0.6
0.1	412	79.31±1.7	-37±0.2
1	413	79.93±0.8	-37±0.9
10	413	80.37±1.8	-40.6 ± 0.3
100	413	82.49±1.9	-41.2±0.8

The LSPR for 'bare' citrate capped Ag NPs was observed at 410 nm and red shifted to 413 nm after the highest concentration of CT(PEG)$_{12}$ (100 μM) was added to the surface (Figure 4.9). The red shift can be associated with the NPs increasing in size due to the successful conjugation of the CT(PEG)$_{12,}$ therefore higher concentrations of CT(PEG)$_{12}$, lead to a slightly greater red shift. As no aggregation peaks were present at any concentration, the NPs were deemed to be stable. The DLS data (Table 4.1) indicated that for all concentrations of CT(PEG)$_{12}$ conjugated to the Ag NPs, there was an increase in size by 4-9 nm. The zeta potential remained fairly constant and, and as it is less than -20 mV, all of the batches of PEG-Ag NPs were stable.[79] However, an anomaly when 0.01 μM was added to the surface as the NPs which produced the largest increase in size of the NPs (9 nm). This was due to not enough CT(PEG)$_{12}$ being on the Ag NPs to protect and stabilise them during the centrifugation step resulting in slight aggregation of the NPs.

From the extinction and DLS data, it was determined that the PEG conjugation was successful and the catalytic activity of the PEG-Ag NP conjugates was then investigated.

4.3.1.2 Catalytic activity of PEG-Ag nanoparticles

As CT(PEG)$_{12}$ conjugation had been successful, the effect of functionalisation on catalytic activity was assessed. 100 µL of 3 mM TMB and 100 µL of 6 mM H$_2$O$_2$ were added to 100 µL of the PEG-Ag NPs conjugates functionalised with varying CT(PEG)$_{12}$ concentrations along with 200 µL of distilled water. The solutions and control experiments without the addition of H$_2$O$_2$ were characterised using extinction spectroscopy and the results are shown in Figure 4.10.
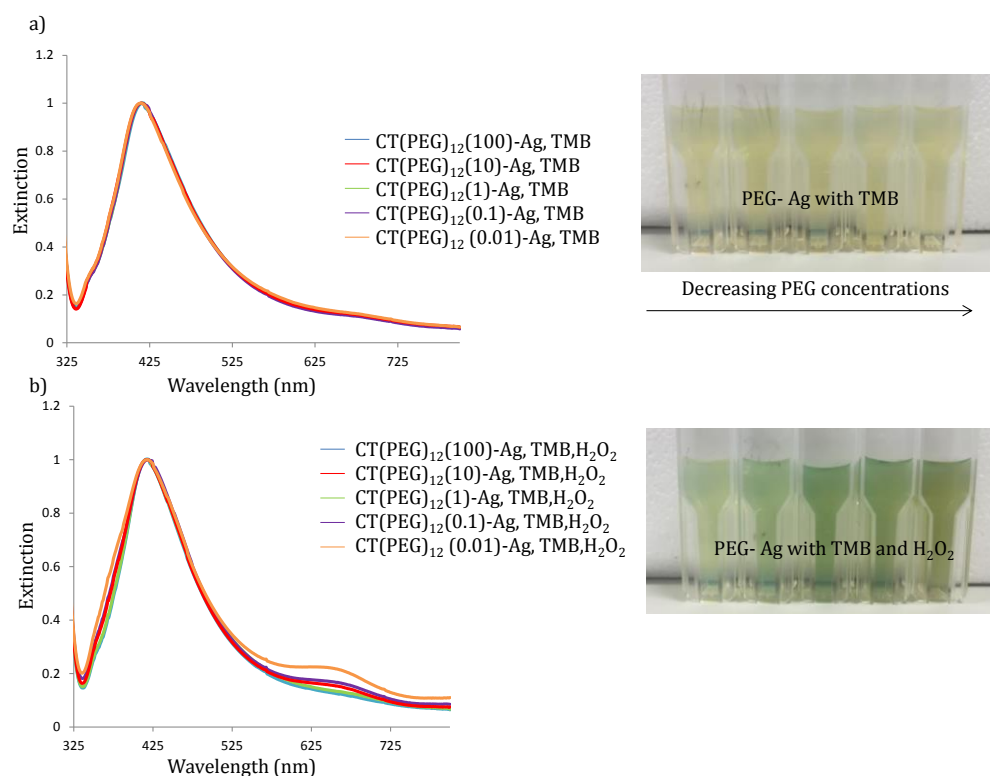
Figure 4.10 Normalised extinction spectra and accompanying photographs of solutions of PEG-Ag NPs and TMB (a) without H$_2$O$_2$ and (b) with H$_2$O$_2$ addition. 50 µL of each sample was diluted in 450 µL of d.H$_2$O for analysis. Spectra have been normalised to 1 for clarity.

It can be observed from Figure 4.10 (a) that when TMB was added to PEG-Ag NPs, no aggregation occurred as there was no change in LSPR peak position or peak broadening. No colour change was also observed, as shown in the accompanying photograph. The lack of aggregation was not unexpected, as even though a high concentration of TMB was added (3 mM), which has been previously shown to aggregate bare citrate capped NP, section 3.2.2.2, the CT(PEG)$_{12}$ protected and stabilised the NPs. When H$_2$O$_2$ was added to PEG-Ag NPs and TMB, the CTC

absorbance band at 650 nm can be observed in Figure 4.10 (b) as the TMB was oxidised, confirming that the Ag metal surface is still available to catalyse the oxidation of TMB. The 650 nm peak is larger at the lower concentrations of $CT(PEG)_{12}$ as there was more Ag NP surface available to catalyse the breakdown of H_2O_2 into free radicals, resulting in a higher concentration of radical present to oxidise the TMB. This is also apparent in the accompanying photograph which shows that the solution changed colour from the original yellow of the Ag NP to a blue/green colour as the CTC was formed.

Following the characterisation of the PEG-Ag NPs with TMB and H_2O_2 by extinction spectroscopy, the same solutions were analysed by SERRS using 638 nm laser excitation. The resulting spectra are shown in Figure 4.11 (a) and Figure 4.11 (b) illustrates the change in the 1610 cm^{-1} peak with decreasing PEG concentration.
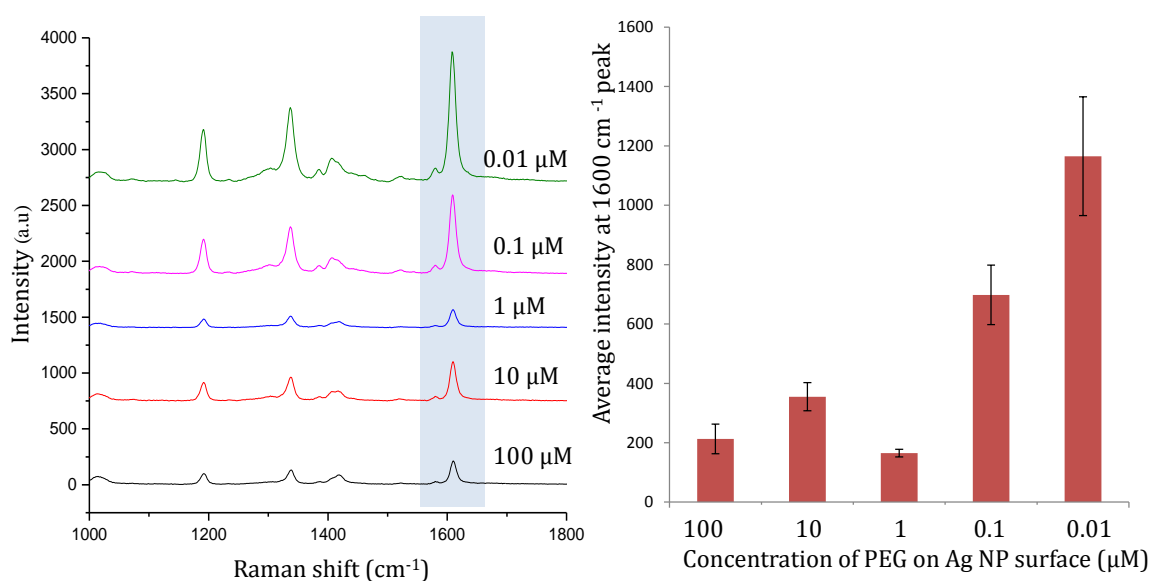
Figure 4.11 (a) SERRS spectra of CTC produced by oxidation of TMB in the presence of PEG-Ag NP conjugates with 100 (black), 10 (red), 1 (blue), 0.1 (pink), 0.01 µM (green) of $CT(PEG)_{12}$ on Ag NP surface. Spectra were obtained using 638 nm laser excitation with a 1 second accumulation time and 4.5 mW laser power. The spectra have all been baseline corrected using Matlab. (b) Bar graph showing the change in the intensity of 1610 cm^{-1} as the TMB is oxidised by PEG-Ag NP conjugates. Spectra and error bars are the average and standard deviation obtained from 5 measurements of 3 replicate samples.

The SERRS spectra obtained in Figure 4.11 (a) show that a SERRS signal is obtained from the TMB due to the catalytic activity of the Ag NPs. This suggests that there is enough metal surface available to catalyse the oxidation of TMB even though PEG-Ag NPs have less bare Ag metal on their surface. The lowest concentration of CT(PEG)$_{12}$ on the surface of the Ag NP (0.01 µM) resulted in the most intense CTC spectrum, with a peak height of around 1200 a.u. This is due to a combination of having the largest Ag metal surface available to act as the catalyst resulting in more TMB oxidation and also more aggregation occurring, shown in the extinction spectrum in Figure 4.10 (b). This was due to the electrostatic attraction of the positive CTC and the negative NPs causing the aggregation therefore an increased SERRS signal in the CTC spectrum. Higher concentrations of CT(PEG)$_{12}$ not only had lower catalytic activity, which can be seen by the less intense SERRS signal obtained (up to 6 times less intense) but also did not experience the same degree of aggregation due to the protection gained by the addition of the CT(PEG)$_{12}$.

Although most of the PEG concentrations follow the trend of less CT(PEG)$_{12}$, more free Ag metal surface available to breakdown H$_2$O$_2$ and therefore more oxidation of TMB, when enough CT(PEG)$_{12}$ was added (1µM) for monolayer coverage, the Ag NP surface was completely covered and protected. Therefore, the lowest concentration of H$_2$O$_2$ and TMB molecules reached the Ag metal surface and the least amount of TMB oxidation and NP aggregation occurred. More TMB oxidation occurred with 10 and 100 µM of CT(PEG)$_{12}$ which is higher than the monolayer concentration which is likely due to the inefficient conjugation, as too many PEG molecules were competing for the NP surface which decreased the efficiency of achieving monolayer coverage. A CT(PEG)$_{12}$ concentration of 0.1 µM was proposed to be the best concentration as it not only provided stability to the NP which would be useful in antibody conjugation methods, but it allowed TMB oxidation to take place.

Comparing the catalytic activity to that of bare Ag NPs, a reduction in the SERRS CTC spectrum obtained was observed which was purely down to some of the surface being occupied by the CT(PEG)$_{12}$ in the functionalisation However, as functionalised Ag NPs could still catalyse the oxidation of TMB with H$_2$O$_2$, antibody conjugation was explored and the catalytic activity of the Ab-Ag NP conjugate was investigated.

4.3.2 Antibody-Ag nanoparticles

The size of an antibody is approximately 14.5 x 8.5 x 4 nm in size, [143] therefore when conjugated to Ag NPs, the surface area available for catalysing the oxidation of TMB will be reduced depending on the number of antibodies per NP. Therefore, to perform well in the SLISA, the Ab-Ag NP conjugates had to have a balance between allowing enough TMB oxidation to occur while still having a sufficient concentration of antibody functionalised to the surface in order to detect the antigen, CRP.

There are various conjugation methods which can be used to functionalise Ag NPs with antibodies.[144] In this work covalent, directional and physical adsorption methods (Figure 4.12) were all investigated.

Covalent conjugation	Directional conjugation	Physical adsorption
Carbodiimide crosslinking	Biotin-Streptavidin link	pH correction
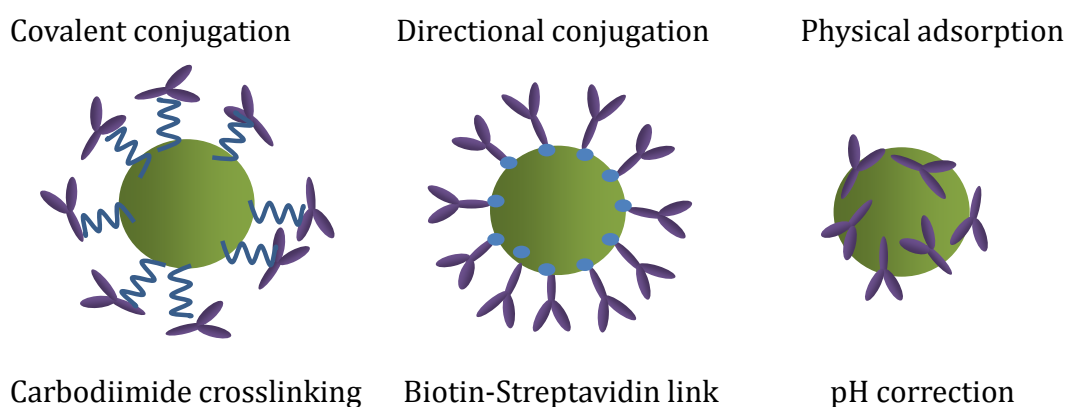
Figure 4.12 Schematic diagram indicating how antibodies are functionalised and orientated on the Ag NP surface in covalent, directional and physical conjugation methods.

As shown in the diagram in Figure 4.12, each conjugation methods orientates the antibody on the Ag NP surface differently, leaving different parts of the antibody exposed. Covalent conjugation utilises carbodiimide crosslinking chemistry, allowing the antibody to bind to the Ag NP via a $CT(PEG)_{12}$ molecule functionalised on the surface, the orientation allows the paratopes to be free to bind to an antigen, if the covalent bond doesn't involve binding to an amine on them.[145] Directional conjugation uses Ag NPs coated in streptavidin which can then form a strong bond to a biotin linked antibody. As the biotin is on the Fc region, the streptavidin-biotin bond will allow the paratopes to be free.[146] Finally, physical adsorption involves

changing the pH of the antibody to allow electrostatic adsorption of the antibody to the NP surface. The orientation of the antibody is unknown in the conjugation and paratopes may be blocked, decreasing the binding efficiency to the antigen.

4.3.2.1 Carbodiimide crosslinking conjugation

Antibodies were conjugated to the surface of the Ag NPs via carbodiimide crosslinking chemistry which creates an amide bond between the carboxylic acid of the CT(PEG)$_{12}$ molecule to an amine group on the antibody. 1-Ethyl-3-(3-dimethylaminopropyl) carbodiimide (EDC) is a readily available, water soluble carbodiimide used for crosslinking. It reacts with the carboxylic acid groups to form an O-acylisourea intermediate which is easily displaced by nucleophilic attack from primary amine groups in the reaction mixture. However, O-acylisourea is unstable in aqueous solution and if it fails to react with a primary amine it undergoes hydrolysis and regeneration of the carboxyl and releases the N-unsubstituted urea which would decrease the efficiency of the coupling. To prevent this from happening, the stability of the O-acylisourea is increased by using sulfo-N-hydroxylsuccinimide (sulfo-NHS). The EDC couples the NHS to the carboxyl, which forms a sulfo-NHS ester which is much more stable and provides much more efficient conjugation to primary amines. Figure 4.13 shows the coupling mechanism between PEG-Ag NP and the antibody using EDC and sulfo-NHS.
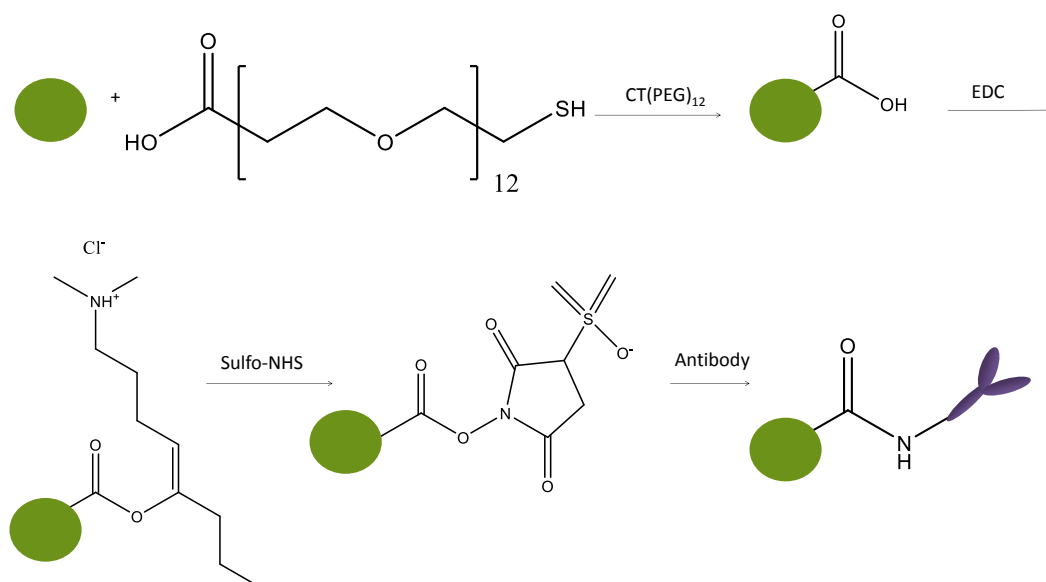
Figure 4.13 Carbodiimide crosslinking chemistry creating an amine bond between a CT(PEG)$_{12}$ attached to the surface of a Ag NP and the amine of an antibody, via the addition of EDC and sulfo-NHS.

CT(PEG)$_{12}$ was first conjugated to the Ag NP (0.3 nM) at a final concentration of 0.1 μM, as this concentration allowed for TMB oxidation to occur while keeping the NP stable (section 4.3.1.2). After functionalising and centrifugation, 20 μL of 1 mg/mL EDC and 40 μL of 1 mg/mL s-NHS in 10 mM MES buffer (pH 6) were mixed together and then added to the PEG-Ag NP pellet and the solution made up to 1 mL with HEPES buffer (pH 7.6). This was left shaking for 30 minutes followed by another centrifuge step and supernatum removal followed. A final concentration of 5 μg/mL monoclonal mouse IgG$_{2B}$ antibody was then added to the pellet and made up to 1 mL with HEPES buffer. This was then left for 4 hours to allow the formation of the amide bond between the carboxyl and amine groups to take place.

Characterisation of the Ab-PEG Ag NPs using extinction spectroscopy, DLS and gel electrophoresis was then carried out. Gel electrophoresis is a method of separation and analysis, based on the size and charge of the samples being analysed. Samples travel through a gel matrix due to an electric charge being applied through the gel. Larger samples travel slower through the gel compared to smaller samples, which can travel faster through the porous matrix. Gel electrophoresis was therefore used to detect a difference in size and charge of Ag, PEG-Ag and Ab-PEG-Ag NPs to confirm the successful conjugation of each stage.

An agarose gel was prepared by dissolving 100 mg of agarose in TBE buffer by applying heat and then leaving the gel to cool and set. Ag, PEG-Ag and Ab-PEG-Ag NPs were centrifuged and the supernatum removed in order to concentrate the samples. Loading buffer was added to the pellet which was then transferred to wells created in the agarose gel. A voltage of 160 V was applied to the gel and left for 30 minutes. The band was visualised using the strong colour of the NP conjugates. Figure 4.14 (b) shows a photograph of the gel after 30 minutes and the extinction spectrum of each conjugate can be seen in Figure 4.14 (a).
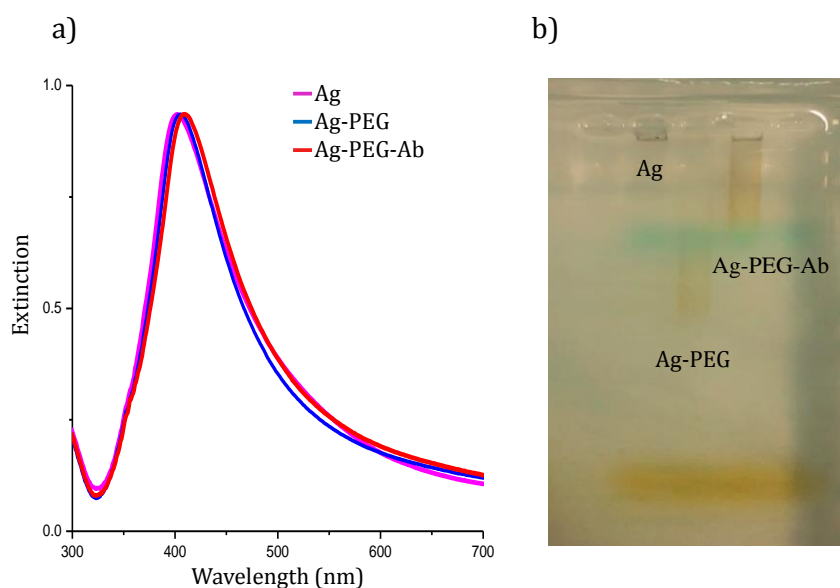
Figure 4.14 (a) Extinction spectra of bare Ag (pink), PEG-Ag (blue) and Ab-PEG-Ag (red) NPs. 50 µL of each sample was diluted in 450 µL of d.H_2O for analysis. Spectra have been normalised to 1 for clarity (b) Image of gel showing the distance travelled by Ag, PEG-Ag and Ag-PEG-Ab NP conjugates.

Table 4.2 LSPR, size and zeta potential for Ag, PEG-Ag and Ab-PEG-Ag NPs

Sample	LSPR (nm)	Size (nm)	Zeta potential (mV)
Ag NPs	410	81.8±1.8	-39.3±1.0
PEG –Ag NPs	412	93.69±2.3	-25.4±2.8
Ab-PEG-Ag NPs	415	96.78±0.6	-16.6±2.2

The spectra in Figure 4.14 (a), show that there was a red shift in LSPR when $CT(PEG)_{12}$ and antibody was added to the surface of Ag NPs from 410 nm for bare Ag, to 412 nm for PEG-Ag and 415 nm for Ab-PEG-Ag NPs, indicating that the NPs increased in size and therefore confirming the successful conjugation of PEG and antibody to the surface. Furthermore, the conjugates did not show any additional peaks due to aggregation in the extinction spectra, indicating the Ag NPs were stable after the addition of $CT(PEG)_{12}$ and antibody. The DLS data in Table 4.2 confirmed the conjugation, as the NPs increased in size and became more positive as each layer was added. The Ab-PEG-Ag NPs were 96 nm in size and had a zeta potential of -16mV. This would suggest that the NPs were unstable, due to the higher zeta potential; however, the amount of antibody (which will be slightly positive) creates an increase in charge on the Ag NP, increasing the overall zeta potential. Therefore the Ab-PEG-Ab NPs were deemed to be stable.

The image in Figure 4.14 (b) shows that Ag NPs did not move at all in the gel electrophoresis, Ab-PEG NPs travelled the furthest and Ag-PEG-Ab NPs travelled less. Although Ag NPs were the smallest in size and should theoretically have moved the furthest down the gel, the Ag NPs had no protecting groups on the surface, so when the high concentration of loading buffer was added to the Ag NP pellet, the NPs aggregated in the well and became too big to move through the gel. As PEG-Ag NPs travelled further than the Ab-PEG-Ag NPs, it could be deduced that the conjugates were of a different size and/or charge, suggesting successful $CT(PEG)_{12}$ and antibody conjugation.

Therefore the LSPR shift, the difference in size and zeta potential and gel electrophoresis result all suggested that the carbodiimide crosslinking chemistry approach of antibody conjugation was successful.

4.3.2.2 Streptavidin-biotin conjugation

Streptavidin and biotin have a very strong binding affinity for each other, therefore a biotin labelled antibody can be conjugated to Ag NPs that have been functionalised with streptavidin. To functionalise Ag NPs with streptavidin (SA), Ag NPs and SA were incubated together at 37°C for 3 hours followed by centrifugation and resuspension. 5 different concentrations of SA (50, 10, 3, 1.9, and 0.9 μM) were

added to 1 mL of Ag NPs (0.3 nM) and the resulting SA-Ag NPs were then characterised using extinction spectroscopy and DLS. The results from the characterisation are shown in Table 4.3.

Table 4.3 LSPR, size and zeta potential of SA-Ag conjugates.

Concentration of SA (μg/mL)	LSPR (nm)	Size (nm)	Zeta potential (mV)
0	410	75±0.3	-40±1.9
0.9	410	78.4 ± 0.3	-41.4 ± 3.2
1.9	411	77 ± 1.7	-39.4 ± 6.3
3	412	78.6 ±0.3	-43.8 ± 0.3
10	413	82.47 ± 1	-36.6 ± 0.9
50	415	84.5 ± 2	-26.0 ± 3.6

The LSPR indicated that when higher concentrations of SA (50, 10 μg/mL) were added to the Ag NPs, the red shift of the LSPR was greater, suggesting that SA was successfully attached to the surface. Further evidence of SA conjugation was seen by the increase in size and zeta potential. Higher concentrations of SA lead to larger NPs and an increase in charge and at lower concentrations the NPs were smaller with a similar size and zeta potential to bare Ag NPs. SA-Ag NPs with 3 μg/mL of SA on the surface was chosen to be used for antibody conjugation as it was hoped that enough SA was on the surface of the Ag NP to bind to the biotin-linked antibody, while still having enough space on the metal NP to allow H_2O_2 to be broken up into radicals. A final concentration of 5 μg/ml of biotin-labelled monoclonal mouse IgG_{2B} antibody was then added to the conjugate and left shaking for 1 hour to allow the biotin-SA bond to occur. The conjugates were then centrifuged and characterised using extinction spectroscopy and compared to bare Ag and SA-Ag NPs. The resulting spectra are shown in Figure 4.15.
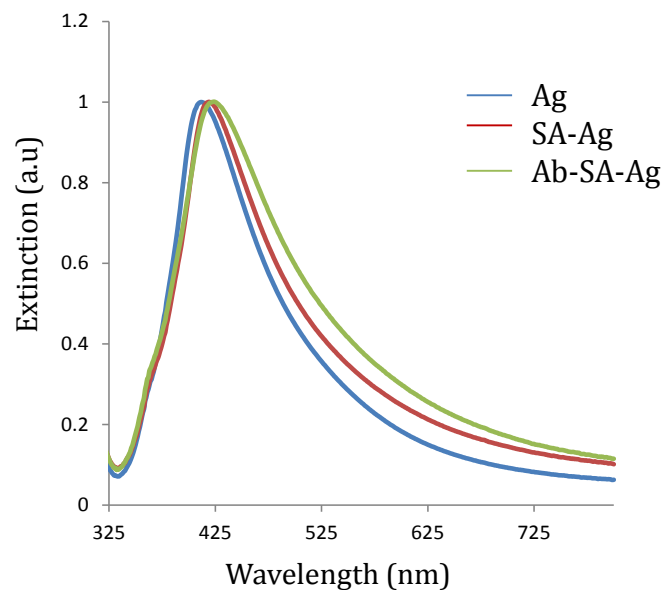
Figure 4.15 Extinction spectra of Ag (blue), Ag-Strep (red) and Ag-Strep-Ab NPs (green). All samples were diluted by adding 50 μL of Ag conjugate to 450 μL of d.H$_2$O Spectra have been normalised to 1 for clarity.

The addition of the antibody to the SA-Ag NPs cause red shifting of the LSPR (to 420 nm) as the antibody increased the size of the conjugate. This can be seen by the peak broadening, suggesting the streptavidin biotin bond has formed and the antibodies were attached to the Ag NPs surface. It was hoped that this conjugation would be favoured as both paratope of the antibody would be free for binding to the CRP as they do not take part in the conjugation to the NP surface.

4.3.2.3 Physical conjugation

The final conjugation method investigated was direct physical adsorption, which binds the antibody to the surfaces of the NP by altering the pH in order to protonate the lysine groups on the Fc chain of the antibody. The positive lysine group would therefore be attracted to the negative Ag NP and would electrostatically bind to the surface. As the lysine groups have a pKa of roughly 9-10, if the pH was below this then the amine group would be positively charged and electrostatic attraction should occur.[147] It should be noted that terminal amines of the paratope could also be protonated and electrostatically bind to the surface as they have a pKa between 7-

8.[148] Therefore by changing the pH to 8, only the lysine groups would be positive and the orientation of the antibody on the NP would allow the terminal amines of the paratope to take place in CRP binding.

Final concentrations of monoclonal mouse IgG$_{2B}$ antibody (2.5, 1, 0.5, 0.25 and 0.05 μg/mL) were added to 1 mL of Ag NPs with a pH of 8 and left to shake overnight. Lower concentrations of antibody were added than in the previous conjugation methods due to NP instability at concentrations of 2.5 μg/mL and above. The solutions were then centrifuged, the supernatum removed and the NPs resuspended in 1 mL of distilled water. The conjugates were then characterised using extinction spectroscopy and DLS and the results are shown below in Figure 4.16.
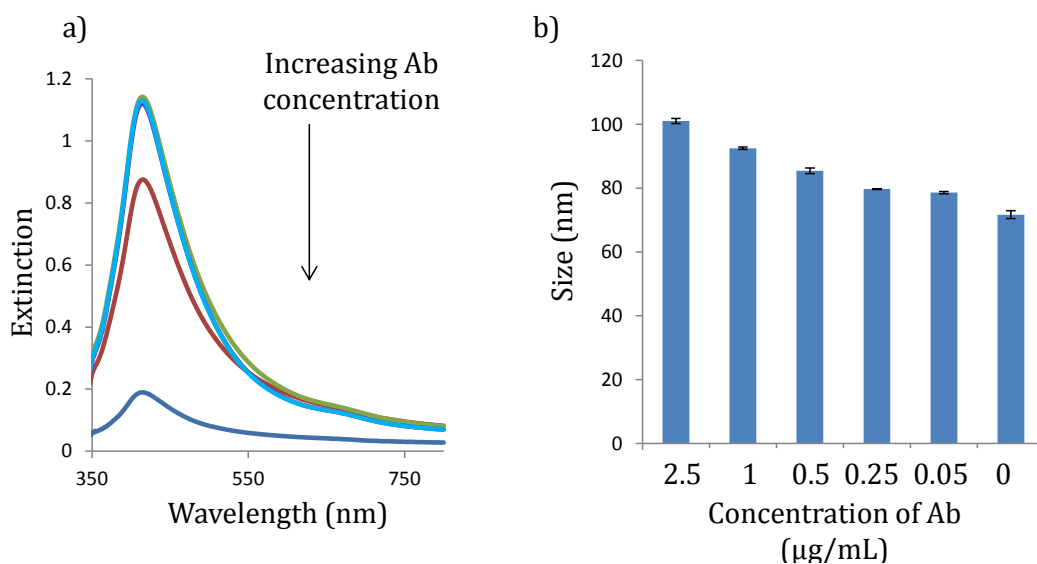
Figure 4.16 (a) Extinction spectra of Ag NPs with different concentrations of antibody physically conjugated to the surface (2.5 μg/mL (dark blue), 1 μg/mL (red), 0.5 μg/mL (light blue), 0.25 μg/mL (green) and 0.05 μg/mL (purple). All samples were dilute 50 μL and 450 μL d.H$_2$O. (b) Size of corresponding Ab-Ag NP conjugates measured by DLS. Error bars obtained from 3 measurements.

As can be observed in the extinction spectra (Figure 4.16 (a)), that when higher concentrations of antibody were added to the Ag NP surface, a dampening in the LSPR peak signal occurred, indicating that the NPs were unstable and had aggregated. Furthermore, the increase in size (Figure 4.15 (b)) confirmed that aggregation occurred at higher concentrations of antibody. Lower concentrations of antibody still resulted in an increase in size, however as the LSPR did not decrease

and only a slight red shift was observed, it suggested that the NPs were stable and had antibody on the surface. As 0.5 μg/mL of antibody gave an increase in size with little aggregation, this concentration was used to compare to the previous conjugation methods.

The characterisation of Ab-PEG-Ag (covalent), Ab-SA-Ag (directional) and Ab–Ag (physical) NPs successfully demonstrated that antibodies had been attached to the Ag NP surface in all three conjugation methods. However, due to efficiency of the coupling method, the concentration of antibody on the NP surface will vary for each approach and a lateral flow immunoassay was used to determine if there were enough antibodies on the surface, in the correct orientation, to detect CRP.

4.3.2.4 Lateral flow immunoassay

One final method of confirming that antibody conjugation had been successful was lateral flow immunosorbent assay (LFA). LFA provides a rapid one step analysis, low operational costs and a user friendly layout.[149]

LFA strips comprise of a sample pad which is dipped in the eluent (HEPES buffer), a conjugate pad to which the NP conjugates are applied, a nitrocellulose strip, where the antigen is immobilised and, finally, an absorbent pad which collects the excess eluent and conjugate. Figure 4.17 is an annotated photograph of a LFA.
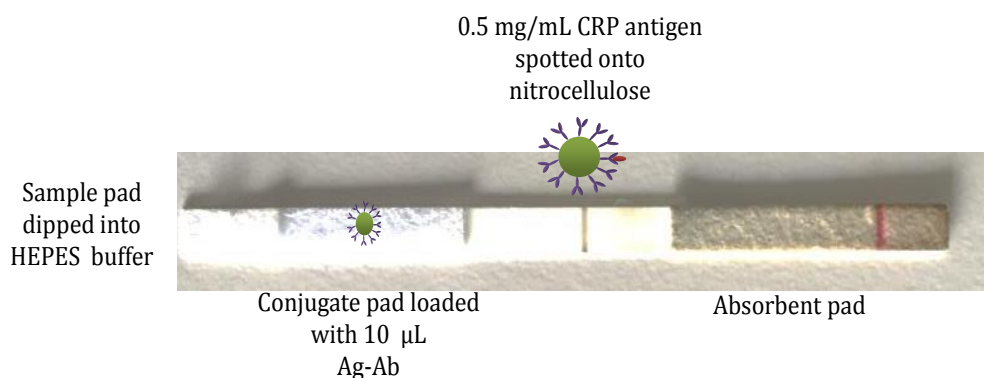
Figure 4.17 Photograph of LFA, highlighting main areas of interest. The antigen is first spotted on the nitrocellulose strip and left to dry. The conjugate pad is loaded with NPs coated wth antibodies. The strip is then placed, sample pad first. in buffer and the buffer flows through the strip on to the conjugate pad which allows the NPs to join the flow. When the conjugates flow over the antigen, the antibodies bind to the ntigen, therfore immobilising the NP on the antigen spot.

To determine if the antibody conjugation had been successful, a solution of CRP antigen (0.5 µL, 0.5 mg/mL) was spotted onto the nitrocellulose strip and left to dry or a line of 0.5 mg/mL CRP sprayed on (obtained from BBI solutions) was used. A solution containing each of the Ab-Ag NPs conjugates (10 µL) was then added to the conjugate pad and when hydrated with HEPES buffer, capillary flow along the strip was initiated. When the HEPES solution runs over the conjugate pad, Ab-Ag NPs join the flow and run over the CRP spot/line were it bound to the CRP and was immobilised on the nitrocellulose resulting in the appearance of a green spot/line, which confirmed the presence of the antibody on the Ag NP. The spot only appeared when CRP and antibody were both present. All three Ab-Ag NP conjugates were tested using the LFA to confirm that the antibody conjugation had been successful. The results are shown in the photograph in Figure 4.18.
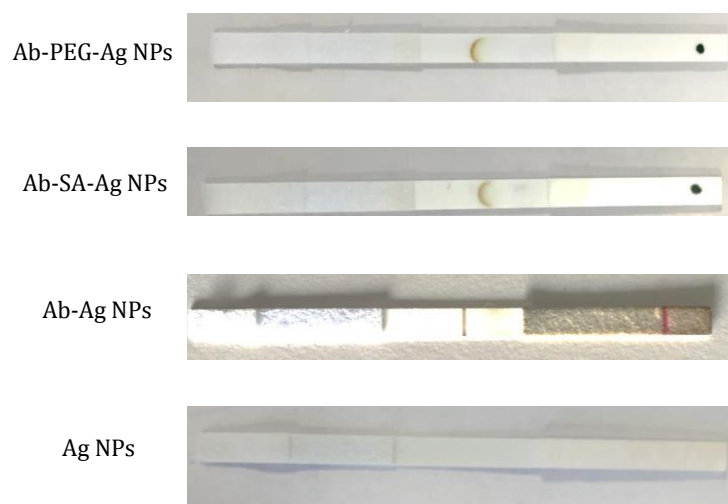
Figure 4.18 Images of LFA strips showing the binding of the NPs to the antigen due to the presence of antibodies on the covalent (Ab-PEG-Ab NPs), directional (Ab-SA-Ag NPs) and physical (Ab-Ab) conjugation methods. Ag NPs were also applied to a strip as a control.

The image in Figure 4.18 shows that all three Ab-Ag NP conjugation methods were proven to be successful by the appearance of a NP spot. The difference in the spot/line appearance was due to the way the CRP had been applied to the nitrocellulose strip. In the case of the Ab-PEG-Ag and the Ab-SA-Ag conjugates, the CRP was spotted onto the strip and dried with the CRP on the edge of the spot. Therefore, when the conjugates were run along the strip they bound to the CRP at the edge of the spot and gave the appearance of a semi-circle. Ab-Ag NP conjugates were tested on a strip from BBI solutions, were a line of CRP was sprayed onto the surface of the nitrocellulose, which gave the appearance of a straight line of NP on the nitrocellulose strip. Ag NPs were also applied to a lateral flow that contained CRP and as no line appeared it further confirmed the binding was due to the antibody on the Ag NP surface, and non-specific bonding between the Ag NP surface and CRP did not occur.

As there were enough antibodies on each conjugate to detect CRP, the catalytic activity of each was tested and compared to ensure that there was enough Ag metal surface available to catalyse the TMB oxidation and the Ab-Ag NP conjugates with the best catalytic performance would subsequently be used in the SLISA.

4.3.2.5 Catalytic activity of Ab-Ag nanoparticles

The peroxidase activity of each Ab-Ag NP conjugate system was investigated by adding 200 µL of TMB blotting solution to 200 µL Ag-Ab conjugate along with 100 µL d.H$_2$O. TMB blotting solution, which would be used in the subsequent SLISA experiments, is a premixed solution containing TMB and H$_2$O$_2$ which is oxidised to the CTC in the presence of an enzyme. The catalytic activity was then assessed by carrying out the SERRS of each conjugate by analysing with 638 nm laser excitation and the results are shown in Figure 4.19. It should be noted that the Ab-Ag NPs were all diluted to have the concentration (0.3 nM).
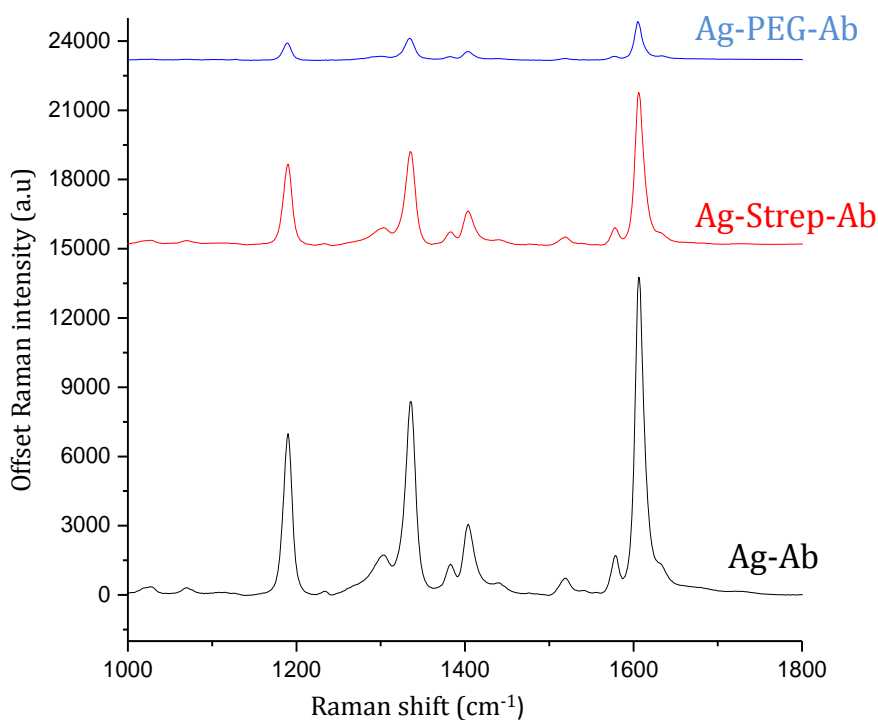
Figure 4.19 SERRS spectra of the CTC of TMB catalysed by Ag-PEG-Ab (blue), Ag-SA-Ab (red) Ag-Ab NPs (black)). Spectra were obtained using 638 nm laser excitation with a 1 second accumulation time and 30 mW laser power. The spectra shown are the average of 5 measurements of 3 replicate samples. The spectra have all been baseline corrected using Matlab.

It can be observed from Figure 4.19 that each Ab-Ag NP conjugate had varying catalytic activities as shown by the different intensities of the SERRS CTC spectra obtained. The physical conjugation method (Ab-Ag NPs) gave rise to the largest

oxidation of TMB as it had the lowest concentration of antibody (0.5 µg/mL) functionalised to the surface and no other molecules had to be added to facilitate the conjugation. Therefore, it had the largest Ag metal surface available to catalyse the formation of radicals from H_2O_2. Covalent and directional conjugation techniques experienced a smaller amount of catalytic activity as there was less metal surface available on the NPs, leaving less Ag metal surface to partake in the oxidation of TMB.

Due to the better catalytic activity, easier conjugation method and lower concentration of antibody added, physical conjugation technique was deemed the most successful and was used in the SLISA to detect CRP.

The catalytic activity of the Ab-Ag NPs, with different concentrations of antibody on the surface, was then investigated with the addition of TMB blotting solution. 100 µL of Ab-Ag NPs, 100 µL of TMB blotting solution and 300 µL of water were mixed together and analysed by SERRS using 638 nm laser excitation and the results are shown in Figure 4.20.
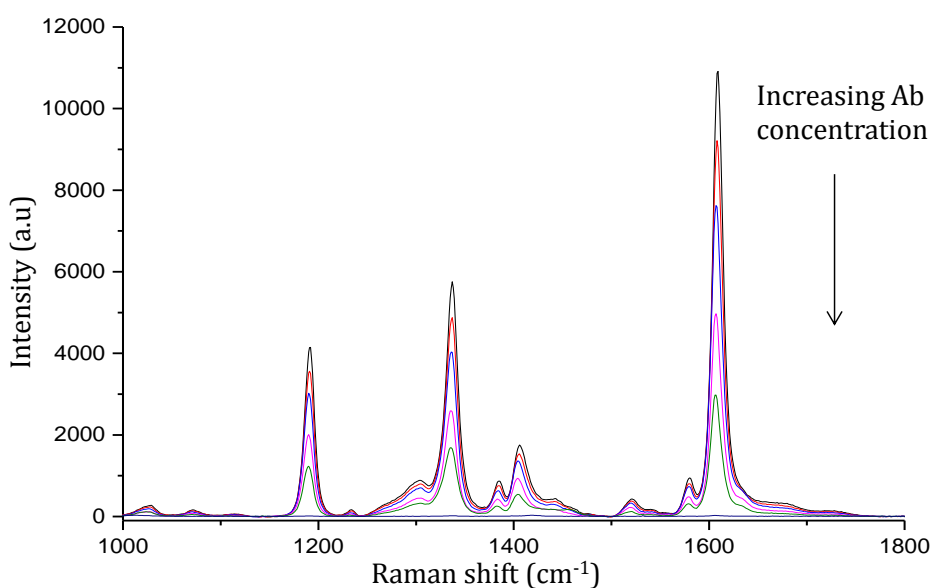
Figure 4.20 SERRS spectra of CTC of oxidised TMB produced by Ag NPs with different concentrations of Ab functionalised on the surface (0 µg/mL (black), 50 ng/mL (red), 250 ng/mL (blue), 500 ng/mL (purple), 1000 ng/mL (green) and 2500 ng/mL (dark blue)). Spectra were obtained using a 638 nm laser excitation with a 1 second accumulation time and 30 mW laser power. The spectra shown are the average of 5 measurements of 3 replicate samples. The spectra have been baseline corrected using Matlab.

From the spectra shown in Figure 4.20, it can be seen that when higher concentrations of antibody (2500 ng/mL and 1000 ng/mL) were functionalised to the Ag NP surface and TMB blotting solution added, little TMB oxidation was observed which was evident in the weak CTC SERRS spectra obtained. As the concentration of antibody on the surface decreased, a more intense CTC SERRS spectrum was obtained, therefore more oxidation had occurred. This was expected as antibodies, which are roughly 150 KDa in size,[128] take up a relatively large amount of space on the Ag NP surface, significantly reducing the surface area of the Ag metal available to partake in the decomposition of H_2O_2. This resulted in less TMB becoming oxidised and a lower concentration of CTC molecules being electrostatically attracted to the surface and experiencing SERRS enhancement. The lowest concentration of antibody on the Ag NP surface (50 ng/mL) gave the largest amount of TMB oxidation and SERRS; however, it was not chosen to be used in the SLISA as the remaining unbound Ag NP surface could potentially give rise to non-specific binding during the SLISA as the free Ag NP surface could bind to more capture antibody. Therefore, Ag NPs with 500 ng/mL of antibody on the surface was chosen as the best compromise as there were enough antibodies present to prevent non-specific binding and bind to the CRP, while sufficient surface area of the Ag metal was still available for TMB oxidation.

4.3.3 SLISA

Ab-Ag NPs were then used in place of enzyme labelled antibodies to form the SLISA for the detection of CRP. By replacing the enzyme with NPs, the cost and time scale of the assay could be reduced. When performing the SLISA on a substrate, there were many different aspects which had to be taken into consideration in order to eliminate the main issue when using NP in surface assays, which is non-specific binding. Non-specific binding occurs when NPs bind to the surface without the presence of the target antigen. This in turn leads to the oxidation of TMB where it is not expected and can give false positives and poor limits of detection. Therefore, there were a number of different stages that had to be optimised, including what surface to use, capture antibody concentration and NP incubation for successful SLISA.

4.3.3.1 Optimisation

4.3.3.1.1 Surfaces

The first step of the SLISA was the immobilisation of capture antibody onto a suitable solid substrate. Nitrocellulose and epoxy-coated glass slides were selected for investigation as each offered different interactions with the antibody and immobilised them in different orientations.[150]

Spin coated nitrocellulose glass slides were used which immobilise the antibody via electrostatic interactions, which is advantageous as no part of the antibody is taken up with a covalent bond to the slide, but gives little control over the orientation of the antibody on the surface. This could mean that the paratope of the antibody could be unavailable for CRP binding in the SLISA. Epoxy-coated glass slides, allow for directionality in the capture antibody immobilisation. In this case the NPs are immobilised by a ring opening mechanism of the epoxy group and subsequent attachment to an amine of the capture antibody. By creating a covalent bond between antibody and surface, the antibodies were strongly attached and cannot be washed away, unlike the electrostatic interactions which are not as strong. However, as there are many amines on the antibody an amine on the paratope could be used in the bonding mechanism and therefore hinder the SLISA. Figure 4.21 shows a diagram of the 2 different immobilisation mechanisms.
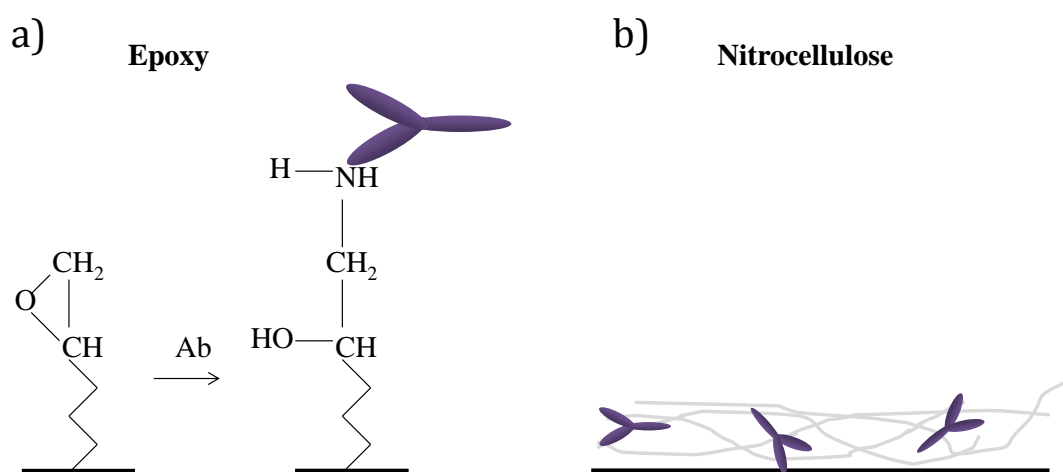
Figure 4.21 Illustration of the binding of capture antibody to (a) epoxy and (b) nitrocellulose coated glass slide.

Both surfaces where investigated in the optimisation steps and their efficiency at preventing non-specific binding in the SLISA were compared.

4.3.3.1.2 Capture antibody optimisation

The first step of the SLISA involved immobilising the capture antibody on the surface of the substrate slide. To investigate this, the volume and concentration of antibody that would be applied to the surface was varied and the non-specific binding assessed.

Initially, a high concentration and volume of CRP specific capture antibody (100 μL, 100 μg/mL) was immobilised onto an epoxide coated glass slide which had been placed in a microarray chamber to isolate the spots. The antibodies were left to incubate overnight to allow full immobilisation. The slide was then washed with 0.05 % Tween 20$^{©}$ in PBS (pH 7.6) three times to remove any unbound antibody. The surface of the epoxide slide that was not coated in antibody was then blocked with 1% BSA solution to stop non-specific binding of the Ab-Ag NPs (0.6 nM) to the surface. Following three more wash steps, a high concentration of CRP (100 μL, 1 μg/mL) was added, which bound to the immobilised antibodies, and a control of 1% BSA was added to a separate well and left to incubate for 2 hours. Further wash steps were carried out followed by the addition of Ag-Ab NPs for another 2 hours which completed the SLISA by binding to the CRP. The assay was then washed leaving a Ab-Ag NP residue on the slide where the capture antibody had originally been deposited, which can be seen in Figure 4.23. Finally, TMB blotting solution was added and the immobilised Ab-Ag NPs were able to catalyse the oxidation. Upon removal of the TMB blotting solution, the positively charged CTC should remain bound to the Ag NPs.

The surface of the SLISA with and without the presence of CRP was analysed using 633 nm laser excitation and an image of the surface was taken using white light with a 50x objective and is shown in Figure 4.22.
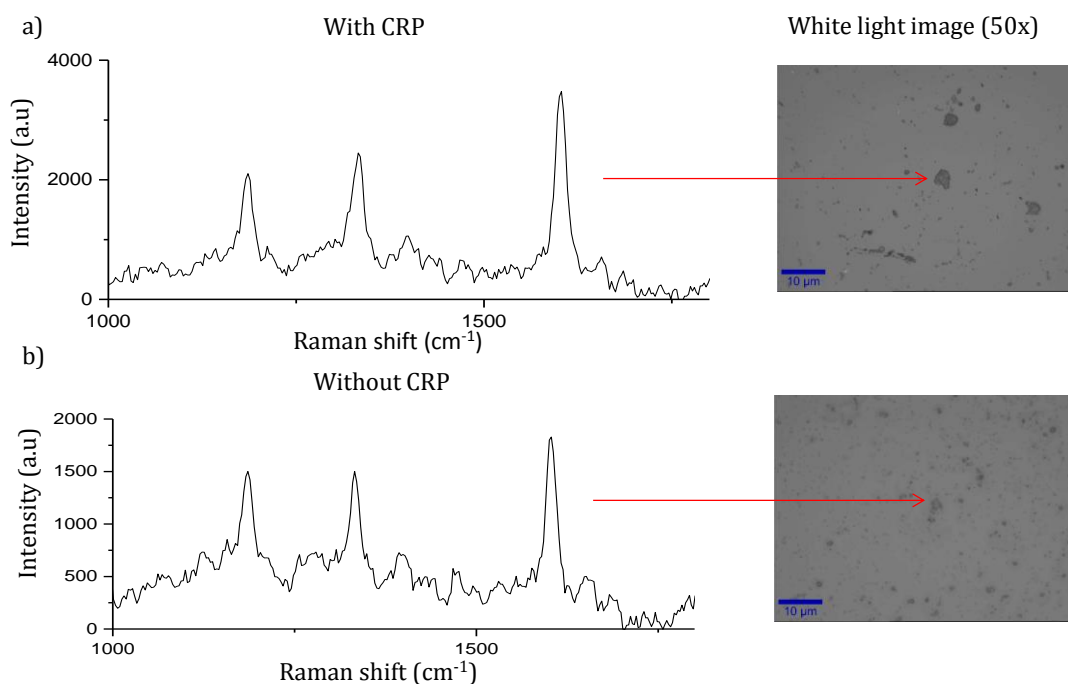
Figure 4.22 SERRS spectra of CTC when CRP (a) and no CRP (b) was present in the SLISA and corresponding image of the surface showing location were spectrum was obtained. Spectra obtained using 633 nm laser excitation with a 1 second accumulation time and 8 mW laser power. The spectra have all been baseline corrected using Matlab.

The oxidised TMB SERRS spectra obtained from the SLISA with and without CRP being present are shown in Figure 4.22 and can be seen that not much difference was observed in the intensity of the CTC SERRS signal when CRP was present or absent. This was not expected as it was envisaged that when a high concentration of CRP was present, there would be more Ag NPs, more TMB oxidation and therefore a more intense SERRS. No signal should be obtained when CRP was absent. The small difference in intensity was attributed to the long 2 hour NP incubation time which led to a large amount of non-specific binding of the Ag NPs to the epoxy surface. It was also thought that the NPs may also be binding to the BSA which was used to block the remaining epoxy groups. This was due to the Ab-Ag NP having free Ag metal surface which, although needed for TMB oxidation, could be a hindrance as it can bind to the epoxy surface and to the amine group of the BSA blocking agent. There was also the possibility that the free Ag metal surface was binding to the capture antibody further increasing the non-specific binding.

Another issue with this method was using such a large volume of capture antibody (100 µL) which created a large surface area of antibody at the beginning of the assay. By spotting 100 µL of capture antibody, the high surface area of the spot created was non-homogenous, as antibody was immobilised on the surface in concentrated areas. This lead to NP aggregation on the surface and a varied CTC spectrum obtained from different parts of the surface, which can be seen in the white light image in Figure 4.22. Therefore, a smaller capture antibody volume with varying concentrations was investigated to try to eliminate non-specific binding.

To investigate the possibility of non-specific binding of the Ab-Ag NPs to the capture antibody when no antigen was present, 0.3 µL of capture antibody at high (500 µg/mL), medium (100 µg/mL) and low concentrations (10 µg/mL) were spotted onto the epoxy coated glass slide and left to incubate and immobilise overnight. The spots were washed and 20 µL of Ab-Ag NPs directly added to the surface, covering the whole capture antibody spot, and left to incubate for only 20 minutes to stop them drying onto the surface. BSA was not added as a block as it was suspected that it may have contributed to the non-specific binding. The Ab-Ag NPs were then removed and TMB blotting solution added to the SLISA and left for 20 minutes on the surface before being removed and the surface washed again. The spots were then analysed using 633 nm laser excitation by taking 10 spectra at different points on the spot and an average SERRS CTC spectrum for each capture antibody was plotted in Figure 4.23.
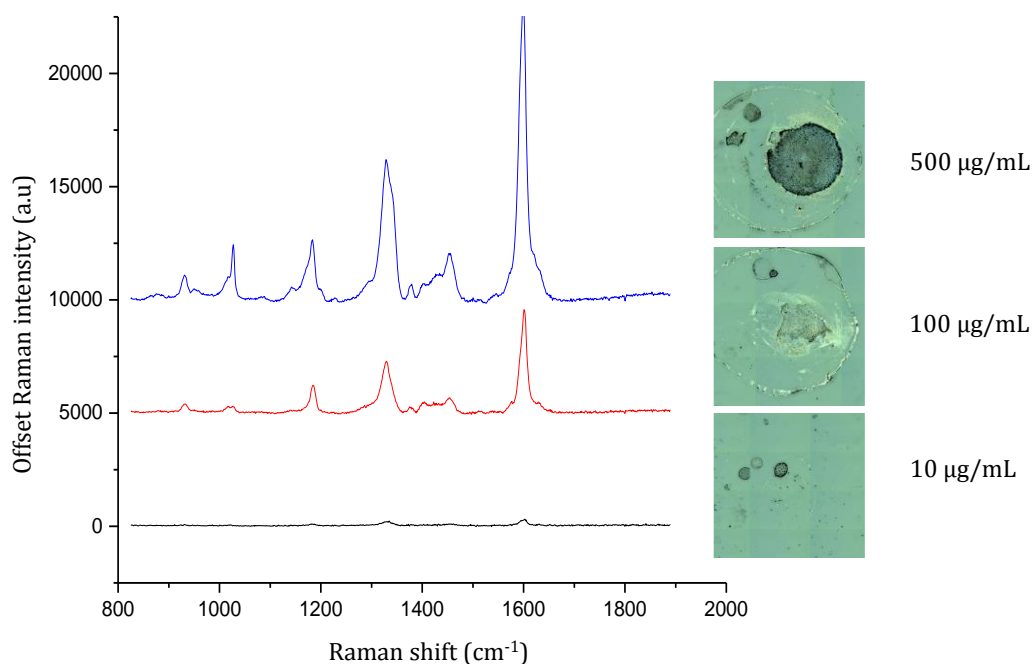
Figure 4.23 SERRS spectra of the CTC of TMB obtained from each SLISA spot when 500 μg/mL (blue), 100 μg/mL (red) and 10 μg/mL (black) of capture antibody was spotted on the epoxy coated surface, incubated overnight, washed and then 20 μL Ag-Ab NP's added and washed after 20 minutes. Spectra were collected using 633 nm laser excitation. Average spectra obtained from taking spectra of 10 different areas of the spot using a 5x laser objective, 8 mV laser power and 3 second acquisition time.

As shown in the CTC spectra in Figure 4.23, when Ab-Ag NPs and TMB were added to the spot containing the high concentration of capture antibody (500 μg/mL), a NP and CTC residue was left on the spot as the Ag NPs bound to the capture antibody causing non-specific binding and high degree of non-specific binding.

A CTC SERRS spectrum was also observed when 100 μg/mL of antibody was spotted, and, although less intense, it also suggested that the Ag NPs were binding to the high concentration of antibody in the spot. Therefore, a lower concentration of antibody had to be spotted to lower the amount of non-specific binding. This was achieved when 10 μg/mL of antibody was spotted and a very low TMB CTC SERRS spectrum was obtained. Therefore, this concentration was used in the subsequent SLISA.

4.3.3.1.3 Nanoparticle incubation

The effect of incubation time of the Ab-Ag NPs on non-specific binding was also investigated by carrying out the SLISA using 100 ng/mL of CRP (in 10 mM PBS) and with 0 ng/mL of CRP. 0.3 μL of capture antibody (10 μg/mL) antibody was spotted onto the epoxy slide, incubated overnight and washed. To the capture antibody spot, 20 μL of CRP (100 ng/mL) or 20 μL of 10 mM PBS (control) were incubated for 20 minutes and the solution removed and surface washed again. 20 μL of Ab-Ag NPs (0.6 nM) were then added to each spot and incubated for 20 or 60 minutes. The NPs were then removed and the surface washed. The resulting Ag NP spot was then used to oxidise the TMB blotting solution by adding 20 μL of TMB blotting solution to the spot which was left for 20 minutes followed by another wash step. After oxidation, 10 spectra taken at different areas were obtained from each spot using 633 nm laser to obtain an average spectrum for the whole spot. Figure 4.24 shows images of the epoxy-coated slide and the average CTC SERRS spectrum collected from each spot.
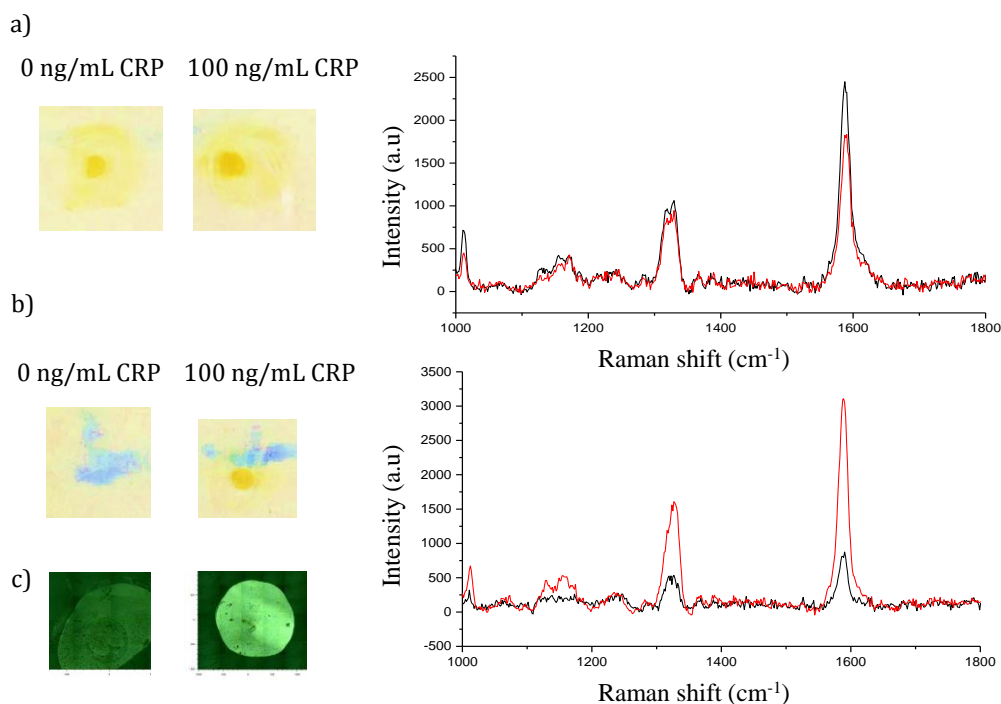
Figure 4.24 (a) Image of SLISA spot with and without CRP when Ag-Ab NPs were incubated for 60 minutes and accompanying average SERRS CTC spectra obtained from the SLISA with CRP (red) and without CRP (black) (b) Image of SLISA spot with and without CRP when Ag-Ab NPs were incubated for 20 minutes and accompanying average SERRS TMB CTC spectra obtained from the SLISA with and without CRP. (c) Dark field image of SLISA spot with and without CRP. Spectra were collected using 633 nm laser excitation. SERRS spectra obtained from taking spectra of 10 different areas of the spot using a 5x laser objective, 8 mW laser power and 3 second acquisition time.

As shown in the image in Figure 4.24 (a) when Ab-Ag NPs were added to the SLISA with and without CRP being present and left for 60 minutes before being removed and washed, a spot due to the NP binding was observed for both samples. Therefore the Ag NPs had bound to the capture antibody of the SLISA spot and caused a false positive. This was unexpected but could be explained due to the free Ag metal surface. As discussed already, there was still free Ag surface on the NP which was available for TMB oxidation. This could bind to the capture antibodies as the NPs were at the correct pH for physical conjugation to occur. The long incubation time facilitated the conjugation, hence the appearance of the spot. It should also be noted that the Ag NPs also bound non-specifically to the epoxy slides which is noticeable by the Ag NP residue around the Ag spot which would affect the TMB oxidation.

123

By decreasing the incubation time to 20 minutes there was a clear difference in spot appearance and no spot was visible by eye for the sample without CRP with a spot observable when CRP was present (Figure 4.24 (b)). Further confirmation took place by imaging the SLISA spot using dark field imaging. When there was no CRP present there was a low concentration of NP on the spot therefore the scattering was low due to the small number of NPs present. When CRP was present the image showed more scattering due to the high NP concentration present and brighter spot was observed.

To further confirm the non-specific binding due to long incubation times, the spots were analysed using 633 nm laser excitation. The resulting SERRS CTC spectra for long incubation times showed no difference with or without the presence of CRP, hence 60 minutes could not be used as it gave a false positive. The 20 minutes incubation time resulted in different SERRS intensities of the CTC spectra with and without CRP, eliminating the non-specific binding issues and this incubation time was used in subsequent SLISA.

4.3.3.2 SLISA performed on epoxide coated glass slide

Once the parameters were optimised, the full SLISA was performed with different concentrations of CRP to determine a limit of detection. First, 0.3 µL of 10 µg/mL CRP-specific capture antibody was immobilised onto the epoxide coated glass slide. The antibodies were left to incubate overnight to allow full immobilisation. The resulting antibody spots were then washed with 0.05 % Tween 20$^{©}$ in PBS three times to remove any unbound antibody. 20 µL of CRP (100, 50, 25, 12.5, 6, 1.5 and 0.75 ng/mL diluted in 10 mM PBS) were added to separate SLISA spots and left to incubate for 20 minutes to allow immobilisation of the antigen to the bound antibody. The surface was washed again and 20 µL of Ab-Ag NP was added to each sample. After 20 minutes, the Ab-Ag NPs (0.6 nM) were removed, the surface was washed and a Ag spot was observed. 20 µL of TMB blotting solution was added and then removed after 20 minutes. The spot was then washed once more, removing any excess TMB. The resulting SLISA spots for each CRP concentration were imaged using a white light with a 5x objective and are shown in Figure 4.25.

50   25   12.5   6   1.5   0.75   0

Concentration of CRP (ng/mL)
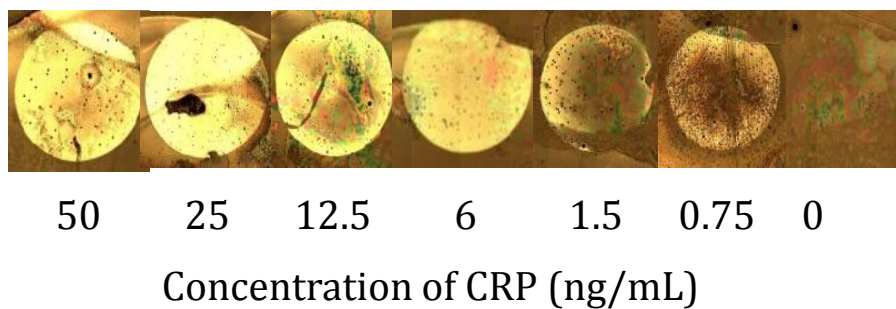
Figure 4.25 Resulting SLISA spots obtained from different concentrations of CRP. Imaged using a white light microscope with a 5x objective.

Figure 4.25 shows the SLISA spots which are yellow in appearance due to the presence of Ag NP gave a clear decrease in Ag NP binding as lower concentrations of CRP were added to the SLISA. To quantify this decrease, SERRS spectra were taken at 50 different points to obtain an overall average CTC SERRS signal at each concentration. The change in the CTC SERRS spectrum with different concentrations of CRP is shown in Figure 4.26.
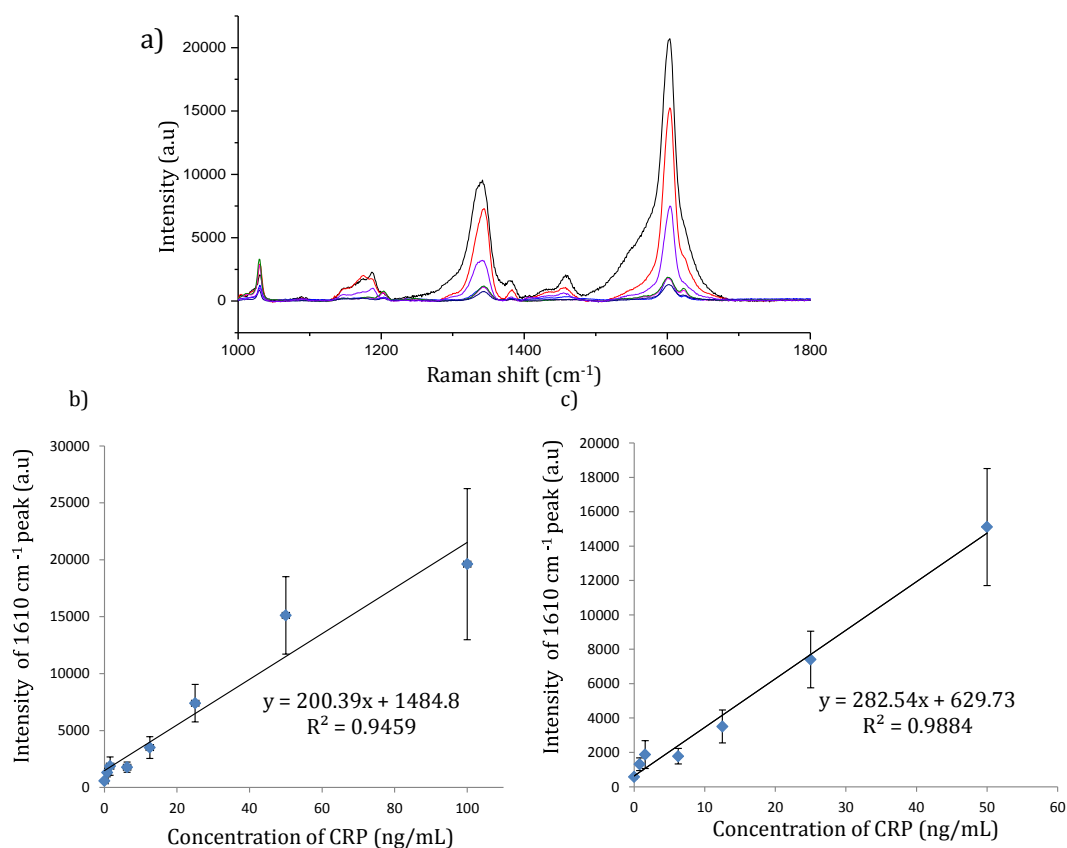
Figure 4.26 (a) CTC SERRS spectra of SLISA spot when different concentrations of CRP were added (100 (black), 50 (red), 25 (purple), 12.5 (green), 6 (pink), 1.5 (blue), 0.75 nM (light blue). Spectra are the average of 50 spectra taken at different parts of the SLISA spot with a 5x objective and 633 nm laser excitation, a 1 second acquisition time and 8 mW laser power was used (b) Intensity of 1610 cm^{-1} peak plotted against concentrations of CRP (0–100 ng/mL) and (c) Intensity of 1610 cm^{-1} peak plotted against concentrations 0 – 50 ng/mL of CRP.

As expected, the CTC SERRS signal intensity decreases as less CRP was added to the SLISA (Figure 4.26(a)). The intensity of the 1610 cm^{-1} peak was then plotted against each concentration and is shown in Figure 4.26 (b). It is clear that the SLISA starts to saturate around 50-100 ng/mL, where it is no longer linear which caused a poor R^2 value of 0.95 which could have been due to limitations in binding sites. By removing points above 50 ng/mL and replotting (Figure 4.26 (c)), a satisfactory R^2 value of 0.988 was achieved and this graph was used to calculate the limit of detection of 2 ng/mL.

The errors were obtained by using the standard deviation of all 50 spectra and demonstrated that the SLISA surface was homogenous as errors within 20% of the average were obtained with the exception of the higher concentrations. Larger errors

are expected at higher concentration of CRP as more NPs are present, hence there is an increased chance of aggregation and hotspots occurring which would give more intense SERRS signals in some areas of the spot, resulting in the larger TMB CTC SERRS spectra obtained which increases the error.

The SLISA was then performed in triplicate and the average CTC spectrum obtained from each spot was then averaged across all three and errors bars obtained were the standard deviation of the three averages. The average CTC SERRS spectrum at each concentration and intensity of 1610 cm^{-1} peak vs concentration of CRP are shown in Figure 4.27.

a)   b)
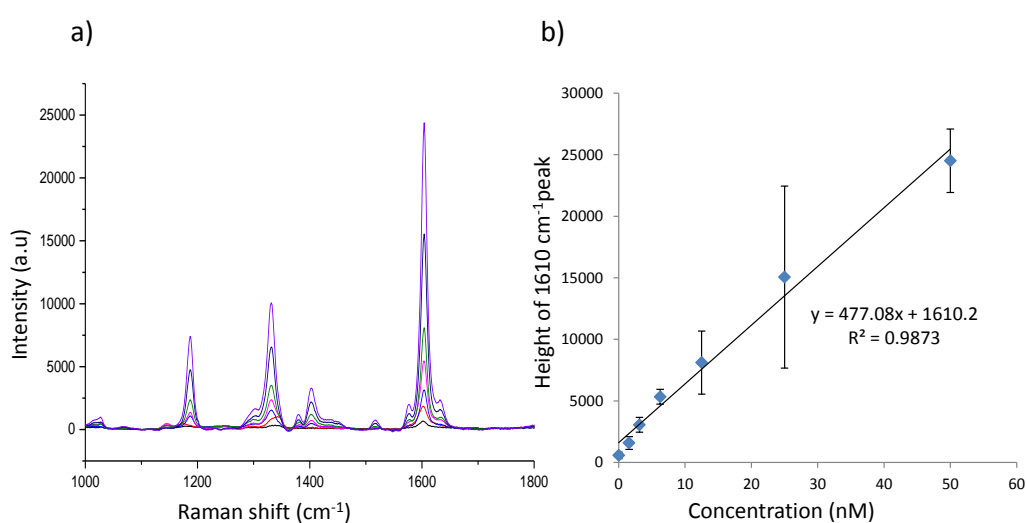
Figure 4.27 (a) CTC SERRS spectra of SLISA spot on epoxy coated glass slide when different concentrations of CRP were added (50 (purple), 25 (dark blue), 12.5 (green) ,6 (pink), 3 (blue), 1.5 (red) and 0 ng/mL (black). Average spectra obtained are from 3 spots where 10 spectra for each spot were taken at different parts of the SLISA spot with a 5x laser objective, 9 second acquisition time and 8 mW laser power (b) Plot of intensity of 1610 cm^{-1} peak plotted against concentrations. Error obtained from the average of three replicates with 10 spectra taken of each.

As shown in Figure 4.27 (a), the same trend was observed as before and higher concentrations of CRP gave rise to a more intense CTC SERRS spectrum as expected. When the intensity of the 1610 cm^{-1} peak was plotted against concentration of CRP, a linear relationship was obtained (Figure 4.27 (b)). The error bars represented the standard deviation of three spots per concentration and a noticeable large error bar associated with the 25 ng/mL concentration was obtained.

To investigate this large error the SLISA spots where imaged using dark field microscopy, and a non-homogenous surface was obtained as shown in Figure 4.28.

| 50 | 25 | 12.5 | 6 | 3 | 1.5 | 0 |

Concentration (ng/mL)
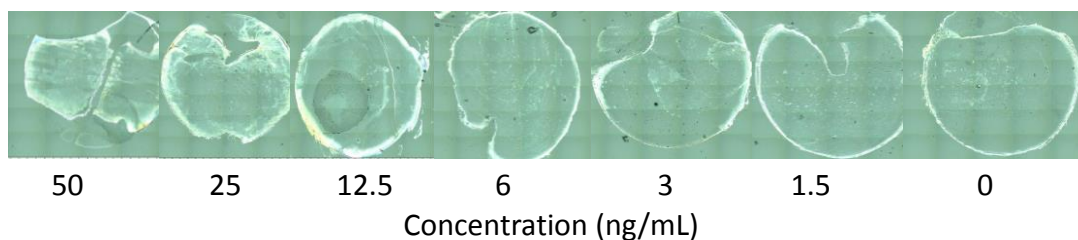
Figure 4.28 Dark field image of SLISA spot with different concentrations of CRP.

The SLISA spots were imaged using dark field at each concentration and from the resulting images, Figure 4.28, it can be seen that a difference in scattering is only noticeable at higher concentrations of CRP (50-12.5 ng/mL) with very little change in intensity between 6 ng/mL and 0 ng/mL. Unlike the images shown in Figure 4.25, the surface appears non-homogenous indicating that the NPS are not evenly distributed across the SLISA spots surface.

This could be due to the oxidation of the epoxy slide and the antibodies not being as efficiently bound to the slide resulting in only a small proportion of the antibodies being immobilised onto the surface whilst the majority were washed away. Therefore when analysing the spots using 633 nm laser excitation, a larger error was obtained due to the inhomogeneous NP concentration across the spot resulting in larger variation and SERRS response within a spot.

Further confirmation of poor binding to the epoxy surface was evident by the coffee ring effect observed in the dark field images. The presence of a bright ring at the edge of the SLISA spot, indicated that the capture antibodies dried around the side of the spot (like a coffee ring) and has not actually conjugated to the epoxy surface.

Due to the non-homogenous SLISA surface caused by the oxidation of the epoxy slides, the SLISA was carried out on nitrocellulose coated glass slides. As well as potentially creating a more homogenous surface, the nitrocellulose coated glass slides are cheaper than epoxy coated slides, reducing the cost of the SLISA.

4.3.3.3 SLISA performed on nitrocellulose coated glass slide

The same SLISA was then performed on a nitrocellulose spin coated glass slide to try and improve the sensitivity and decrease the error within samples with the same concentration. The SLISA was performed with varying concentrations of CRP (25, 12.5, 6, 3, 1.5 and 0 g/mL) and 100 spectra were taken at different areas with a 9 second accumulation time. 100 spectra were taken this time to get a better representation of the TMB oxidation occurring on the spot. To avoid burning the nitrocellulose surface, a 10% laser power (0.8 mV) had to be which limited the signal that could be achieved from the oxidised TMB signal. The results are shown in Figure 4.29.
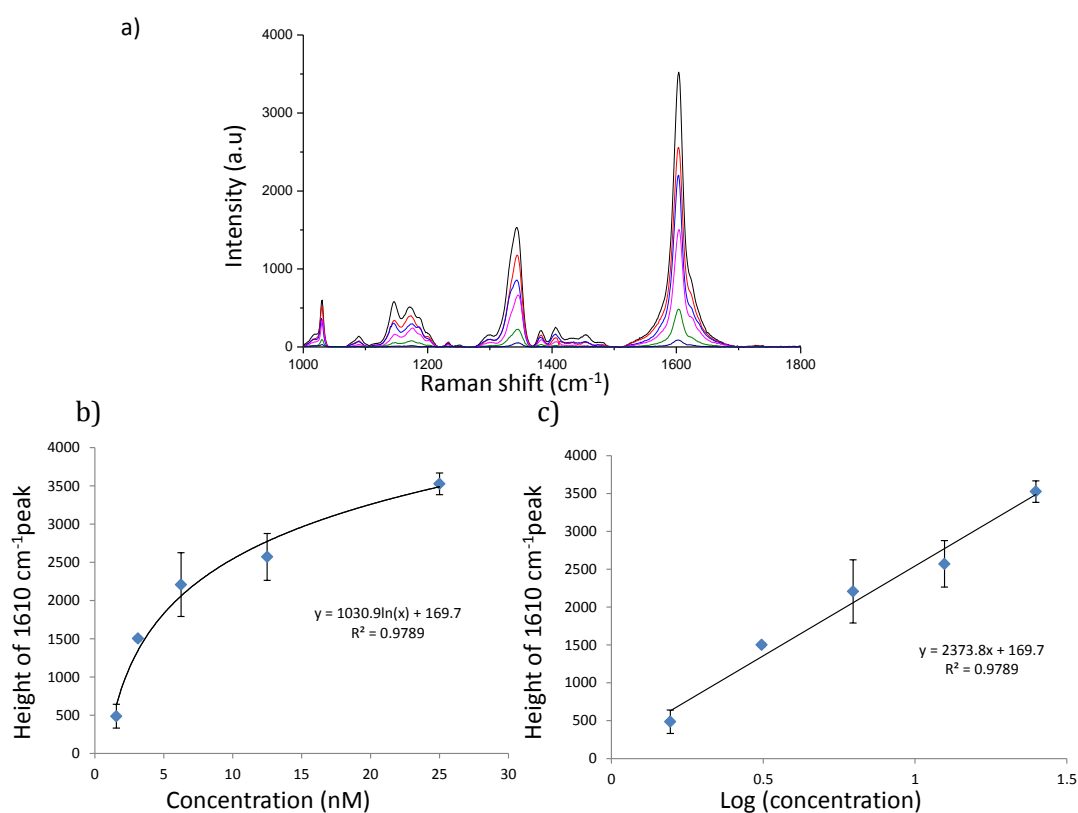
Figure 4.29 (a) CTC SERRS spectra of SLISA spot on nitrocellulose with different concentrations of CRP (25 (dark blue), 12.5 (green), 6 (pink), 3 (blue), 1.5 (red) and 0 ng/m L (black). Average spectra obtained from 100 spectra taken at different locations of each SLISA spot with a 5x laser objective, 9 second acquisition time and 0.8 mW laser power (b) intensity of 1610 cm^{-1} peak plotted against the CRP concentrations. c) Plot of intensity of 1610 cm^{-1} peak plotted against Log$_{10}$ of the CRP concentrations.

As seen in Figure 4.29 (a), as lower concentrations of CRP were added, less Ag NP where present to oxidise the TMB, and a smaller TMB CTC SERRS signal was obtained. When the intensity of the 1610 cm^{-1} peak was plotted against the concentration of the CRP, a logarithmic relationship was observed (Figure 4.29 (b)) which may have been due to the SLISA becoming saturated at the higher concentration which was lower than observed when the SLISA performed on epoxy coated glass slide which appeared saturated after 50 ng/mL. The difference in saturation concentration may be due to the more efficient binding of the capture antibody to the nitrocellulose surface, hence higher concentrations of Ag NPs are present, making it harder to differentiate between higher concentrations of CRP.

When the intensity of the 1610 cm^{-1} peak was plotted against the Log_{10} of the CRP concentration the resulting linear graph in Figure 4.29 (b) was obtained and the limit of detection was calculated to be 1 ng/mL. Error bars were obtained by taking 100 spectra of each spot, averaging and taking the standard deviation of the three. Due to the error being between ± 20% of the average and a lower limit of detection being achieved, the SLISA performed on nitrocellulose was deemed to be more sensitive and reproducible when performed on the epoxy coated glass slide. Overall, the SLISA has demonstrated the sensitive and quantitative detection of CRP, without the need for a conventional enzyme and is comparable to LODs that have been achieved using fluorescence, [151] colorimetric,[152] and electrochemical detection[152] which have been reported between 1-2 ng/mL.

A spot from each concentration was then mapped using 638 nm laser excitation to visualise the change in intensity of the CTC on and off the spot and with lowering concentrations. Each SLISA spot was mapped using a 5x objective lens, with 25 μm step size with an area of 58x47 mm. A false colour image monitoring the intensity of the 1610 cm^{-1} peak of each spectrum in the map was created and is shown in Figure 4.30.
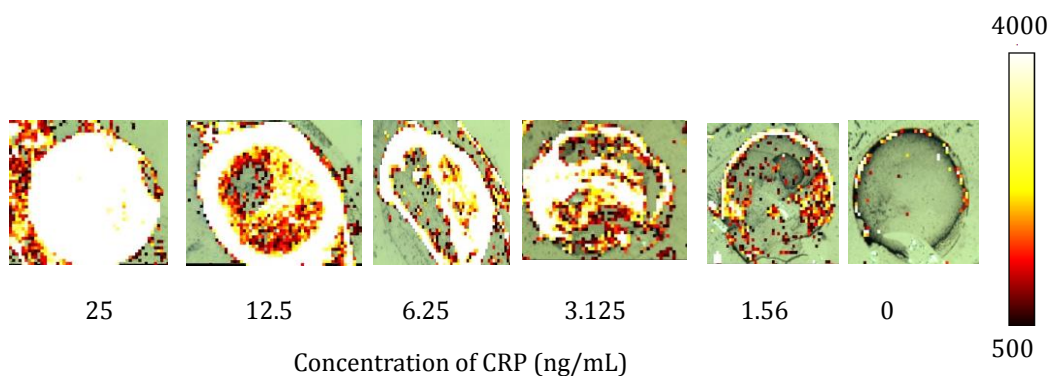
Figure 4.30 White light image of SLISA spot on nitrocellulose produced when different concentrations of CRP were added to the assay with false colour SERRS image of SLISA spot superimposed from SERRS map of the 1610 cm^{-1} peak for different concentration of CRP. Mapping took place using a 5x laser objective, 638 nm laser excitation, 1 second acquisition time and 0.8 mW laser power.

The false colour SERRS images in Figure 4.30, provided additional information about the decrease in oxidation of the TMB as the concentration of CRP decreased. By setting the intensity of the 1610 cm^{-1} peak to be the same at every concentration, a clear decrease in intensity of the white pixels, which represented a spectra with a high oxidised TMB signal, was visible. There is also a clear difference between the signal on and off spot, which confirms that the oxidised TMB signal is confined to the SLISA spot and oxidised due to the presence of the Ag NP bound to the spot.

To further quantify this, the maps were analysed in Matlab and the number of spectra with intensity above 800 a.u for the 1610 cm^{-1} peak was obtained. An intensity of 800 a.u was chosen as it showed the biggest change between concentrations. The bar graph in Figure 4.31 indicates the number of spectra with an intensity above 800 a.u in each map.
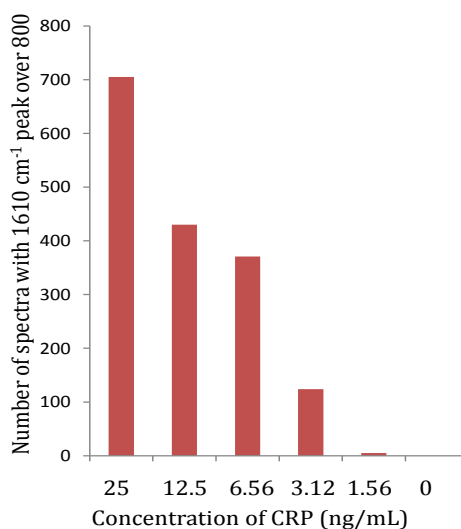
Figure 4.31 Bar graph indicating change in the number of spectra with a 1610 cm^{-1} peak with an intensity above 800 a.u for each SLISA map when different concentrations of CRP were added.

It is clear from the bar graph in Figure 4.31, that the number of spectra with an intensity above 800 a.u for the peak at 1610 cm^{-1} decreases as lower concentration of CRP were added to the SLISA. This was to be expected and was further clarification that lower concentrations of Ab-Ag NP bound to the SLISA as the CRP concentration decreased and a lower amount of TMB could be oxidised. When 0 ng/mL of CRP was added, there were no spectra with a 1610 cm^{-1} peak above 800 a.u. confirming that non-specific binding did not occur.

Although more data was collected in the mapping of the SLISA spot, the long mapping times (1 hour and 15 minutes per spot) limited the analysis that could be completed in a single day. It was therefore deemed that as the same outcome was achieved for the 100 spectra analysis of each spot (which took 11 minutes to complete per spot) along with small error bars that this analysis method was suitable to keep in tone with the fast SLISA completion.

4.3.3.4 SLISA selectivity

The selectivity of the SLISA was investigated by performing the SLISA with different biomolecules to ensure that Ab-Ag NPs and the oxidised TMB signal were only present when CRP was added.

The SLISA was repeated as described in section 4.3.3.3 with BSA, human chorionic gonadotrophin (hCG), an antigen used in lateral flow pregnancy tests and CRP (25 ng/mL) acting as a control. The surface of the SLISA spot was then interrogated 100 times at different areas and an average of the spot when each biomolecule was present was obtained. The results are shown in Figure 4.32.
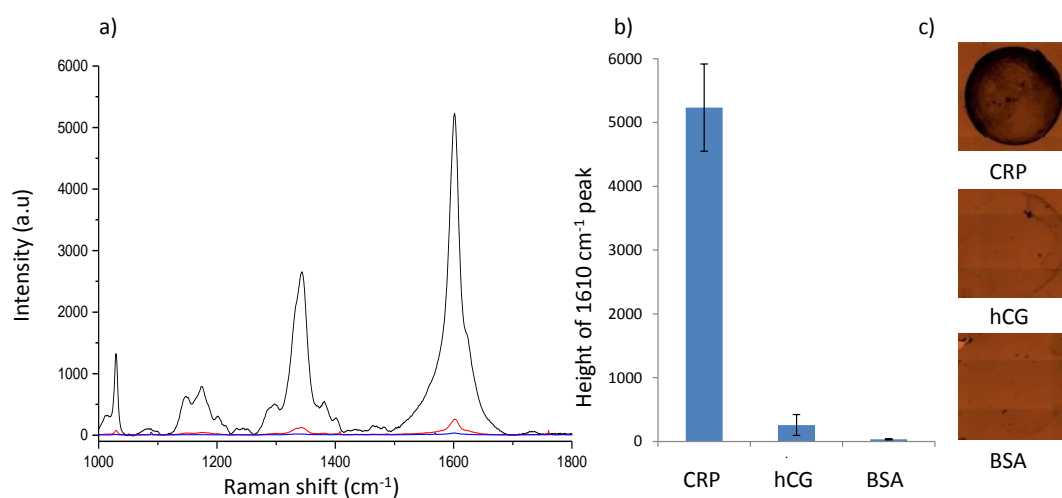
Figure 4.32 (a) CTC SERRS spectra of SLISA spot on nitrocellulose when CRP (black), hCG (pink) and BSA (blue) was added (b) Bar graph showing the change in intensity of the 1610 cm^{-1} peak when each biomolecule was added and (c) white light image of SLISA spot when each biomolecule was added. Spectra and error bars obtained from average of three samples. Spectra obtained using 638 nm laser excitation, with a 5x laser objective, 1 second acquisition time and 0.8 mW laser power.

When CRP was added to the SLISA, as expected, an intense SERRS spectrum of the CTC was obtained as the CRP had bound to the capture antibody, which allowed the Ab-Ab NPs to then bind to the CRP and in turn oxidise the TMB (Figure 4.32 (a) black spectrum). When BSA and hCG were added, little TMB oxidation took place as there was a low concentration of Ag NPs present in the SLISA. This therefore confirmed that the SLISA was selective for CRP as the other biomolecules did not bind to surface of the capture antibody or the nitrocellulose. The selectivity is also visualised in the change in the SLISA spots (Figure 4.32 (c)) and only CRP gave the appearance of bound NPs to the capture

133

antibody spot. The spots obtained when BSA and hCG were added were very hard to visualise as little Ab-Ag NPs bound to the surface, again confirming the selectivity.

4.3.3.5 CRP detection in serum

Due to the SLISAs success at detecting low concentrations of CRP when diluted in PBS, the detection of a biologically relevant CRP concentration in serum was investigated.

The SLISA was performed, as described in section 4.3.3.3, replacing CRP diluted in PBS with a solution of 100 ng/mL of CRP which was spiked into 1 % seraSub. SeraSub is a synthetic polymer in buffered solution which is physically equivalent to serum and plasma with respect to specific gravity, viscosity and osmolality.[153] A control of 1 % seraSub was applied to the SLISA as a control. The resulting spots were analysed with 633 nm laser excitation and 100 spectra were taken at different areas with a 9 second accumulation time to achieve an average of each spot. The oxidised TMB spectra, bar chart of intensity of 1610 cm^{-1} peak and white light image of spot from the SLISA with and without CRP are shown in Figure 4.33.
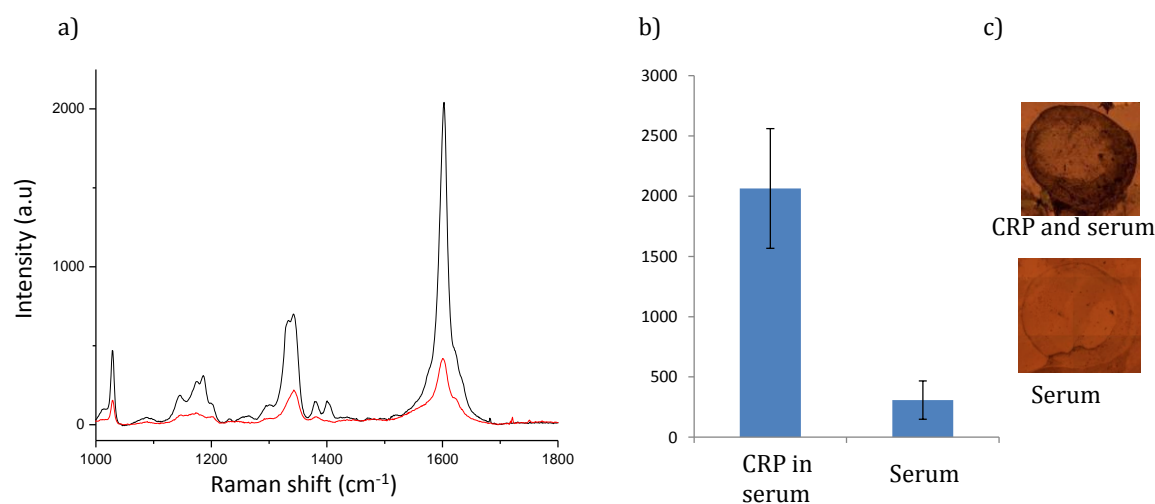
Figure 4.33 (a) Average CTC SERRS spectra of SLISA spot on nitrocellulose when CRP in serum (black) and serum (red) was added. (b) Bar graph showing the change in intensity of the 1610 cm^{-1} peak with or without CRP. (c) White light image of SLISA spot with or without CRP. Spectra and error bars obtained from average of three samples. Spectra obtained using 638 nm laser excitation, with a 5x laser objective, 1 second acquisition time and 0.8 mW laser power.

Figure 4.33 (a) indicates that CRP can be detected in 1 % serum as there is a clear difference in oxidised TMB spectra and resulting SLISA spot when performed with and without CRP. By spiking 100 ng/mL of CRP in 1% serum, it can be deduced that 10 μg/mL of CRP can be detected in a 100% serum sample. A concentration of 10 μg/mL of CRP in serum is considered a high concentration and therefore the body would be in a state of inflammation.[153] It should be noted that the oxidised TMB signal is lower than expected in serum. This is probably due to the components of the serum blocking sites on the capture antibody spot, which could lower the amount of CRP and Ab-Ag NPs that can bind to the capture antibody spot. There is also an increase in signal obtained for the blank as Ag NPs may be binding to components in the serum which are immobilised onto the nitrocellulose surface and are therefore present to oxidise the TMB.

Despite the lower signal, the SLISA can be used to detect CRP at a clinically relevant concentration and matrix. Future work would include a limit of detection study run in seraSub, however it should be expected that this would give an LOD much higher than CRP diluted in PBS due to the reduced oxidised TMB signal in serum.

4.3.3.6 SLISA performed on lateral flow strip

The SLISA performed on a surface decreased incubation times needed for an ELISA performed in solutions. However, to shorten the time scale of the SLISA even further, it was performed on a lateral flow assay (LFA) strip. As already discussed, the LFA is a fast and cheap method for the detection of antigens. LFA was previously used in section 4.3.2 to confirm the presence of antibody on the Ag NP by spotting a high concentration of CRP directly on the nitrocellulose of the strip. However, by changing the format the LFA can also be used to detect antigens in a solution. To achieve this, capture antibody can be spotted onto the nitrocellulose strip and let to dry. The antibody conjugates are then loaded on to the sample pad and the strip placed in HEPES buffer, which is spiked with the antigen to be detected. The buffer then flows along the strip and the conjugates bind to antigen in the flow solution. The conjugates bonded to the antigen flow along the nitrocellulose strip and complete the sandwich assay when they come into contact

with the spotted capture antibody.[154] Figure 4.34 shows a schematic of the LFA for the detection of antigens.
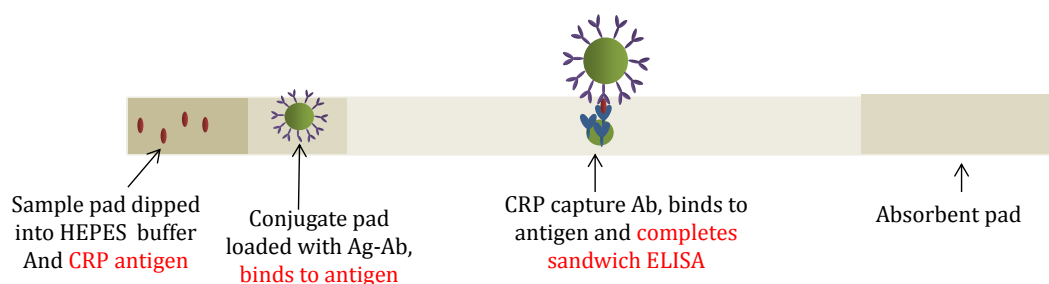
Figure 4.34 Diagram of LFA, highlighting main areas of interest. Capture antibody is first spotted on the nitrocellulose strip and left to dry. The conjugate pad is loaded with NPs coated wth antibodies. The strip is then placed, sample pad first. in buffer which has been spiked with the anigen to be detected. The buffer flows through the strip onto the conjugate pad which allows the NP to bind to the antigen and join the flow. When the conjugates bound to antigen flow over the captre antibody spot, the antigen bind to the capture antibodies, therfore completing the sandwich assay.

0.3 µL of two different capture antibody concentrations (360 µg/mL and 100 µg/mL) were spotted onto the nitrocellulose part of the lateral flow strip and left to dry. 10 µL of Ag-Ab NP conjugate were then applied to the sample pad and the strip placed in 100 µL of HEPES buffer which had been spiked with 100 µg/mL CRP. The HEPES and CRP solution then started the capillary action and flowed through the strip and onto the sample pad containing the Ag-Ab NPs. The CRP should then bind to the Ab-Ag NPs and flow onto the nitrocellulose strip. When Ag-Ab-CRP HEPES solution meets the antibody spotted on the strip, the CRP binds to the spotted antibody therefore immobilising the Ag NPs onto the antibody spot, completing the SLISA. An Ag NP spot is therefore present where the antibody was originally spotted confirming the presence of CRP. The image in Figure 4.35 shows the resulting spots obtained after the SLISA was performed when 100 µg/mL of CRP present and 0 µg/mL of CRP was spiked into the HEPES buffer.

a) | 360 µg/mL of antibody spotted | | 100 µg/mL CRP

0 µg/mL CRP

b) | 100 µg/mL of antibody spotted | | 100 µg/mL CRP

0 µg/mL CRP
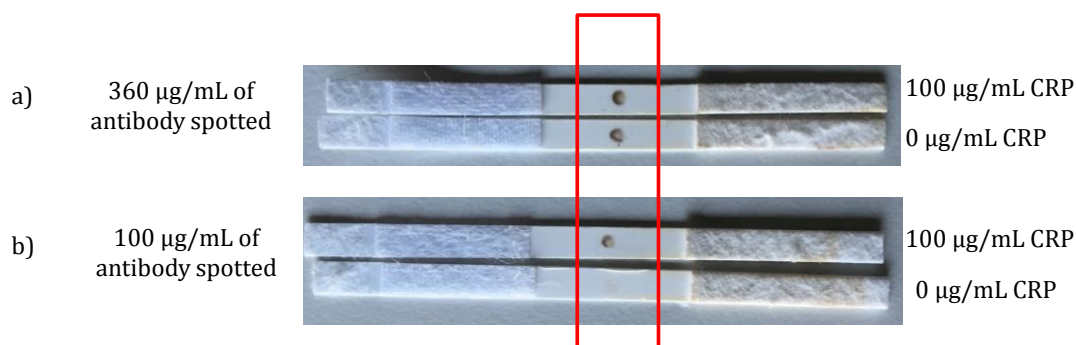
Figure 4.35 SLISA performed on lateral flow strip when (a) 360 µg/mL of capture antibody was spotted onto the LFA strip in the presence and absence of CRP and (b) 100 µg/mL of capture antibody spotted on LFA with and without CRP.

The image in Figure 4.35 (a) indicates that when 360 µg/mL of capture antibody was spotted onto the nitrocellulose strip and 0 and 100 µg/mL CRP used in the SLISA, a spot appeared on both strips therefore non-specific binding occurred. This was expected and agreed with the previous findings that high antibody concentration resulted in binding between the free Ag NP surface and Ab causing false positives. The concertation of the antibody spot was therefore reduced to 100 µg/mL and the SLISA repeated with or without CRP. In this SLISA, a spot appeared when CRP was present and no spot was visible when CRP was not added, hence CRP was successfully detected.

This was not in agreement with the previous findings which suggested that 100 µg/mL of spotted antibody lead to non-specific binding between it and the Ag–Ab NPs. However, in the LFA there is a difference in time that the Ag-Ab NPs are in contact with the capture antibody due to the flow of the solution through the nitrocellulose strip. The time the Ag-Ab NP were in contact with the antibody is very low (seconds). Compared to the 20 minutes incubation used in the surface based SLISA, it is therefore clear there is a reduction in non-specific binding due to the reduced incubation time.

Once the lateral flow strip had dried, it was placed in 100 µL of TMB blotting solution which flowed through the strip via capillary action. When the TMB solution reached the Ag NP spot, the TMB should be oxidised to the CTC which is then electrostatically attracted to the Ag NP surface. Unoxidised TMB should then continue to flow through the strip to the sample pad.

To confirm that the Ag NP oxidised the TMB to the CTC and that the CTC signal was confined to the Ag NP spot, the section of the strip that contained the Ag NP spot was analysed by mapping the surface using 633 nm laser excitation. Figure 4.36 shows the resulting Ag NP spot imaged using a 5x objective lens and the false colour image created by monitoring the intensity of 1610 cm^{-1} peak of the CTC from the spectra obtained from the map.
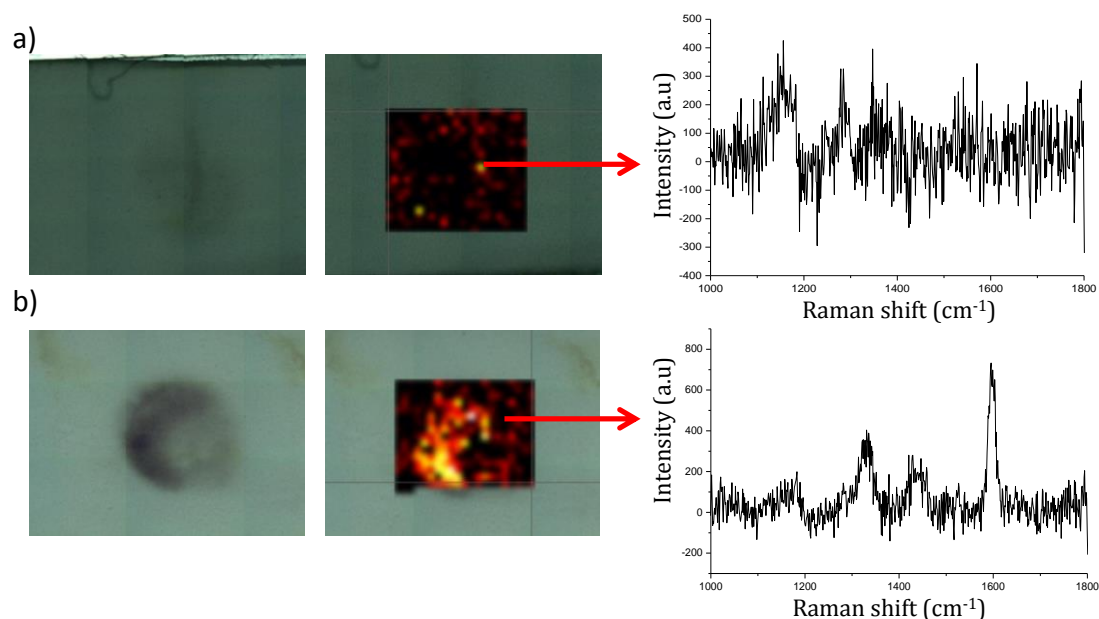
Figure 4.36 (a) White light image of SLISA spot with no CRP, false colour image created by monitoring 1610 cm^{-1} peak and spectrum associated from map. (b) White light image of SLISA spot with 100 μg/mL of CRP, false colour image created by monitoring 1610 cm^{-1} peak and spectrum associated from map. Surface mapped using a 633 nm laser excitation with a 9 second acquisition time and 0.8 mW laser power. Spectrum were baseline corrected using intelligent fir on WiRE software.

There was no CTC SERRS spectra present in the map where no CRP was added (Figure 4.36 (a)) therefore suggesting that little non-specific binding had occurred. The map obtained from the strip that was detecting CRP (Figure 4.36 (b)), indicated the presence of the CTC due to the yellow pixels, hence enough Ag NPs were bound to the CRP and able to catalyse the oxidation. The signal however was very low, with an intensity count below 800 a.u obtained. This was likely due to the flow of the TMB solution along the lateral flow strip which limited the contact between the Ag NP and TMB, hence shortening the time available for the catalytic reaction to occur and increase generation of the CTC of TMB.

The result indicated that the SLISA could be adapted and used in a lateral flow assay for the detection of CRP at high concentrations. By applying the LFA the time taken to run and analyse the SLISA was much shorter and the low cost of lateral flow strips compared to the nitrocellulose coated glass slide made this approach attractive. However, as a result of the shorter incubation times in the LFA, the signal generation of the CTC was much lower resulting in much lower SERRS responses. However, with more optimisation, the LFA SLISA could be improved and a limit of detection could be achieved.

4.4 Conclusion

Ab-Ag NPs were used to replace enzymes used in ELISAs to create a silver nanoparticle linked immunosorbent assay for the detection of CRP. For Ag NPs to be included in the SLISA their catalytic activity when functionalised with biomolecules had to be investigated and it was determined that when Ag NPs were functionalised with high concentrations of $CT(PEG)_{12}$ that their catalytic activity decreased. This was due to the decrease in the concentration of H_2O_2 which could be broken into free radical and go on to oxidise TMB to the CTC. However, as PEG-Ag NPs did retain some of their catalytic activity, antibody conjugation to Ag NPs was investigated via covalent, directional and physical methods and their catalytic activity compared with the addition of TMB and H_2O_2 and analysing using Raman spectroscopy. It was determined that physical conjugation was not only the easiest conjugation method, it also allowed for the greatest TMB oxidation and was used in the SLISA.

Due to Ab-Ag NPs retaining their catalytic activity, they were used in the SLISA which was optimised by investigating different aspects which could affect the non-specific binding leading to a higher LOD. For instance, when a large volume and high concentration of antibody were applied to the SLISA, non-specific binding was observed, hence a low volume and capture antibody concentration (0.3 μL, 10 μg/mL) was immobilised onto the surface. The incubation of the Ag-Ab NPs was also investigated and it was determined that long incubation times (1 hour) also lead to non-specific binding and had to be decreased to 20 minutes.

Once the SLISA was optimised, it was carried out on epoxy and nitrocellulose coated glass slides by varying the concentration of CRP. As lower concentrations of CRP were added, less Ab-Ag NPs were present on the SLISA spot. This lead to a

decrease in oxidised TMB signal and LODs of 1-2 ng/mL were obtained. . Clinically relevant CRP concentrations in serum could also be detected using the SLISA and although poorer oxidised TMB signal were obtained due to the complicated matrix, 10 µg/mL of CRP was detected in serum which is indicative of inflammation present in the body.

Furthermore, the SLISA could be applied to other formats such as a lateral flow assay which provided a quick and fast detection method, dramatically reducing the time scale of the SLISA. Only a high concentration of CRP was detected, with a very low oxidised signal as the TMB blotting solution could not be left on long enough to allow the Ag NPs to oxidise the TMB as much as it can on the nitrocellulose or epoxy surface SLISA. However, the possibility of using Ag NPS and TMB in LFA could be achieved with more optimisation and a satisfactory limit of detection in a short time scale could be obtained.

Overall, the SLISA could detect low concentrations of CRP in PBS and clinically relevant concentrations of CRP in biological matrices. By using the SLISA set up the incubation times of CRP and Ab-Ag NPs were lowered to 20 minutes each. When comparing this to the two hours needed for each CRP and Ab-HRP in an ELISA it is clear that the time scale has been significantly lowered and the assay, along with analysis, could be carried out in the working day. The limit of detection of 1 ng/mL also rivalled conventional ELISA detection methods such as fluorescence, [151] colorimetric,[152] and electrochemical detection[152] which have been reported between 1-2 ng/mL. These method all utilise enzymes, which can be expensive, difficult to isolate and can require difficult conjugation to antibodies, therefore by using Ag NPs the cost of the SLISA can be significantly reduced as NP can be made relatively cheap, synthesised in bulk and Ab-Ag NPs can be prepared with the simple passive conjugation method. The SLISA can also be applied to other clinically relevant antigens and the SERRS readout could potentially lower the limits of detection.

5. Detection of oxidative stress in cells

5.1 Introduction

5.1.1 Metal nanoparticles and cells

Metal NPs and their interaction with cells has become an increasingly interesting area of research due to the unique optical properties and chemical stability of NPs which make them ideal probes for studying biological systems.[155] As already discussed, metal NPs have excellent scattering properties allowing the visualisation of individual nanoparticles which can be used to monitor their position within a cell and their interaction with cellular components.

NPs with sizes of 50-200 nm can be uptaken into cells by a variety of different mechanisms.[156] The introduction of NPs into cells predominantly occurs via endocytosis, in which the NPs are engulfed by the plasma membrane.[157] After it has been engulfed, a portion of the membrane that surrounds the NPs detaches, resulting in endosome formation. The NPs have to escape from the endosome in order to reach other parts of the cell or they could be removed. Surface modification can also aid the uptake into cells and by functionalising NPs with positively or negatively charged ligands they can interact with membrane receptors and cross the membrane barrier.[158]

Once NPs have been uptaken up into a cell they can be analysed using SERS, and the first SERS measurements within a cell were carried out by Nabiev *et al*. in 1991.[159] They reported the incubation of unlabelled Ag NPs with living cancer cells and could detect the presence of the antitumor drug doxorubicin in the nucleus and cytoplasm using SERS. Since this initial study, a variety of biological markers have been detected such as monitoring cellular functions,[160] stress response[161] and cell death.[162]

Cell-based SERS can be achieved by using label free metal NPs, which can give a SERS signal based on the cellular medium surrounding the NP or by NP functionalisation with a Raman reporter and targeting molecule, which will give a strong SERS signal indicating its location in the cell. When NPs are functionalised

with a Raman reporter, SERS can be used to monitor and study the uptake of NPs into living cells and by adding a specific recognition molecule can target specific sites within the a cell. Recently, Zhai *et al*. reported Ag NP functionalised with beta-cyclodextrin (CD) modified with para-aminothiophenol (p-ATP) and folic acid (FA).[163] When incubated into a cell the FA has a very high affinity for folate receptors which are over expressed in cancer cells. Therefore SERS can be used to monitor the NPs entering the cell by endocytosis and targeting folate receptors. As a result, the Ag NP could be used as a SERS probe to monitor the effect of folate receptor targeted drugs, by quantifying the number of NPs entering the living cell before and after drug administration thus monitoring the drug effect of the drug on the cancer cell.

As well as targeting specific sites on a cell and using the Raman reporter to quantify the number of NPs present, the addition of a reporter to NPs can also be used to investigate a variety of mechanisms that occur within the cell. For example, Au NPs can be functionalised with the molecule 5-bromo-4-chloro-3-indolyl-β-D-galactopyranoside (X-Gal) which yields a minimal SERS signal.[164] However, the dimerised hydrolysis product, which is produced by β-galactose activity, gives a strong SERS peak at 598 cm^{-1}. The Au-X-Gal NPs were incubated with and taken up by macrophage cells and following washing and cell fixation to a cover slide were then analysed using 633 nm laser excitation. A Raman map was the obtained, based on the major peak at 598 cm^{-1}, indicated the presence of the X-Gal dimerised hydrolysis product and therefore the presence of β-galactose activity. Figure 5.1 indicates the change in SERS response due to X-Gal hydrolysis to its SERS active product and the resulting SERS map indicating the presence of it inside a cell.

Figure 5.1 (a) X-Gal undergoing hydrolysis with β-galactose to produce the SERS active dimerised hydrolysis product 5,5'-dibromo-4,4'-dichloro-indigo and (b) intracellular SERS detection. The bright field image (left) shows the location of the cells and the Raman signal obtained outside the cell and the false colour image (right) indicates the presence of the hydrolysis product due to the 598 cm^{-1} peak inside the cell and the accompany Raman spectrum.[164] Adapted from Stevenson, R., et al., *Analysis of intracellular enzyme activity by surface enhanced Raman scattering.* Analyst, 2013. **138**(21): p. 6331-6336. Published by from The Royal Society of Chemistry.

Raman reporters have also been used as pH sensors in cells which is significant as the extracellular matrix, cytoplasm, nucleus and other membrane bound organelles such as lysomes vary in pH.[165] Ag NPs have been functionalised with 4-mercaptobenzoic acid (4-MBA) which gives a change in SERS response to due to the pH of its surrounding environment and is sensitive in the pH range 6-8. Ag-4-MBA NPs were incubated with Chinese Hamster Ovary (CHO) cells by passive uptake and analysed using 633 nm laser excitation. The resulting SERS spectra indicated that the pH surrounding the NP was below 6 and it could therefore be deduced that the NPs were located inside a lysome (pH of roughly 5).

5.1.2 Oxidative stress

A major issue associated with cells is oxidative stress, which is due to the elevated levels of reactive oxygen species (ROS).[166] ROS are bi-products of cellular metabolism and detoxified by antioxidants. However, when the production of ROS overwhelms a cells antioxidant capacity, this leads to an imbalance and damage to the DNA, proteins or lipids occurring as the ROS sequesters electrons from important cellular components in order to become stabilised.[167] This, in turn, destabilises the cell component molecules which then seek and take an electron from another molecule, therefore triggering a chain of free radical reactions.[168]

ROS are radical ions or molecules that have a single unpaired electron in their outermost shell of electrons and are therefore highly reactive. Examples include; hydroxyl radicals ($^{\bullet}OH$), superoxide ($O_2^{\bullet-}$), nitric oxide ($NO^{\bullet}$), organic radicals ($R^{\bullet}$), peroxyl radicals ($ROO^{\bullet}$), alkoxyl radicals ($RO^{\bullet}$), thiyl radicals ($RS^{\bullet}$), sulfonyl radicals ($ROS^{\bullet}$), thiyl peroxyl radicals ($RSOO^{\bullet}$), and disulfides ($RSSR$).[169]

ROS in cells can be detected using various methods with the most common being fluorescence spectroscopy. These methods generally involve staining the cell with fluorophores such as 2',7' –dichlorofluorescin diacetate (DCFDA), a fluorogenic dye that measures hydroxyl, peroxyl and ROS's within the cell.[169] SERS has also been used for ROS detection, for example, the ROS superoxide anion radical ($O_2^{\bullet-}$) has been detected by functionalising oxidised cytochrome c (Cyt c) onto Au NPs which can gives different SERS signals depending on whether it is in its oxidised and reduced form.[170] The nanosensor was delivered into live HeLa cells and normal human liver cells and the cells were analysed using 532 nm laser excitation to monitor changes in the SERS signal obtained from oxidised or reduced Cyt c to calculate the concentration of $O_2^{\bullet-}$. This could lead to a greater understanding of oxidative-stress related diseases at a cellular level.

By applying SERS for the detection of ROS, it could be possible to detect lower concentrations of ROS within a cell. This chapter focuses on applying the catalytic activity of Ag NPs and their ability to oxidise TMB in the presence of H_2O_2, a common ROS found in cells. This could therefore potentially detect the presence of ROS in cells by analysing the SERS signal obtained from the oxidation of TMB to the CTC.

5.2 Aim

The aim of this chapter was to use Ag NP and their ability to catalyse the oxidation of TMB to detect oxidative stress in cells. As already investigated in section 3.3, when H_2O_2 is added to TMB and Ag NPs, the TMB can be oxidised to its CTC which gives a very characteristic SERRS signal. Therefore, by incubating Ag NPs and TMB into a cell, ROS's, such as H_2O_2 and OH radical, would be present if the cell was under oxidative stress and could oxidise TMB to the CTC in the presence of the Ag NP. The cell could then be Raman mapped using 633 nm laser excitation and false colour images produced by using the 1610 cm^{-1} peak of the CTC. This would therefore determine the location of NP and the CTC within the cell indicating that ROS species are present and the cell is under stress. Figure 5.2 shows the proposed TMB oxidation to the CTC that occurs when in the Ag NPs and TMB come into contact with a ROS, the characteristic CTC SERRS signal and the false colour SERS image showing the location of the Ag NP and CTC within a single cell.
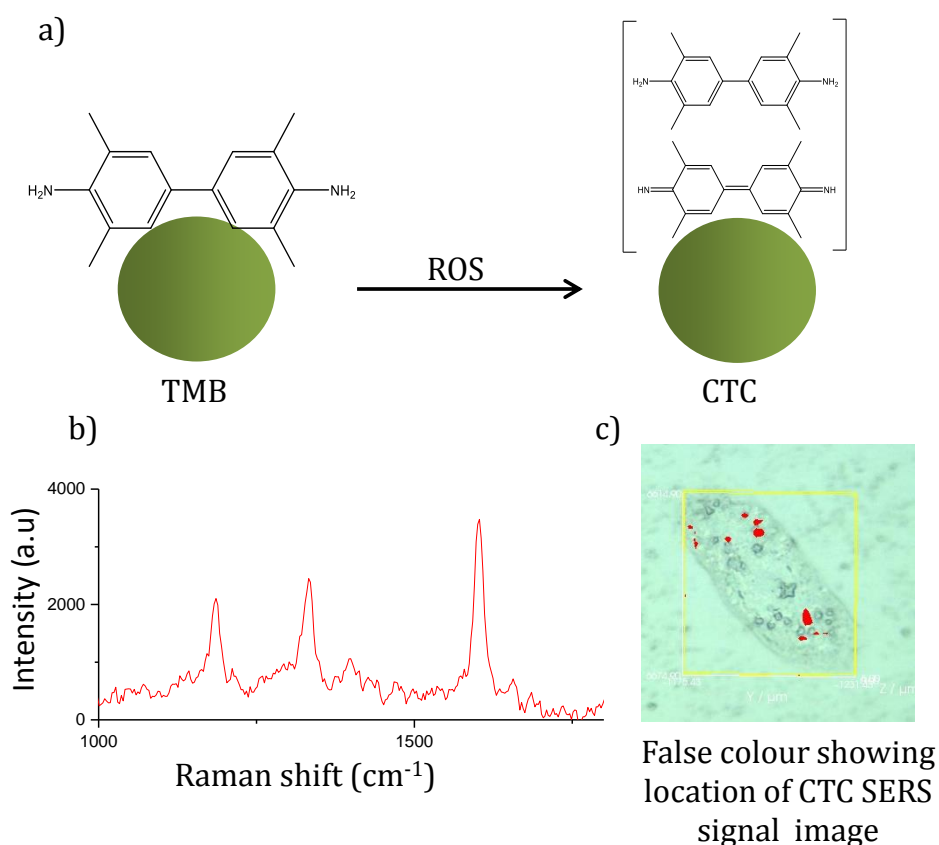
Figure 5.2 (a) Oxidation of TMB in the presence of Ag NPs and H_2O_2 to the CTC. (b) SERRS spectrum of CTC and (c) False colour image showing location of CTC within the cell (red), produced by mapping 1610 cm^{-1} peak overlaid on white light image of cell.

5.3 Results and discussion

As seen in chapter 3, Ag NPs can catalyse the oxidation of TMB in the presence of H_2O_2. Therefore, it is proposed that by incubating cells with Ag NPs and TMB that oxidative stress within the cellular environment could be monitored using SERRS.

5.3.1 Silver nanoparticle incubation

First, the incubation of 70 nm Ag NPs were investigated to analyses the SERS signal that are obtained from bare Ag NPs. Ag NPs (200 μL, 0.3 nM) were added to 30×10^4 human prostate cancer cells (PC3) in 2 mLs of cell media and left to incubate for 14 hours to allow the NP to be taken up by the cells. The cell media was then removed and the cells that immobilised onto a glass coverslip were washed twice with sterile PBS and the cells were then fixed using 4 % formaldehyde. The formaldehyde was removed after 15 minutes and the coverslip was washed once more with sterile PBS and sterile water. The cells were then 3D Raman mapped with a volume of 38x34x6 μm and a 1.5 μm step size, to confirm whether the NPs had been taken up by the cell. All spectra in the 3D Raman map were baselined using intelligent fitting by WiRE and underwent cosmic ray removal. All cell maps in this chapter were treated this way.

It was expected that the introduction of Ag NPs into the PC3 cells would result in cellular components within the cell being surface enhanced when they were in close proximity to the Ag NP surface. False colour images were created which highlighted areas of the cell which represent common cellular components. All the spectra in the 3D map were analysed for peaks within a certain range of wavenumbers which represented the cellular components of amino acids (1412-1425 cm^{-1}), CH wagging from proteins and lipids (1426-1472 cm^{-1}) and phenylaniline (998-1008 cm^{-1}).[171] These components were selected as they are found throughout the cell and also proteins and lipids are an integral component of the cell membrane.

To confirm that the Ag NPs were actually inside the cell and the resulting spectra were due to Ag NPs enhancing cellular components inside the cell and not just components on the cell surface, false colour images were created for 3 different layers of the maps z axis (0 μm, 3 μm and 6 μm in depth). The resulting maps and a composite map, which was a combination of the false colour images from all layers in the z axis (6 in total) are shown in Figure 5.3 along with a schematic of the 3D

map. It should be noted that enhanced spectra were only obtained from the location where the NPs end up and no Raman signals were obtained from PC3 cells without the addition Ag NPs.
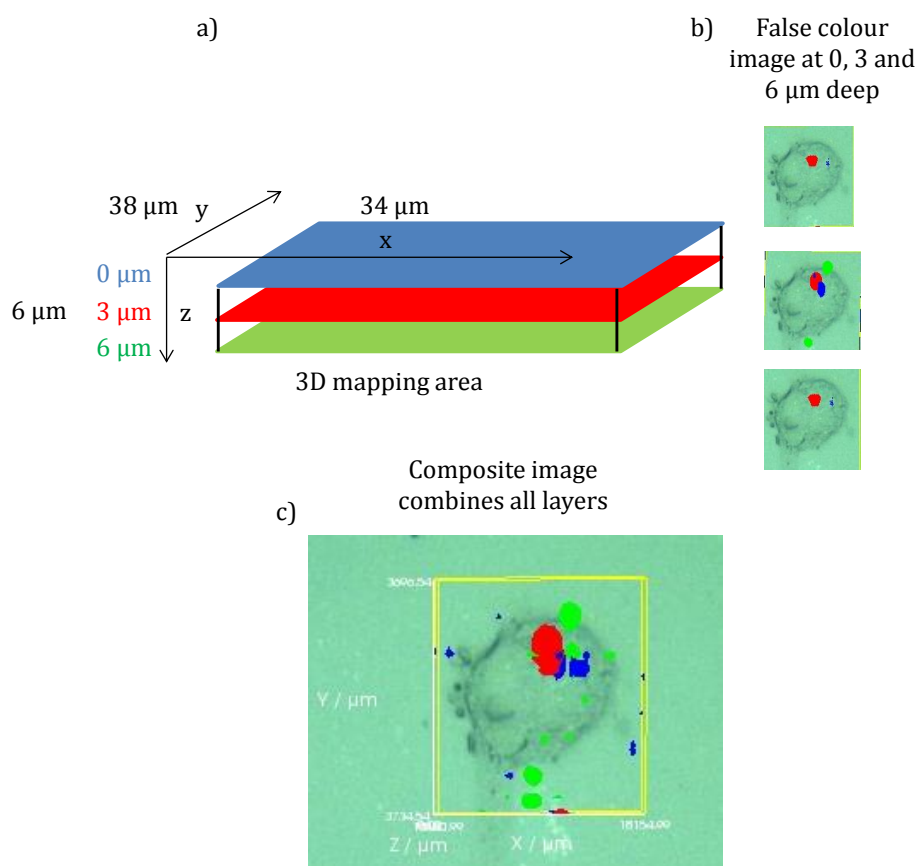
Figure 5.3 (a) Schematic showing the volume of cell which was 3D mapped and z layers at depth 0 (blue), 3 (red) and 6 (green) which produced the false colour images in (b). False colour image representing areas were amino acids (red) CH wagging from proteins and lipids (green) and phenylalanine (blue) were present. (c) Composite false colour image comprised of all 6 z layers of the map. The cells were 3D mapped with a volume of 38x34x6 μm with a 1 μm step size using 633 laser excitation, with 1 second acquisition and 0.8 mW laser power

Figure 5.3 (a) shows the volume of the cell that was mapped and the depth in the z axis which resulted in the false colour images in Figure 5.3 (b) from 0 μm, which is from the top of the cell where it was focuses, 3 μm is the middle and 6 μm is the bottom of the map, but does not represent the bottom of the cell as the cell is thicker than 6 μm. The coloured pixels in the false colour image indicated the presence of a peak within the range of wavenumbers suggesting the cellular component was present. The coloured pixels are also present at each depth of the cell which

suggested that the enhanced signals were coming from these components inside the cells. The composite image in Figure 5.3 (c) combines each layer of the z axis and gives indication of the presence of the cellular components throughout the cell.

The analysis of cellular components was repeated on another set of PC3 which had been incubated with Ag NPs and the resulting spectra analysed. Figure 5.4 shows the composite false colour images created when mapping each cellular component and the resulting spectra obtained from the cell.
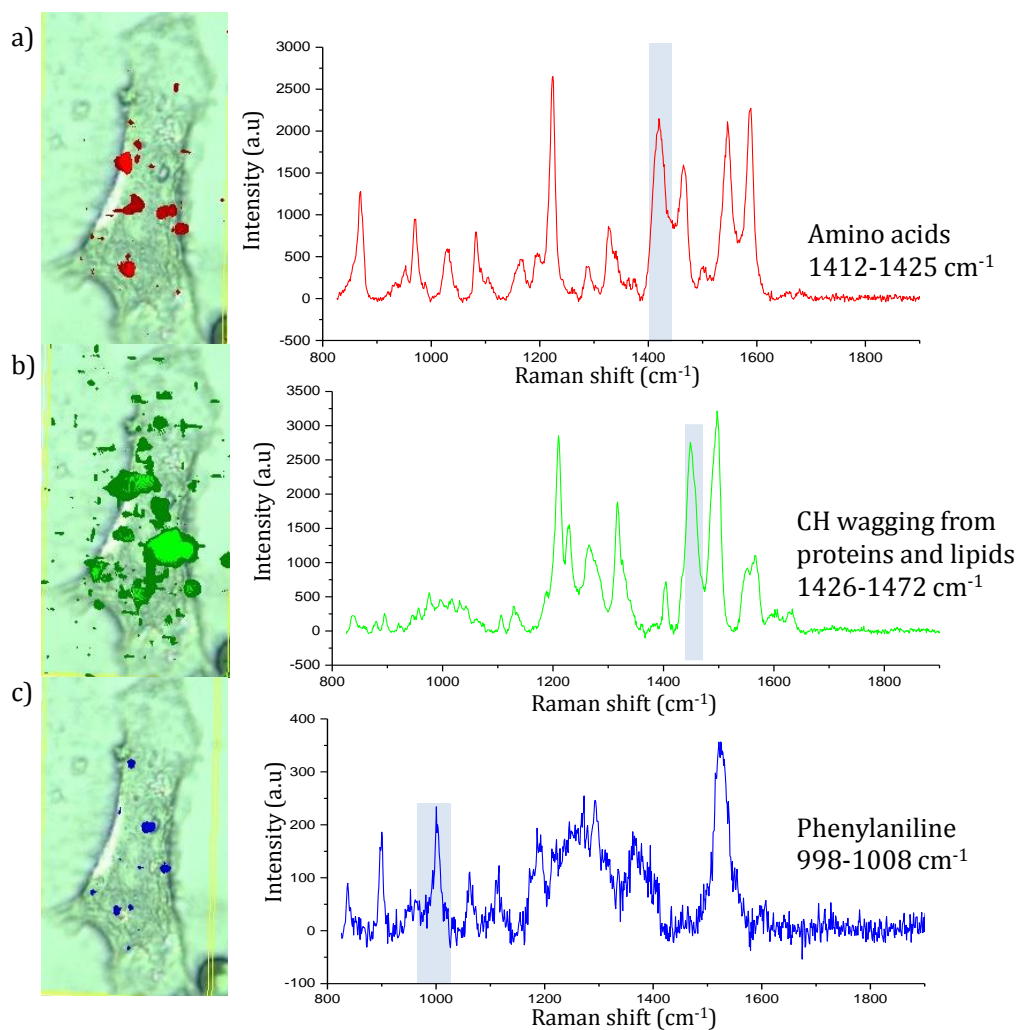
Figure 5.4 Cellular components tracking via SERS. The cells were 3D mapped with a volume of 15x17x6 μm with a 1 μm step size, using 633 laser excitation, with 1 second acquisition and 0.8 mW laser power. (a) False colour image representing areas were (a) amino acids (b) CH wagging from proteins and lipids and (c) phenylalanine and accompanying spectra with the peak of interest used to plot the false colour image highlighted.

Figure 5.4 (a) corresponds to the areas of the cell where peaks representative the δ(CH3) asymmetric and υ(COO-) structure of amino acids, between 1412-1425 cm^{-1}, were present. This was due to amino acids within the cell being in close proximity to the surface of an Ag NP indicating that amino acids are present throughout the cell which is to be expected. The corresponding spectrum highlights the amino acid peak present but also shows that other cellular components are present which are also enhanced from the Ag NPs being on close proximity to them as expected. These peaks were assigned to C=C stretching of a benzoid ring at 1499 cm^{-1} and guanine at 1319 cm^{-1}.[171],[172]

The presence of CH wagging from proteins and lipids were imaged by creating a map of peaks in present at 1426-1472 cm^{-1}, shown in Figure 5.3 (b) and again there were many areas where they were present in the cell. This was expected as there are approximately 10^9 lipid molecules in the plasma membrane of animal cells.[173] The associated spectrum again indicates other enhanced cellular components, for example the peak at 1446 cm^{-1} that has previously been assigned to bound and free NADH.[174]

Phenylalanine is found ubiquitously and the cell and is routinely used as a marker for it delineation.[175] However, the presence of the ring breathing mode of the amino acid phenylalanine, which is present at 1001 cm^{-1}, was unexpectedly only present in a small portion of the cell (Figure 5.3 (c). This was again due to Raman signals only coming from the phenylalanine in close proximity to the Ag NPs and to visualise the delineation of the phenylalanine the cell would have to be mapped using 532 laser excitation which would give Raman signals from the cells without the need for Ag NPs to enhance cellular components.[175]

5.3.2 Ag TMB incubation

TMB could be introduced into the cell in a two different ways. TMB was either functionalised onto the Ag NP surface due to the affinity the amine of the TMB has for the Ag NP surface or the TMB and Ag NPs were added separately to the cells. This later approach would require the TMB to come into contact with the Ag NP and ROS within the cell resulting in its oxidation to the CTC, i.e. signal would only occur where all the components were present within the cell.

TMB was functionalised onto the surface of Ag NPs by adding 200 µL Ag NPs (0.3 nM) to 200 µL of TMB (3 mM) and leaving to shake for 30 minutes to allow the TMB to adsorb onto the surface of the Ag NPs. The solution was then added to 2 mL of cell media containing $30x10^4$ of PC3 cells and incubated for 14 hours. 200 µL of Ag NP alone and 200 µL of DMSO were also added to separate batches of cells and cell media to act as a control. The cells were washed, fixed with formaldehyde and 3D Raman mapped with a volume of 37x32x6 µm and 1 µm step size, using 633 nm laser excitation.

Due to metabolic and signalling aberrations, cancer cells have an elevated level of ROS and can promote tumour formation by inducing DNA mutations and pro-oncogenic signalling pathways. [176] It was therefore that PC3 cells which were incubated with Ag-TMB NPs are likely to have increased levels of ROS's present to oxidise the TMB to give a SERRS response.

The maps obtained were analysed using direct classical least square (DCLS) analysis which is included on WiRE software. DCLS finds the linear combination of spectra that most closely resembles a reference spectrum, which in this case was the oxidised TMB CTC SERRS spectrum. False colour images can be created by assigning a colour to the pixels which match the reference spectrum. Figure 5.5 shows the results of the Raman DCLS mapping for a PC3 cell with and without TMB and an image from the WiRE software showing an example spectrum assigned to the CTC of TMB by DCLS.
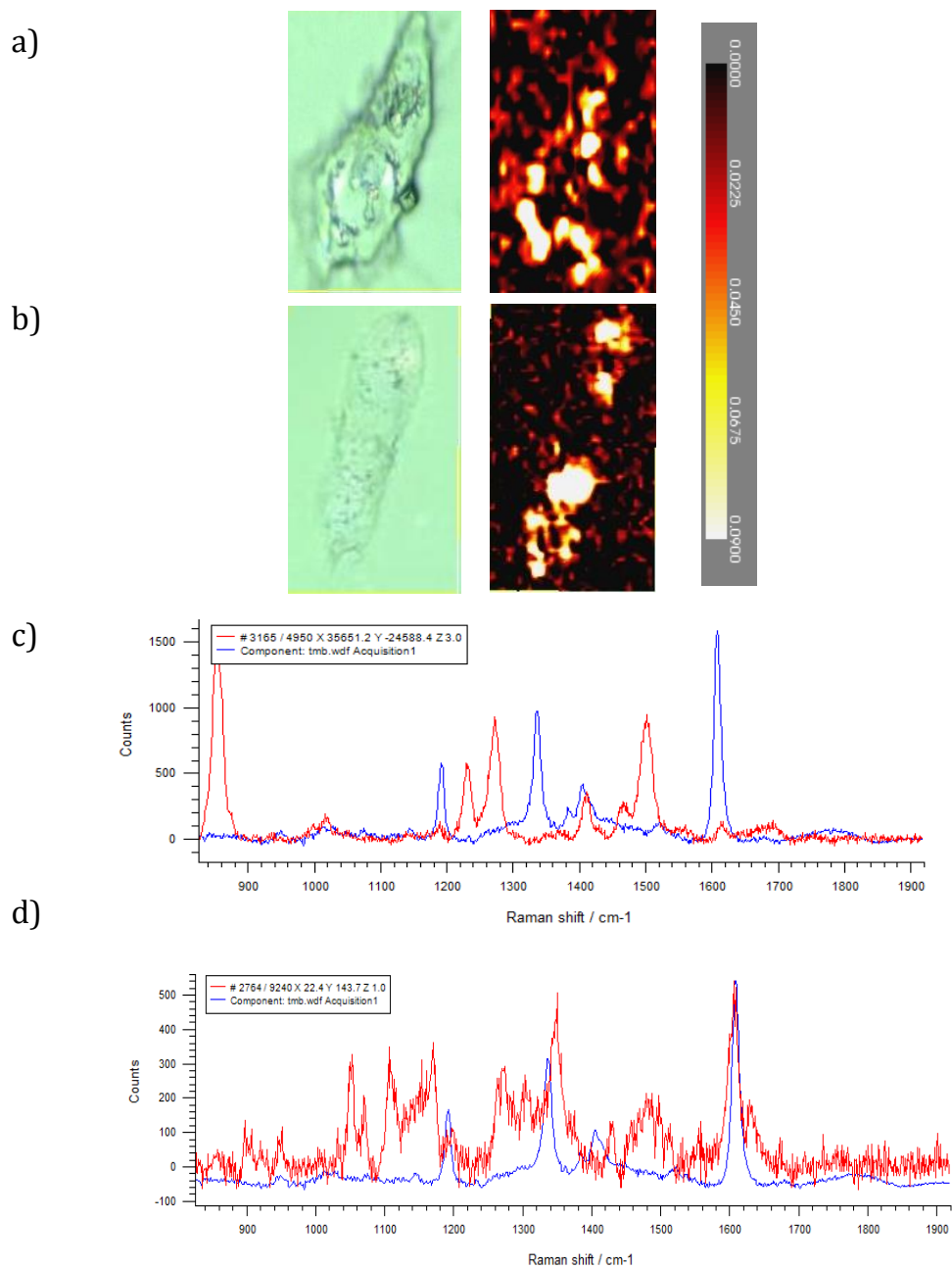
Figure 5.5 Raman of PC3 cells incubated with Ag NPs with and without TMB. The cells were 3D Raman mapped using 37x32x6 μm and 1 μm step size, 633 nm laser excitation, 1 second acquisition and 8 mW laser power. White light and heat intensity map from DCLS result and look up table (LUT) table of cells (a) without and (b) with TMB. CTC TMB SERRS reference spectra (blue) and spectra from cell (red) for cells without (c) and with TMB (d).

The TMB-Ag NPs were incubated with PC3 cells and DCLS was carried out on the data and the resulting heat intensity map is shown in Figure 5.5 (b). The data indicated areas within the cells where the oxidised TMB spectra were present, white pixels, and no oxidised TMB spectra were present, black pixels. The outline of the

cell can be visualised using the heat intensity map, and the oxidised TMB spectrum only occurs within the cell, suggesting that the TMB has only been oxidised due to the ROS. The SERRS spectrum in Figure 5.5 (d) indicates that the spectrum from the cell (red) resembles that of the oxidised TMB spectra (blue). As the 3 main characteristic TMB peaks were present at 1610, 1335 and 1190 cm^{-1}. The SERRS spectra obtained from the cell also has extra peaks that do not correspond to the oxidised TMB and can be assigned to cellular components being enhanced by the Ag NPs. This is a result of the Ag NPs not having a full monolayer of TMB on the surface, allowing cellular components to come into close proximity with the metal surface.

The DCLS heat intensity map obtained from the cell which did not contain TMB is shown in Figure 5.5 (a) and suggests that peaks which are similar to the oxidised TMB are present which has resulted in areas where it appears that the oxidised TMB signal is present. This was unexpected as TMB was not added to the cell; however, it can be explained due to the bare Ag NP surface. As seen in section 5.3.1, when Ag NPs were incubated into the PC3 cells, cellular components were visualised due to the enhancement experienced by them being in close proximity to the Ag NPS. Some cellular components have very similar Raman peaks to the oxidised TMB spectrum and therefore gave false positives when using DCLS to detect the oxidised TMB signal. These cellular components include cytosine which also has a peak at 1610 cm^{-1} and collagen which appears at 1335 cm^{-1}.[177] This means that false positives may also occur in the cell with TMB, however by inspecting the raw spectra it can be seen that the three suspected TMB peaks at 1610, 1335 and 1190 cm^{-1} in the cell spectrum had the same peak height ratio as the pure oxidised TMB spectrum, it can therefore by confidently suggested that TMB and been oxidised due to the ROS within the cell.

To reduce the SERS background of the cellular components, a lower concentration of Ag NPs were added separately to the PC3 cells and left to incubate overnight and cell stress was induced to increase the concentration of ROS in the cell which could oxidise the TMB.

5.3.3 Induce cell stress

Although cancerous cells are already under oxidative stress,[178] the concentration of ROS with in the cell was low, therefore a weak oxidised TMB signal was obtained, which made it hard to distinguish from the background. To increase the amount of ROS within the cell, cell stress was induced. This can be achieved in a number of ways such as the addition of tert-butylhydroperoxide (tert-BHP),[179] monensin,[180] or H_2O_2.[181]

As H_2O_2 could induce cell stress, it was chosen to not only stress the cells, but to also be present in a high enough concentration to allow Ag NPs to catalyse the oxidation of TMB in its presence. This would therefore hopefully allow a big enough CTC SERRS signal to be obtained when the cell was 3D Raman mapped and indicate whether TMB could be oxidised in a cellular environment at the oxidised TMB signal actually detected.

The addition of H_2O_2 to induce cell stress was investigated by adding 10 μM of after the addition of Ag NPs. The concentration of H_2O_2 used to induce cell stress was investigated using a LIVE/DEAD viability/cytotoxicity kit. As the concentration of H_2O_2 added to the cells was high, it may have induced cell death rather than only cell stress. Viability studies would also allow information to be obtained on the viability of the cells after the addition of Ag-TMB NPs.

The addition of fluorescent probes used in the viability kit can distinguish between live and dead cells due to the intracellular esterase activity which is determined by the enzymatic conversion if the virtual non-fluorescent calcein AM to the fluorescence calcei (live stain). This produces a uniform green fluorescence in live cells with an excitation/emission at 495/515 nm. The addition of ethidium homodimer (EthD-1) is used to infer cell death as the probe enters cells with damaged cell membranes and undergoes fluorescent enhancement when it binds to nucleic acids (dead stain). Hence when a cell is dead a bright red colour is produced (excitation /emission, 528/635).

To carry out the viability studies, Ag-TMB NPs (100 μL of Ag NP and 100 μL of TMB were mixed together) were added to PC3 cells ($30x\ 10^4$) in 2 mLs of media and incubated for 14 hours. The media and Ag-TMB NPs that were not taken up by cells were removed and fresh media containing a final concentration of H_2O_2 was added to

the cells and left for 1 hour. 5 µL of calcein AM and 20 µL of EthD-1 were mixed together in 10 mL PBS and 2 mLs of this solution was added to the cells, with and without the addition of H_2O_2. This was left for half an hour and the cells were then washed and fixed.

The cells were imaged using fluorescence microscopy with a fluorescein optical filter (485 ± 10 nm) to excite calcein and a typical rhodamine optical filter (530 ± 12.5 nm) which was compatible with EthD-1. The fluorescence images in Figure 5.6 were obtained from the cells, with and without the addition of H_2O_2.
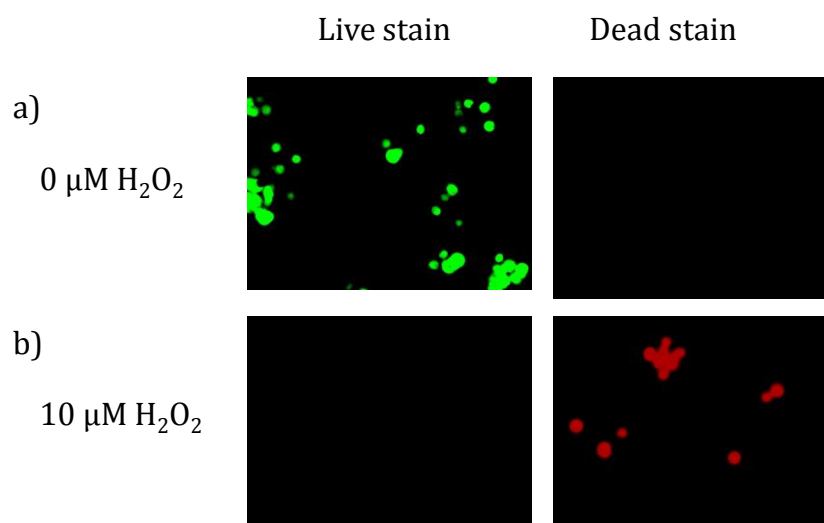
Figure 5.6 Fluorescent images obtained from staining thePC3 cells incubated with Ag-TMB NPs with calcein and EthD-1. (a) Cells without H_2O_2 and (b) with H_2O_2 imaged using fluorescein optical filter (485 ± 10 nm) to excite calcein and a typical rhodamine optical filter (530 ± 12.5 nm).

When H_2O_2 was added to the cells, followed by the live and dead stain, red fluorescence was observed due to the EthD-1 indicating the cells were dead. (Figure 5.6 (b)).The concentration of H_2O_2 was therefore too high and instead of just inducing cell stress, cell death also occurred. When no H_2O_2 was added, the calcein fluoresced green, indicating that the cells were still alive after Ag-TMB NPs were added to the cell.

PC3 cells with 200 μL Ag-TMB NP and 10 μM H_2O_2 were also prepared, without staining, and 3D Raman mapped using 638 nm laser excitation. The results are shown in Figure 5.7 along with a control map with no added H_2O_2.
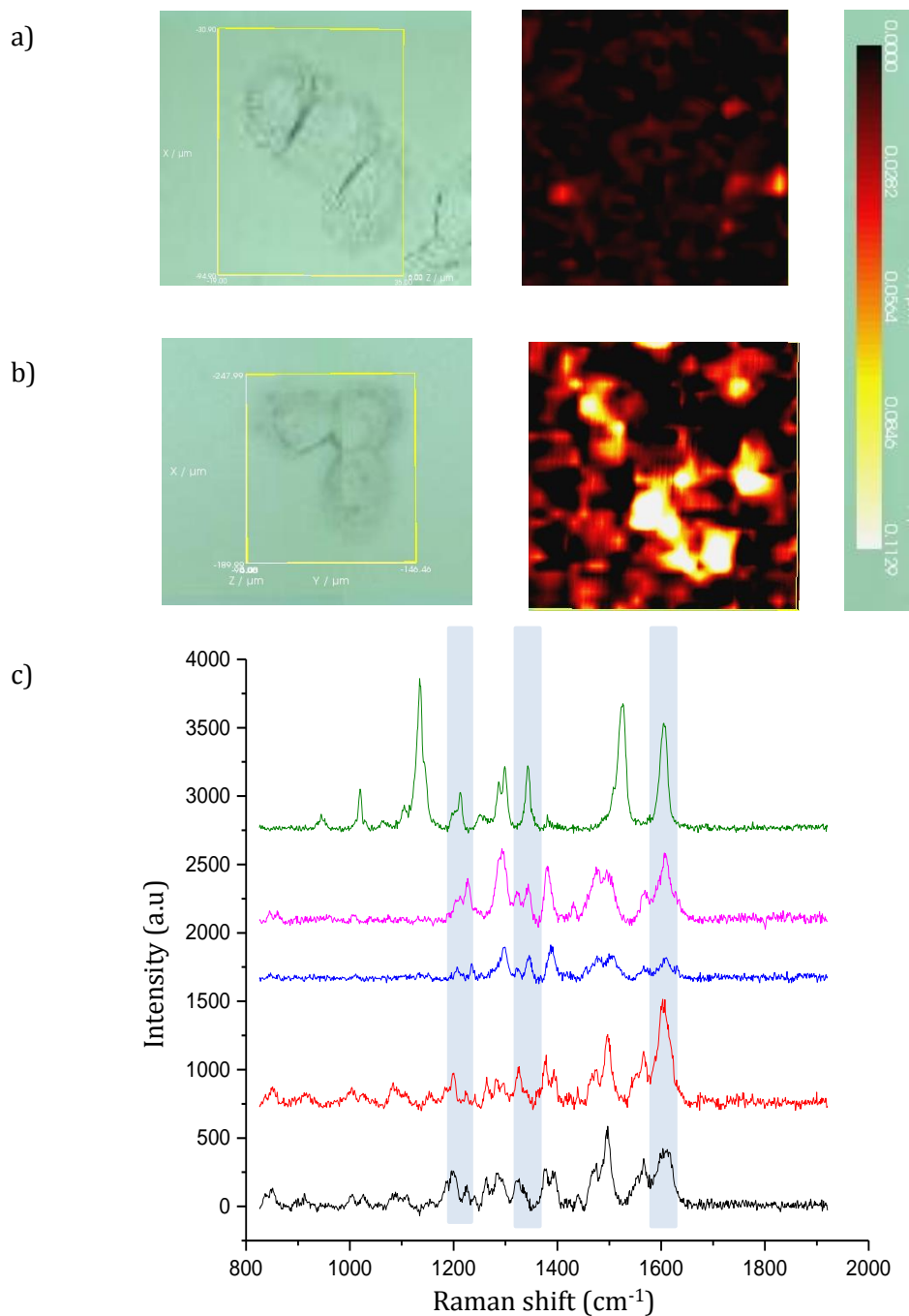
Figure 5.7 DCLS heat intensity image indicating the presence of the oxidised TMB in (a) cell without H_2O_2 and (b) cells with H_2O_2. (c) Spectra from 3D map which contain TMB SERRS signal. The cells were 3D mapped using 633 laser excitation, with 1 second acquisition and 0.8 mW laser power.

Figure 5.7 show the difference in DCLS heat intensity maps that were obtained from cells that weren't stressed with H_2O_2 (a) and were stressed (b). When no H_2O_2 was added to the cells, little TMB oxidation occurred which can be observed due to the low intensity of white pixels in the SERRS map as little spectra in the map matched the reference TMB CTC SERRS spectrum. This also confirmed that the lower concentration of Ag NP had limited the amount of cellular components enhanced and being able to match the oxidised TMB spectrum.

The heat intensity map obtained from the cell that H_2O_2 had been added to indicate the presence of a high amount of oxidised TMB within the cell due to the presence of the white pixels inside the cell. This suggested that the oxidation of TMB due to the addition of H_2O_2 and the presence of Ag NPs can occur within a cell and the oxidative TMB SERRS signal can be monitored using 638 nm laser excitation.

Spectra from the cell are shown in Figure 5.7 (c) and the appearance of the oxidised TMB 1610 cm^{-1} peak is very prominent. The 1335 and 1190 cm^{-1} peak are also present however they are weaker and are potentially obscured by the enhancement of cellular components.

Although the high concentration of H_2O_2 caused cell death, it allowed for the highest amount of TMB oxidation to occur and gave a good discrimination between the control with no induced stress and the cell with stress induced. Therefore TMB can be oxidised inside the cell and detected using SERRS.

5.4 Conclusion

Overall, Ag NPs can be taken up in PC3 cells and cellular components such as amino acids, proteins and phenylalanine can be visualised using SERS when the cells are 3D Raman mapped. The oxidative stress experienced by PC3 cancerous cells was investigated by using the catalytic activity of Ag NPs, by incubating Ag-TMB NPs or Ag NP with PC3 cells. Due to the surface enhancement of the cellular components experienced when Ag NP were incubated with PC3 cells, it was hard to differentiate the SERS signal from the oxidised TMB signal and the cellular components.

Cell stress could be induced by the addition of H_2O_2 after the addition of Ag-TMB NPs, resulting in the TMB being oxidised due to the presence of the H_2O_2 and increase in ROS's present. Therefore the catalytic activity of Ag NPs can be applied to a cellular environment and the TMB oxidation due to the presence of H_2O_2 and Ag NPs can be detected using 638 nm laser excitation.

Unfortunately, the high concentration of H_2O_2 used caused cell death, however the technique could benefit from further optimisation including investigating other mechanisms of inducing cell stress or by using other cell lines.   The technique also has the potential to give additional information from the cell by utilising the enhancement gained from the Ag NP and cellular components. By analysing the SERS spectra the location of major organelles or the state of the cell could be inferred, as it has recently been reported that the change in Raman scattering of DNA could indicate if cell death will occur via apoptosis or necrosis.[182] This additional information would not be possible with other cell stress detection methods such as fluorescence, which increases the benefits of the Ag NPs inclusion into the cell.

6. Conclusion

Nanoparticles have been shown to have catalytic activity and can behave as artificial enzymes which have become an increasingly interesting area of research due to their many advantages over natural protein enzymes which are expensive, difficult to isolate and unable to stand harsh environments. Nanoparticles with this catalytic activity are known as nanozymes and can be tailored to fit a number of different applications by varying their size and composition all with a lower cost when compared to conventional enzymes. Nanozymes are also considered to be stable in harsh environments and protective coatings can be added to not only increase the stability but increase the catalytic activity of certain nanotags.

To increase the stability of NP that could be used as nanozymes in harsh environments eventually mimicking HF, Raman reporters, silica and platinum coatings were added to Au NPs and the resulting Au-MGITC-SiO$_2$-Pt nanotags were stable in 1M of NaCl, 1 M of NaOH, 1M of H$_2$O$_2$ and 2 M of HCl over the course of a week. The stability was increased by coating the commercially available Cabot nanotag in Pt and stronger LSPR and Raman signals were obtained in the harsh environments for longer. By increasing the stability of the nanotags, the Au coated nanoparticles could be used in a number of different applications where high concentrations of salt or acid /alkali conditions are needed.

The platinum coating not only increased the stability but gave the nanotags catalytic activity which was evaluated along with Au, Ag and Fe$_2$O$_3$ NPs by utilising them to catalyses the oxidation of TMB and ABTS in the presence of H$_2$O$_2$. The oxidation was monitored using UV-Vis and Raman spectroscopy and the catalytic activity of all four NPs was compared. By utilising Raman as a detection method, more information about the unoxidised and oxidised states of ABTS and TMB was obtained. It was concluded that the surface chemistry of the NPs played an important role in the catalytic activity as negatively charged Au and Ag NPs performed better with the positively charged TMB and poorly with the negatively charged ABTS.

The catalytic activity of positively charged Fe$_2$O$_3$ NPs performed very well with the negatively charged ABTS and an intense oxidised signal was obtained, which could be detected with RRS by using a 785 nm laser excitation. The catalytic oxidation and

RRS detection were combined into an ABTS decolourisation assay for the detection of glutathione. The hydrogen donating glutathione reduced the oxidised ABTS and the decrease in 1403 cm^{-1} peak at varied concentrations of glutathione was monitored. By combining the catalytic activity of the Fe$_2$O$_3$ NPs and Raman detection an observable limit of detection of 200 nM was obtained, which rivalled conventional oxidation and detection methods. The RRS detection was also carried out on a handheld CBex instrument which gave the assay portability and could extend its use for infield detection, possibly in clinical environments. Overall the novel RRS detection of the decolourisation of ABTS and use of Fe$_2$O$_3$ NPs could be used for detection of other antioxidants or to detect overall antioxidant capacity in biological fluids. The Fe$_2$O$_3$ NPs can also be easily reclaimed using a magnet after they have catalysed the oxidation and used again which will lower the cost of the assay and overcome problems associated with using other enzymes which are harder to retrieve.

The catalytic activity of Ag NPs yielded a very intense SERRS response for the oxidised TMB and their catalytic activity, along SERRS detection, was applied to a number of applications. First, it was applied for the detection of H$_2$O$_2$ by monitoring the change in oxidised TMB SERRS signal as lower concentration of H$_2$O$_2$ were added. A limit of detection of 3 μM was achieved on a portable Raman instrument, hence the application could be applied for the in-field detection of H$_2$O$_2$ which could have importance in forensics applications as H$_2$O$_2$ is a common precursor in bomb making or to evaluate potential pollutants in wastewater treatment plants.

Furthermore, the catalytic activity of Ag NP that had been functionalised with antibodies was investigated and used to replace conventionally used enzymes in ELISA to create a silver nanoparticle linked immunosorbent assay. When antibodies were added to the surface, the catalytic activity decreased as the surface was taken up in the functionalisation, however using a physical conjugation technique, enough antibody was added to the surface to detect CRP and allow TMB oxidation to still occur. Ag-Ab NPs were then used to replace natural enzymes in a conventional ELISA, allowing for the novel detection of CRP with SERRS analysis with a calculated detection limit of 1.09 ng/mL which was comparable to colourimetric, fluorescence and electrochemical detection methods. A clinically relevant concentration of CRP (10 μg/mL) was also detected with little interference when in a

biological matrix. The SLISA had many advantages over conventional ELISAs such as the decrease in incubation time required for a positive result (20 minute incubation of each component as opposed to 2 hours) which allowed the SLISA to be completed and analysed in a matter of hours instead of a whole day. Again there is also a decrease in cost due to the cheap synthesis of Ag NP and the passive conjugation of antibodies to the Ag surface which provides an easy, reliable conjugation technique which avoids the complicated conjugation of enzyme to antibody (which is time consuming and can require conjugation kits).

Finally the catalytic activity of the Ag-TMB NPs system was applied for the detection of ROS in PC3 cells. When Ag-TMB NPs were added to PC3 cells which were 3D Raman mapped, the appearance of the oxidised TMB signal would infer that ROS were present. However, it was hard to discriminate between PC3 cell with and without TMB due to the enhancement of cellular components via the Ag NP surface and cell stress was induced using H_2O_2. When H_2O_2 was added to the cells, the TMB could be oxidised due to its presence, hence the catalytic activity of Ag NP and TMB could occur within a cellular environment.

Overall, it was demonstrated that nanozyme assays with Raman spectroscopy detection is an exciting, developing field. By combining the two, the detection of varies biomolecules has been demonstrated in different mediums and the technique could be applied to a variety of applications. This could lead to lower limits of detection of biomolecules by using Raman detection of the oxidised peroxidase signal, cheaper assays due to the low cost associated with the synthesis of NPs and assays being performed in harsher environments including a wider range of pH's or high salt concentrations. This therefore opens the possibility of nanozymes in many future applications and although the field is still in its infancy, the improvement it offers to assays highlights the growing need for nanozymes in nanotechnology.

7. Experimental

7.1 Materials

Mouse monoclonal antibody and biotinylated mouse monoclonal antibody were purchased from R&D systems. $CT(PEG)_{12}$ and MGITC was purchased from ThermoFischer. All other chemicals were purchased from Sigma Aldrich unless stated otherwise.

7.2 Instrumentation

7.2.1 Extinction spectroscopy

All UV-vis spectroscopy was carried out on a Varian Cary 3000 Bio UV-visible spectrophotometer with Win V scan application 2.00 software. The instrument was left to warm up and equilibrate for at least 10 minutes. The range of wavelengths scanned was 200-800 nm.

7.2.2 DLS and zeta potential

A Malvern Zetasizer Nano ZS was used to carry out all zeta sizing and zeta sizing measurements along with Zetasizer μV and APS version 6.20 software. Approximately 1.7 cm of sample was run in a 1 m L disposable plastic cuvette, with a standard Malvern Dip cell.

7.2.3 SERS Measurements

Solution spectra were collected using a Snowy Range Sierra series reader with a 638 nm excitation wavelength with a 30 mW laser power or 785 nm excitation wavelength with a 45 mW laser power. Raman spectra from surfaces and cells were

collected using a Renishaw InVia microscope with a 633 nm excitation wavelength with 0.8 mW laser power. Portable Raman measurements were taken on a handheld CBex Snowy Range instrument with a 785 nm laser excitation and a 70 mW laser power. Each spectrum was baselined corrected using the asymmetric least squared smoothing method on Matlab unless stated otherwise.

7.2.4 SEM measurements

Samples were analysed using a Sirion 200 Shottky field emission electron microscope operating at an accelerating voltage of 30 kV and a magnification of 500 nm.

7.2.4 NanoSight

A NanoSight LM20 and accompanying NTA software was used to determine the concentration of Cabot nanotags.

7.3 Nanoparticles in harsh environments

7.3.1 Synthesis and stability of gold nanoparticles

40 nm Au NPs were synthesised by adding sodium tetrachloroaurate (67.5 mg) to distilled water (500 mL) which was heated until boiling in a 3 necked round bottom flask (1 L). At this point sodium citrate (60.5 mg) was added and the boiling maintained for 15 minutes before being allowed to cool to room temperature. Constant stirring was maintained throughout using a glass linked stirrer. The resulting Au NPs (400 μL, 0.1 nM) were added to 100 μL of distilled water, saturated NaCl, 1 M NaOH, 2 M HCl or 1 M H_2O_2 and analysed using extinction spectroscopy.

7.3.2 SEM preparation

Samples for SEM were prepared by spotting 10 μL of NPs onto a silica wafer and leaving it to dry overnight.

7.3.3 Platinum coating of gold nanoparticles

MGITC (5 μL, $1x10^{-4}$ M) was added to Au NPs (5 mL, 0.1 nM) and the solution was left to shake for 30 minutes. H_2PtCl_6 (400 μL, 3 mM) was added to Au NPs (5 mL, 0.3 nM) and sodium citrate (800 μL, 8 mM) were refluxed for 30 minutes and the resulting solution analysed using 638 nm laser excitation with a 1 second acquisition time and 30 mW laser power.

7.3.4 Silica coating of gold nanoparticles and stability

APTMS (400 μL, 3 mM) was added to Au-MGITC NPs (5 mL, synthesis described in section 7.3.3) and left stirring for 3 hours. Na_2SiO_3 (final concentrations of 1.4, 3.7 or 6.1 mM) were added and the solution was heated to 90°C for 20 minutes with constant stirring. The solutions were then left to cool. 450 μL Au-MGITC-SiO_2 with 50 μL of water or 50 μL of 3 mM NaCl were analysed using extinction spectroscopy and DLS and Raman spectroscopy using 638 nm laser excitation, 1 second accumulation and 30 mW laser power.

7.3.5 Platinum coating of silica coated gold nanoparticles

H_2PtCl_6 (5, 10, 25, 50, 100 or 200 μL of 20 mM solution) was added to Au-MGITC-SiO_2 (400 μL, synthesis described in section 7.3.4). This was left to shake for 30 minutes followed by addition of $NaBH_4$ (2.5, 10 or 50 μL of 10 mM solution). The resulting solutions were analysed using extinction spectroscopy and DLS.

450 μL of each Au-MGITC-SiO_2-Pt nanotag was analysed with 50 μL of water or 50 μL of 3 mM HCl using 638 nm laser excitation, 5 second acquisition time and 30 mW laser power.

7.3.5.1 Stability study

Au-MGITC-SiO$_2$ (250 µL, synthesis described in section 7.3.4) and Au-MGITC-SiO$_2$-Pt (250 µL, synthesis described in section 7.3.5) were added, separately, to saturated salt (50 µL 1 M), NaOH (50 µL, 1 M), H$_2$O$_2$ (50 µL, 1 M), HCl (50 µL, 2M) or water (50 µL) and the solution were made up to 600 µL with water. The solutions were characterised after 1, 7 and 14 days using extinction, DLS and Raman spectroscopy using a 638 nm laser excitation, 5 second acquisition and 30 mW laser power.

7.3.6 Platinum coating of Cabot nanotags

Cabot nanotags (100 µL, 0.08 nM) was added to H$_2$PtCl$_6$ (100 µL or 10 µL of 20 mM solution) and left to shake for 30 minutes. NaBH$_4$ (10 µL, 10 mM) was then added to the solution. Cabot nanotags (100 µL diluted in 600 µL of water) and Cabot-Pt nanotags (volume made up to 700 µL) were analysed using extinction and Raman spectroscopy using 638 and 785 nm laser excitation, 1 second acquisition and 4.5 mW laser power. Spectra for each wavelength were normalised using an ethanol standard. Cabot-Pt nanotags were also analysed using SEM, using the protocol described in section 7.3.2.

7.3.6.1 Stability study

Cabot nanotags (250 µL of nanotags diluted 1 in 7) or Cabot-Pt nanotags (250 µL, synthesis described in section 7.3.6) were added separately to saturated salt (100 µL 1 M), NaOH (100 µL, 1 M), H$_2$O$_2$ (100 µL, 1 M), HCl (100 µL, 2 M) or water (100 µL) and the solutions were made up to 600 µL with water. The solutions were characterised after 1, 7, 14, 21 and 28 days using extinction, DLS and Raman spectroscopy using a 785 nm laser excitation, 5 second acquisition and 4.5mW laser power.

7.4 Catalytic activity of nanoparticles

7.4.1 Synthesis of silver nanoparticles

70 nm Ag NPs were synthesised by heating distilled water (500 mL) to 45° in a 3 necked round bottom flask (1 L). AgNO3 (90 mg dissolved in 10 mL of distilled water) was added and heated until boiling. Sodium citrate (10 mL, 1% aqueous solution) was added and the boiling maintained for 90 minutes before being allowed to cool to room temperature. Constant stirring was maintained throughout using a glass linked stirrer. The resulting NPs were characterised using extinction and DLS by diluting the Ag NPs by 10 (50 μL of Ag NPs with 450 μL of water).

7.4.2 Synthesis of ferromagnetic nanoparticles

Fe_2O_3 NPs were synthesised using a co-precipitation method. $FeCl_2.4H_2O$ (1.98g), $FeCl_3.6H_2O$ (5.335g) and concentrated HCl (821 μL) were added to 25 mL of distilled water and the solution was stirred. NaOH (15.058g) was added to a round bottom flask containing 250 mL of distilled water and heated to 50 °C. To this solution, the acidified iron salt was added drop wise with vigorous stirring. The solution was let stirring for 20 mins at 50 °C after which the solution was left to settle and cool. The black precipitate was washed twice with distilled water and once with 0.1 M HNO_3. 125 mL of 0.1 M HNO_3 was also added and the solution heated to 95 °C with constant stirring for 40 minutes. The resultant solution was centrifuged in triplicate and resuspended in distilled water and characterised using extinction and DLS by diluting the solution 1 in 20 with water.

7.4.3 Oxidation of TMB using nanoparticles

Ag NPs (100 μL, 0.3 nM), Au NPs (100 μL, 0.1 nM), Au-MGITC-SiO$_2$-Pt nanotags (100 μL) or Fe_2O_3 NPs (100 μL) were added to TMB (100 μL, 3 mM), H_2O_2 (100 μL, 6 mM) and water (200 μL). Control experiments were carried out by removing the NPs, TMB or H_2O_2 and replacing with water to maintain the same volume. The resulting solutions were characterised with extinction spectroscopy (solutions containing Ag NPs were diluted 50 μL in 450 μL of water) and using 638 nm laser excitation with a 1 second accumulation and 4.5 mW laser power for Ag NP and 1

second and 30 mW laser power for Au NP and Fe_2O_3 NPs and 5 second and 30 mW laser power for Au-MGITC-SiO_2-Pt nanotags. Samples were prepared in triplicate and 5 scans of each were taken.

7.4.4 Detection of H_2O_2 using the catalytic activity of silver nanoparticles

Final concentrations of H_2O_2 (450, 270, 90, 45, 9 and 0 µM) were added to Ag NPs (100 µL, 0.3 nM) and TMB (100 µL, 3 mM) and the volume made up to 500 µL using water. The solutions were then analysed using 638 nm laser excitation using a 1 second accumulation and 30 mW laser power. Samples were prepared in triplicate and 5 measurements taken to achieve an average and error bars obtained using the standard deviation of all 15 measurements.

7.5.5. Oxidation of ABTS using nanoparticles

Ag NPs (100 µL, 0.3 nM), Au NPs (100 µL, 0.1 nM), or Fe_2O_3 NPs (100 µL) were added to ABTS (100 µL, 3 mM), H_2O_2 (100 µL, 6 mM) and water(200 µL) Control experiments were carried out by removing the NPs, TMB or H_2O_2 and replacing with water to maintain same the volume. The resulting solutions were characterised with extinction spectroscopy (solutions containing Ag NPs were diluted 50 µL in 450 µL of water). The Raman properties of the oxidised and unoxidised ABTS solutions were then analysed using 638 nm and 785 nm laser excitation with a 5 second accumulation time and 30 or 40 mW laser power.

7.5.6 Detection of Glutathione using the catalytic activity of ferromagnetic nanoparticles

The oxidised ABTS was prepared as follows: ABTS (100 µL, 3 Mm), Fe_2O_3 NPs (100 µL) and H_2O_2 (10 µL, 9 M) were mixed together for 5 minutes and the Fe_2O_3 NPs were removed with a strong magnet. Final concentrations of glutathione (2000, 1600, 800, 400, 200 and 0 nM) were added to 100 µL of the oxidised ABTS and the

volume made up to 500 μL with water. 5 minutes after glutathione addition the solutions were analysed using a 785 nm on a Snowy range CBex instrument with a 1 second accumulation and 40 mW laser power.

7.5 Silver linked immunosorbent assay

7.5.1 CT(PEG)$_{12}$ functionalisation to silver nanoparticles

CT(PEG)$_{12}$ (100, 10, 1, 0.1 or 0.01 μM) was added to citrate capped Ag NPs (0.3 nM, 1 mL) and left to shake for 3 hours. The solutions were then centrifuged at 6000 RPM for 20 minutes, the supernatum removed and the pellet resuspended in water (1 mL). The resulting PEG-Ag NPs were then characterised using extinction spectroscopy and DLS by diluting 50 μL in 450 μL of water.

7.5.2 Catalytic activity of PEG-silver nanoparticles

The CT(PEG)$_{12}$-Ag NPs samples synthesised in section 6.3.1 (100 μL) were added to TMB (100 μL, 3 mM), H$_2$O$_2$ (100 μL, 6.5 mM) and water (200 μL). Control sample replacing H$_2$O$_2$ with water were also prepared. The resulting solutions were characterised with extinction spectroscopy (by diluting 50 μL in 450 μL of water) and using 638 nm laser excitation with a 1 second accumulation and 4.5 mW laser power. Samples were prepared in triplicate and 5 scans of each were taken.

7.5.3 Antibody conjugation to silver nanoparticles

7.5.3.1 Carbodiimide crosslinking

1 mg/mL solutions of EDC and s-NHS were prepared in MES buffer (10 mM, pH 6) and 20 μL EDC and 40 μL of s-NHS were mixed together and then added to a pellet of PEG-Ag NP (0.1 μM of CT(PEG)$_{12,}$ synthesis described in section 6.3.1) the volume was then made up to 1 mL with HEPES buffer (10 mM, pH 7.6). The solution was left to shake for 30 minutes and then centrifuged at 6000 rpm for 20 minutes. The supernatum was removed and to the pellet, mouse monoclonal

antibody (500 µg/mL,10 µL) was added and the volume made up to 1 mL with HEPES buffer. The resulting solution, along with PEG-Ag and Ag NPs were characterised using extinction spectroscopy, DLS and Zetasizer by diluting 50 µL in 450 µL of water.

7.5.3.1.1 Gel electrophoresis

An agarose gel was prepared by dissolving 100 mg of agarose in TBE buffer by applying heat and then leaving the gel to cool and set. Ag, PEG-Ag and Ab-PEG-Ag NPs were centrifuged and the supernatum removed in order to concentrate the samples. 1 µL of loading buffer was added to the pellet which was then transferred to wells created in the agarose gel. A voltage of 160 V was applied to the gel and left for 30 minutes.

7.5.3.2 Streptavidin-biotin conjugation

SA (50,10, 3, 1.9 or 0.9 µg/mL) was added to citrate capped Ag NPs (0.3 nM, 1 mL) and incubated at 37°C for 3 hours followed by centrifugation at 6000 RPM for 20 minutes. The supernatum was removed and the pellet resuspended in water (1 mL). The resulting SA-Ag NPs were characterised using extinction spectroscopy, DLS and Zetasizer by diluting 50 µL in 450 µL of water.

Monoclonal antibody (500 µg/mL,10 µL) was added to Ag NPs with 3 µg/mL of SA on the surface (1 mL) and left to shake for 1 hour. The solution was then centrifuged, the supernatum removed and the pellet resuspended in water (1 mL). Ab-SA-Ag NPs were then characterised using extinction spectroscopy by diluting 50 µL in 450 µL of water.

7.5.3.3 Physical conjugation

Monoclonal antibody (2.5, 1, 0.5, 0.25 or 0.05 µg/mL) were added to citrate capped Ag NPs (0.3 nM, 1 mL, pH 8) and left to shake for 14 hours. The solutions were then centrifuged at 6000 rpm for 20 minutes and resuspended in water (1 mL). The

conjugates were then characterised using extinction spectroscopy and DLS by diluting 50 µL in 450 µL of water.

7.5.3.4 Lateral flow assay

CRP (0.5 µg/mL, 0.5 µL) was spotted onto the nitrocellulose strip and left to dry. 10 µL of Ab-PEG-Ag, Ab-SA-Ag or Ab-Ag NPs was then added to the conjugate pad and the strip placed in 100 µL of HEPES buffer, which initiated the flow.

7.5.3.5 Catalytic activity of antibody-silver nanoparticles

Ab-PEG-Ag, Ab-SA-Ag or Ab-Ag NPs (200 µL, 0.3 nM) was added to TMB blotting solution (200 µL) and water (100 µL). The solutions were then analysed using 638 nm laser excitation with 1 second accumulation and 30 mW laser power. Samples were prepared in triplicate and 5 scans of each were taken.

7.5.4 SLISA

7.5.4.1 Capture antibody optimisation

An epoxy coated glass slide was placed inside a microarray chamber to create separate wells for sample. Capture monoclonal antibody (100 µ g/mL, 100 µL) were then added to separate wells and left over night to allow the antibodies to immobilise onto the epoxy surface. The unbound antibody was then removed and the surface of the slide was washed three times with 0.05% Tween 20 in PBS (10 mM, pH 7.6). 1% BSA in PBS (100 µL) was then added to the surface of the slide and left for 2 hours before it was removed. The slides were washed three times, followed by the addition of CRP (1 µg/mL, 100 µL) or PBS (10 mM, 100 mL) and left for 20 minutes followed by removal and wash steps. Ag-Ab NPs (100 µL, 0.6 nM) were then added. The Ab-Ag NPs were left on the slides for 2 hours and once removed the slides washed three times. Finally, TMB blotting solution (100 µL) was added, left for 2 hours and removed. The slides were washed three times and the surface of the SLISA was imaged using a 5x white light objective and analysed using 633 nm

laser excitation by taking spectra at 10 different areas of the SLISA spot using a 9 second acquisition time and 30 mW laser power.

0.3 µL of capture antibody (500, 100 or 10 µg/m L) were spotted onto an epoxy coated glass slide and left to immobilise overnight. The surface was washed three times followed by Ab-Ag NP addition (20 µL). The Ab-Ag NPs were left for 20 minutes and after removal the slides were washed three times. TMB blotting solution (20 µL) was then added to the SLISA spot and removed after 20 minutes. The resulting spots were washed three times and analysed using 638 nm laser excitation by taking spectra at 10 different areas of the SLISA spot using a 9 second acquisition time and 30 mW laser power.

7.5.4.2 Nanoparticle incubation

Capture antibody (0.3 µL, 10 µg/mL) was spotted onto an epoxy coated glass slide and left to immobilise overnight. The surface was washed three times followed by CRP (100 ng/mL, 20 µL) or PBS (10 mM, 20 µL) addition for 20 minute after which it was removed and the slides washed three times. Ab-Ag NPs (20 µL, 0.6 nM) were then added to each sample and either left for 20 or 60 minutes. After removal the slides were washed three times. TMB blotting solution (20 µL) was then added to the SLISA spot and removed after 20 minutes. The resulting spots were washed three times and analysed using 638 nm laser excitation by taking spectra at 10 different areas of the SLISA spot using a 9 second acquisition time and 30 mW laser power.

7.5.4.3 SLISA performed on epoxy coated glass slide

Capture antibody (0.3 µL, 10 µg/mL) was spotted onto an epoxy coated glass slide and left to immobilise overnight. The surface was washed three times followed by 20 µL of CRP (100, 50, 25, 12.5, 6, 1.3 and 0.75 ng/mL) or 20 µL of PBS (10 mM) which was left for 20 minutes, removed and the slides washed three times. Ab-Ag NP (20 µL, 0.6 nM) were then added to each sample left for 20 minutes. After removal the slides were washed three times. TMB blotting solution (20 µL) was then added to the SLISA spot and removed after 20 minutes. The resulting spots

were washed three times and analysed using 638 nm laser excitation by taking spectra at 50 different areas of the SLISA spot using a 9 second acquisition time and 0.8 mW laser power.

7.5.4.4 SLISA performed on nitrocellulose coated glass slide

SLISA was repeated in triplicate as described in section 6.3.5.1 on nitrocellulose coated glass slide with CRP concentrations of 25, 12.5, 6, 3, 1.5 and 0 ng/mL. The resulting spots were analysed using 638 nm laser excitation by taking spectra at 100 different areas of the SLISA spot using a 9 second acquisition time and 8 mW laser power. The SLISA spots were also mapped over an area of 58x57 mm with a 15 μm step size using 638 nm laser excitation, 9 second acquisition time and 8 mW laser power.

7.5.4.5 SLISA specificity

To check the specificity of the SLISA, it was repeated as described in section 7.5.4.3 on nitrocellulose, with CRP, hCG or BSA (25 ng/m L, 20 μL) added as the antigen to detect. The resulting spots were washed three times and analysed using 638 nm laser excitation by taking spectra at 100 different areas of the SLISA spot using a 9 second acquisition time and 0.8 mW laser power.

7.5.4.6 Detection of CRP in serum

SLISA was performed as described in section 7.5.4.3 replacing CRP in PBS with a solution on 1% SeraSub spiked with100 ng/mL of CRP. The resulting spots were washed three times and analysed using 638 nm laser excitation by taking spectra at 100 different areas of the SLISA spot using a 9 second acquisition time and 0.8 mW laser power

7.5.4.7 SLISA performed on LFA

0.5 μL of capture antibody (360 or 100 μg/mL) was spotted onto the nitrocellulose strip and left to dry. Ab-Ag NPs (10 μ L, 0.6 nM) were then added to the

conjugation pad and the strip placed in a HEPES solution with or without CRP (final concentration of 100 µg/mL). Once the strip had dried, it was placed in TMB blotting solution (100 µL). The resulting SLISA spots were mapped over an area of 58x57 µm with a 2 µm step size using 638 nm laser excitation, 9 second acquisition time and 0.8 mW laser power.

7.6 Detection of oxidative stress in cells

7.6.1 Silver nanoparticle incubation

Human prostate cancer cells were obtained from Corinna Wetherill within the Centre for Molecular Nanometrology. 200 µL of Ag NPs (0.3 nM) were added to $30x10^4$ PC3 cells in 2 mLs of Roswell Park Memorial Institute (RPMI) medium and left to incubate at $37^{o}C$ for 14 hours. The cell media was then removed and the cells washed 3 times with 2 mLs of sterile PBS, and were then fixed onto a glass cover slip with 2 mLs of 4% formaldehyde which was left for 15 minutes then removed. The cells were then washed once with PBS and water and analysed via 3D Raman mapping with a 633 nm laser excitation, 1 second acquisition and 0.8 mW laser power.

7.6.2 Silver nanoparticle and TMB incubation

Ag NPs (200 µL,0.3 nM) and TMB (200 µL,3 mM) were added together and left for 30 minutes before being incubated into PC3 cells using the same procedure in section 7.6.1. Ag NPs (200 µL, 0.3 nM) and DMSO (200 µL) were added to separate cells as a control. The cells were 3D Raman mapped using the same parameters in section 7.6.1.

7.6.3 Viability study

Pc3 Cells were incubated with Ag-TMB NPs as described in section 7.6.2. The cells media was removed after 14 hours and 2 mLs of RPMI cell media which had a final

concentration of 10 μM of H_2O_2 and left for 1 hour. A control with no H_2O_2 was also prepared. The media was then removed.

5 μL of calcein AM and 20 μL of EthD-1 were mixed together in 10 mLs of sterile PBS and 2 mLs of this solution was added to the washed PC3 cells that had or hadn't been stressed and left for half an hour. Once removed the cells were washed and fixed and analysed using fluorescence microscopy with a fluorescein optical filter and rhodamine optical filter.

Cells were incubated with Ag-TMB NPs and stressed without the addition of the fluorescent probes and were 3D Raman mapped using the parameters described in section 7.6.1.

8. References

1.   Michigan State University, *Plenty of room at the bottom*,
        http://www.pa.msu.edu/~yang/RFeynman_plentySpace.pdf

Accessed 30th June, 2014.

2.   J. D. Meyers, T. Doane, C. Burda and J. P. Basilion, *Nanomedicine (London, England)*, 2013, **8**, 123-143.
3.   D. Jaque, L. Martinez Maestro, B. del Rosal, P. Haro-Gonzalez, A. Benayas, J. L. Plaza, E. Martin Rodriguez and J. Garcia Sole, *Nanoscale*, 2014, **6**, 9494-9530.
4.   M. M. Harper, K. S. McKeating and K. Faulds, *Physical chemistry chemical physics : PCCP*, 2013, **15**, 5312-5328.
5.   K. Gracie, D. Lindsay, D. Graham and K. Faulds, *Analytical Methods*, 2015, **7**, 1269-1272.
6.   N. L. Rosi and C. A. Mirkin, *Chemical reviews*, 2005, **105**, 1547-1562.
7.   J. Turkevich, P. C. Stevenson and J. Hillier, *Discussions of the Faraday Society*, 1951, **11**, 55-75.
8.   P. C. Lee and D. Meisel, *The Journal of Physical Chemistry*, 1982, **86**, 3391-3395.
9.   P. K. Khanna, S. Gaikwad, P. V. Adhyapak, N. Singh and R. Marimuthu, *Materials Letters*, 2007, **61**, 4711-4714.
10.   N. C. Bigall, T. Härtling, M. Klose, P. Simon, L. M. Eng and A. Eychmüller, *Nano Letters*, 2008, **8**, 4588-4592.
11.   I. Freestone, N. Meeks, M. Sax and C. Higgitt, *Gold Bulletin*, 2007, **40**, 270-277.
12.   P. T. Lee, K. R. Ward, K. Tschulik, G. Chapman and R. G. Compton, *Electroanalysis*, 2014, **26**, 366-373.
13.   M. Faraday, *Philosophical Transactions of the Royal Society of London*, 1857, **147**, 145-181.
14.   G. FRENS, *Nature Phys Sci*, 1973, **241**, 20-22.
15.   X. Huang and M. A. El-Sayed, *Journal of Advanced Research*, 2010, **1**, 13-28.
16.   J. Pérez-Juste, I. Pastoriza-Santos, L. M. Liz-Marzán and P. Mulvaney, *Coordination Chemistry Reviews*, 2005, **249**, 1870-1901.
17.   W. Niu, Y. A. A. Chua, W. Zhang, H. Huang and X. Lu, *Journal of the American Chemical Society*, 2015, **137**, 10460-10463.
18.   W. Meng, F. Hu, X. Jiang and L. Lu, *Nanoscale Research Letters*, 2015, **10**, 34.
19.   A. Zielińska, E. Skwarek, A. Zaleska, M. Gazda and J. Hupka, *Procedia Chemistry*, 2009, **1**, 1560-1566.
20.   N. S. Lee, R. S. Sheng, M. D. Morris and L. M. Schopfer, *Journal of the American Chemical Society*, 1986, **108**, 6179-6183.
21.   N. Leopold and B. Lendl, *J. Phys. Chem. B*, 2003, **107**, 5723-5727.
22.   P. L. Hariani, M. Faizal and D. Setiabudidaya, *International Journal of Environmental Science and Development*, 2013, **4**, 336.
23.   X. Mou, Z. Ali, S. Li and N. He, *Journal of nanoscience and nanotechnology*, 2015, **15**, 54-62.
24.   G.-Q. Gao, L. Lin, C.-M. Fan, Q. Zhu, R.-X. Wang and A.-W. Xu, *Journal of Materials Chemistry A*, 2013, **1**, 12206-12212.

25. G. S. Devi and V. J. Rao, *Bulletin of Materials Science*, 2000, **23**, 467-470.
26. C. S. Lin, M. R. Khan and S. D. Lin, *J Colloid Interface Sci*, 2006, **299**, 678-685.
27. Y. Hong, Y.-M. Huh, D. S. Yoon and J. Yang, *Journal of Nanomaterials*, 2012, **2012**, 13.
28. G. Mie, *Annalen der Physik*, 1908, **330**, 377-445.
29. V. Amendola, R. Pilot, M. Frasconi, O. M. Marago and M. A. Iati, *Journal of physics. Condensed matter : an Institute of Physics journal*, 2017, **29**, 203002.
30. Y. Chen and H. Ming, *Photonic Sensors*, 2012, **2**, 37-49.
31. K. A. Willets and R. P. Van Duyne, *Annu. Rev. Phys. Chem.*, 2007, **58**, 267-297.
32. W. Zhou, X. Gao, D. Liu and X. Chen, *Chemical reviews*, 2015, **115**, 10575-10636.
33. A. Smekal, *Naturwissenschaften*, 1923, **11**, 873-875.
34. C. V. Raman and K. S. Krishnan, *Nature*, 1928, **121**, 501-502.
35. I. R. Lewis, N. W. Daniel, N. C. Chaffin, P. R. Griffiths and M. W. Tungol, *Spectrochimica Acta Part A: Molecular and Biomolecular Spectroscopy*, 1995, **51**, 1985-2000.
36. M. Vendrell, K. K. Maiti, K. Dhaliwal and Y.-T. Chang, *Trends in Biotechnology*, 2013, **31**, 249-257.
37. E. Smith and G. Dent, *Modern Raman Spectroscopy: A Practical Approach*, John Wiley & Sons, Ltd, Chichester, UK, 2005.
38. E. V. Efremov, F. Ariese and C. Gooijer, *Analytica Chimica Acta*, 2008, **606**, 119-134.
39. H. A. Szymanski, *Raman Spectroscopy: Theory and Practice*, Springer US, 2012.
40. in *Infrared and Raman Spectroscopy*, Wiley-VCH Verlag GmbH, 2007, pp. 189-410.
41. M. J. Baker, C. S. Hughes and K. A. Hollywood, Morgan & Claypool Publishers, 2016.
42. J. R. Ferraro, *Introductory Raman Spectroscopy*, Elsevier Science, 2003.
43. K. Katrin, K. Harald, I. Irving, R. D. Ramachandra and S. F. Michael, *Journal of Physics: Condensed Matter*, 2002, **14**, R597.
44. B. Robert, *Photosynth Res*, 2009, **101**, 147-155.
45. M. Fleischmann, P. J. Hendra and A. J. McQuillan, *Chemical Physics Letters*, 1974, **26**, 163-166.
46. D. L. Jeanmaire and R. P. Van Duyne, *Journal of Electroanalytical Chemistry and Interfacial Electrochemistry*, 1977, **84**, 1-20.
47. M. G. Albrecht and J. A. Creighton, *Journal of the American Chemical Society*, 1977, **99**, 5215-5217.
48. A. Campion and P. Kambhampati, *Chemical Society Reviews*, 1998, **27**, 241-250.
49. X. Zhao and M. Chen, *RSC Advances*, 2014, **4**, 63596-63602.
50. J. R. Lombardi and R. L. Birke, *Accounts of Chemical Research*, 2009, **42**, 734-742.
51. A. M. Stacy and R. P. V. Duyne, *Chem. Phys. Lett.*, 1983, **102**, 365-370.
52. G. McNay, D. Eustace, W. E. Smith, K. Faulds and D. Graham, *Applied spectroscopy*, 2011, **65**, 825-837.
53. S. I. Stoeva, J.-S. Lee, C. S. Thaxton and C. A. Mirkin, *Angewandte Chemie International Edition*, 2006, **45**, 3303-3306.

54.   S. Laing, K. Gracie and K. Faulds, *Chemical Society Reviews*, 2016, **45**, 1901-1918.

55.   S. L. Kleinman, B. Sharma, M. G. Blaber, A.-I. Henry, N. Valley, R. G. Freeman, M. J. Natan, G. C. Schatz and R. P. Van Duyne, *Journal of the American Chemical Society*, 2013, **135**, 301-308.

56.   L.-J. Xu, C. Zong, X.-S. Zheng, P. Hu, J.-M. Feng and B. Ren, *Analytical Chemistry*, 2014, **86**, 2238-2245.

57.   S. Harmsen, M. A. Wall, R. Huang and M. F. Kircher, *Nat. Protocols*, 2017, **12**, 1400-1414.

58.   Z. Guo, T. Pereira, O. Choi, Y. Wang and H. T. Hahn, *Journal of Materials Chemistry*, 2006, **16**, 2800-2808.

59.   L. Rocks, K. Faulds and D. Graham, *Chemical Communications*, 2011, **47**, 4415-4417.

60.   S. P. Mulvaney, M. D. Musick, C. D. Keating and M. J. Natan, *Langmuir*, 2003, **19**, 4784-4790.

61.   W. Stöber, A. Fink and E. Bohn, *Journal of Colloid and Interface Science*, 1968, **26**, 62-69.

62.   J. F. Li, Y. F. Huang, Y. Ding, Z. L. Yang, S. B. Li, X. S. Zhou, F. R. Fan, W. Zhang, Z. Y. Zhou, Y. WuDe, B. Ren, Z. L. Wang and Z. Q. Tian, *Nature*, 2010, **464**, 392-395.

63.   D. Graham, *Angewandte Chemie International Edition*, 2010, **49**, 9325-9327.

64.   B. Küstner, M. Gellner, M. Schütz, F. Schöppler, A. Marx, P. Ströbel, P. Adam, C. Schmuck and S. Schlücker, *Angewandte Chemie International Edition*, 2009, **48**, 1950-1953.

65.   S. Wojtysiak, J. Solla-Gullón, P. Dłużewski and A. Kudelski, *Colloids and Surfaces A: Physicochemical and Engineering Aspects*, 2014, **441**, 178-183.

66.   C. Shankar, A. T. Dao, P. Singh, K. Higashimine, D. M. Mott and S. Maenosono, *Nanotechnology*, 2012, **23**, 245704.

67.   P. Pinkhasova, B. Puccio, T. Chou, S. Sukhishvili and H. Du, *Chemical Communications*, 2012, **48**, 9750-9752.

68.   M. F. Mrozek, Y. Xie and M. J. Weaver, *Anal Chem*, 2001, **73**, 5953-5960.

69.   W. He, X. Wu, J. Liu, K. Zhang, W. Chu, L. Feng, X. Hu, W. Zhou and S. Xie, *Langmuir*, 2009, **26**, 4443-4448.

70.   C.-L. Lee and C.-M. Tseng, *The Journal of Physical Chemistry C*, 2008, **112**, 13342-13345.

71.   L. Chen, W. Zhao, Y. Jiao, X. He, J. Wang and Y. Zhang, *Spectrochimica Acta Part A: Molecular and Biomolecular Spectroscopy*, 2007, **68**, 484-490.

72.   Y. Li, Q. Lu, S. Wu, L. Wang and X. Shi, *Biosensors and Bioelectronics*, 2013, **41**, 576-581.

73.   E. Mazzotta, S. Rella, A. Turco and C. Malitesta, *RSC Advances*, 2015, **5**, 83164-83186.

74.   Columbia Univesity, http://ehs.columbia.edu/HydrogenFlourideBrochure.pdf, Accessed 7th July, 2014.

75.   S. E. McLain, C. J. Benmore, J. E. Siewenie, J. Urquidi and J. F. C. Turner, *Angewandte Chemie International Edition*, 2004, **43**, 1952-1955.

76.   J. C. Bertolini, *The Journal of Emergency Medicine*, 1992, **10**, 163-168.

77.   B. D. Craig, D. S. Anderson and A. International, *Handbook of Corrosion Data*, ASM International, 1994.

78.   T. R. Jensen, G. C. Schatz and R. P. Van Duyne, *The Journal of Physical Chemistry B*, 1999, **103**, 2394-2401.

79. J. Eastman, in *Colloid Science*, Blackwell Publishing Ltd., 2009, pp. 36-49.
80. J. Yguerabide and E. E. Yguerabide, *Analytical biochemistry*, 1998, **262**, 137-156.
81. L. Ming, K. C. Scott, Z. Jianming, L. Jessica, P. A. Zoraida, M. Dongling and W. Nianqiang, *Nanotechnology*, 2012, **23**, 115501.
82. J. F. Li, X. D. Tian, S. B. Li, J. R. Anema, Z. L. Yang, Y. Ding, Y. F. Wu, Y. M. Zeng, Q. Z. Chen, B. Ren, Z. L. Wang and Z. Q. Tian, *Nature protocols*, 2013, **8**, 52-65.
83. B. Seger, A. Kongkanand, K. Vinodgopal and P. V. Kamat, *Journal of Electroanalytical Chemistry*, 2008, **621**, 198-204.
84. M. Keating, Y. Chen, I. A. Larmour, K. Faulds and D. Graham, *Measurement Science and Technology*, 2012, **23**, 084006.
85. R. Pamies, J. G. H. Cifre, V. F. Espín, M. Collado-González, F. G. D. Baños and J. G. de la Torre, *J Nanopart Res*, 2014, **16**, 2376.
86. H. ShamsiJazeyi, C. A. Miller, M. S. Wong, J. M. Tour and R. Verduzco, *Journal of Applied Polymer Science*, 2014, **131**, n/a-n/a.
87. X. Wang, Y. Hu and H. Wei, *Inorganic Chemistry Frontiers*, 2016, **3**, 41-60.
88. L. Gao, J. Zhuang, L. Nie, J. Zhang, Y. Zhang, N. Gu, T. Wang, J. Feng, D. Yang, S. Perrett and X. Yan, *Nature nanotechnology*, 2007, **2**, 577-583.
89. H. Jiang, Z. Chen, H. Cao and Y. Huang, *Analyst*, 2012, **137**, 5560-5564.
90. K. S. McKeating, S. Sloan-Dennison, D. Graham and K. Faulds, *Analyst*, 2013, **138**, 6347-6353.
91. J. R. Crowther, *The ELISA Guidebook*, Humana Press, 2000.
92. P. D. Josephy, T. Eling and R. P. Mason, *Journal of Biological Chemistry*, 1982, **257**, 3669-3675.
93. G. Volpe, R. Draisci, G. Palleschi and D. Compagnone, *Analyst*, 1998, **123**, 1303-1307.
94. E. N. Kadnikova and N. M. Kostić, *Journal of Molecular Catalysis B: Enzymatic*, 2002, **18**, 39-48.
95. R. Re, N. Pellegrini, A. Proteggente, A. Pannala, M. Yang and C. Rice-Evans, *Free Radical Biology and Medicine*, 1999, **26**, 1231-1237.
96. K. Beyzavi, S. Hampton, P. Kwasowski, S. Fickling, V. Marks and R. Clift, *Annals of clinical biochemistry*, 1987, **24 (Pt 2)**, 145-152.
97. N. C. Veitch, *Phytochemistry*, 2004, **65**, 249-259.
98. M. Kent, *Advanced Biology*, OUP Oxford, 2000.
99. S. Zhang, X. Zhao, H. Niu, Y. Shi, Y. Cai and G. Jiang, *Journal of Hazardous Materials*, 2009, **167**, 560-566.
100. P. Xu, G. M. Zeng, D. L. Huang, C. L. Feng, S. Hu, M. H. Zhao, C. Lai, Z. Wei, C. Huang, G. X. Xie and Z. F. Liu, *Science of The Total Environment*, 2012, **424**, 1-10.
101. Y. Jv, B. Li and R. Cao, *Chemical Communications*, 2010, **46**, 8017-8019.
102. S. Wang, W. Chen, A.-L. Liu, L. Hong, H.-H. Deng and X.-H. Lin, *ChemPhysChem*, 2012, **13**, 1199-1204.
103. J.-S. Lee, A. K. R. Lytton-Jean, S. J. Hurst and C. A. Mirkin, *Nano letters*, 2007, **7**, 2112-2115.
104. J. Yguerabide and E. E. Yguerabide, *Analytical biochemistry*, 1998, **262**, 137-156.
105. T. Donnelly, W. E. Smith, K. Faulds and D. Graham, *Chemical Communications*, 2014, **50**, 12907-12910.
106. G. V. P. Kumar, N. Rangarajan, B. Sonia, P. Deepika, N. Rohman and C. Narayana, *Bulletin of Materials Science*, 2011, **34**, 207-216.

107. S. Laing, A. Hernandez-Santana, J. Sassmannshausen, D. L. Asquith, I. B. McInnes, K. Faulds and D. Graham, *Analytical Chemistry*, 2011, **83**, 297-302.

108. K. Cui, Y. Song, Y. Yao, Z. Huang and L. Wang, *Electrochemistry Communications*, 2008, **10**, 663-667.

109. C. Wang, H. Daimon, T. Onodera, T. Koda and S. Sun, *Angewandte Chemie International Edition*, 2008, **47**, 3588-3591.

110. W. Oppolzer, *Angewandte Chemie International Edition in English*, 1989, **28**, 38-52.

111. Y. Jv, B. Li and R. Cao, *Chemical communications (Cambridge, England)*, 2010, **46**, 8017-8019.

112. K. B. Mabrouk, T. H. Kauffmann and M. D. Fontana, *Journal of Physics: Conference Series*, 2013, **450**, 012014.

113. D. S. Moore and R. J. Scharff, *Analytical and Bioanalytical Chemistry*, 2009, **393**, 1571-1578.

114. A. Garcia-Leis, D. Jancura, M. Antalik, J. V. Garcia-Ramos, S. Sanchez-Cortes and Z. Jurasekova, *Physical Chemistry Chemical Physics*, 2016, **18**, 26562-26571.

115. A. Zulueta, M. J. Esteve and A. Frígola, *Food Chemistry*, 2009, **114**, 310-316.

116. I. F. F. Benzie and J. J. Strain, *Analytical biochemistry*, 1996, **239**, 70-76.

117. M. B. Arnao, A. Cano, J. Hernández-Ruiz, F. García-Cánovas and M. Acosta, *Analytical biochemistry*, 1996, **236**, 255-261.

118. Y. Li, X. Liu and R. Zhang, *Spectrochimica Acta Part A: Molecular and Biomolecular Spectroscopy*, 2017, **173**, 880-885.

119. A. Pompella, A. Visvikis, A. Paolicchi, V. D. Tata and A. F. Casini, *Biochemical Pharmacology*, 2003, **66**, 1499-1503.

120. N. Ballatori, S. M. Krance, S. Notenboom, S. Shi, K. Tieu and C. L. Hammond, *Biological chemistry*, 2009, **390**, 191-214.

121. Y. Ma, Z. Zhang, C. Ren, G. Liu and X. Chen, *Analyst*, 2012, **137**, 485-489.

122. H. J. Chun, Y. M. Park, Y. D. Han, Y. H. Jang and H. C. Yoon, *BioChip Journal*, 2014, **8**, 218-226.

123. J. A. Alberts B, Lewis J, et al., *Molecular Biology of the Cell*, New York, 2002.

124. V. Morrison and P. Bennett, *An Introduction to Health Psychology*, Pearson Education, 2009.

125. C. Janeway, *Immunobiology: The Immune System in Health and Disease*, New York 2001.

126. S. B. Inc., http://www.elisa-antibody.com/elisa-antibody/elisa-antibody-structure, Accessed 15th Feb 2017

127. S. A. Frank, *Immunology and Evolution of Infectious Disease*, Princeton University Press, 2002.

128. I. Sela-Culang, V. Kunik and Y. Ofran, *Frontiers in Immunology*, 2013, **4**, 302.

129. E. Gruys, M. J. M. Toussaint, T. A. Niewold and S. J. Koopmans, *Journal of Zhejiang University. Science. B*, 2005, **6**, 1045-1056.

130. S. Black, I. Kushner and D. Samols, *Journal of Biological Chemistry*, 2004, **279**, 48487-48490.

131. P. Blazer, https://pgblazer.com/c-reactive-protein-microbiology-mcq/, Accessed 15th Feb 2017

132. Y. Doi, Y. Kiyohara, M. Kubo, T. Ninomiya, Y. Wakugawa, K. Yonemoto, M. Iwase and M. Iida, *The Hisayama Study*, 2005, **28**, 2497-2500.

133. G. P. Castelli, C. Pognani, M. Meisner, A. Stuani, D. Bellomi and L. Sgarbi, *Critical Care*, 2004, **8**, R234.

134. A. M. Wilson, M. C. Ryan and A. J. Boyle, *International Journal of Cardiology*, 2006, **106**, 291-297.

135. *Bulletin of the World Health Organization*, 1976, **54**, 129-139.

136. A. Ambrosi, F. Airo and A. Merkoci, *Anal Chem*, 2010, **82**, 1151-1156.

137. L. Guo, S. Xu, X. Ma, B. Qiu, Z. Lin and G. Chen, *Scientific Reports*, 2016, **6**, 32755.

138. F. M. Campbell, A. Ingram, P. Monaghan, J. Cooper, N. Sattar, P. D. Eckersall and D. Graham, *Analyst*, 2008, **133**, 1355-1357.

139. F. M. Campbell, A. Ingram, P. Monaghan, J. Cooper, N. Sattar, P. D. Eckersall and D. Graham, *Analyst*, 2008, **133**, 1355-1357.

140. D. Duan, K. Fan, D. Zhang, S. Tan, M. Liang, Y. Liu, J. Zhang, P. Zhang, W. Liu, X. Qiu, G. P. Kobinger, G. Fu Gao and X. Yan, *Biosensors and Bioelectronics*, 2015, **74**, 134-141.

141. M. I. Kim, Y. Ye, M.-A. Woo, J. Lee and H. G. Park, *Advanced Healthcare Materials*, 2014, **3**, 36-41.

142. Y. Song, X. Xia, X. Wu, P. Wang and L. Qin, *Angewandte Chemie (International ed. in English)*, 2014, **53**, 12451-12455.

143. Y. H. Tan, M. Liu, B. Nolting, J. G. Go, J. Gervay-Hague and G.-y. Liu, *ACS nano*, 2008, **2**, 2374-2384.

144. M. H. Jazayeri, H. Amani, A. A. Pourfatollah, H. Pazoki-Toroudi and B. Sedighimoghaddam, *Sensing and Bio-Sensing Research*, 2016, **9**, 17-22.

145. C. Parolo, A. de la Escosura-Muñiz, E. Polo, V. Grazú, J. M. de la Fuente and A. Merkoçi, *ACS Applied Materials & Interfaces*, 2013, **5**, 10753-10759.

146. C. Oliver, in *Immunocytochemical Methods and Protocols*, eds. C. Oliver and M. C. Jamur, Humana Press, Totowa, NJ, 2010, pp. 375-380.

147. H. M. Zakaria, A. Shah, M. Konieczny, J. A. Hoffmann, A. J. Nijdam and M. E. Reeves, *Langmuir*, 2013, **29**, 7661-7673.

148. R. van Vught, R. J. Pieters and E. Breukink, *Computational and Structural Biotechnology Journal*, 2014, **9**, e201402001.

149. M. Sajid, A.-N. Kawde and M. Daud, *Journal of Saudi Chemical Society*, 2015, **19**, 689-705.

150. S. L. Seurynck-Servoss, C. L. Baird, K. D. Rodland and R. C. Zangar, in *Front Biosci*, 2007, vol. 12, pp. 3956-3964.

151. S. F. Yang, B. Z. Gao, H. Y. Tsai and C. B. Fuh, *Analyst*, 2014, **139**, 5576-5581.

152. W. Fakanya and I. Tothill, *Biosensors*, 2014, **4**, 340.

153. A. SCHWARTZ, CLINICAL CHEMISTRY, 1990.

154. L. Blanco-Covian, V. Montes-Garcia, A. Girard, M. T. Fernandez-Abedul, J. Perez-Juste, I. Pastoriza-Santos, K. Faulds, D. Graham and M. C. Blanco-Lopez, *Nanoscale*, 2017, **9**, 2051-2058.

155. J. Taylor, A. Huefner, L. Li, J. Wingfield and S. Mahajan, *Analyst*, 2016, **141**, 5037-5055.

156. V. Mailänder and K. Landfester, *Biomacromolecules*, 2009, **10**, 2379-2400.

157. L. Shang, K. Nienhaus and G. U. Nienhaus, *Journal of Nanobiotechnology*, 2014, **12**, 5-5.

158. K. Murugan, Y. E. Choonara, P. Kumar, D. Bijukumar, L. C. du Toit and V. Pillay, *International Journal of Nanomedicine*, 2015, **10**, 2191-2206.

159. I. R. Nabiev, H. Morjani and M. Manfait, *European biophysics journal : EBJ*, 1991, **19**, 311-316.
160. C. A. Auchinvole, P. Richardson, C. McGuinnes, V. Mallikarjun, K. Donaldson, H. McNab and C. J. Campbell, *ACS Nano*, 2012, **6**, 888-896.
161. M. F. Escoriza, J. M. VanBriesen, S. Stewart and J. Maier, *Applied spectroscopy*, 2007, **61**, 812-823.
162. Y. H. Ong, M. Lim and Q. Liu, *Opt Express*, 2012, **20**, 22158-22171.
163. Z. Zhai, F. Zhang, X. Chen, J. Zhong, G. Liu, Y. Tian and Q. Huang, *Lab on a Chip*, 2017, **17**, 1306-1313.
164. R. Stevenson, S. McAughtrie, L. Senior, R. J. Stokes, H. McGachy, L. Tetley, P. Nativo, J. M. Brewer, J. Alexander, K. Faulds and D. Graham, *Analyst*, 2013, **138**, 6331-6336.
165. C. E. Talley, L. Jusinski, C. W. Hollars, S. M. Lane and T. Huser, *Analytical Chemistry*, 2004, **76**, 7064-7068.
166. M. Schieber and N. S. Chandel, *Current biology : CB*, 2014, **24**, R453-R462.
167. J.-M. Lü, P. H. Lin, Q. Yao and C. Chen, *Journal of Cellular and Molecular Medicine*, 2010, **14**, 840-860.
168. J. A. Imlay, *Nat Rev Micro*, 2013, **11**, 443-454.
169. P. D. Ray, B.-W. Huang and Y. Tsuji, *Cellular signalling*, 2012, **24**, 981-990.
170. L.-L. Qu, D.-W. Li, L.-X. Qin, J. Mu, J. S. Fossey and Y.-T. Long, *Analytical Chemistry*, 2013, **85**, 9549-9555.
171. Z. Movasaghi, S. Rehman and I. U. Rehman, *Applied Spectroscopy Reviews*, 2007, **42**, 493-541.
172. D. Naumann, 1998.
173. A. Uzman, *Biochemistry and Molecular Biology Education*, 2003, **31**, 212-214.
174. R. Malini, K. Venkatakrishna, J. Kurien, K. M. Pai, L. Rao, V. B. Kartha and C. M. Krishna, *Biopolymers*, 2006, **81**, 179-193.
175. S. McAughtrie, K. Lau, K. Faulds and D. Graham, *Chemical Science*, 2013, **4**, 3566-3572.
176. C. Gorrini, I. S. Harris and T. W. Mak, *Nat Rev Drug Discov*, 2013, **12**, 931-947.
177. N. Stone, C. Kendall, J. Smith, P. Crow and H. Barr, *Faraday discussions*, 2004, **126**, 141-157; discussion 169-183.
178. H. Pelicano, D. Carney and P. Huang, *Drug Resistance Updates*, 2004, **7**, 97-110.
179. K. Haidara, I. Morel, V. Abaléa, M. Gascon Barré and F. Denizeau, *Biochimica et Biophysica Acta (BBA) - Molecular Cell Research*, 2002, **1542**, 173-185.
180. K. Ketola, P. Vainio, V. Fey, O. Kallioniemi and K. Iljin, *Molecular cancer therapeutics*, 2010, **9**, 3175-3185.
181. S. S. Wijeratne, S. L. Cuppett and V. Schlegel, *Journal of agricultural and food chemistry*, 2005, **53**, 8768-8774.
182. E. Brauchle, S. Thude, S. Y. Brucker and K. Schenke-Layland, 2014, **4**, 4698.

Appendix
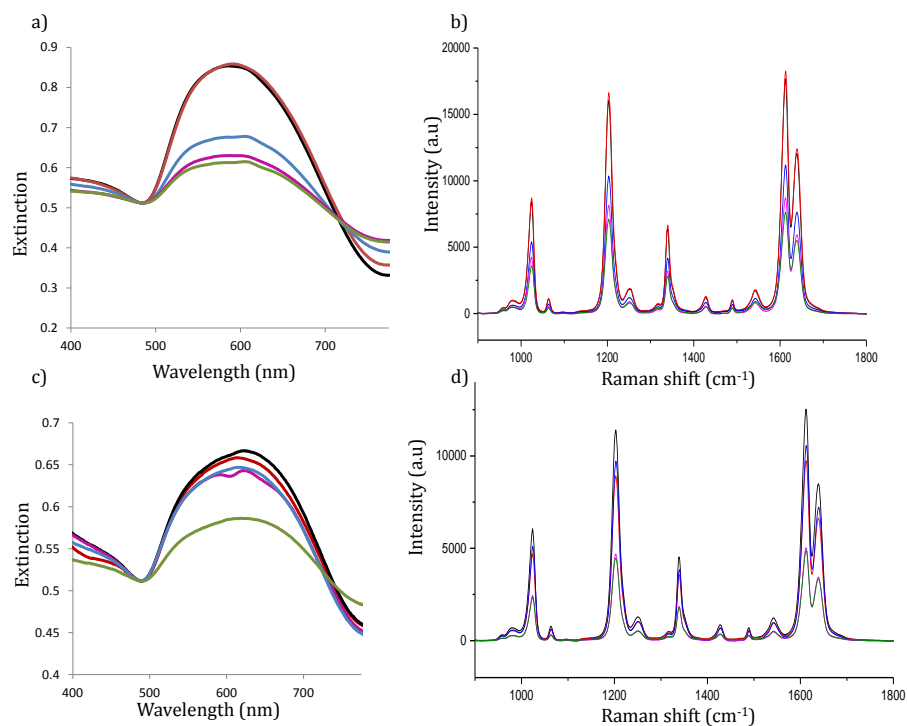
Figure 8.1 Extinction spectra of (a) Cabot nanotags and (b) Cabot-Pt nanotags and SERS signal from (c) Cabot nanotags and (b) Cabot-Pt nanotags in water after day 1 (black), day 7 (red), day 14 (blue), day 21 (pink) and day 28 (green). Spectra taken using a 785 nm laser excitation, 5 second acquisition time and a 4.5 mV laser power. Spectra were baseline corrected using Matlab.
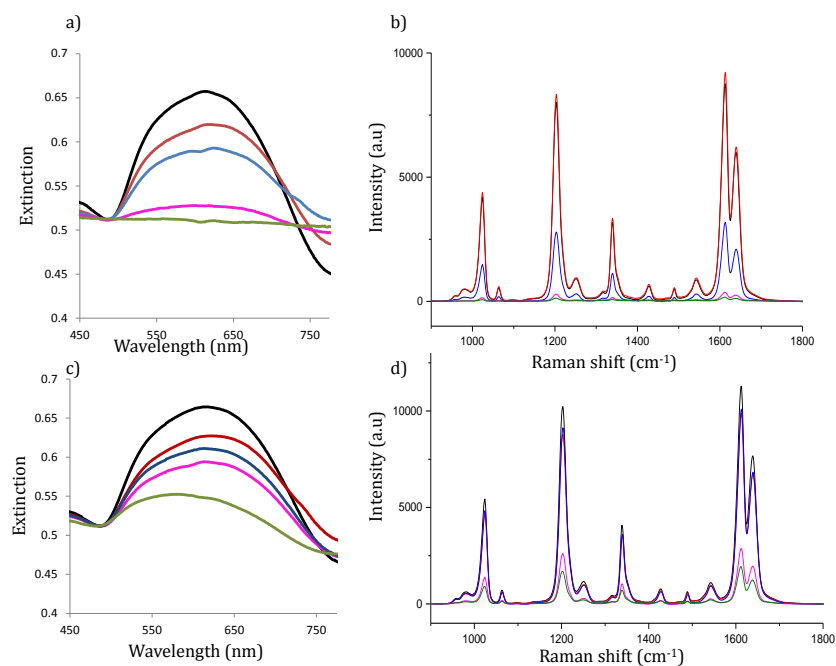
Figure 8.2 Extinction spectra of (a) Cabot nanotags and (b) Cabot-Pt nanotags and SERS signal from (c) Cabot nanotags and (b) Cabot-Pt nanotags in 1 M of NaCl after day 1 (black), day 7 (red), day 14 (blue), day 21 (pink) and day 28 (green). Spectra taken using a 785 nm laser excitation, 5 second acquisition time and a 4.5 mV laser power. Spectra were baseline corrected using Matlab.
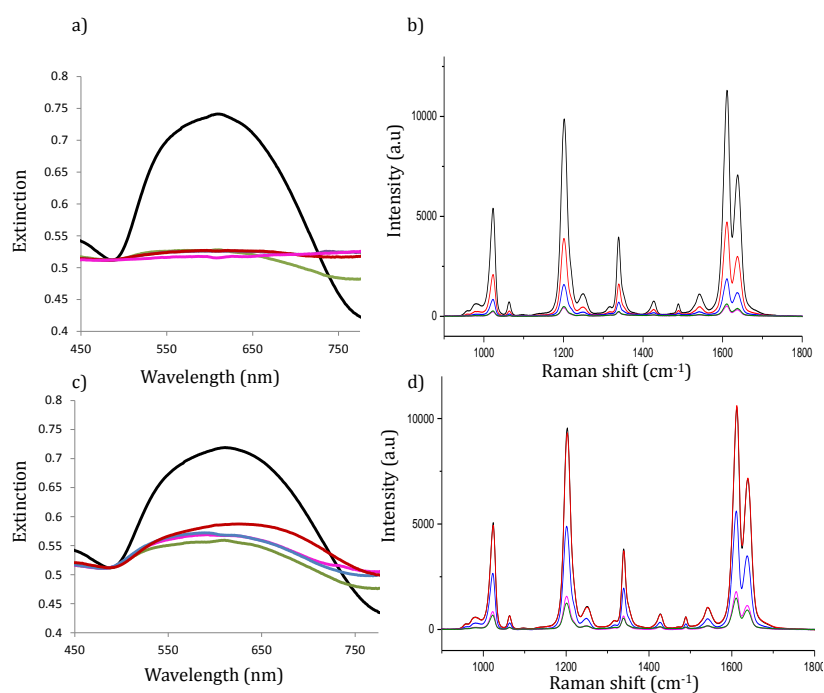
Figure 8.3 Extinction spectra of (a) Cabot nanotags and (c) Cabot-Pt nanotags and SERS signal from (b) Cabot nanotags and (d) Cabot-Pt nanotags in 1 M of NaOH after day 1 (black), day 7 (red), day 14 (blue), day 21 (pink) and day 28 (green). Spectra taken using a 785 nm laser excitation, 5 second acquisition time and a 4.5 mV laser power. Spectra were baseline corrected using Matlab.
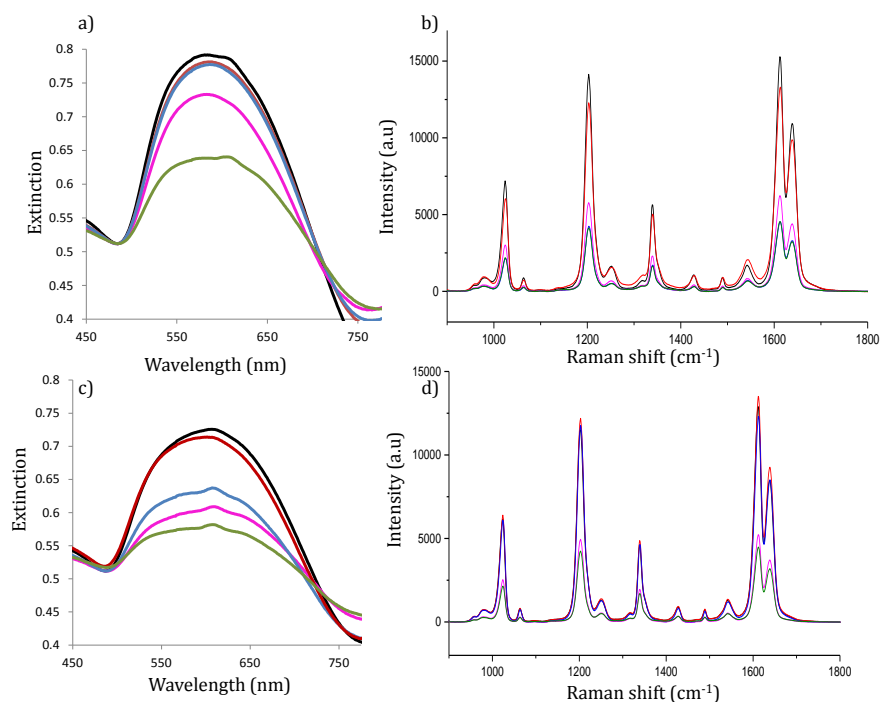
Figure 8.4 Extinction spectra of (a) Cabot nanotags and (c) Cabot-Pt nanotags and SERS signal from (b) Cabot nanotags and (d) Cabot-Pt nanotags in 1 M of H_2O_2 after day 1 (black), day 7 (red), day 14 (blue), day 21 (pink) and day 28 (green). Spectra taken using a 785 nm laser excitation, 5 second acquisition time and a 4.5 mV laser power. Spectra were baseline corrected using Matlab
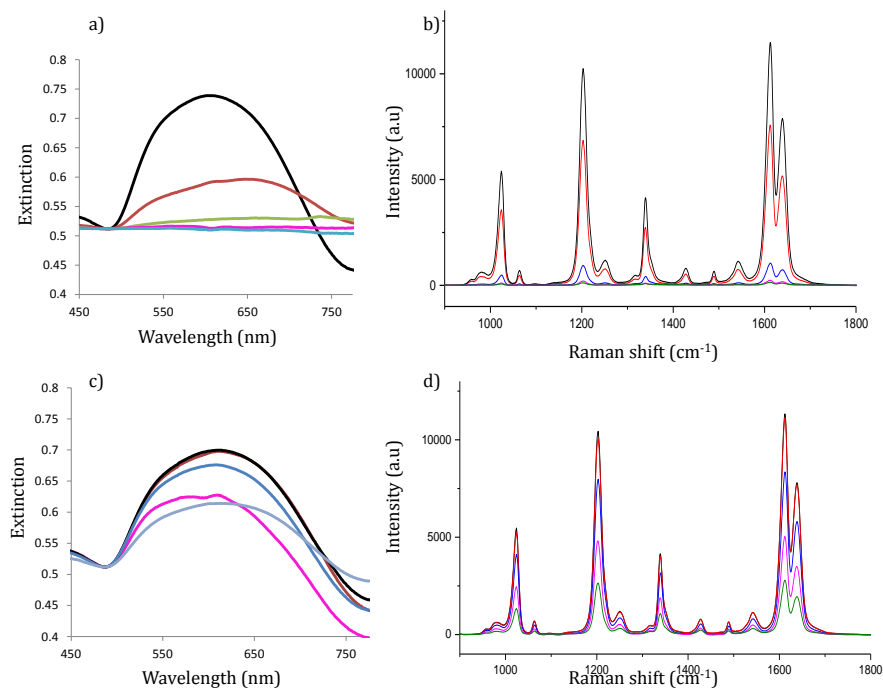
Figure 8.5 Extinction spectra of (a) Cabot nanotags and (c) Cabot-Pt nanotags and SERS signal from (b) Cabot nanotags and (d) Cabot-Pt nanotags in 1 M of HCl after day 1 (black), day 7 (red), day 14 (blue), day 21 (pink) and day 28 (green). Spectra taken using a 785 nm laser excitation, 5 second acquisition time and a 4.5 mV laser power. Spectra were baseline corrected using Matlab

Publications

1. *A novel nanozyme assay utilising the catalytic activity of silver nanoparticles and SERRS*
   S. Sloan-Dennison, S. Laing, N. Shand, D. Graham and K. Faulds
   Analyst, 2017, **142**, 2484-2490

2. *Resonance Raman detection of glutathione using an iron oxide nanoparticle catalysed decolourisation assay*
   S. Sloan-Dennison, N. Shand, D. Graham and K. Faulds (under review)